

THE STUDY OF THE BETA TO GAMMA PHASE TRANSFORMATION IN  
HIGH-Nb Ti-Al-Nb ALLOYS

By

SONALIKA GOYEL

A DISSERTATION PRESENTED TO THE GRADUATE SCHOOL  
OF THE UNIVERSITY OF FLORIDA IN PARTIAL FULFILLMENT  
OF THE REQUIREMENTS FOR THE DEGREE OF  
DOCTOR OF PHILOSOPHY

UNIVERSITY OF FLORIDA

2011

© 2011 SONALIKA GOYEL

To  
My father, mother and late Dr. Fereshteh Ebrahimi

## ACKNOWLEDGMENTS

First and foremost I thank my advisor Late Dr. Fereshteh Ebrahimi, who guided me for 4.5 years of my PhD. She invested long hours of discussions and analysis in this work and gave me extremely valuable suggestions. I will forever be indebted to her for all that I learnt from her in the past few years. Without her constant encouragement, challenging my ideas, critical input and belief in me, this work would not have been possible. She was an exceptionally great advisor and stands to be one of the few most influential people in my life.

I would also like to thank Dr. Martin Glicksman, for kindly consenting to be my advisor as Dr Ebrahimi's health was deteriorating. His suggestions and remarks really helped me put together loose ends of my work, in its final stage. I thank him for the time he invested in going through my thesis and providing insight into making it more coherent. Without his contribution, I may not have been able to finish my work so promptly after the demise of my advisor Dr. Fereshteh Ebrahimi.

I thank my committee members- Dr. Valentin Craciun, Dr. Michele Manuel, Dr. Ghatu Subhash and Dr. Nagaraj Arakere for their valuable time and inputs to my work. I am grateful for their support and valuable suggestions to improve my work.

I deeply appreciate the support of my family- my father Mr. Jawahar Goyel, mother Asha Goyel, sister Rupalika and brother Utkarsh. Their constant encouragement during all the ups and downs during this Phd and in general throughout my life is commendable. I owe a lot to my parents, for the sacrifices they made, for the virtues they taught and the understanding they showed. A special thank goes out to my father for being my guide in life, believing in me and to both my parents for being my good friends.

I thank my colleagues Orlando Rios and Michael Kesler who started on this project with me in 2006. I thank Orlando for the insightful discussions and for supporting me in my work. I am thankful to Michael for making long hours of work in the lab so much more fun and easy and for helping with research equipment in the lab. The hours of meetings and discussions we all had were very helpful in our research and in building an understanding of the various aspects of the project. I thank my colleague Yanli Wang for helping me set my foothold in the lab and in research when I had just started my work while she was on her way out of the group after her PhD. Apart from the research work, I thank my group members - Orlando, Michael, Mahesh, Sankara and Daniel for the great rapport we all shared and for making the 4 years of my PhD truly cherishable.

I am thankful to my friend Satyajit Phadke for being there in hours of need and for being a good companion through the ups and downs of PhD with me. I am grateful to my friend Avidipto Biswas for being a caring and supporting friend. I really thank him for lending a friendly ear at all times and for giving me great advice. I am thankful to Shruti Seshadri for her constant help, care and affection. I thank my friends Adhish Majumdar and Ravi Vasudevan for their friendship all these years. Without the help, support, encouragement and insight of all these people, this work would not have been the same and the 4 years of my PhD would not have been as memorable.

Last but not the least I would like to acknowledge NSF and AFOSR for their continuous financial support through grant numbers DMR-0605702 and DMR-0856622 for this research.

# TABLE OF CONTENTS

	<u>page</u>
ACKNOWLEDGMENTS.....	4
TABLE OF CONTENTS .....	6
LIST OF TABLES.....	9
LIST OF FIGURES.....	10
ABSTRACT .....	15
CHAPTER	
1 INTRODUCTION AND BACKGROUND .....	18
1.1 Introduction .....	18
1.2 Background .....	24
1.2.1 TiAlNb Ternary System .....	24
1.2.2 $\alpha_2+\gamma$ Alloys .....	25
1.2.3 $\gamma+\sigma$ Alloys .....	28
1.2.4 Phases of Interest.....	30
2 EXPERIMENTAL PROCEDURES.....	41
2.1 Materials Used .....	41
2.2 Heat Treatments .....	42
2.3 Characterization Techniques.....	44
2.4 Sample Preparation.....	45
2.4.1 Optical Microscopy .....	45
2.4.2 Scanning Electron Microscopy (SEM) and Electron Probe Micro- Analysis (EPMA).....	46
2.4.3 X-Ray Diffraction .....	46
2.4.4 Differential Scanning Calorimetry (DSC) .....	47
2.4.5 Transmission Electron Microscopy (TEM) .....	48
3 THE NATURE OF THE $\beta$ -TO- $\gamma$ PHASE TRANSFORMATION .....	49
3.1 Introduction .....	49
3.2 Selection of Alloys.....	49
3.3 As-Cast .....	50
3.3.1 Microstructural Analysis.....	50
3.3.2 Morphology of the $\gamma$ -Phase .....	52
3.3.3 Compositional Analysis .....	53
3.4 Thermal Analysis.....	54
3.5 Solutionized-Water Quenched (WQ).....	55

3.5.1	Microstructural Analysis.....	55
3.5.2	Rate of Formation of the $\gamma$ -Phase .....	56
3.5.3	Transformation Sequence Upon Quenching .....	58
3.6	Effect of Composition on the Retention of the $\beta$ -Phase Upon Quenching .....	59
3.7	$\beta \rightarrow \gamma$ Phase Transformations at High Temperatures.....	62
3.8	Effect of $\beta$ -Phase Grain Boundaries on the Nucleation of the $\gamma$ -Phase .....	66
4	TWO STEP NUCLEATION OF $\gamma$ -PHASE FROM $\beta$ -PHASE.....	101
4.1	Introduction .....	101
4.2	Transformation Under the First DSC Peak on the Cooling Curve .....	103
4.2.1	Continuous Cooling (CC) Heat Treatments .....	103
4.2.1.1	Solutionized-CC1350C-WQ.....	104
4.2.1.2	Solutionized-CC1305C-WQ.....	105
4.3	Transformation Under the Second DSC Peak.....	106
4.3.1	Continuous Cooling (CC) Heat Treatment.....	106
4.3.2	Double Heat Treatment (DHT).....	107
4.3.3	TEM Analysis of the Secondary $\gamma$ -Phase Morphology (B) .....	108
4.4	Aging Heat Treatment .....	110
4.5	Discussion.....	110
5	EFFECT OF CHROMIUM ADDITION ON THE $\beta$ -TO- $\gamma$ PHASE TRANSFORMATION .....	132
5.1	Introduction .....	132
5.2	Selection of the $\beta$ -Stabilizer.....	133
5.3	Alloy 11-5Cr .....	134
5.3.1	As-Cast.....	134
5.3.2	Thermal Analysis .....	135
5.3.3	Solutionized-WQ.....	136
5.3.4	Transformations Under the DSC Peaks .....	137
5.3.5	Aged.....	138
5.4	Alloy 12 .....	139
5.5	Alloys 12-xCr.....	141
5.5.1	As-Cast.....	141
5.5.2	Solutionized-WQ.....	142
5.5.3	Double Heat Treatment (DHT).....	143
5.6	Discussion.....	144
6	EFFECT OF BORON ON THE $\beta$ -TO- $\gamma$ PHASE TRANSFORMATION.....	167
6.1	Introduction .....	167
6.2	Alloys 11-5Cr+xwt%B.....	168
6.2.1	As-Cast.....	169
6.2.2	Solutionized-WQ.....	169
6.3	Alloys 41 and 41+xwt%B.....	170
6.3.1	As-Cast .....	170

6.3.2	Solutionized-WQ.....	170
6.3.3	DTA Studies .....	172
6.3.4	Continuous Cooling Heat Treatments.....	172
6.4	Discussion.....	174
7	SUMMARY .....	189
8	FUTURE WORK .....	193
	LIST OF REFERENCES .....	195
	BIOGRAPHICAL SKETCH.....	203

## LIST OF TABLES

<u>Table</u>		<u>page</u>
3-1	Nominal and actual compositions of alloy 11 as measured by the EPMA .....	75
3-2	Compositions of the phases in the as-cast alloy 1 measured by the EPMA .....	75
3-3	Actual compositions of alloy 21 and 31 as measured by the EPMA (at%) .....	85
3-4	EPMA compositions of the phases in the DHT samples of alloy 11 .....	97
4-1	Compositions of phases in CC1350 sample of alloy 11.....	119
4-2	Compositions of phases in DHT1240 sample of alloy 11 .....	125
5-1	EPMA compositional analysis of alloy 11-5Cr DHT1320/2h sample.....	152
5-2	EPMA compositional analysis of alloy 12-5Cr DHT1200/2h sample.....	164

## LIST OF FIGURES

<u>Figure</u>	<u>page</u>
1-1	Graph showing the high temperature data of tests performed on $\gamma+\sigma$ alloys in comparison to $\alpha_2+\gamma$ alloys [83-85]..... 34
1-3	A isothermal section of the TiAlNb ternary superimposed over the liquidus and depicting the selected region for $\gamma+\sigma$ alloy selection[24]..... 35
1-4	An 1100 C isothermal section of the TiAlNb ternary depicting regions of $\alpha_2+\gamma$ and $\gamma+\sigma$ alloys..... 36
1-5	Unit cell of ordered $\beta/B2$ phase. A) disordered. B) ordered ..... 37
3-1	Isopleth section of the TiAlNb ternary at constant Al mole fraction of 0.45 depicting the transformation path of alloy 11[24] ..... 70
3-2	Schematic of an arc melted button showing the sectioned slice that was used for compositional and microstructural analysis of the as cast alloy 11..... 71
3-3	BSE micrograph of the as cast sample of alloy 11 depicting the presence of dendrites..... 71
3-4	Alloy 11, as-cast. .... 72
3-5	XRD profile of a powdered sample of the as-cast alloy 11 ..... 73
3-6	Alloy 11, as-cast. A) Optical micrograph showing $\gamma$ -phase laths emerging from prior $\beta$ -phase grain. B) BSE micrograph depicting colonies of $\gamma$ -laths ..... 74
3-7	DSC plot of the final run of alloy 11 sample..... 75
3-8	Optical micrograph of solutionized-WQ alloy 11 showing large $\beta$ -phase grains that grew upon solutionizing ..... 76
3-9	Alloy 11, solutionized-WQ. .... 77
3-10	XRD profile of a powdered sample of solutionized-WQ alloy 11..... 78
3-11	Alloy 11, solutionized-WQ. A) TEM BF micrograph showing the $\gamma$ -phase laths. B) Corresponding diffraction pattern of the $\gamma$ laths at $\gamma[110]$ zone axis..... 79
3-12	BSE micrograph of solutionized-WQ alloy 11 ..... 80
3-13	Alloy 11, solutionized-WQ. A) TEM BF micrograph showing APBs in the $\beta$ -phase matrix. B) Corresponding diffraction pattern of the $\beta$ -phase matrix..... 81

3-14	TEM BF image from solutionized-WQ alloy 11 showing fine APBs indicating extensive ordering in the $\beta$ -phase.....	82
3-15	Alloy 11, solutionized-WQ. A) TEM BF image $\alpha$ -phase and APBs in the $\beta$ -phase matrix. B) Corresponding diffraction pattern of the $\beta$ -phase matrix.....	83
3-16	Alloy 11, solutionized-WQ. A) TEM BF image showing APBs passing through the $\alpha$ -phase plates. B) Corresponding diffraction pattern of the $\alpha$ -phase.....	84
3-17	Optical micrographs of as-cast microstructure of alloy 21. A) top region showing equiaxed $\beta$ -phase grains. b) bottom region showing columnar $\beta$ .....	86
3-18	Optical micrograph from the top region of the as-cast button of alloy 31 showing equiaxed $\beta$ -phase grains and fine $\gamma$ -phase laths.....	87
3-19	DSC profiles showing temperatures chosen for solutionizing. A) Alloy 21. B) Alloy 31.....	88
3-20	Alloy 21, solutionized-WQ. A) BSE micrograph showing a single $\beta$ -phase. B) XRD profile taken on a powdered sample .....	89
3-21	Alloy 31, solutionized-WQ. A) Optical micrograph showing fine $\gamma$ -phase laths at the $\beta$ -phase grain boundaries; inset-low magnification image .....	90
3-22	A schematic showing the heat treatment schedule performed on alloy 11 sample (DHT1350/2h) .....	91
3-23	XRD profile taken on a powdered sample of DHT1350/2hsample of alloy 11 ....	92
3-24	Alloy 11 DHT1350/2h. A) BSE image showing coarse Widmanstätten $\gamma$ -laths;. B) Optical images showing $\gamma$ -phase allotriomorphs.....	93
3-25	Optical image from DHT1350/2h sample of alloy 11 showing square and rectangular cross section of the $\gamma$ -phase laths.....	94
3-26	Alloy 11 DHT1350/2h. A) Optical image showing ledges in the $\gamma$ -laths. B) TEM BF image showing ledges in the $\gamma$ -phase laths .....	95
3-27	Alloy 11 DHT1350/5h. A) BSE image showing $\gamma$ laths and dark high Al $\gamma$ -allotriomorphs at the $\beta$ -grain boundary. B) Optical image from DHT1350/5h ....	96
3-28	Polarized light micrographs of alloy 11 DHT1350/5h. A) at +45degree rotation of the wave-plate. B) at -45degree rotation of the wave-plate .....	98
3-29	Optical micrographs of alloy 11, solutionized-WQ. A) single crystal sample. B) images from single and poly crystal sample.....	99

3-30	Optical images from CC1350 single crystal sample of alloy 11 showing $\gamma$ -lath nucleating at the sample surface .....	100
3-31	DSC plot of the final run of alloy 11 single crystal.....	100
4-1	DSC curve of alloy 11 showing the expected transformation path of the alloy upon cooling .....	115
4-2	BSE micrographs of a solutionized and slow cooled (at 9K/min) sample of alloy 11 showing a two phase microstructure .....	115
4-3	XRD plot of a powdered sample of solutionized- slow cooled alloy 11 .....	116
4-4	Optical micrographs of alloy 11, solutionized-slow cooled. A) Primary Widmanstätten morphology. B) The secondary lamellar-like morphology .....	117
4-5	Alloy 11 CC1350. A) BSE micrograph showing denuded zones B) Optical micrographs showing Widmanstätten $\gamma$ -phase laths C) Optical micrograph ....	119
4-6	BSE micrograph from the CC1305 sample of alloy 11 Widmanstätten $\gamma$ -phase laths (dark) and the quenched $\gamma$ -phase;.....	120
4-7	XRD plot of a powdered sample of CC1240 sample of alloy 11 .....	120
4-8	BSE micrograph from the CC1240 sample of alloy 11 showing a two phase microstructure.....	121
4-9	Optical micrographs of alloy 11CC1240. A) Coarse primary Widmanstätten $\gamma$ -phase. B) Lamellar morphology of the $\gamma$ -phase. C) Lamellar morphology .....	122
4-10	XRD plot of a powdered sample of DHT1240 sample of alloy 11 .....	123
4-11	BSE micrograph from the DHT11240 sample of alloy 11 showing the coarse primary Widmanstätten $\gamma$ -phase laths nucleating at the $\beta$ grain boundaries .....	123
4-12	Optical micrographs of alloy 11DHT1240/2h. A) Lamellar morphology of the $\gamma$ -phase. B) Higher magnification. C) Lamellar morphology.....	125
4-13	TEM micrographs from the CC1240 sample of alloy 11 showing (a) diffraction pattern from the $\gamma$ -lath along the $[112]_{\gamma}$ zone axis;(b)&(c) BF and DF images..	126
4-14	TEM micrographs from the CC1240 sample of alloy 11.A) diffraction pattern from the $\beta$ -matrix. B)&C)BF and DF images.....	127
4-15	TEM micrographs of the CC1240 sample showing APBs in the $\beta$ matrix .....	128
4-16	TEM micrographs from the CC1240 sample of alloy 11 showing APBs in the $\beta$ matrix. A) Lower magnification. B) Higher magnification .....	128

4-17	TEM micrographs from the CC1240 sample of alloy 11 showing lamellar-like morphology (B) growing between the coarse $\gamma$ -laths (A) .....	129
4-18	Alloy 11 aged at 1200C/2h. A) BSE micrograph showing a two phase $\gamma+\sigma$ microstructure. B) XRD plot from a powdered sample.....	130
4-19.	Schematic showing the plate-like morphology of the secondary $\gamma$ -phase (B) growing over the existing primary Widmanstätten $\gamma$ -phase laths (A) .....	131
5-1.	Alloy 11-5Cr as-cast. A) BSE micrograph. B) XRD profile of a powdered sample.....	147
5-2	Optical micrograph of alloy 11-5Cr as-cast. A) Bottom of the sample. B) Top of the sample .....	148
5-3	DSC profile of the final run of alloy 11-5Cr .....	149
5-4	Alloy 11-5Cr solutionized-WQ. A) Optical micrograph. B) BSE micrograph of the matrix.....	150
5-5	TEM BF micrographs of the matrix of solutionized-WQ alloy 11-5Cr showing orthorhombic plates in the $\beta$ -matrix .....	151
5-6	XRD profile of the powdered sample of solutionized-WQ alloy 11-5Cr.....	151
5-7	Optical micrograph from the DHT1320 sample alloy 11-5Cr .....	152
5-8	Optical micrographs of alloy 11-5Cr solutionized-slow cooled. A) Low magnification. B) Higher magnification .....	153
5-9	BSE micrograph of aged sample of alloy 11-5Cr.....	154
5-10	BSE micrographs of alloy 12. A) As-cast. B) BSE. ....	155
5-11.	XRD profiles of the as-cast and solutionized-WQ samples of alloy 12.....	156
5-12	Alloy 12 DHT1340/6h. A) BSE micrograph. B) Corresponding XRD profile of a powdered sample. ....	157
5-13	Alloy 12-1.5Cr as-cast. A) Optical micrograph. B) Corresponding XRD plot of a powdered sample .....	158
5-14	Alloy 12-3.5Cr as-cast. A) Optical micrograph. B) Corresponding XRD plot of a powdered sample .....	159
5-15	Alloy 12-5Cr as-cast. A) Optical micrograph. B) Corresponding XRD plot of a powdered sample. ....	160

5-16	Optical micrographs of solutionized-WQ alloy 12-1.5Cr .....	161
5-17	Optical micrographs of solutionized-WQ alloy 12-3.5Cr .....	161
5-18	Optical micrograph of solutionized-WQ alloy 12-5Cr .....	162
5-19	XRD plot of a powdered sample of alloy 12-5Cr in the solutionized-WQ condition .....	162
5-20	Alloy 12-5Cr DHT1200/2h. A) BSE micrograph. B)Corresponding XRD plot of a powdered sample. ....	163
5-21	DSC profiles of alloys 12 and 12-5Cr [92] .....	165
5-22	DSC profiles of alloys 11 and 11-5Cr .....	166
6-1	Optical micrographs of alloys 11-5Cr and 11-5Cr+xwt%B in the as-cast condition .....	179
6-2	Optical micrographs of alloys 11-5Cr and 11-5Cr+xwt%B in the solutionized- WQ state .....	180
6-3	XRD profiles of alloys 11-5Cr and 11-5Cr+xwt%B in the solutionized-WQ condition .....	181
6-4	Optical micrographs of alloys 41 and 41+xwt%B in the as-cast condition .....	182
6-5	Optical micrographs of alloys 41and 41+xwt%B in the solutionized-WQ state..	183
6-6	BSE micrographs from alloy 41+0.01 wt%B in the solutionized-WQ state, showing presence of fine borides .....	184
6-7	XRD profiles of alloys 41 and 41+xwt%B in the solutionized-WQ condition .....	185
6-8	DSC plots. A) Alloy 41. B) Alloy 41+0.005wt%B.....	186
6-9	Optical micrographs from CC1280 samples. A) Alloy 41. B) Alloy 41+0.005wt%B .....	187
6-10	Micrographs from CC1050 samples. A) Alloy 41. B) Alloy 41+0.005 wt%B.....	188

Abstract of Dissertation Presented to the Graduate School  
of the University of Florida in Partial Fulfillment of the  
Requirements for the Degree of Doctor of Philosophy

THE STUDY OF THE BETA TO GAMMA PHASE TRANSFORMATION IN HIGH-NB TI-  
AL-NB ALLOYS

By

SONALIKA GOYEL

August 2011

Chair: Martin Glicksman

Major: Materials Science and Engineering

TiAl-based alloys with an  $\alpha_2+\gamma$  microstructure have been studied extensively for their potential applications in aerospace turbine engines, due primarily to their attractive strength-to-weight ratio, and high- and room-temperature properties. These alloys are, however, limited in their maximum service temperature and room-temperature toughness. Additions of Nb, leading to a  $\sigma+\gamma$  microstructure instead, has been shown to improve considerably the high-temperature properties of these alloys.  $\beta$ -phase remains the single high-temperature phase in these alloys, and complete quenching of  $\beta$ -phase to room temperature is required for further evolution of the  $\gamma+\sigma$  microstructure upon subsequent aging. The formation of large phase fractions of  $\gamma$ -phase upon quenching, however, was found to be unavoidable at prior  $\beta$ -phase grain boundaries in the alloys studied. Thus, it became important to study the  $\beta$ -to  $\gamma$ -phase transformation in order to be able to inhibit, or control, the formation of  $\gamma$ -phase upon quenching.

Several specifically chosen alloys were prepared by arc melting and were studied under different heat treatments. These heat treatments were designed specifically to understand the nature of transformation of the  $\beta$ -to  $\gamma$ -phase, by using various

temperature ramp rates. Detailed microstructural evaluation was carried out using optical, scanning electron microscopy (SEM) and transmission electron microscopy (TEM) in order to understand the evolution of microstructure and explain the morphology of the phases. X-ray diffraction (XRD) techniques were also employed for phase identification, in addition to TEM. Differential scanning calorimetry (DSC) analyses were carried out to measure transformation temperatures and evaluate phase stabilities. This research was aimed at the nature of the  $\beta$ -to- $\gamma$  phase transformation, including its kinetics, effects of composition, grain boundaries, and surfaces—both internal and external. Further, in order to inhibit the formation of  $\gamma$ -phase upon quenching the  $\beta$ -phase, the influence of Cr-a  $\beta$ -stabilizer-and the effects of boron segregation were also studied.

This research shows that the  $\beta$  grain boundaries always act as the preferred nucleation sites for  $\gamma$ -phase formation upon quenching as well as during slower cooling. The  $\alpha$ -phase was observed to form with a Widmanstätten lath morphology at all temperatures and cooling rates, including high temperatures and slow cooling rates. In the absence of any grain boundaries, the sample surfaces act as the preferred nucleation sites for the Widmanstätten  $\gamma$ -phase. The  $\gamma$ -phase was observed to nucleate in two distinct stages upon cooling at relatively slower rates, and produced two morphologies: 1) Widmanstätten laths and 2) a plate-like  $\gamma$ -phase morphology. The  $\sigma$ -phase did not form upon slow cooling to room temperature, as was predicted by thermodynamic calculations. Aging a quenched  $\beta$ -phase, however, yielded a  $\gamma$ + $\sigma$  microstructure. It was noted that additions of as little as 1.5 at% Cr could drastically reduce the  $\gamma$ -phase volume fraction, primarily by slowing its growth rate. Alloys with low

amounts of boron additions were studied to investigate the effect of  $\beta$  grain boundary 'poisoning' on  $\gamma$ -phase formation upon quenching. Boron additions were shown to increase the nucleation rate of the  $\gamma$ -phase at the  $\beta$ -phase grain boundaries.

# CHAPTER 1 INTRODUCTION AND BACKGROUND

## 1.1 Introduction

The aerospace industry employs gas turbine engines in order to extract maximum power and achieve high fuel efficiency at high speeds. These jet engines are specifically designed for use at high temperatures and pressures produced by controlled fuel combustion and high rotary engine speeds. The enhancement of the performance, namely higher speeds and fuel efficiency of the turbine, depends on reaching higher service temperatures, higher rotary speeds, and reduced total weight of the engine. Apart from improvements in component design, these engineering requirements call for a material that can withstand high temperatures, provide good creep properties and a high strength/weight ratio, all at the same time.

Ni-based superalloys are being used in the high-temperature high-pressure regions of gas turbine engines, because of their excellent high-temperature strength and creep properties, and their microstructural stability. Ni-based superalloys as well provide acceptable room-temperature mechanical properties and good manufacturability. The high density of Ni-based superalloys, however, imparts high weight to the engine, thereby reducing its efficiency and performance. Thus, the need for materials with comparable, or even better, room- and high-temperature mechanical properties remains. Developing new superalloys, which have lower density can further improve the performance of jet engines, which currently poses a challenging problem for materials scientists.

Ti-alloys are long used in the aerospace industry due to their low density and high strength/weight ratio. Over the past three decades, Ti-Al intermetallics attracted

attention for their promising high-temperature properties and lower mass densities. However, Ti-alloys have a service temperature limitation (<800 C) and possess relatively poor room-temperature toughness. Various iterations have been made during the development of these alloys, including adding alloying elements, and at this point such alloys are employed in the low-pressure region of gas turbines.

Equimolar Ti-Al based alloys (near-TiAl) started as a simple binary system. These alloys in general occur as single  $\alpha$ -phase at elevated temperature, and upon cooling yield an  $\alpha_2+\gamma$  microstructure. Various microstructures may be generated using different heat treatments and cooling rates. A fully lamellar microstructure was found to be most suitable for high-temperature applications. However, the room-temperature toughness and ductility of these alloys was inadequate, and their high-temperature creep properties required further improvement. Nb additions were shown to improve these properties along with providing enhanced high-temperature oxidation resistance. Nb additions of up to 10 at% were subsequently made to optimize critical mechanical properties. Other alloying elements such as W, Ta, B, etc., were made in small amounts to induce required microstructural changes.

At higher Nb contents  $\sigma$ -phase forms, as was shown by various experimental and simulated phase diagram data. Studies performed by our research group on high-Nb alloys in this system showed that in the presence of high Nb content, the  $\alpha$ -phase is replaced by  $\beta$ -phase at high temperature, and upon cooling  $\sigma$  and  $\gamma$ -phases precipitate. It was shown that a two-phase  $\gamma+\sigma$  microstructure possessed better creep properties than did the near-TiAl ( $\alpha_2+\gamma$ ) alloys, even at temperatures as high as 1000 C, as shown in Figure 1-1. Nonetheless, their room temperature toughness needed further

improvement. The studied alloys contained about 60% volume fraction of  $\sigma$ -phase that was interconnected throughout the microstructure, whereas the rest of the microstructure constituted of the  $\gamma$ -phase. The research showed that a low volume fraction of disconnected  $\sigma$ -phase particles in a  $\gamma$ -matrix would further enhance the high temperature strength and creep. Also, high Nb content of the alloys would be helpful in improving the room-temperature toughness of these alloys.

The current project focuses on developing alloys with a single  $\beta$ -phase at high temperatures. This would impart forgeability to these alloys, which presents an inherent problem in near-TiAl alloys due to the presence of the hcp  $\alpha$ -phase. It would also allow better microstructural control in these alloys.  $\beta$ -phase must be retained to room temperature as a metastable phase upon quenching. The alloy should exist as two phase  $\gamma+\sigma$  at the engine's service temperatures, such that upon aging the quenched metastable  $\beta$ -phase a  $\gamma+\sigma$  microstructure is obtained. It is known that once the  $\gamma+\sigma$  microstructure forms, it is then stable to room temperatures due to limited diffusion, and no new phases are formed. The service-temperature microstructure should consist of ultrafine equiaxed  $\gamma$ -phase grains and nano-sized  $\sigma$ -phase grains distributed homogeneously throughout the microstructure, as illustrated in Figure 1-2. The ideal alloy is expected to have a low volume fraction of the  $\sigma$ -phase (<20%). Further, a high Al content (40-45 at%) is required for optimum high-temperature oxidation resistance. When alloys fulfilling the above requirements are selected using the most current calculated TiAlNb ternary phase diagram, a small section of the ternary is obtained as shown in Figure1-3.

The preliminary studies on such alloys showed that when the phase fraction of the  $\sigma$ -phase is low, then  $\gamma$  is the first phase to precipitate in the  $\beta$ -phase upon cooling.  $\sigma$ -phase forms at lower temperatures and finally a  $\gamma+\sigma$  two-phase microstructure is obtained. The simulated phase diagrams also suggest the same, as shown in Figure 3-1 depicting the isopleths at Al mole fraction of 0.45. Note that at suitable compositions, the alloy solidifies as single  $\beta$ -phase and, upon cooling, develops a  $\beta+\gamma$  two-phase region before the  $\sigma$ -phase is formed. However, upon quenching the alloys from the solutionizing temperature, none of the alloys retained the  $\beta$ -phase. A second phase ( $\gamma$ -phase) laths inevitably formed during quenching, most extensively in the microstructure that remained in the sample during aging. The presence of this relatively coarse phase and its lath morphology in the quenched samples hindered the formation of the required fine  $\gamma+\sigma$  microstructure that was aimed at, during aging. The orientation relationship between the  $\gamma$  and the  $\beta$ -phases imparted texturing to the microstructures due to the presence of the directional  $\gamma$ -phase laths that further deteriorated the mechanical properties of the samples.

Thus, in order to obtain the desired fine  $\gamma+\sigma$  microstructures, it was imperative that the  $\beta$ -phase be quenched to room temperature without the formation of any  $\gamma$ -phase. Limited work has been done on the study of the  $\beta$  to  $\gamma$  phase transformation and not much is known about the nature and kinetics of it. Most work in the past has been performed on the  $\alpha$  to  $\gamma$  phase transformation. Since the  $\gamma+\sigma$  alloys are in their early stages of research, an understanding of the  $\beta$  to  $\gamma$  phase transformation is required. This study was performed with an aim to investigate the nature of the  $\beta$  to  $\gamma$  phase

transformation, including its kinetics, and the effect of factors such as composition, cooling rate, grain boundaries, free surfaces, alloying additions and segregation.

Samples were prepared by arc melting high-purity elements in the desired composition into 5-10 g buttons. Microstructural analysis of as-cast, quenched and various other heat-treated samples was performed using standard microscopic techniques, including optical, polarized, scanning electron microscopy (SEM) in secondary and backscattered mode (BSE) and transmission electron microscopy (TEM) including bright field (BF), dark field (DF) and diffraction modes. Compositional data on the samples were obtained using electron probe micro-analysis (EPMA). Phase analysis was performed using x-ray diffraction (XRD) techniques on powdered samples. To obtain transformation temperatures, differential scanning calorimetry (DSC) tests were carried out on individual alloys. DSC was also used to study phase stability and the effect of alloying additions by employing different ramp rates during the tests.

Chapter 3 focuses on the nature of the  $\beta$  to  $\gamma$ -phase transformation. The kinetics of the  $\beta$  to  $\gamma$  phase transformation is discussed along with possible explanations for these observed kinetics. TEM techniques were employed to investigate the various transformations occurring in the  $\beta$ -phase upon quenching, namely, ordering, formation of the  $\gamma$ -phase and formation of the metastable  $\sigma$ -phase. Further, the effect of the presence of the  $\beta$ -grain boundaries are investigated using microscopy, heat treatments, and DSC by performing tests on single and polycrystal samples. The effect of composition on the formation of  $\gamma$ -phase upon quenching the  $\beta$ -phase is also illustrated.

During the study of the transformation path of an alloy upon cooling, it was discovered that  $\sigma$ -phase did not form upon slow cooling the sample, and a  $\beta+\gamma$

microstructure was obtained at room temperature. DSC data, however, showed the existence of two distinct transformation peaks upon cooling. A systematic study was performed for which specific heat treatments were designed and extensive microstructural analysis was carried out to elucidate the transformation occurring under the two DSC peaks. It was found that the two DSC peaks observed upon cooling were both related to the formation of the  $\gamma$ -phase. The details of the transformations occurring under the two peaks are presented in Chapter 4. The microstructures and morphologies obtained were examined using TEM techniques. Further, an explanation for the absence of the  $\sigma$ -phase in the slow-cooled structure is presented along with experimental evidence from aging heat treatments.

One of the main aims of this study was to be able to suppress the formation of the  $\gamma$ -phase upon quenching such that the  $\beta$ -phase could be quenched to room temperature for further aging treatments. Additions of Cr, a known  $\beta$ -phase stabilizer, were made to selected alloys in an attempt to stabilize the  $\beta$ -phase to lower temperatures such that the formation of the  $\gamma$ -phase would be inhibited. The results on the study are presented in Chapter 5. Evaluation of DSC data combined with microstructural analysis and EPMA is shown, and the effect of Cr addition on the stability of the two phases is discussed.

During the course of the study it was established that  $\beta$ -phase grain boundaries were the preferred nucleation sites for the nucleation of the  $\gamma$ -phase. Boron, a known segregant was added in small amounts to selected alloys such that it remained in solution. Effects of its addition on the nucleation of the  $\gamma$ -phase at the  $\beta$ -phase grain boundaries are discussed in Chapter 6. Although the results of the study are preliminary, they are clearly indicative of the effect of B on  $\gamma$  nucleation.

## 1.2 Background

### 1.2.1 TiAlNb Ternary System

The TiAlNb ternary system drew considerable attention due to the potential of developing low-density alloys with high-temperature applications that could replace the currently used Ni-based superalloys in aerospace turbine applications. Various equilibrium studies were performed in order to evaluate the phase diagram of the ternary system, the understanding of which at the time was limited. Due to the presence of many binary, ternary and metastable phases, the system was found to be immensely complicated for full comprehension of equilibrium studies. The initial studies were performed on diffusion couples of the alloys [1-3]. There were, however, various discrepancies in the data obtained by different researchers [4, 5]. Due to high temperatures involved and equipment limitations, most of the initial data were available only up to 1200 C. The compositional extent of the various phase fields was shown to be different in different studies performed depending on the particular methodology chosen: e.g., diffusion couple, as-cast microstructures, or heat-treated samples [3, 6-11]. Due to limited knowledge of the various phases and their stability, the evaluation of the microstructural data and its incorporation into the phase diagram was subject to interpretation [3-5, 12, 13]. The presence of various metastable phases further complicated these microstructures and made precise analysis more difficult.

The available experimental data were used in the optimization of the TiAlNb ternary in several different studies over the years. Major anomalies present in the Ti-Al binary [14] made this optimization difficult. The data were used to project various isothermal sections including the liquidus for the ternary [1, 15, 16]. The first thermodynamic simulation of the TiAlNb phase diagram was done and published by

[17]. Zdziobek performed a recalculation for the phase diagram later [18]. A comprehensive re-evaluation of the phase diagram was then performed by [19-21]. Various assessments produced different ternary projections and numerous discrepancies were generated, including the extent of the  $\beta$ -phase region in the liquidus, and the extent of various other phase fields at different temperatures.

The most recent thermodynamic simulation study is presented by [22-24] and has been used for alloy selection during the course of this study. Some data from the initial stages of this research were incorporated in the preparation of the dataset by Cupid et al. [25-27]

### **1.2.2 $\alpha_2+\gamma$ Alloys**

The  $\alpha_2+\gamma$  alloys lie in the central region of the Ti-Al binary and, depending on the addition of Nb, may or may not extend into the ternary TiAlNb, as shown in Figure 1-4. These alloys have been studied over the past three decades for potential applications in turbine engines. These alloys offer high specific yield strength, good oxidation resistance, good creep properties and high stiffness [28-30]. Their low density in comparison to the Ni-based superalloys, which are currently used in turbine engines, makes them an attractive candidate to improve the efficiency of turbine engines [28]. Their poor room temperature ductility, high temperature creep properties, and limited service temperature (<800 C) renders them unsuitable for replacing current Ni-based superalloys [31, 32]. Further, these alloys tend to solidify with prominent texturing in the microstructure, which is also extremely coarse. Coarseness causes anisotropy in the properties and thus inhibits their development for near-net shape casting of turbine components [32]. A typical  $\alpha_2+\gamma$  alloy solidifies as a single  $\alpha$ -phase (disordered A3

hexagonal solid solution structure). Upon cooling, these alloys form two phase  $\alpha_2$  (ordered  $D0_{19}$ )+ $\gamma$  ( ordered face centered tetragonal,  $L1_0$ ) microstructure. The morphology and scale of the microstructure depends on the cooling rate and alloying additions, and heat treatments employed [32-35]. In the as-cast structure, coarse columnar grains with lamellar  $\alpha_2+\gamma$  microstructure are present. Due to the directional growth of the columnar grains, as well as of that of the lamellae, the resulting microstructure is textured, inducing anisotropy to the mechanical properties of the as-cast structure. Refining the  $\alpha$ -grain size by alloying additions and heat treatments, employing different processing routes, heat treatments, and cooling rates, has allowed improvement in the resulting microstructures and mechanical properties[33, 36-40].

When  $\alpha_2+\gamma$  alloys are solutionized in the single  $\alpha$ -phase region, the grains grow. Typical solutionizing temperatures lie between 1250 C and 1350 C, and solutionizing treatments are performed for about 30 minutes in most cases. The grains grow to about 50-200  $\mu\text{m}$ . Upon slow cooling (furnace cooling) of this structure, a lamellar microstructure is generated composed of  $\alpha_2$  and  $\gamma$  lamellae [31, 33, 34]. At slightly higher cooling rates (sand, air cooling), Widmanstätten  $\gamma$ -phase laths and a feathery morphology of the  $\gamma$ -phase is observed along with the lamellar structure [32, 39, 41-44]. At faster cooling rates (oil or water quenching), only massive  $\gamma$ -phase is observed formed via a diffusionless transformation from the  $\alpha$ -phase [33, 45].

Among the above microstructures, the fully lamellar morphology is known to yield the best and most suitable properties for these alloys [46-48]. This structure is characterized through its colony size, lamellar interspacing and interphase boundary structure [42]. Upon slow cooling from the single phase a region,  $\gamma$ -lamellae precipitate

in the  $\alpha$ -phase with a Blackburn orientation relationship viz:  $\{111\}_\gamma \parallel (0002)_\alpha$  and  $\langle 110 \rangle_\gamma \parallel \langle 110 \rangle_\alpha$

At lower temperatures, the untransformed  $\alpha$ -phase that exists inside the existing  $\alpha$ - $\gamma$  lamellar structure, transforms to the ordered  $\alpha_2$  phase, maintaining the original orientation [31]. Thus the final  $\alpha_2+\gamma$  lamellar structure is obtained. Due to the limited variants between the  $\alpha$  and  $\gamma$  phases, smaller initial  $\alpha$ -grain size and final lamellar colony size was required to impart isotropy to the microstructure[28]. Addition of B was found to be helpful in reducing the  $\alpha$ -grain size due to the pinning of  $\alpha$ -grain boundaries by borides at solutionizing temperatures [49, 50]. However, the presence of borides was found to be detrimental to the mechanical properties of these alloys [29, 39]. Massive  $\gamma$  phase was used to refine the microstructure by providing nucleation sites for the  $\alpha$ -phase [39, 51-53]. Further, cyclic heat treatments and alloying additions such as W and B were used to refine lamellar colony size and to refine the lamellar thickness [33, 35, 54].

It was found that addition of B and Mn caused an increase in the critical cooling rate for formation of the different microstructures discussed above [33, 55]. Addition of B also caused coarsening of the lamellar structure by reducing the active grain boundary nuclei for lamellae generation [33, 56]. B addition was reported to be beneficial in improving both strength and ductility of the  $\alpha_2+\gamma$  alloys [40]. Further, additions of slow diffusing refractory elements such as W, Ta and Nb were found to extend the formation of the massive  $\gamma$ -phase to lower cooling rates by suppressing the diffusional transformations such as lamellar, feathery and Widmanstätten due to slower diffusion [28, 57]. Further, to improve the high-temperature creep resistance of the alloys, single

crystal samples with fully lamellar microstructure were also studied [58]. Various studies showed the effect of different alloying elements on phase stabilities. In  $\alpha_2+\gamma$  alloys, where only  $\alpha$  and  $\gamma$ -phases were present, Mn, Ru and Zr were found to be  $\gamma$ -stabilizers [59, 60]. Cr was found to partition strongly into the  $\alpha/\alpha_2$  phase in comparison to the  $\gamma$ -phase. Nb content in both  $\alpha$  and  $\gamma$  phases remains consistent, and it does not show any tendency to partition to either of the two phases [37, 61]. Cr, Mo, W, V, Ta, Nb were identified to be  $\beta$ -phase stabilizers in alloys where  $\beta$ -phase was present [54, 57, 62-64].

The  $\alpha_2+\gamma$  alloys in some cases consisted of limited amounts of Nb (<2at%, TNB second generation alloys). It was shown to improve high-temperature oxidation [36, 65, 66] and room temperature strength of the  $\gamma$ -phase [46, 67-69]. It was further found to enhance the ductility and fracture toughness of the alloys [70]. Later Nb and other  $\beta$ -stabilizers were added (<8-9 at%, to third generation alloys [38]) to the alloys to stabilize the  $\beta$ -phase at high temperatures in order to improve forgeability. It was also observed to improve the creep resistance of these alloys [30]. These alloys also either existed as single phase  $\beta$  or  $\beta+\alpha$  at high temperatures and yielded an  $\alpha+\gamma+\beta$  microstructure at room temperature. However, retained  $\beta$  was found to be detrimental to the alloy properties [71].

### 1.2.3 $\gamma+\sigma$ Alloys

When higher Nb additions were made to the near- $\gamma$  alloys, the  $\alpha$ -phase was replaced by the  $\beta$ -phase at high temperature and by the  $\sigma$ -phase at lower temperatures, yielding a two phase  $\gamma+\sigma$  or three phase  $\gamma+\sigma+\beta$  microstructure depending on alloy composition [8, 72, 73]. Limited studies have been performed on these alloys so far. These alloys exist in the central part of the TiAlNb ternary with high Al and Nb content,

shown in Figure 1-5. Due to high Al contents in these alloys, they show improved oxidation properties [74]. Single  $\beta$ -phase existed at high temperature in these alloys that could be quenched to room temperature. Extensive ordering of the  $\beta$ -phase was observed upon cooling, and was found to depend on the alloy composition where higher Al was found to cause ordering in the  $\beta$ -phase. The  $\beta$ -phase was found to be metastable at room temperature, and cooling of the high-temperature  $\beta$ -phase led to the formation of other metastable phases, such as orthorhombic and  $\omega$ -phases. Orthorhombic phase was observed to form via a diffusionless martensitic transformation upon rapid quenching of the  $\beta$ -phase [73, 75-77] whereas the  $\omega$ -phase formed at relatively slower cooling rates and forms coherent GP zones [9-11, 73, 77-81].

Upon aging the quenched metastable  $\beta$ -phase,  $\gamma+\sigma$  phases were precipitated. These  $\gamma+\sigma$  alloys were found to have good creep properties and high-temperature strength [82-85]. It was also seen that microstructures with disconnected  $\sigma$ -phase yielded better properties as compared to those with connected  $\sigma$ -phase [83, 85]. The crystallographic relationship between the  $\beta$  and the  $\sigma$ -phases was found to be [8]

$$[110] \sigma \parallel [110] \beta \text{ and } (-110) \sigma \parallel (-110) \beta$$

The crystallographic relationship between the  $\gamma$  and the  $\sigma$ -phases was found to be

$$[110] \sigma \parallel [110] \gamma \text{ and } (111) \sigma \parallel (001) \gamma$$

Further, the  $\gamma$  and the B2-phases were found to share the following orientation relationship [73]

$$\langle 110 \rangle \gamma \parallel \langle 111 \rangle \beta \text{ and } \{1-11\} \gamma \parallel \{-110\} \beta$$

In the previous studies performed, the as-cast samples were held at different temperatures for a specific time and then WQ. It was found that at 1300 C and above, the studied alloys (alloy-2, 40Al-33Ti-27Nb at%) existed as single  $\beta$ -phase that upon quenching formed the  $\alpha$  and  $\omega$ -phases. Upon holding the samples at temperatures between 1300 C and 1200 C,  $\beta+\sigma$  microstructure was obtained with an equiaxed morphology of the  $\sigma$ -phase at the  $\beta$ -phase grain boundaries and matrix. At temperatures 1200 C and less  $\gamma+\sigma$  microstructure was obtained [8, 73, 83, 85]. Thus  $\sigma$ -phase was said to be the first phase forming from the  $\beta$ -phase in the transformation sequence upon cooling. Evaluation of various stable and metastable phases was performed using extensive TEM analysis. However, no studies were performed on alloys with  $\gamma$  as the first precipitating phase from the  $\beta$ -phase.

#### 1.2.4 Phases of Interest

The present study was conducted on alloys lying in a specific compositional regime of the Ti-Al-Nb ternary system. The factors governing the compositions of the alloys are discussed earlier in the chapter. In this particular compositional range, we mainly dealt with three equilibrium phases, namely,  $\beta$ ,  $\gamma$ , and  $\sigma$ . In addition a metastable  $\alpha$ -phase was also constantly encountered. Table 1-1 provides details of the crystal structures of these phases of interest. Further details of all phases are discussed in the following sections.

**$\beta$ -phase.** This is a BCC phase that exists at high temperatures in the TiAlNb ternary system. The B2 (ordered  $\beta$ ) phase has a BCC CsCl structure with a Pm-3m space group. It is essentially a binary solid solution of Ti-Nb, but extends well into the TiAlNb ternary [19]. It is a relatively soft phase, and its existence at high temperatures in

alloys improves forgeability and helps to achieve better microstructural control.  $\beta$ -phase has been shown to undergo an ordering transformation upon cooling that leads to some reduction in ductility [86, 87]. It has been shown that  $\beta$  to B2 transition temperature increases with an increase in the Nb content. In the ordered structure, Al occupies a separate sublattice whereas Ti and Nb share the other sublattice mutually [73, 86]. Figure 1-6 a & b depict the disordered and ordered crystal unit cells developed based on the available crystal structure data for the  $\beta$ -phase. In our laboratory, one aims at developing alloys that have  $\beta$ -phase as the single high-temperature phase that can be retained upon quenching. Subsequent aging would precipitate out the required  $\gamma$  and  $\sigma$  phases to yield the desired microstructure. However, upon quenching, it has been shown, that  $\beta$ -phase is not fully retained [25].

**$\gamma$ -phase.** This phase, also known as the TiAl phase, was studied widely for aerospace applications, due to its low density, high oxidation resistance and good mechanical properties. It is a binary intermetallic phase with a relatively high solubility for Nb. This phase has an ordered face-centered tetragonal  $L1_0$  crystal structure and the  $P4/mmm$  space group [88]. Al occupies the face centers of the four parallel faces whereas Nb and Ti share the corners and face centers of the top and bottom faces. This leads to alternating layers of Ti and Nb atoms. Lattice parameters for a stoichiometric composition of the phase were calculated to be  $a=3.976\text{\AA}$  and  $c=4.049\text{\AA}$  [73]. These values, however, are shown to depend on the Al content,  $c/a$  ratio increasing with Al content [35]. Mn additions have also been shown to reduce the  $c/a$  ratio [59]. In the ternary system, for limited Nb content, Nb atoms occupy the Ti sites, as Al prefers to occupy a separate sublattice[73]. A schematic of the crystal unit cell, based on the

available data, is shown in Figure 1-6. A double ordering of the phase has been claimed, suggesting ordering between Nb and Ti atoms, but has not been conclusively proved.

**$\sigma$ -phase.** This is a commonly found phase in many transition alloy systems, such as superalloys and steels. In the TiAlNb ternary system it is essentially a binary phase, but has a significant solubility for Ti. This phase was found to be extremely brittle at room temperature[84]. Thus, the mechanical properties of alloys containing  $\sigma$ -phase are poor at room temperature, due to easy crack propagation. It has been shown by members of our laboratory that at high temperatures this phase exhibits good creep properties[82, 83]. It was also proposed that when present in specific phase fraction and size, this phase is expected to impart excellent creep resistance to the microstructure at high temperatures. This phase has a complex ordered structure with 30 atoms per unit cell[89]. It has a P42/mmm space group, and exhibits a tetragonal structure. A schematic of the  $\sigma$ -phase, based on the available data is shown in Figure 1-7. At the stoichiometric composition, Nb<sub>2</sub>Al, this phase was observed to have a lattice parameter of a=9.935Å and c=5.169Å[73]. However, the lattice parameter of the  $\sigma$ -phase has shown to be a function of the Al content.

**$\alpha$ -phase.** This is a metastable phase that forms upon cooling the  $\beta$ -phase to temperatures where the  $\beta$ -phase is no longer stable. Upon quenching, the  $\beta$ -phase is rendered unstable, and undergoes a compositionally invariant martensitic transformation leading to the formation of orthorhombic plates[73, 75, 78, 90, 91]. These plates are observed to have a Pmma or Cmcm symmetry, based on their formation temperatures and ordering between the Ti and Nb atoms in the unit cell [75, 76]. Their

thickness can vary from 0.01  $\mu\text{m}$  to 0.5  $\mu\text{m}$ , depending on their temperature of formation. A schematic of the crystal structure is presented in Figure 1-8.

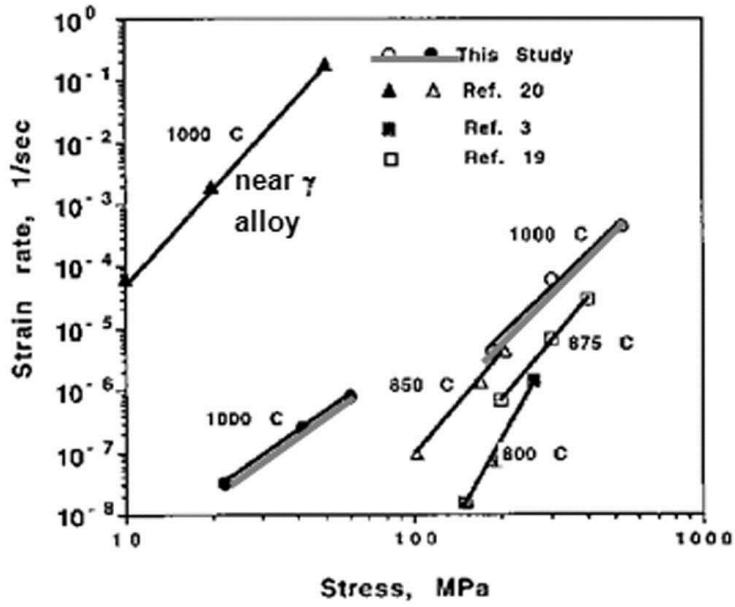


Figure 1-1. Graph showing the high temperature data of tests performed on  $\gamma+\sigma$  alloys in comparison to  $\alpha_2+\gamma$  alloys [83-85]

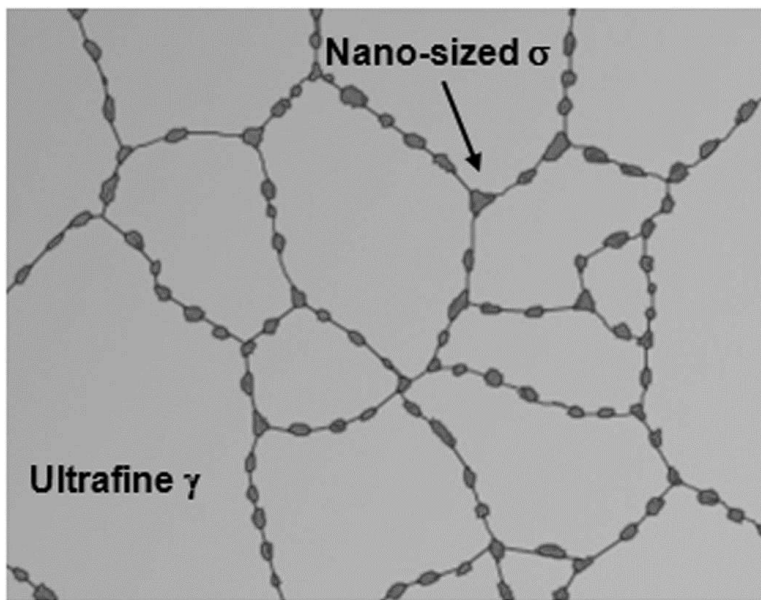


Figure 1-2. Schematic showing the targeted ideal  $\gamma+\sigma$  microstructure

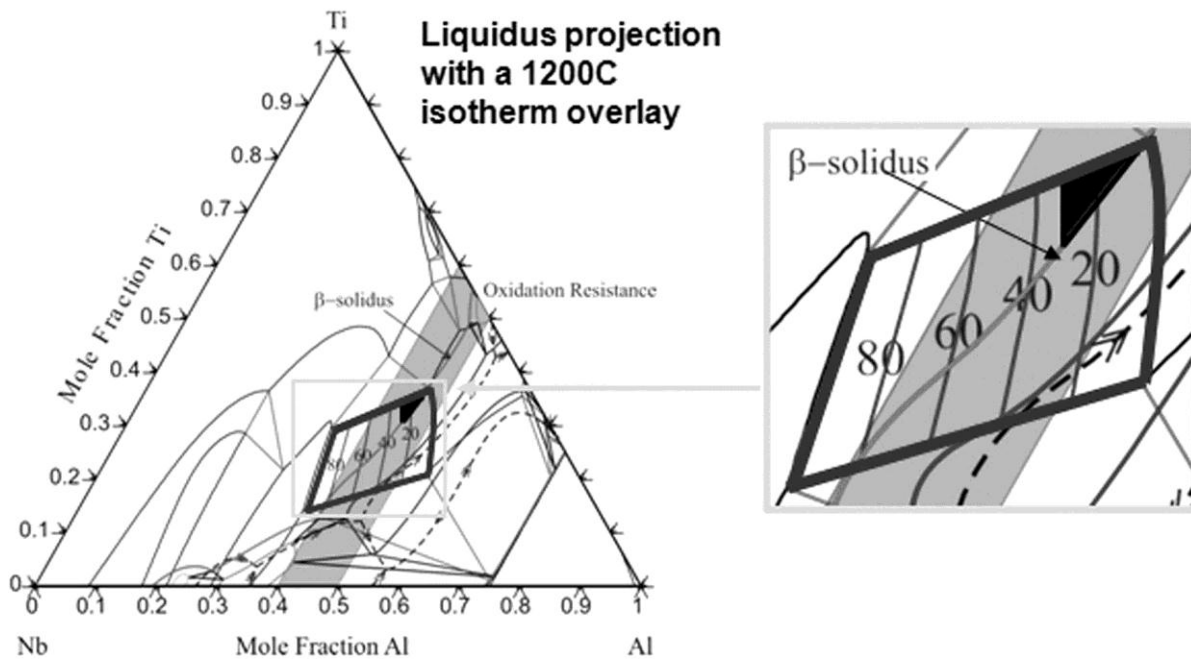


Figure 1-3. A isothermal section of the TiAlNb ternary superimposed over the liquidus and depicting the selected region for  $\gamma+\sigma$  alloy selection[24]

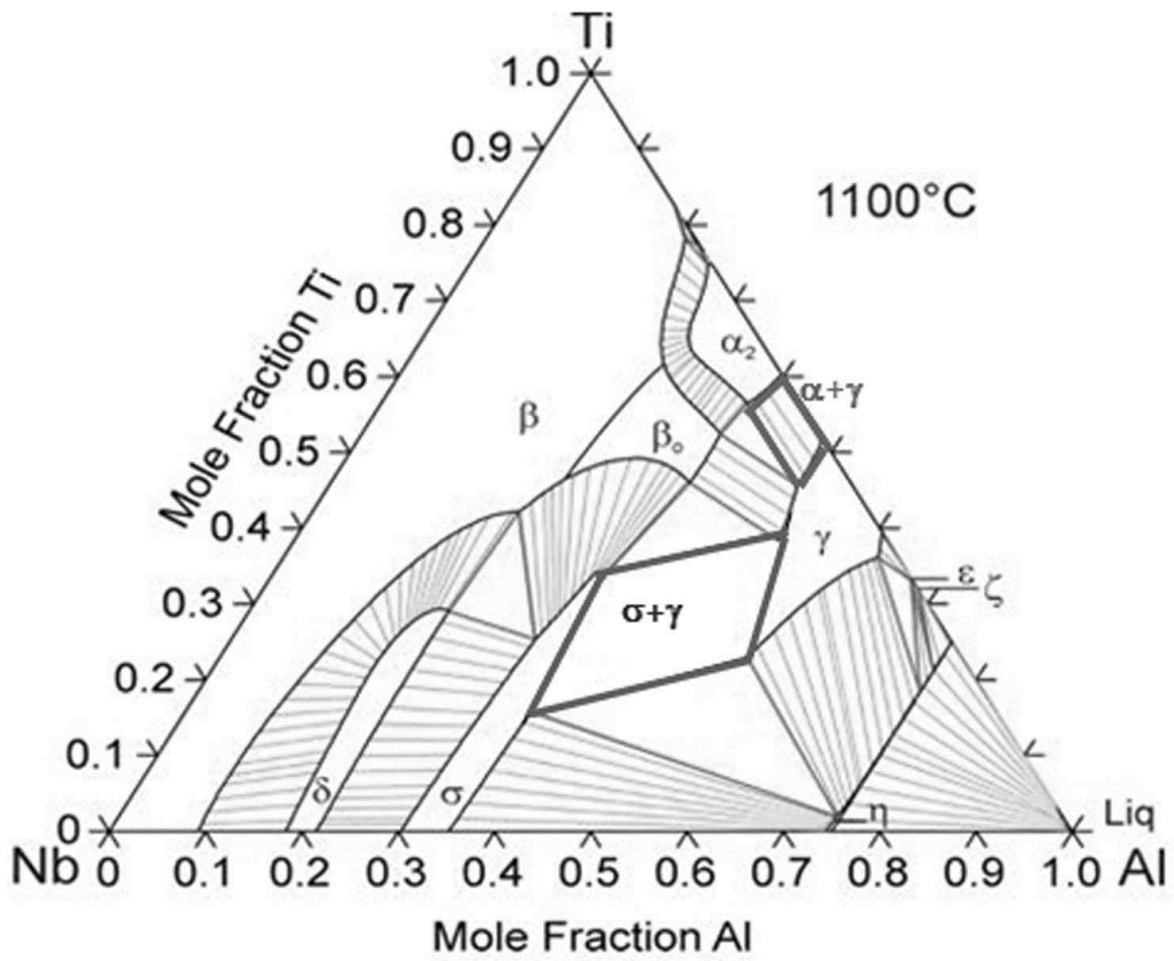


Figure 1-4. an 1100 C isothermal section of the TiAlNb ternary depicting regions of  $\alpha_2+\gamma$  and  $\gamma+\sigma$  alloys

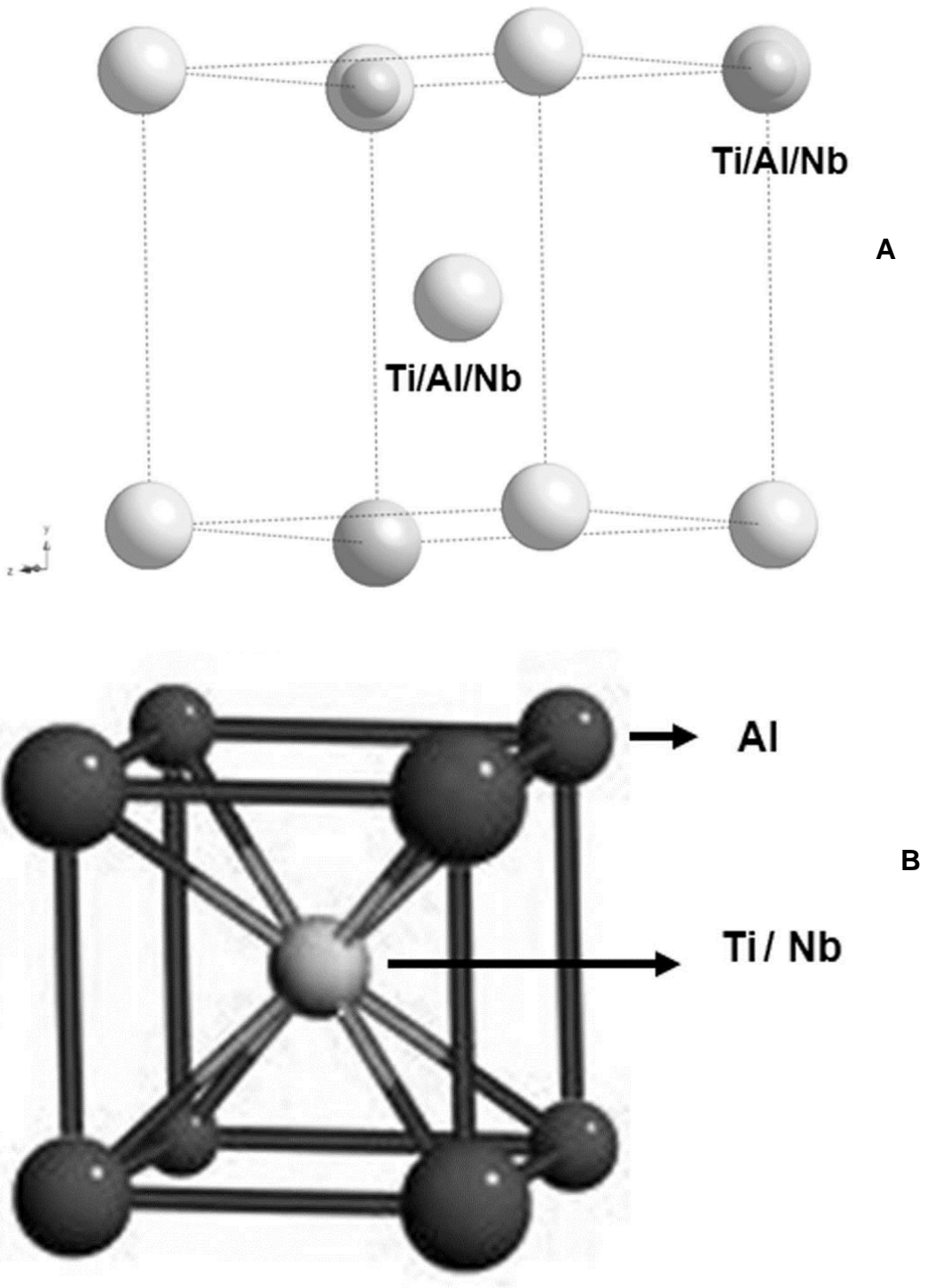


Figure 1-5. Unit cell of ordered  $\beta$ /B2 phase. A) disordered. B) ordered

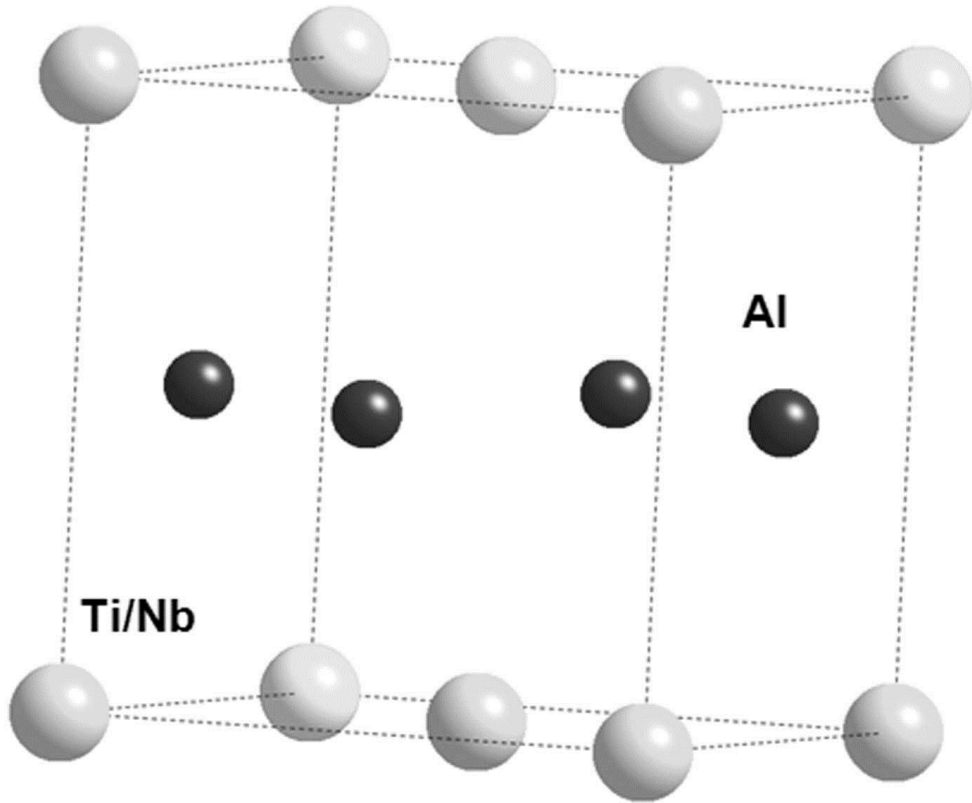


Figure 1-6. Unit cell of  $\gamma$ -TiAl

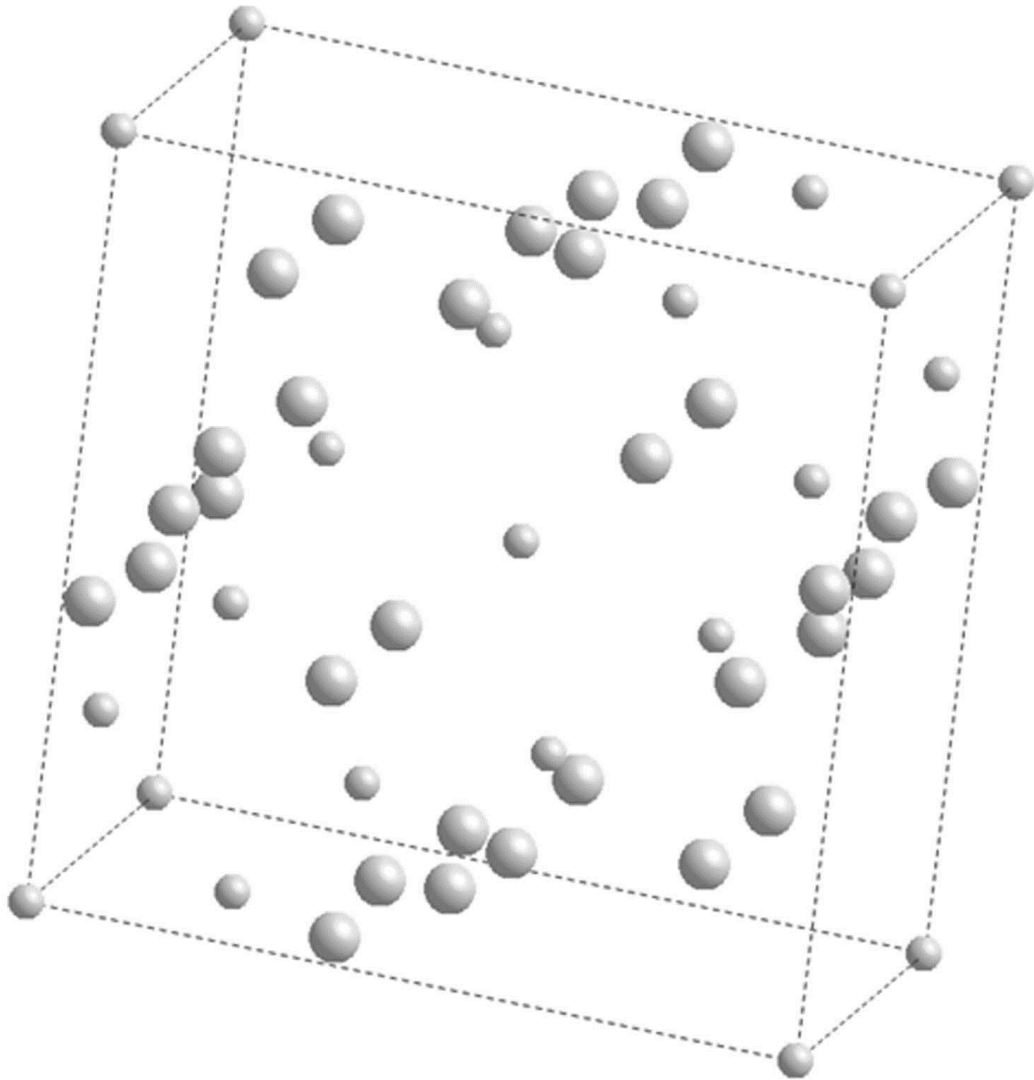


Figure 1-7. Unit cell of the  $\sigma$ -Nb<sub>2</sub>Al phase

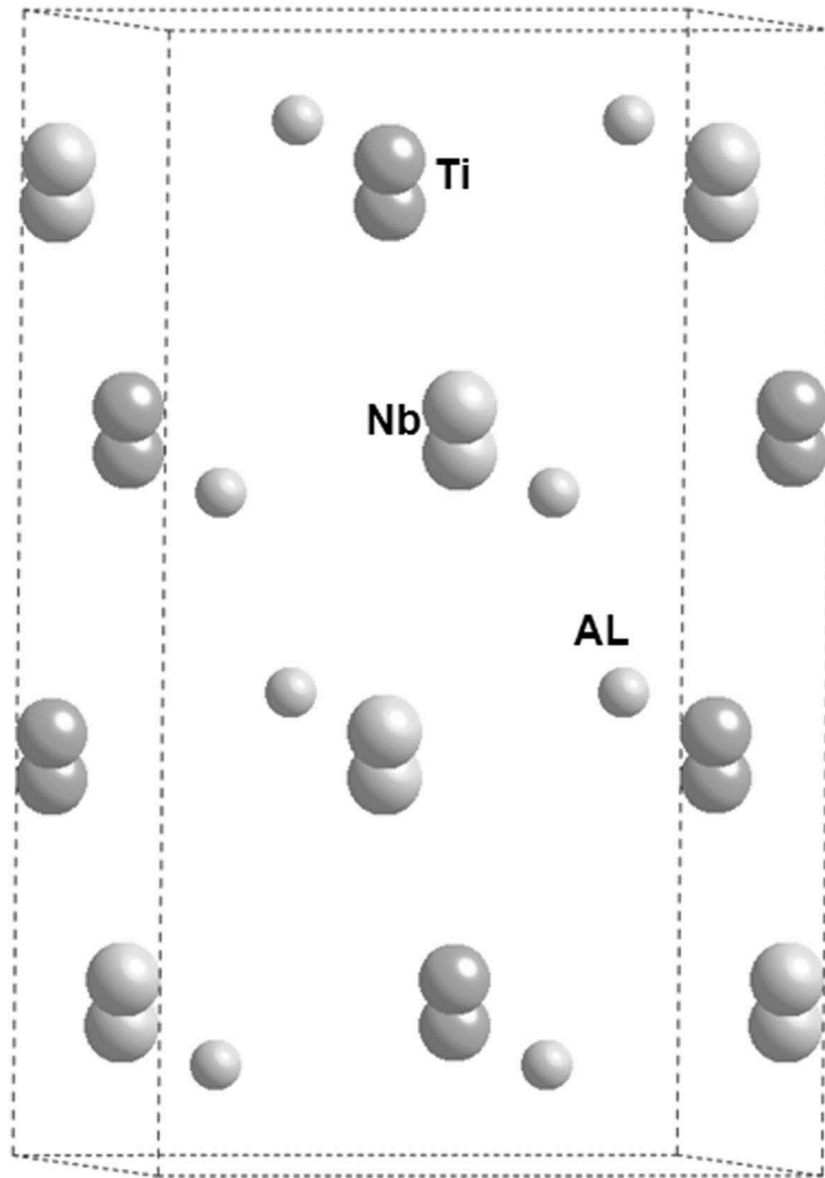


Figure 1-8. Unit cell of the o-phase

## CHAPTER 2 EXPERIMENTAL PROCEDURES

### 2.1 Materials Used

For the current studies, several alloys were selected from the available phase diagrams based on the requirements stated earlier. Alloy 11 (nominal composition : 45Al-37Ti-18Nb) was selected in order to study the transformation path and mechanism from a single-phase  $\beta$ -phase at high temperature, to a  $\gamma+\sigma$  two-phase microstructure at lower temperatures. Emphasis was on the study of  $\beta$ -to- $\gamma$  phase transformation, and this alloy was predicted to form  $\gamma$ -phase first from a single high-temperature  $\beta$ -phase upon cooling. Further, alloy 11-5Cr was prepared by adding 5 at%Cr replacing Nb in alloy 11 (nominal composition: 45Al-37Ti-13Nb-5Cr) to study the effect of Cr on the  $\beta$ -to- $\gamma$  phase transformation. Alloys 21 (nominal composition: 37.4Al-37.6Ti-25Nb at% ) and 31 (nominal composition: 42.4Al-37.6Ti-20Nb at% ) were prepared and studied in order to evaluate the effect of composition on the formation of  $\gamma$ -phase upon quenching. Alloy 41 was selected to study the effect of Boron addition on  $\gamma$ -phase formation upon aging, as it did not form  $\gamma$ -phase upon quenching from the high temperature  $\beta$ -phase. Furthermore, alloys were prepared with three different amounts of boron added to 11-5Cr and 41 in order to study effect of boron on  $\gamma$ -phase formation upon quenching and aging, respectively.

All alloys were prepared by arc melting in a bell jar type arc melter under a 2 psi positive pressure of argon. Pure elements of Nb (99.99%), Ti (99.99%), Al(99.99%), Cr 99.99% were used for arc melting. Boron was introduced in the form of AlB<sub>2</sub> powder of 200 mesh size. All elements were weighed based on the required alloy compositions for a 5 or 10 g button. All elements were cleaned first in 3% Nital (3% nitric acid in alcohol)

and sonicated in a Branson 1500 ultrasonicator to remove any oxide layer, oil or dirt. They were then thoroughly rinsed in alcohol and dried well. The arc melter was cleaned using 3% Nital solution and finally rinsed with isopropyl alcohol. The stinger was ground to a sharp tip and all oxide layer was removed from its surface. The relief valve was taken apart and cleaned, and then replaced such that it released at about 2 psi overpressure. The rim of the bell jar was greased with vacuum grease, and all the elements were placed in the hearth cavities for different alloy buttons. The bell jar was sealed and then pumped three times and purged with ultrahigh-purity argon gas. The first pump reduced the pressure to 60 mTorr, and the second and third pumps reduced the pressure to 20 or 30 mTorr. During purging, the argon pressure was raised to 5 Torr absolute for the first two times. In the final purge the pressure was allowed to go beyond 2 psi gauge such that the relief valve started to release the gas. Water cooling was then started and the arc melter turned on. The settings for arc melting were kept at (define GTAW) GTAW and the current used was 250-300 amps. for a 5g button. All buttons were arc melted 6 times flipping them over each time to ensure proper melting and homogeneous mixing of all elements.

## **2.2 Heat Treatments**

For all microstructural analysis and heat treatments, the arc melted buttons were cut into 1-2 mm slices. For all heat treatments the slices were wrapped in Ta foils that acted as getters for residual oxygen during heat treatments, which reduced oxidation of the sample.

All the heat treatments requiring quenching were performed in an alumina tube vertical quenching furnace. The two ends of the alumina tube were fitted with custom made brass caps through which water would flow to maintain cold ends. There was a

spool arrangement on the top brass cap from which the samples were hung. The samples, after being wrapped in Ta foil, were wound around with a Ta wire, and hung from a silica-borica-alumina sleeve. The other end of the sleeve was attached to a Ta wire that was then hooked onto the spool arrangement on the top brass cap. The length of this whole arrangement was such that the samples stayed at the same position as the tip of the internal thermocouple in the furnace. The arrangement remained hung vertically in the furnace during heat treatment. The thermocouple was set inside the tube vertically and both caps were closed. The furnace was then pumped and purged six times with ultra-high purity argon gas. The argon was passed through a gettering furnace before it entered the furnace tube to getter any traces of oxygen that might be present in the gas. In the final purge, the pressure was increased to beyond 2 psi, so that the extra pressure of the gas is released through the relief valve. The gas was allowed to keep flowing at an overpressure of 2 psi throughout the heat treatment, so as to minimize any oxygen in-flow into the tube. For quenching, the bottom cap was first opened, and then the spool arrangement was unwound so as to release the Ta wire at the top cap, thereby dropping the sample directly into the quenching bucket at the bottom.

Solutionizing heat treatment was performed by heating the samples to a single phase region and holding for an hour followed by water quenching (WQ). Metastable phases, such as the  $\alpha$ -phase, always formed upon quenching the high temperature  $\beta$ -phase. In order to study the transformation path for the alloy, a two step heat treatment was designed and used that is termed a double heat treatment (DHT). In this, the sample was solutionized in the single-phase region for 1 hr, and then cooled to a

desired temperature at a specific rate in the furnace, then held for a certain length of time, after which they were WQ. This heat treatment helped attain the equilibrium microstructure at the holding temperature, and the rapid WQ helped retain that microstructure to room temperature. Continuous cooling (CC) heat treatments were designed to study a phase transformation in progress by interrupting it at a certain temperature. The samples were solutionized and then cooled at a certain rate to a desired temperature and immediately WQ without any holding. The microstructure obtained would correspond to the microstructure existing at the temperature of quenching as it was cooled from higher temperatures. A slow cooling (SC) heat treatment was also performed where the samples were solutionized and then cooled to room temperature at a desired rate.

Aging heat treatments were performed on sol-WQ samples to study the phase transformations at lower temperatures. All aging heat treatments were performed in a box type furnace. Since the furnace was not atmosphere controlled, the samples were first wrapped in a Ta foil and then encapsulated in a quartz tube evacuated and backfilled with argon along with some Ti getter. This encapsulated tube was then put in the box furnace at the required temperature and time, and then either cooled with the furnace or water quenched by breaking the tube in water.

### **2.3 Characterization Techniques**

Optical microscopy was employed for the macroscopic characterization of the samples in different heat treated states. It was helpful in the study of grain size, detecting the presence of relatively coarse phases, and in the study of quenched structures, which were difficult to study using SEM due to lack of compositional variation. Polarized light microscopy was employed to confirm the presence of the  $\gamma$ -

phase in different samples as the  $\gamma$ -phase is known to react to polarized light. Further microstructure analysis was performed using scanning electron microscopes Jeol 6400 and Philips XL-40 in both secondary electron (SE) and backscattered modes (BSE) to evaluate the phases present, their morphology and scale. EPMA was conducted to calculate overall alloy compositions as well as compositions of individual phases present in different heat treated samples of the same alloy using a Jeol Superprobe 733 system . X-ray diffraction (XRD) analysis was performed for the preliminary phase identification in the samples using a Philips 3720 equipment. XRD coupled with optical and scanning electron microscopy proved to give a reasonably good idea of the phases present before further diffraction analysis was performed under a transmission electron microscope-Jeol 200CX. TEM studies were then employed for selected samples in order to examine the phases more closely. Along with diffraction analysis, dark field (DF) and bright field (BF) imaging was carried out. TEM was also found useful in investigating the finer metastable phases that formed upon quenching, and which were difficult to view under the optical or scanning electron microscope. Differential scanning calorimetric (DSC) studies were carried out using Setaram Setsys Evolution 1750 with a DSC1600 rod. These measurements were performed on alloys in order to obtain transformation temperatures that helped in designing heat treatment schedules. Samples were cycled multiple times so as to ensure consistent transformation temperatures in consecutive cycles.

## **2.4 Sample Preparation**

### **2.4.1 Optical Microscopy**

Standard metallographic methods were used to prepare samples for optical microscopy. Most of the samples were in the form of a 1-2 mm thick and 10-15 mm long

slice cut out of an arc melted button using a diamond edge cutting wheel. All subsequent heat treatments were also performed on such slices. All samples, as cast or heat treated, were first mounted in Bakelite powder using a hot mounting press. In most cases a cross section of the slices was also mounted alongside using a sample clip holder. These were then ground using grits ranging from 240 to 800 SiC grinding paper. Subsequent polishing was performed using 5, 1, 0.3 and 0.05  $\mu\text{m}$   $\text{Al}_2\text{O}_3$  slurries on polishing cloths. Two different kinds of etchants were used prior to optical microscopy. A macro-etchant consisting of 55% $\text{H}_2\text{O}$ +25% $\text{HF}$  +20% $\text{HNO}_3$  was used when large  $\beta$ -grains were to be identified, such as in the solutionized-WQ samples. In samples where various phases and their morphology were required to be evaluated, a micro-etchant was used which consisted of 75% $\text{H}_2\text{O}$ + 10% $\text{HF}$ +15% $\text{HNO}_3$ .. Both etched and unetched samples were used for polarized light analysis.

#### **2.4.2 Scanning Electron Microscopy (SEM) and Electron Probe Micro-Analysis (EPMA)**

Samples for SEM/EPMA were prepared in same manner as for optical microscopy, except that the final polishing was done using a Vibromet® with a Buehler Mastermet®-2 silica polishing slurry. Final silica polishing was performed as the  $\text{Al}_2\text{O}_3$  slurry particles that were left on the sample interfered with the EDS/EPMA compositional results due to the presence of Al in both the slurry and the sample. Samples were thoroughly sonicated in water to remove all slurry particles as much as possible.

#### **2.4.3 X-Ray Diffraction**

All samples were finely powdered using in a ball-mill which used a tungsten attrition ball. It was used at 1000 rpm for 1-3 min. depending on each sample. The

powders were then spread on the centre of a glass slide using a double-sided tape. The leveling procedure was performed as per the instructions and the sample was then run in the XRD. The standard XRD conditions used were 0.09 deg -step size, 2.5 sec per step, using a  $\text{CuK}\alpha_1$  and  $\text{CuK}\alpha_2$  wavelengths.

The powdering of all samples was found to be important for obtaining correct x-ray diffraction pattern. In non-powdered bulk samples, a significant texturing was observed in peak intensities. Thus a correct phase and phase fraction analysis was found to be difficult. This arises due to the fact, that after solutionizing, the  $\beta$ -phase grains grow and become few millimeters in size. Thus, each sample slice has about 4-5  $\beta$ -phase grains. This limited number of  $\beta$ -grains is statistically insufficient in obtaining a standardized peak intensity of the phases. Further, it is known that  $\beta$  and  $\gamma$  phases share an orientation relationship. Thus, when  $\gamma$ -phase forms in these large  $\beta$ -phase grains, there limited number of  $\gamma$ -phase variants generated giving rise to an overall textured XRD pattern.

#### **2.4.4 Differential Scanning Calorimetry (DSC)**

The samples requiring DSC were powdered into small pieces of about 0.5 mm diameter. About 100-150 mg of these powders were then placed into the DSC's alumina crucibles and inserted inside the equipment. The powdering of samples is required by NIST standards for DSC studies as an alternative to melting of the samples in the crucible, for better conductivity and heat flow measurements. A baseline correction was performed by running the same crucible without the sample through the same cycles and then eventually subtracting the obtained heat flow values from those obtained upon running the sample. The transformation temperatures were obtained by performing the

first deviation from the baseline analysis on the endothermic and exothermic peaks on the cooling and heating curves, respectively. Details of DSC calibration can be found in [25].

#### **2.4.5 Transmission Electron Microscopy (TEM)**

Samples for TEM were prepared by two methods depending on the sample and the information required.

Most of the TEM samples were prepared by the electro-polishing method. The sample slices were first mechanically thinned to about 120-150  $\mu\text{m}$  and then polished to a 0.3  $\mu\text{m}$  finish to eliminate any scratches and provide a shiny mirror surface on both sides of the slices. Subsequently, 3 mm diameter discs were then punched from these slices using a TEM disc punch. These slices were then electro-polished in a Fischione twin jet type electro-polisher. An electrolyte consisting of 86% methanol, 10%  $\text{H}_2\text{SO}_4$  and 4% HF was used. The electro-polishing conditions varied from sample to sample, but the temperatures used ranged from -20 C to -30 C, with voltages varying between 25V to 45V. A few samples for each type of heat treatment were first used to create an I-V profile, and then the proper voltage was chosen for electro-polishing.

## CHAPTER 3 THE NATURE OF THE $\beta$ -TO- $\gamma$ PHASE TRANSFORMATION

### 3.1 Introduction

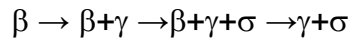
A substantial amount of work has been done on the study of the  $\alpha_2+\gamma$  alloys that solidify and exist as single  $\alpha$ -phase at high temperatures and undergo  $\alpha\rightarrow\gamma$  or  $\alpha\rightarrow\alpha_2+\gamma$  phase transformations in the TiAlNb system. However, alloys solidifying as single - phase  $\beta$  at high temperatures phase have not been studied in detail in the past in this ternary system. For the development of the targeted alloys as discussed in chapter 1, alloys are required that solidify as single  $\beta$ -phase at high temperature, have above 40%Al for oxidation resistance and a two phase  $\gamma+\sigma$  microstructure at service temperatures with a suitable low phase fraction of the  $\sigma$ -phase. Based on the calculated phase diagrams [22, 24, 26] and preliminary experiments it was observed that alloys satisfying the above criteria existed in a region of the phase diagram such that  $\gamma$  is the first phase to form out of the single  $\beta$ -phase upon cooling, i.e.  $\beta\rightarrow\beta+\gamma$  phase transformation takes place upon cooling. Thus, it becomes important to study the nature of this transformation, in order to be able to obtain the desired microstructure at lower temperatures and for further microstructural control.

The present chapter discusses the basic nature of the  $\beta$  - to -  $\gamma$  phase transformations such as rate of formation, effect of composition, morphology of phases and the influence of microstructural features such as grain boundaries and surfaces.

### 3.2 Selection of Alloys

For the preliminary studies, an alloy with a nominal composition of 45Al-37Ti-18Nb was chosen. According to the isopleth from the latest calculated phase diagram shown

in Figure 3-1 this alloy was expected to solidify as single  $\beta$ -phase and then follow the phase transformation path as shown below:



As can be seen in the ternary isotherms the  $\beta$  - to -  $\beta+\gamma$  transformation starts at 1750K and  $\sigma$ -phase starts to form at 1485K where the alloys enters a  $\beta+\gamma+\sigma$  three phase field. Discrepancies have existed in the past regarding the extent of the  $\beta$  phase field as per the various calculated phase diagrams in the TiAlNb system[1, 2, 19], therefore it was required to confirm the existence of the single - phase  $\beta$  phase field as predicted by the latest calculated phase diagram. HTXRD test data and experimental microstructural evidence from the alloy proved that the alloy indeed solidified as a single  $\beta$ -phase[26].

### 3.3 As-Cast

In order to study the as - cast state of the alloy, a 2mm slice was cut out of the arc melted button for analysis. The slice was taken from the center of the round button as shown in the schematic in Figure 3-2, so that variation of microstructure and composition along the diameter and height of the button could be studied. Since the cooling occurs from the hearth of the arc melter, the bottom of the button cools the fastest. Any segregation happening due to differences in cooling rate could be detected on the slice thus cut from the center of the button.

#### 3.3.1 Microstructural Analysis

Figure 3-3 shows the SEM/BSE micrographs of the dendritic structure as seen in the as - cast sample. The contrast comes from the difference in composition between the dendrites and the inter-dendritic regions. The dendrites are rich in higher melting

point elements such as Nb as opposed to the inter-dendritic regions that are rich in the lower melting point elements such as Al. This makes the dendrites lighter in contrast to the inter-dendritic regions. Fine pores were observed at the top of the button that formed upon cooling due to emission of gases and contraction upon cooling.

Figures 3-4 a & b depict the BSE and optical micrographs from the top and bottom of the as cast sample of alloy 11, respectively. Equiaxed grains about 200-400  $\mu\text{m}$  in diameter can be observed in the top region of the button slice where the solidification occurred last and the cooling rates were much slower. The bottom of the button, on the other hand, depicts columnar grains of about 500-750 $\mu\text{m}$  width growing in the direction opposite to that of the heat flow at the hearth. Equiaxed and columnar grains at the top and bottom of the button indicates that the alloy solidified as a single phase from the liquid. A second phase can be seen to originate from these columnar and equiaxed grain boundaries with a fine lathlike morphology. This phase accounts for much of the fraction of the microstructure, with a phase fraction of about 84%. The lathlike morphology of the phase suggests that this phase did not solidify from the liquid but formed via a solid -state transformation from the single high-temperature phase. The coarseness of the second phase varies with distance from the bottom of the button hence with cooling rate. The laths at the top and bottom of the sample have an average width of 5-10  $\mu\text{m}$  and 2-6  $\mu\text{m}$ , respectively.

Figure 3-5 presents the XRD plot of a powdered sample of the as-cast alloy. It clearly consists of the  $\beta$  and the  $\gamma$  phases,  $\gamma$ -phase being higher in amount. Peaks from the metastable  $\sigma$ -phase also can be seen which form from the cooling unstable  $\beta$ -phase at lower temperatures. This phase is fine and is not seen in the optical and BSE images.

It has been established by the recent calculated phase diagrams[24] and experimentally [26] that alloy 11 solidifies as a single  $\beta$ -phase from the liquid. The as-cast microstructure and phase morphologies are further indicative of the same. The second phase can then be said to be the  $\gamma$ -phase, which forms at the  $\beta$ -phase grain boundaries upon cooling of the  $\beta$ -phase

### 3.3.2 Morphology of the $\gamma$ -Phase

It can be seen that the  $\gamma$ -phase forms with a lathlike morphology in the as-cast microstructure. Figure 3-6a shows a prior  $\beta$ -phase grain boundary. It can be seen that the entire grain boundary has been decorated with  $\gamma$ -phase allotriomorphs. These  $\beta$ -phase boundaries can be seen to be the nucleating sites for these  $\gamma$ -phase allotriomorphs, which then grow into the bulk matrix with a lathlike morphology. It is known that  $\beta$  and  $\gamma$  phase share an orientation relationship[73]. All these are characteristic of a Widmanstatten transformation and morphology. The laths originating from the same  $\beta$ -phase grain boundary grow with different orientations in different grains. This can be explained by the orientation relationship between the  $\beta$  and the  $\gamma$ -phases. When a  $\gamma$ -phase allotriomorphs forms at the  $\beta$  grain boundary it is surrounded by different  $\beta$  grain at different orientations. Only one of these orientations is suitably oriented for the  $\gamma$ -phase to grow with the  $\beta$ - $\gamma$  orientation relationship and low energy semi-coherent or coherent interfaces. Thus, in this particular grain the  $\gamma$ -phase grows with a lathlike morphology, whereas in the other grains, it remains to grow with equiaxed morphology and incoherent interfaces.

Laths growing together from a given  $\beta$  grain boundary and parallel to each other in a given grain form a colony as shown in Figure 3-6b. Many colonies of the  $\gamma$ -phase laths can exist in a given  $\beta$  grain. The non lathlike cross sections of the laths as seen in the micrograph indicate that the  $\gamma$ -phase in the as cast sample indeed grows with a lath morphology and not a plate morphology.

### 3.3.3 Compositional Analysis

Table 3-1 shows the nominal and actual composition of alloy 11 as measured by the EPMA with a 20  $\mu\text{m}$  electron beam on a solutionized-WQ sample of the alloy. Note that the sample was only solutionized and not homogenized. The compositional variation along the height and width of the button in the solutionized-WQ sample was found to be homogeneous with a variation of less than 1 at% throughout. These differences could be attributed to the existence of prior dendritic structure that led to segregation of the elements. Although solutionizing treatment got rid of these compositional inhomogeneities to a large extent, a proper homogenizing treatment would be required to completely homogenize the composition in the button. Due to furnace limitations, homogenizing heat treatment could not be performed, and only solutionizing was performed to obtain a single  $\beta$ -phase for all heat treatment purposes.

The table 3-2 shows the compositions of individual phases in the as-cast microstructure. It can be seen from the compositional data of the  $\beta$ - and the  $\gamma$ -phases that the  $\beta$ -phase is richer in Nb and Ti and depleted in Al content. Nb is known to be a  $\beta$ -stabilizer, therefore it is expected that it will have a tendency to partition into the  $\beta$ -phase. The  $\gamma$ -phase, on the other hand, has a composition close to the bulk alloy composition being slightly richer in Al and depleted in Ti and Nb. It appears that as the

$\gamma$ -phase grows, it rejects slight amount of Nb into the matrix, while accepting a little amount of Ti and Al from the matrix  $\beta$ -phase. Due to the large volume fraction of the  $\gamma$ -phase, this slight rejection and acceptance of elements shows up as a large compositional change in the  $\beta$  matrix.

### 3.4 Thermal Analysis

To obtain further information on the alloy and calculate temperatures for solutionizing and heat treatments, Differential Scanning Calorimetric (DSC/DTA) tests were performed on the as-cast alloy sample as explained in Chapter 2. A small piece of the as-cast alloy weighing about 50 mg was cut from the as-cast button and used for the DSC. Samples were cycled several times as explained earlier, and the final curve was used for all analysis purposes.

Figure 3-7 shows the final DSC profile for alloy 11. The top and bottom curves depict the heating and cooling profiles, respectively. On the cooling curve two distinct exothermic transformation peaks can be observed. The first peak upon cooling begins at 1474 C and ends at 1362 C, while the second peak begins at 1297 C and ends at 1161 C. All temperatures were calculated using first deviation from the baseline method. Thus the alloy is a single phase above 1474 C. The HTXRD tests were performed at 1500 C on alloy 11 and a single  $\beta$ -phase was found to exist. Further analysis on the DSC curve of alloy 11 can be found in the work performed by O. Rios [92]. Two endothermic peaks were observed in the heating curve of the alloy. The shape of the first peak upon heating indicates that it is a convolution of two peaks. This convoluted double peak begins at 1239 C and ends at 1356 C upon heating. The second peak,

which is much shallower, begins at the end of the first peak and ends at 1479 C. A detailed analysis of these peaks was performed by Cupid et.al [24].

### **3.5 Solutionized-Water Quenched (WQ)**

A 2mm slice was cut from the as-cast button and solutionized in the vertical tube type furnace at 1500 C for 1hr, followed by water quenching. The temperature for solutionizing was chosen from the DSC curve for the alloy. The quenched slice was then cut perpendicular to the flat parallel surfaces to study any cooling rate effect on the microstructure. Note that slices were wrapped in Ta foil to minimize oxidation during heat treatment.

#### **3.5.1 Microstructural Analysis**

Figure 3-8 shows optical micrographs from the macro-etched solutionized and WQ sample of alloy 11. Large equiaxed grains about 2-5 mm in size can be seen. Clearly, these grains grew at high temperatures in the single phase  $\beta$  region during solutionizing. Upon looking closely at the microstructure, it was observed that the quenched sample was not all retained quenched  $\beta$ -phase. Figures 3-9 a & b show optical micrographs from the micro-etched sample of solutionized-WQ alloy 11. As can be noticed, the microstructure consists of 2-4  $\mu\text{m}$  thick laths forming a 'basket-weave' structure. The microstructure appears to be homogenous throughout the sample and no variations in the scale or morphology were observed. The laths can be seen to be originating at the prior  $\beta$ -phase grain boundary, as shown in Figure 3-9a, and also from the sample surface, as shown in Figure 3-9b. Clearly the laths formed upon quenching and did not exist at the solutionizing temperature. The phase fraction of the  $\gamma$ -phase was calculated to be greater than 90%.

Figure 3-10 presents the XRD profile of a powdered sample of a solutionized-WQ alloy 11. Peaks indicate the presence of a large amount of the  $\gamma$ -phase along with  $\beta$ -phase in the microstructure. Peaks of the metastable orthorhombic phase are also clearly distinguishable, which, again, forms upon quenching the  $\beta$ -phase. TEM micrographs and diffraction patterns obtained from the solutionized-WQ sample of alloy 11 are shown in Figure 3-11. Figures 3-11a & b show a BF image and a corresponding diffraction pattern taken from a solutionized-WQ sample of alloy 11. Comparison between the laths forming the basket-weave structure in Figure 3-9 and the ones in Figure 3-11b shows them to be of the same scale. The diffraction pattern was taken on the marked area in Figure 3-11b and is indexed to be that of the  $\gamma$ -phase along the  $\gamma$ [110] zone axis. Thus, clearly, the fine laths forming the basket-weave structure in the solutionized-WQ sample are of the  $\gamma$ -phase. The TEM investigation of the presence of the orthorhombic laths is discussed in the next section.

A BSE micrograph of the sample shown in Figure 3-12 shows a two - phase microstructure. However, the compositional contrast was difficult to obtain under the SEM, which suggests that the matrix and the  $\gamma$ -phase have similar compositions. This is expected, as under such fast cooling rates as WQ there is limited time for any diffusion and the transformation would have to take place with essentially negligible compositional change.

### **3.5.2 Rate of Formation of the $\gamma$ -Phase**

From the results of the solutionized WQ sample, it can be concluded that although the  $\beta$ -phase is the single high-temperature phase in alloy 11 and exists at the solutionizing temperature, it is not able to be fully retained to room temperature upon

quenching. Even at fast cooling rates, such as those attained during water quenching a 2mm thick slice, the  $\beta$ -phase is not retained due to the formation of the  $\gamma$ -phase. In other words, the  $\gamma$ -phase forms at such fast rates upon cooling the  $\beta$ -phase that even WQ does not inhibit its formation.

Such fast rates of formation of the  $\gamma$ -phase can be attributed to a few factors. The  $\beta$  and the  $\gamma$  phases are known to share an orientation relationship. This means that they share a low energy coherent/semi-coherent interface. Thus  $\gamma$  allotriomorphs grow fast in the direction of the mobile incoherent interfaces in a suitably oriented grain maintaining these low energy interfaces with the  $\beta$ -phase matrix. Since these low energy semi-coherent/coherent interfaces are less mobile, it leads to the formation of the Widmanstätten morphology. The further thickening of the Widmanstätten laths is interfacially controlled and is known to occur by a ledge mechanism [93] when sufficient time is available.

Further, from the data obtained, it appears that although  $\gamma$ -phase prefers to have higher Al and lower Nb content as compared to the  $\beta$ -phase, it is able to grow equally easily within a wide compositional range when diffusion is limited. The extremely limited compositional variation between the  $\beta$  and the  $\gamma$  phases in the solutionized-WQ sample is indicative of this behavior. However, when given sufficient time for diffusion, as in an as cast sample (and in other heat treatments to be discussed later), elements are able to partition and  $\gamma$  is able to attain a composition closer to equilibrium.

The  $\beta$ -phase is a high temperature bcc solid solution. It is supersaturated with elements, which upon cooling of the  $\beta$ -phase, cause it to become unstable. In such a case it is unable to be retained to room temperature and must transform. Presence of

low energy interfaces between  $\beta$  and  $\gamma$  phases, and the fact that diffusion is not a necessity for the  $\gamma$ -phase laths to form, leads to a fast rate of formation of the  $\gamma$ -phase even upon quenching. A part of the  $\beta$ -phase also transforms to the metastable orthorhombic phase via a martensitic transformation.

### 3.5.3 Transformation Sequence Upon Quenching

It has already been shown that the  $\beta$ -phase transforms to  $\gamma$  and orthorhombic phases upon quenching. Further, it is known that  $\beta$ -phase, which is a disordered bcc solid solution at high temperatures, undergoes ordering transformation upon cooling[86, 87]. The temperature of ordering varies with composition of the alloys. However, the sequence of occurrence of these three transformations in the  $\beta$ -phase is unknown in alloy 11. This knowledge could prove essential in understanding the  $\beta$  - to -  $\gamma$  phase transformation, and also in achieving further microstructural manipulations.

Figure 3-13 presents BF micrographs and a diffraction pattern of the  $\beta$ -phase along the [111] zone axis. The  $\beta$ -phase forms the matrix in the microstructure and was found in small pockets surrounding the  $\gamma$ -phase laths. Upon looking closely, as seen in Figure 3-13a and in Figure 3-14, a network of fine APBs could be seen throughout the  $\beta$ -phase indicating extensive ordering. Fine scale of the APBs suggests that ordering occurred upon quenching and not at solutionizing temperature, which means that the  $\beta$ -phase was disordered at the solutionizing temperature.

Further, fine lenticular shaped plates of the  $\sigma$ -phase were seen in the  $\beta$ -phase. Figure 3-15a shows a BF micrograph and a corresponding diffraction pattern of the  $\beta$ -phase along the [-122] zone axis. Lenticular shaped  $\sigma$ -phase plates are visible in the  $\beta$ -phase matrix. As mentioned before,  $\sigma$ -phase forms from the cooling  $\beta$ -phase via a

martensitic transformation. Figure 3-16 shows another BF micrographs of the  $\beta$ -phase with the  $\sigma$ -phase plates. The corresponding diffraction pattern is of the  $\sigma$ -phase along the [001] zone axis. Notice the APBs in the  $\beta$  matrix, which clearly are continuous through the  $\sigma$ -phase plates. This leads to the conclusion that the  $\beta$  - to -  $\sigma$ -phase transformation occurred after the ordering transformation of the  $\beta$ -phase.

At the solutionizing temperature, the  $\beta$ -phase is disordered in alloy 11. As it is quenched, ordering takes place at lower temperatures, as suggested by the scale of the APBs. At still lower temperatures, the  $\sigma$ -phase forms in the  $\beta$ -phase. Comparing the scales and amount of the  $\gamma$  and  $\sigma$  phases, it can be speculated that the  $\gamma$ -phase forms before the  $\sigma$ -phase. However, whether ordering occurs before or after the  $\gamma$ -phase formation, cannot be claimed with certainty at this point.

### **3.6 Effect of Composition on the Retention of the $\beta$ -Phase Upon Quenching**

To study the effect of composition on the  $\gamma$ -phase formation during quenching, two different alloys were chosen-alloy 21 (nominal composition 37.4Al-37.6Ti-25Nb at%) and alloy 31(nominal composition: 42.4Al-37.6Ti-20Nb at%). The alloys were chosen based on a constant Ti=37.6at% isopleths passing through alloy 11. The alloys lie on either side of alloy 11 on the isopleth. The actual compositions of the alloys are given in Table 3-3. According to Cupid et.al and their latest calculated phase diagram, all 3 alloys solidify as  $\beta$  single phase. Alloy 21 undergoes a  $\beta \rightarrow \beta + \sigma$  transformation upon cooling, whereas alloys 31 and 11 undergo a  $\beta \rightarrow \beta + \gamma$  phase transformation. In other words,  $\sigma$  is the phase that forms first out of a cooling  $\beta$ -phase in alloy 21, while  $\gamma$ -phase forms first from the  $\beta$ -phase in alloys 31 and 11 upon cooling.

Figure 3-17 shows optical micrographs of alloy 21 in the as cast condition. Micrograph in Figure 3-17a depicts equiaxed grains of a single phase at the top region of the as cast button. No second phase can be seen at the grain boundaries. Figure 3-17b shows dendrites in the as cast sample at the bottom of the button, and on closer observation, fine columnar grain boundaries can be seen running through the sample. The alloy clearly solidified as a single phase, and no second phase formed upon cooling of the button. Thus, a single  $\beta$ -phase exists at room temperature.

An optical micrograph from the top region of the as-cast button of alloy 31 is shown in Figure 3-18. Equiaxed  $\beta$ -phase grains are visible but the microstructure is clearly not a single phase. Fine laths of a second phase can be seen to emerge from the  $\beta$  grain boundaries and grow into the matrix forming colonies, much like those seen in the as cast micrographs of alloy 11 except that the laths are much finer. Clearly, alloy 31 solidified as a single phase, but upon cooling, fine  $\gamma$ -phase laths form in the  $\beta$ -phase via a solid-state phase transformation.

To study the effect of composition on  $\gamma$ -phase formation upon quenching, the alloys were solutionized. The solutionizing temperatures were chosen based on the DSC curves of the two alloys as shown in Figure 3-19. Temperatures above the first peak on both the cooling and heating curve were chosen for solutionizing the alloys. Alloy 21 and 31 were solutionized at 1485 C for 30mins each, respectively. The BSE micrograph and XRD plot of the solutionized WQ alloy 21 is shown in Figure 3-20. The BSE micrograph depicts a single phase, and no other phase contrast was observed. The XRD substantiates the presence of a single  $\beta$ -phase. Optical micrograph of solutionized-WQ alloy 31 in Figure 3-21a clearly shows fine second phase laths of the  $\gamma$ -

phase emerging from the  $\beta$ -phase grain boundary. The image in the inset shows a lower magnification view of the sample clearly showing large prior  $\beta$ -phase grains and second phase laths at the boundaries. The XRD plot shown in Figure 3-21b indicates the presence of a single phase, which can be attributed to the low amount of  $\gamma$ -phase in the microstructure that could not be picked up by the XRD.

When  $\sigma$ -phase is the first equilibrium phase to form in the cooling  $\beta$ -phase in the phase transformation sequence of an alloy, quenching of the  $\beta$ -phase leads to retention of the  $\beta$ -phase at room temperature without any  $\sigma$ -phase formation. This can be attributed to the complex crystal structure of the  $\sigma$ -phase, which creates a higher nucleation barrier for sigma nucleation and requires time for movement of atoms. Further, due to high Nb content of the  $\sigma$ -phase, sufficient diffusion is required for its formation, and Nb, having low diffusivity, makes this transformation difficult at the high cooling rates of WQ. Further, the temperature of formation of the  $\sigma$ -phase is about 1300 C according to the DSC curve of alloy 21. Thus  $\beta$ -phase in alloy 21 is stable down to low temperatures. Once the  $\sigma$ -phase acquires enough driving force to nucleate at low temperatures, the temperatures are not conducive to diffusion of atoms. Thus  $\sigma$  formation is inhibited and  $\beta$ -phase is retained to room temperature. On the other hand, in alloy 31,  $\gamma$  is the first phase to form from a cooling  $\beta$ -phase. The reasons for the fast formation of the  $\gamma$ -phase from a cooling  $\beta$ -phase have been discussed earlier. Further, the  $\beta$ -phase does not extend to such lower temperatures in alloy 31 as in alloy 21. Thus  $\beta$ -phase becomes unstable at much higher temperatures and  $\gamma$ -phase attains enough driving force to nucleate. This, coupled with the limited diffusion required for  $\gamma$  formation

and the existing orientation relationship between the  $\beta$  and the  $\gamma$ -phases, makes the  $\gamma$ -phase form fast in alloy 31 even upon quenching.

Thus, in the alloys studied, it was seen that it was not possible to completely inhibit  $\gamma$ -phase formation upon quenching of the  $\beta$ -phase in alloys 11 and 31 where  $\gamma$ -phase formed first from the  $\beta$ -phase. It can be speculated that in such cases  $\gamma$ -phase always forms upon quenching the  $\beta$ -phase, particularly in alloys with high Al and lower Nb, since the presence of high Al aids the  $\gamma$  formation and high Nb slows it down due to its tendency to partition into the  $\beta$ -phase as will be discussed in chapter 5. When  $\sigma$  is the first phase to form from the  $\beta$ -phase, its complex crystal structure and need for diffusion may inhibit its formation from the  $\beta$ -phase upon quenching, and  $\beta$ -phase can be retained to room temperature.

### **3.7 $\beta \rightarrow \gamma$ Phase Transformations at High Temperatures**

Figure 3-22 shows a heat treatment schedule that was employed on a sample of alloy 11. The slice was solutionized at 1500C for 1hr, cooled at a rate of 12K/min to 1350 C, where it was held for 2hrs before WQ to retain the high temperature microstructure (DHT1350/2h). The temperature of 1350 C was chosen based on the DSC curve of the alloy, and lies between the first and the second exothermic peaks on the cooling curve. Based on the thermodynamic calculations, it was expected that the first peak would be due to the formation of the  $\gamma$ -phase from the  $\beta$ -phase. Thus the region on the DSC curve between the two exothermic peaks represents a two phase  $\beta+\gamma$  region.

Figure 3-23 presents an XRD of the powdered DHT1350/2h sample. Distinct peaks of the  $\beta$  and the  $\gamma$  phases are visible along with those of the orthorhombic phase.

A low magnification BSE image of the microstructure is presented in Figure 3-24a. Notice the presence of coarse Widmanstätten  $\gamma$ -phase laths nucleating at the  $\beta$  grain boundaries in one grain, while cross sections of laths cutting the sample surface can be seen in the adjacent grain. No  $\gamma$  laths were observed nucleating at the surface of the sample. Thus, it can be said that the  $\beta$  grain boundaries, when present, serve as primary nucleation sites for the  $\gamma$ -phase laths. The coarseness of the laths suggests that they formed at the heat treatment temperature of 1350 C and not upon quenching. Occasionally a  $\gamma$  allotriomorph with a much darker contrast than the rest of the  $\gamma$ -phase laths was observed in the sample. This will be discussed further in the subsequent part of this section. The  $\alpha$ -phase forms in the remaining  $\beta$  matrix upon quenching, as shown in the inset of Figure 3-24a. Figure 3-24b depicts the coarse  $\gamma$ -phase allotriomorphs at the  $\beta$  grain boundaries from which the  $\gamma$ -laths can be seen growing into the one preferred  $\beta$  grain. The average thickness of the laths was found to be about 40-70  $\mu\text{m}$ . The total  $\gamma$ -phase fraction was found to be about 30% in the microstructure.

Closer look at the microstructure reveals the square or rectangular shaped cross sections of the  $\gamma$ -phase laths. As shown in the optical micrograph in Figure 3-25, the interface between the  $\beta$ -matrix and  $\gamma$  laths is straight, indicating the presence of low energy coherent/ semi coherent interfaces. Formation of the Widmanstätten morphology at such high temperatures itself indicates that interface plays an important role in the formation of the  $\gamma$ -phase. The  $\gamma$ -phase laths form by maintaining the low energy interfaces even at high temperatures, which gives a near-square or rectangular shape to the cross sections. Further, the growth/ thickening of such lath possibly occurs by ledge mechanisms. Figure 3-26a shows an optical micrograph showing ledges on a  $\gamma$

lath. The BF micrograph in Figure 3-26b shows possible ledges on a  $\gamma$ -lath. Table 3-4 presents the EPMA compositional analysis on the DHT1350/2h heat treated sample. The two separate compositions of the  $\gamma$ -phase are given in the table, one for a darker higher Al and for a lighter lower Al  $\gamma$ -phase.

As can be noticed, again, Al tends to partition into the  $\gamma$ -phase, whereas Nb has a tendency to partition into the  $\beta$ -matrix. Ti content remains relatively constant throughout the phases. In order to study the effect of longer holding times on the scale, morphology and composition the  $\gamma$ -phase, another double heat treatment (DHT) was designed which employed slower cooling rates and longer holding times during the heat treatment. The sample was heated to 1500C and held for 1hr followed by cooling to 1350C at a rate of 1K/min. It was held at 1350C for 5 hrs and then WQ. The resulting sample consisted of  $\beta+\gamma$  two-phase microstructure. No change in the amount, morphology or scale of the  $\gamma$ -phase was observed, as can be seen in the BSE micrograph in Figure 3-27a. However, note the presence of some  $\gamma$ -phase allotriomorphs that appear much darker than the rest of the  $\gamma$ -phase laths. An optical micrograph depicting a much clearer difference in the contrasts is shown in Figure 3-27b. These dark grain boundary  $\gamma$  allotriomorphs were rarely seen in the DHT1350/2h too. The phase fraction of these dark  $\gamma$  allotriomorphs is small and they were observed only on the  $\beta$ -grain boundaries. Comparison between the compositions of the lighter  $\gamma$ -laths and the darker  $\gamma$  allotriomorphs, given in Table 3-4, shows that the allotriomorphs have much higher Al and lower Ti content relative to the lighter  $\gamma$  laths. This composition of the dark  $\gamma$ -phase allotriomorphs, which is higher in Al and lower in Nb and Ti compared to that of the  $\gamma$ -

phase laths, is close to the equilibrium composition of the  $\gamma$ -phase at temperatures higher than 1350 C as calculated by the thermodynamic calculations of Cupid et al. Thus, it can be said that the allotriomorphs with higher Al have a composition close to the equilibrium composition of  $\gamma$ -phase at higher temperatures than 1350 C, whereas the laths have a composition closer to the equilibrium composition at 1350 C.

Upon cooling from the solutionizing temperature, the first  $\gamma$ -phase nucleates at about the beginning of the first exothermic peak on the DSC curve. Once the allotriomorphs formed at the grain boundary and found suitable orientation relationships with a  $\beta$  grain, the  $\gamma$ -phase Widmanstätten laths formed at these high temperatures. As a sample was cooled at a rate of 12 K/min or 1 K/min, these laths attained close to equilibrium composition with a high Al content. By the end of the first exothermic peak, almost all  $\gamma$ -phase has formed in the microstructure. As we cool further down to 1350C, the tie lines in the two-phase  $\beta+\gamma$  region start to move, thereby changing the equilibrium composition of the phases. When the sample is held at 1350 C for 2 or 5 hrs, enough diffusion takes place such that the laths are able to attain the compositions close to equilibrium at 1350 C. However, some of the allotriomorphs continue to maintain the high Al composition. This would explain the presence of two compositions of the  $\gamma$ -phase observed in the DHT1350/5h microstructure. The question as to why some of these allotriomorphs do not undergo compositional changes upon holding could not be fully understood and needs further analysis. Note that the composition of the  $\gamma$ -phase laths is changing when comparing the two short term and long term heat treatments at 1350 C.

Some polarized light optical microscopy was conducted on the DHT1350/5h samples. A  $\lambda/2$  wave-plate was used to obtain the two corresponding polarized light micrographs by making a 45 degree rotation on either side. The  $\gamma$ -phase is known to react to polarized light due to its anisotropy, whereas the  $\beta$ -phase does not. Figure 3-28a & b shows two corresponding PL micrographs at the  $\beta$ -phase grain boundaries. It can be clearly seen that the orientation of the laths growing in the two grains is different. Further, the presence of twins within the  $\gamma$ -laths can also be seen. Note that each of the  $\gamma$ -laths is one single crystal of the  $\gamma$ -phase. It does not seem to be made of finer  $\gamma$ -laths growing parallel to each other as is seen in many  $\alpha_2+\gamma$  alloys.

### **3.8 Effect of $\beta$ -Phase Grain Boundaries on the Nucleation of the $\gamma$ -Phase**

It has been discussed earlier that in the DHT1350C sample the  $\gamma$ -phase laths nucleated preferentially at the  $\beta$ -phase grain boundaries (polycrystalline sample) as shown in Figure 3-24. No sign of any nucleation on the sample surface was observed. It appeared that the presence of  $\beta$ -phase grain boundaries was essential to the nucleation of the  $\gamma$ -phase. In this case the volume fraction of the  $\gamma$ -phase was about 30%. However, in a polycrystalline solutionized-WQ sample,  $\gamma$  laths were observed to nucleate both at the  $\beta$  grain boundaries as well as the sample surface (and pores), which is depicted in Figure 3-9. The volume fraction of the  $\gamma$ -phase in this case, however, was much higher at over 90%.

The resulting microstructure of a single crystal sample of solutionized-WQ sample of alloy 11 looked as is shown in Figure 3-29a. The  $\gamma$  laths can be seen to nucleate at the sample surface in the single crystal sample, similar to the observation made in the polycrystalline sample. A comparison of the microstructures of the single and

polycrystalline samples of alloy 11 in the solutionized-WQ state, shown in Figure 3-29b indicates the microstructures to be similar. The scale of the  $\gamma$  laths as well the amount of the  $\gamma$ -phase in both cases is rather close, both samples exhibiting a fine basket-weave structure.

Figure 3-30 shows optical micrographs of a single crystal sample of alloy 11 which was solutionized at 1500 C for 1hr, cooled to 1350 C at a rate of 9 K/min and WQ without holding. It can be seen that, again, a two-phase  $\beta+\gamma$  microstructure is obtained, with the formation of coarse  $\gamma$  laths in the matrix. These laths are clearly nucleating at the sample surface since there are no  $\beta$  grain boundaries available for nucleation.

In order to understand the comparative role of the  $\beta$ -phase grain boundaries and that of the sample surface in acting as the  $\gamma$ -lath nucleation sites, DSC tests were performed on the single crystal sample of alloy 11, similar to those performed on the polycrystalline sample. Figure 3-31 shows a DSC curve obtained upon running a single crystal sample of alloy 11 at a ramp rate of 10 K/min, which can be compared to the DSC curve of the polycrystalline alloy 11 shown in Figure 3-7. The curve is similar to the one from the polycrystalline sample. Comparing the cooling curves in the two DSC plots, it can be seen that the first peak begins at a much lower temperature of about 1249 C for a single crystal sample as compared to 1274 C in the case of the polycrystalline sample. Also, this first peak on the cooling curve is not as sharp and is rather diffused over a larger temperature range in the case of the single crystal.

Based on these data, the role of the  $\beta$  grain boundaries and sample surface can be speculated. As a polycrystalline sample of alloy 11 is slowly cooled from the solutionizing temperature, the relative stability of the  $\gamma$ -phase is increased and at a

specific temperature its nucleation at the  $\beta$ -phase grain boundaries becomes thermodynamically possible. Since limited diffusion is required for the  $\gamma$ -laths at these temperatures, (as discussed in section 3.7) these laths readily form. Further, when a single crystal sample of the alloy is slowly cooled from the solutionizing temperature, again, the relative stability of the  $\gamma$ -phase increases. However, in the absence of the  $\beta$  grain boundaries the nucleation of the  $\gamma$ -laths can only occur at other high energy sites such as the sample surface. However, it appears that the nucleation of the  $\gamma$ -laths at the sample surface becomes thermodynamically possible only at temperatures lower than those for grain boundary nucleation. This could possibly be due to possible differences in concentration of the grain boundaries and sample surface that make the grain boundary a more favorable nucleation site in comparison to the sample surface. However, from the data it appears that the relative energies of the  $\beta$ -grain boundaries and sample surface are not different but quite close. Further study is required in order to fully understand the difference in the role of the  $\beta$  grain boundaries and sample surface in the nucleation of the  $\gamma$ -phase.

When samples of alloy 11 (single or poly crystalline) are solutionized and WQ, the sample cools to room temperature at an extremely fast rate. As the single phase  $\beta$  is cooled fast, no  $\gamma$ -phase can form due to lack of time for diffusion. The  $\beta$ -phase becomes supersaturated and unstable at lower temperatures. The driving force for the formation of the  $\gamma$ -phase becomes high and nucleation barriers for nucleation along grain boundaries and sample surface both are overcome, and thus at these low temperatures the  $\gamma$ -phase nucleates extensively at all available nucleation sites along the grain boundaries and sample surface, whichever is available. The  $\gamma$ -laths, thus formed, are

fine and have essentially no compositional difference from the  $\beta$ -matrix due to lack of time for diffusion and growth.

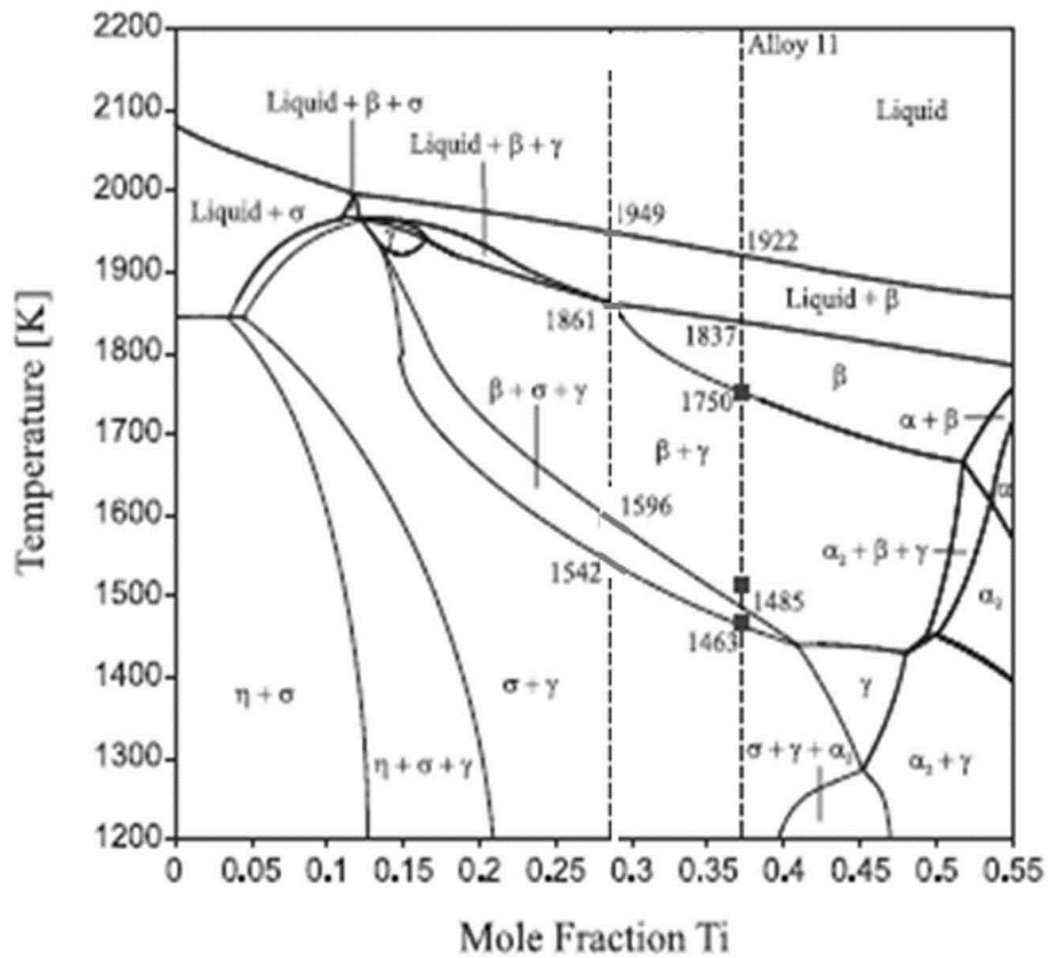


Figure 3-1. Isopleth section of the TiAlNb ternary at constant Al mole fraction of 0.45 depicting the transformation path of alloy 11[24]

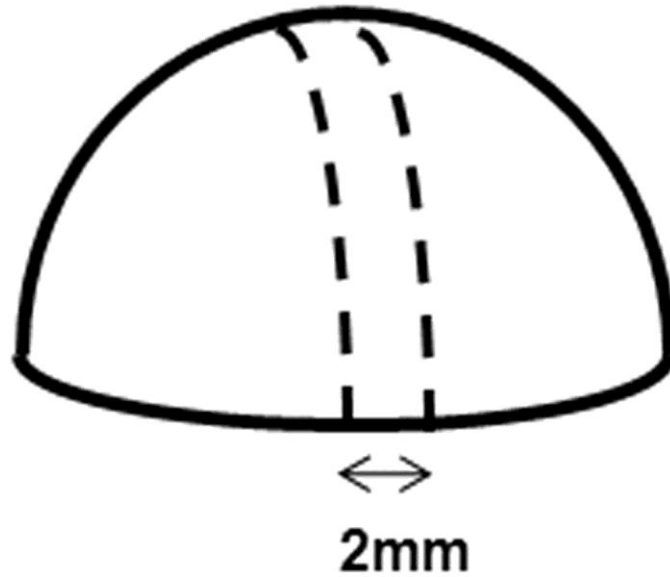


Figure 3-2. Schematic of an arc melted button showing the sectioned slice that was used for compositional and microstructural analysis of the as cast sample of alloy 11

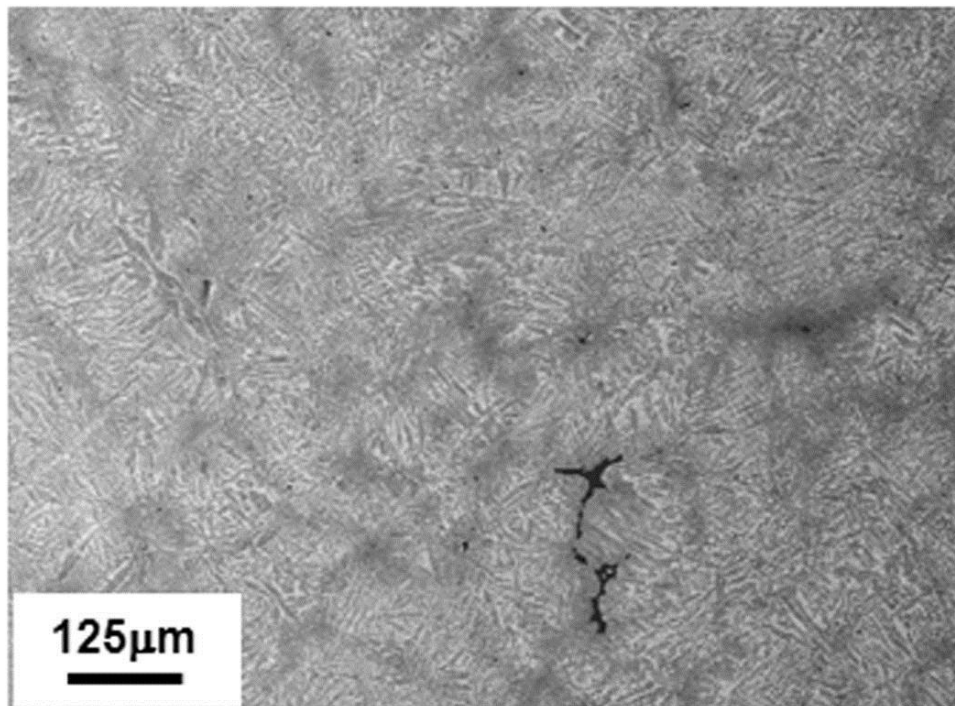


Figure 3-3. BSE micrograph of the as cast sample of alloy 11 depicting the presence of dendrites

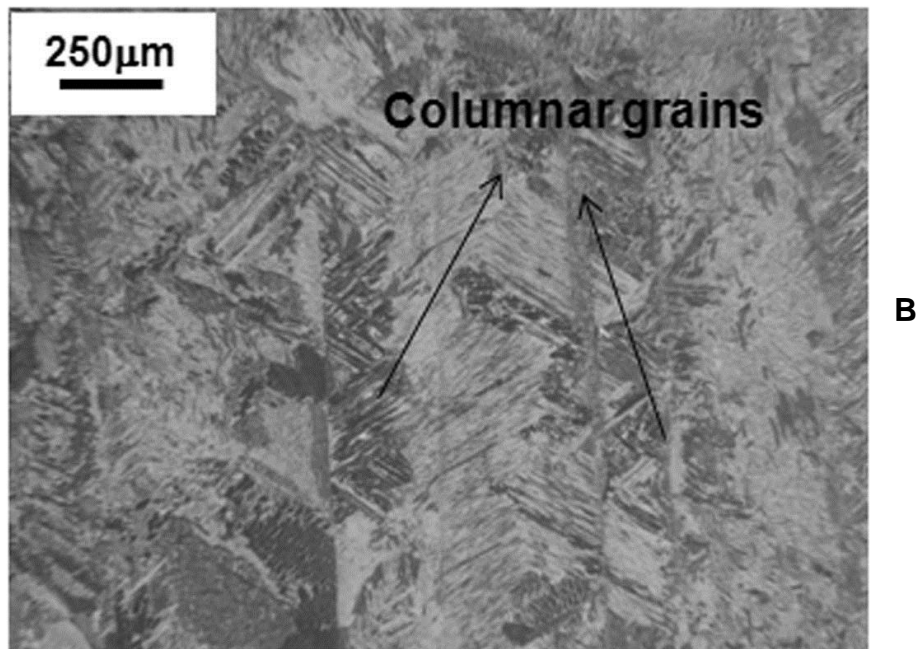
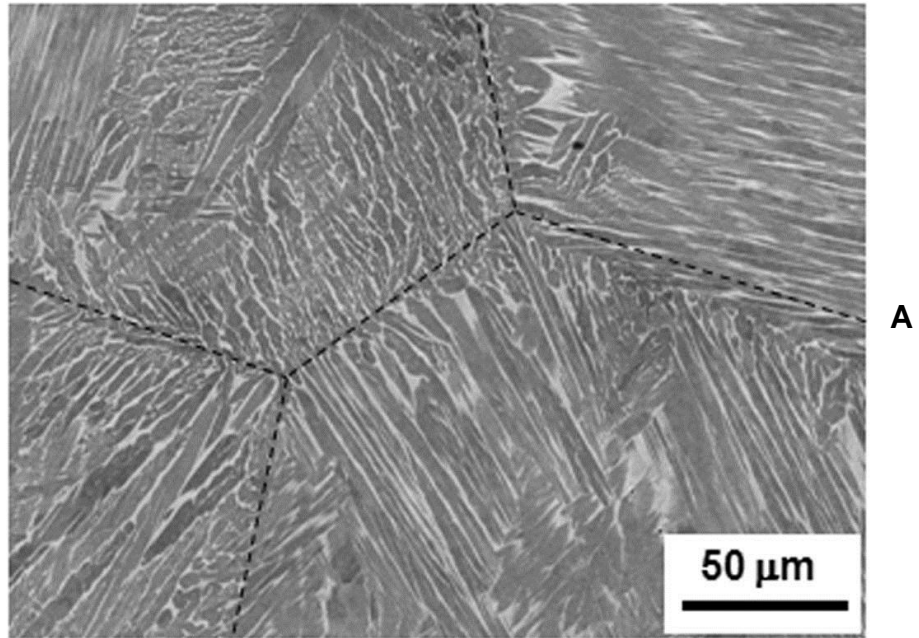


Figure 3-4. Alloy 11, as-cast. A) BSE micrograph from the top region of the button showing equiaxed prior  $\beta$ -phase grains and  $\gamma$ -phase Widmanstätten laths. B) Optical micrograph from the bottom region of the button showing columnar  $\beta$ -phase grains and fine  $\gamma$ -phase Widmanstätten laths

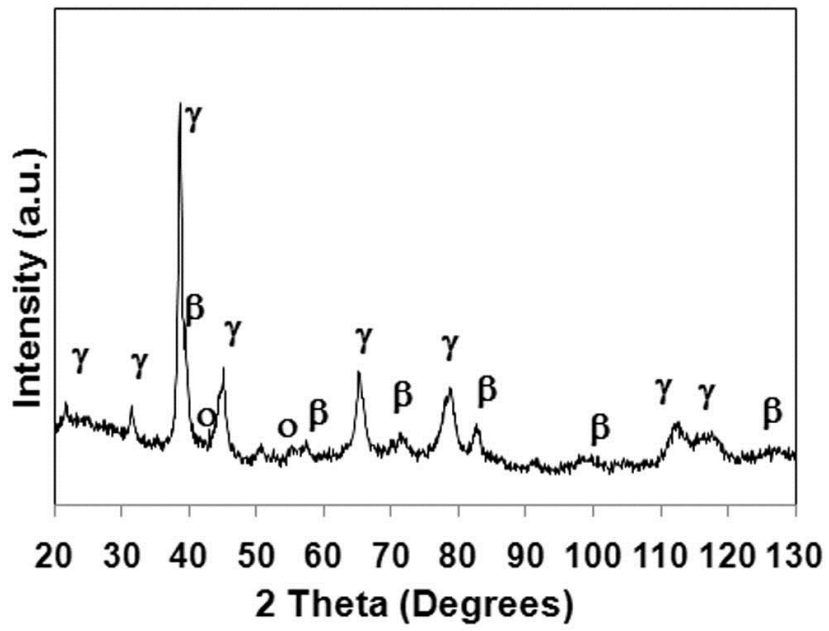
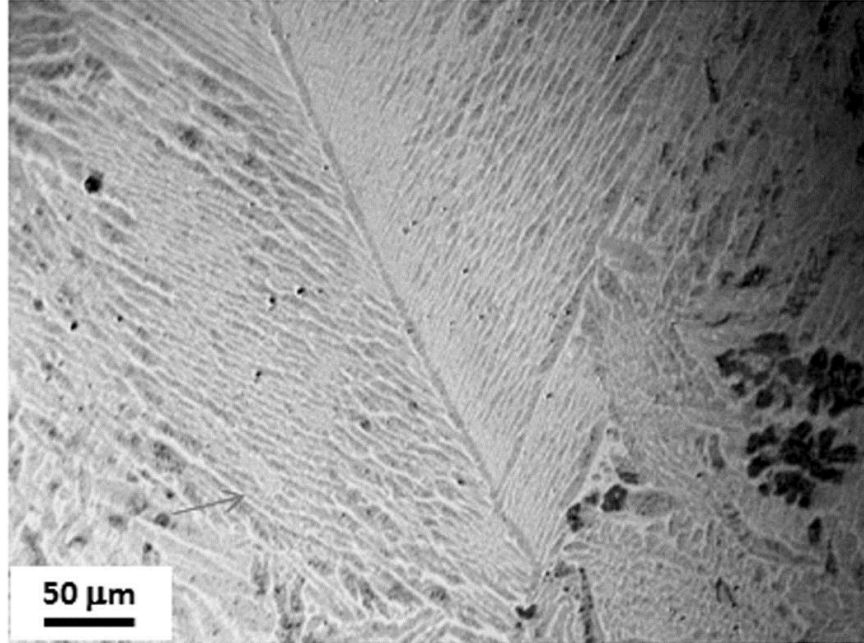
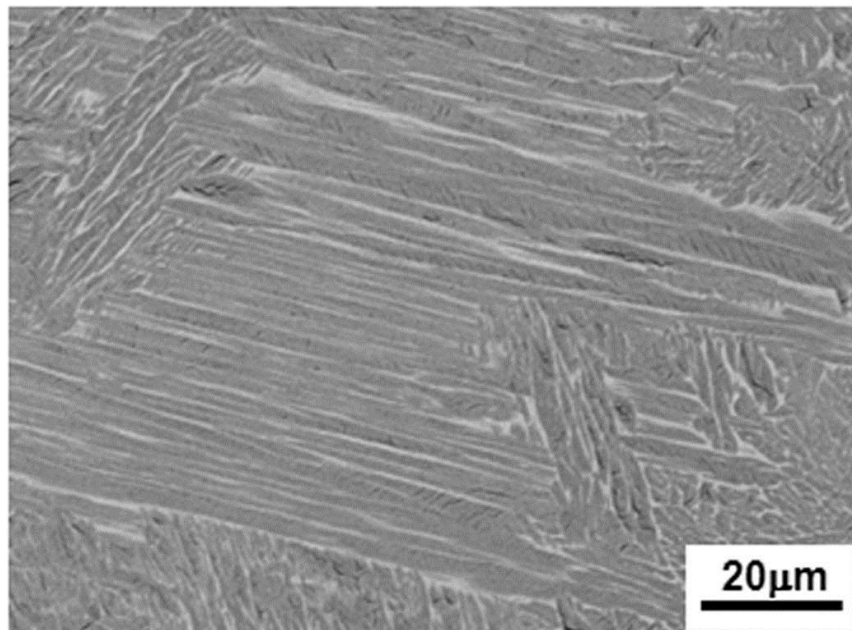


Figure 3-5. XRD profile of a powdered sample of the as-cast alloy 11



A



B

Figure 3-6. Alloy 11, as-cast. A) Optical micrograph showing  $\gamma$ -phase laths emerging from prior  $\beta$ -phase grain. B) BSE micrograph depicting colonies of  $\gamma$ -laths in the microstructure

Table 3-1. The nominal and actual compositions of alloy 11 as measured by the EPMA

	Al	Ti	Nb
Nominal	45.0	37.0	18.0
Actual	44.5 ( $\pm 0.6$ )	36.7 ( $\pm 0.2$ )	18.8 ( $\pm 0.7$ )

Table 3-2. The compositions of the phases in the as-cast alloy 1 measured by the EPMA

	Al	Ti	Nb
$\beta$ -phase	36.8 ( $\pm 0.5$ )	41.2 ( $\pm 0.6$ )	22.0 ( $\pm 0.7$ )
$\gamma$ -phase	47.2 ( $\pm 0.8$ )	35.1 ( $\pm 0.7$ )	17.7 ( $\pm 0.8$ )

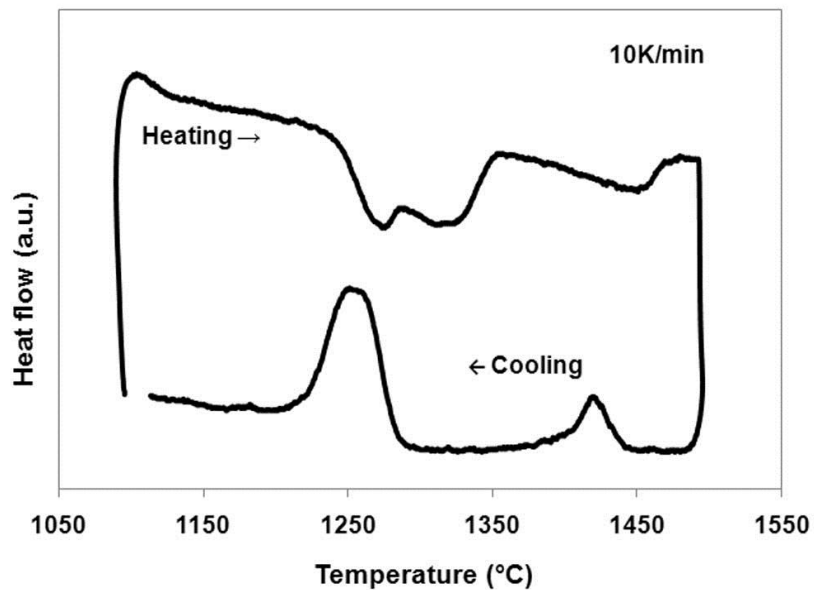


Figure 3-7. DSC plot of the final run of alloy 11 sample

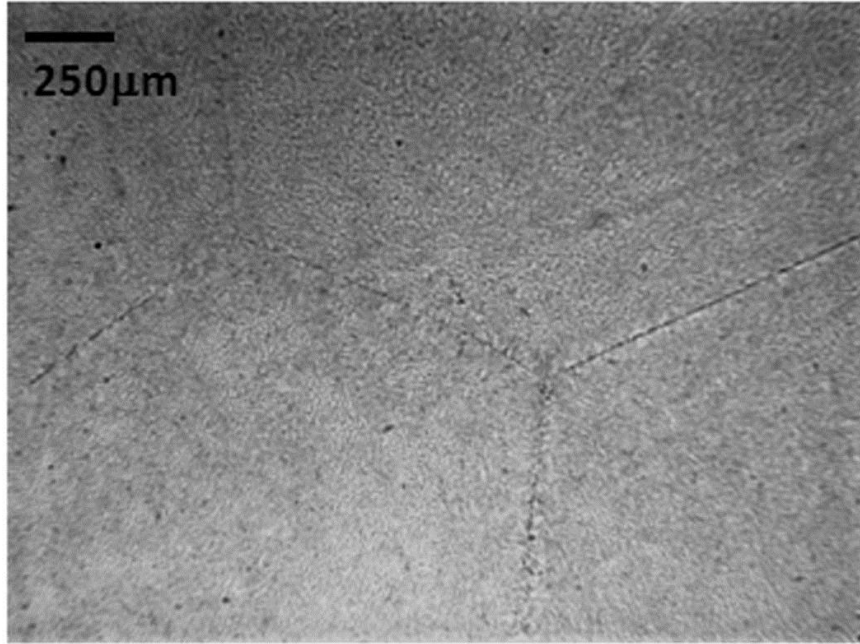


Figure 3-8. Optical micrograph of solutionized-WQ alloy 11 showing large  $\beta$ -phase grains that grew upon solutionizing

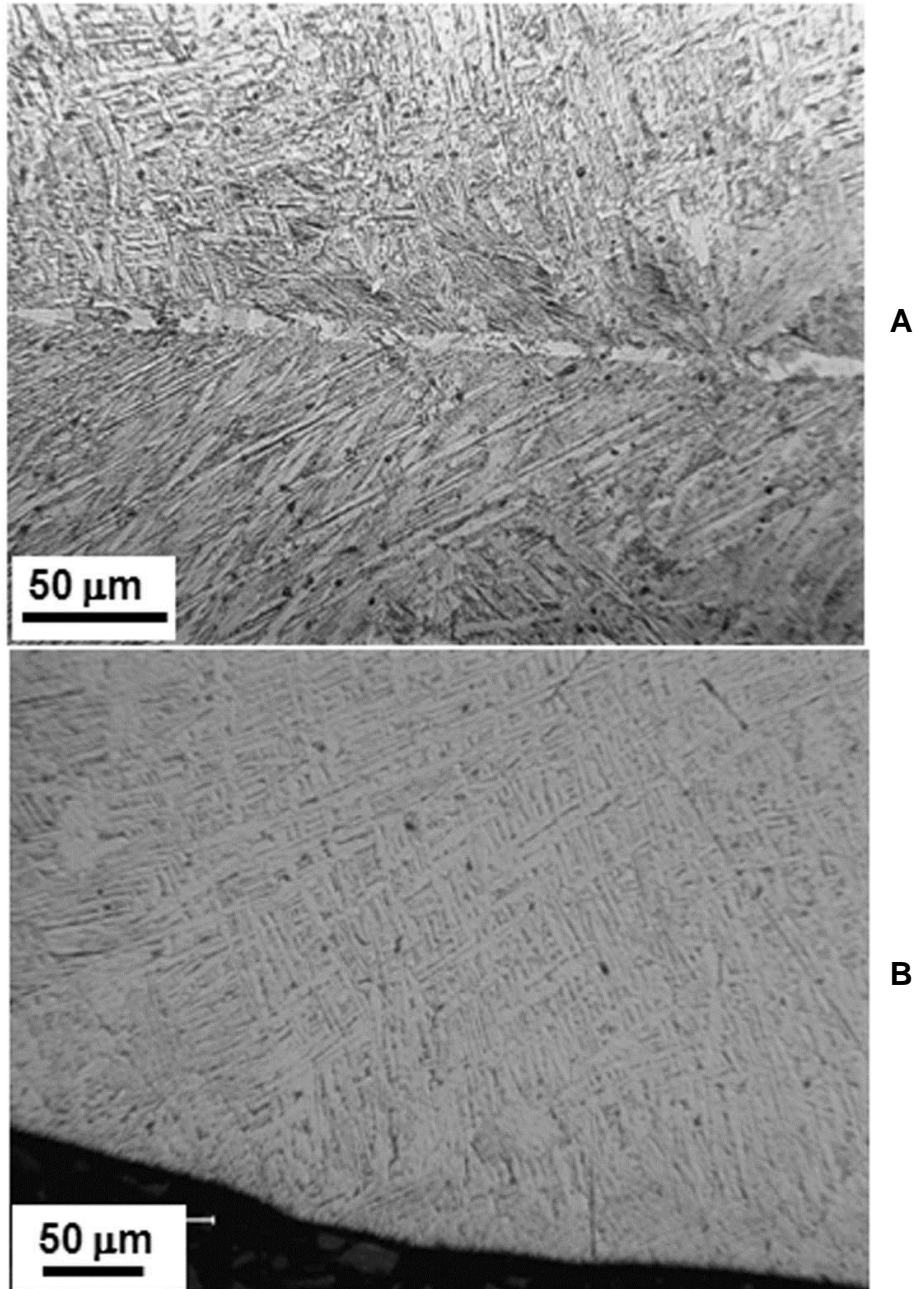


Figure 3-9. Alloy 11, solutionized-WQ. A) Optical micrograph showing nucleation of fine  $\gamma$ -phase Widmanstätten laths at the  $\beta$  grain boundaries. B) Optical micrograph showing nucleation of fine  $\gamma$ -phase Widmanstätten laths at the sample surface

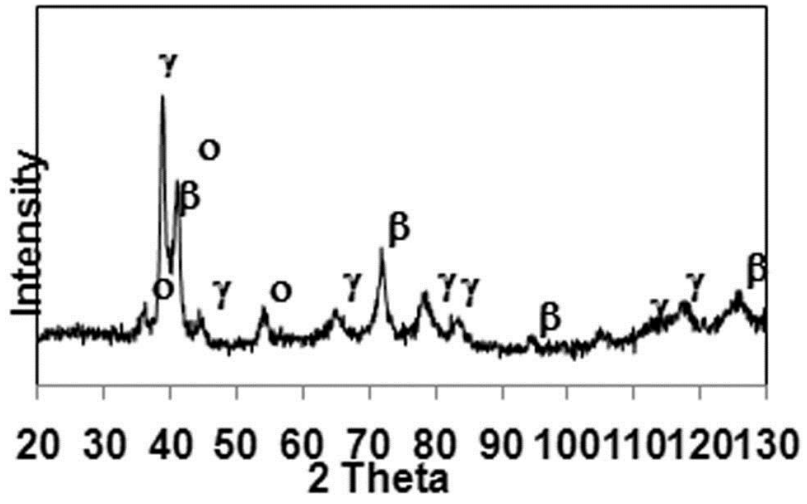


Figure 3-10. XRD profile of a powdered sample of solutionized-WQ alloy 11

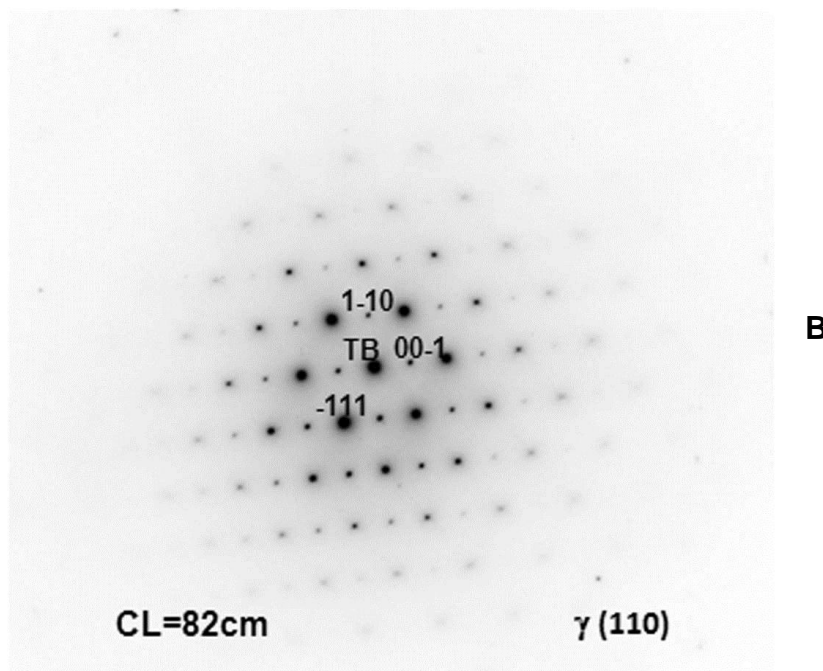
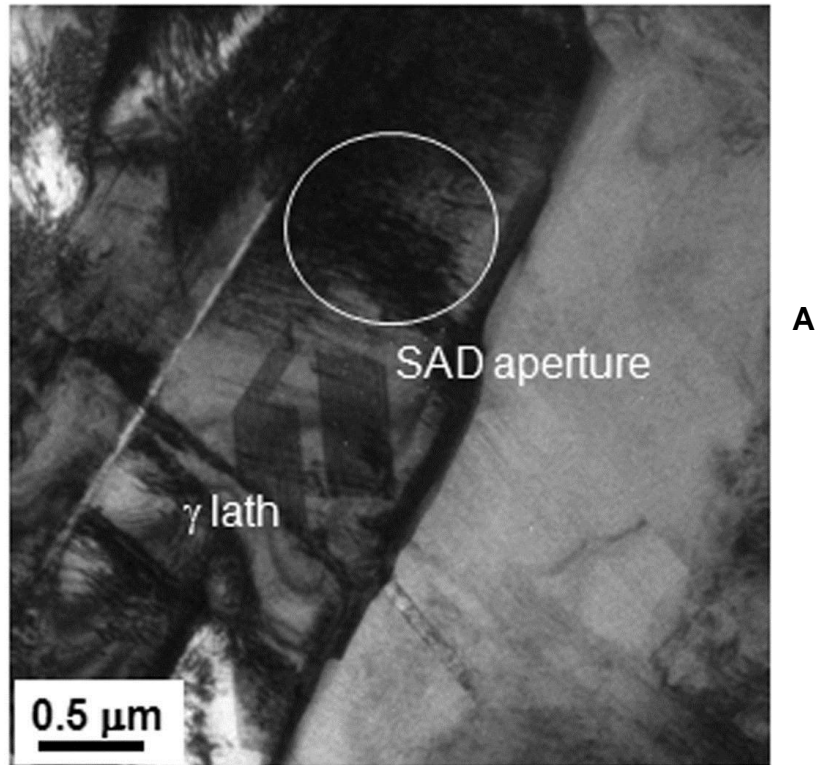


Figure 3-11. Alloy 11, solutionized-WQ. A) TEM BF micrograph showing the  $\gamma$ -phase laths. B) Corresponding diffraction pattern of the  $\gamma$  laths at  $\gamma$ [110] zone axis

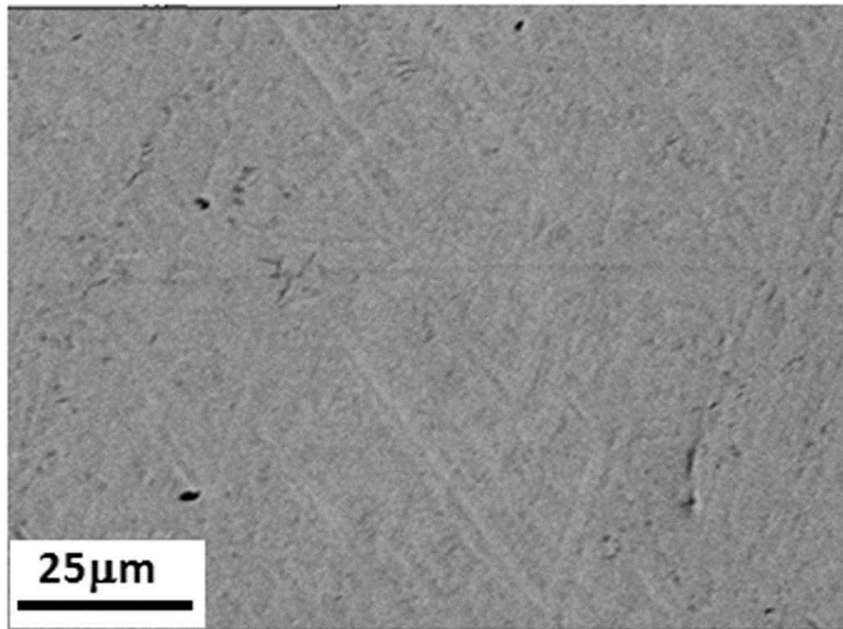


Figure 3-12. BSE micrograph of solutionized-WQ alloy 11

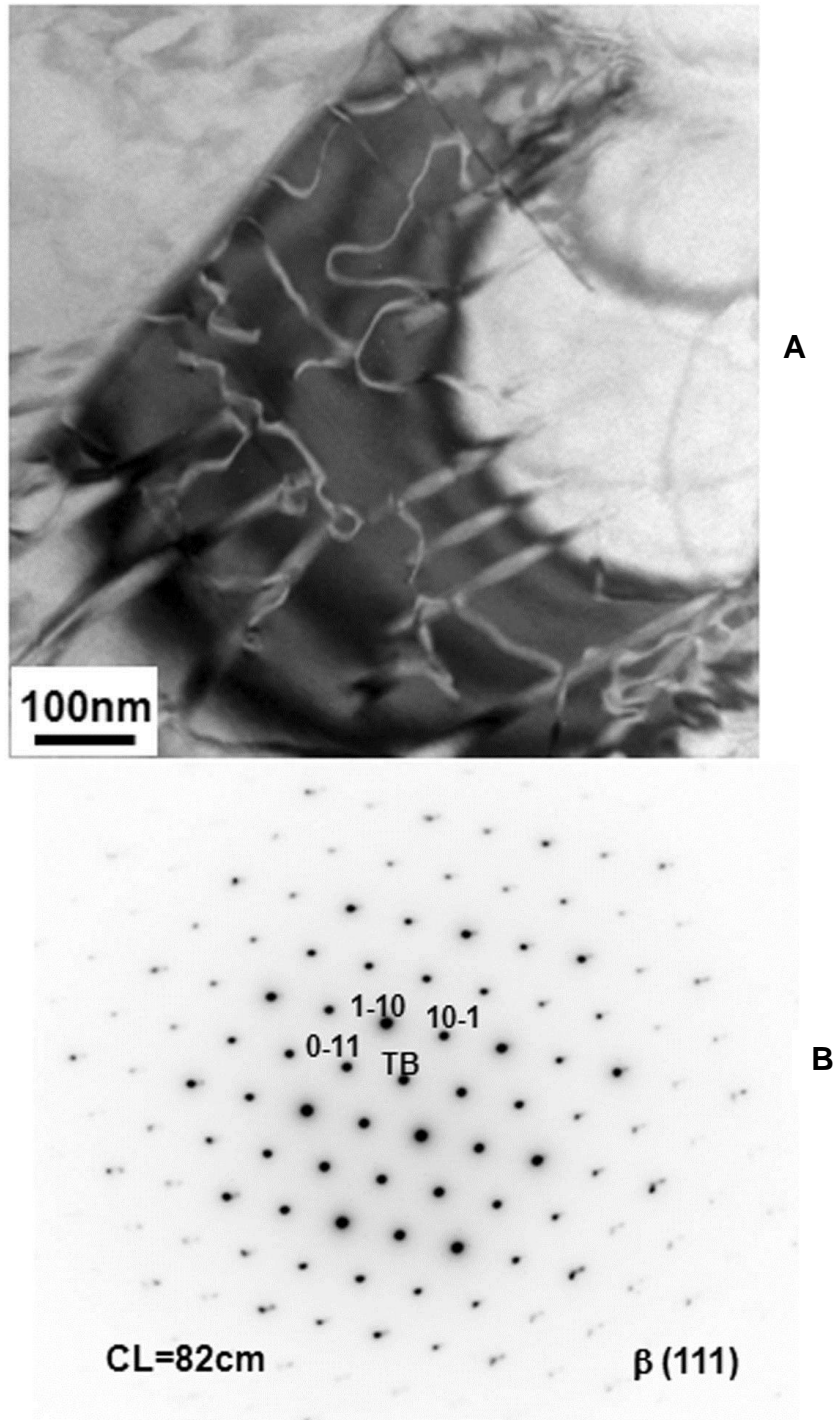


Figure 3-13. Alloy 11, solutionized-WQ. A) TEM BF micrograph showing APBs in the  $\beta$ -phase matrix. B) Corresponding diffraction pattern of the  $\beta$ -phase matrix along the  $\beta$ [111] zone axis

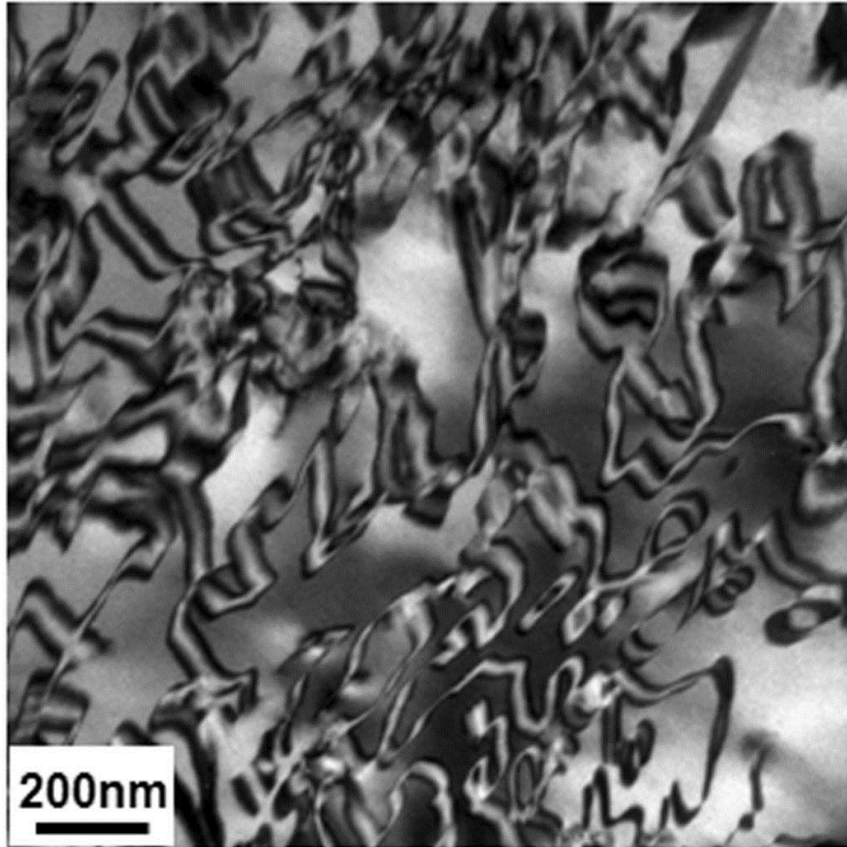


Figure 3-14. TEM BF image from solutionized-WQ alloy 11 showing fine APBs indicating extensive ordering in the  $\beta$ -phase

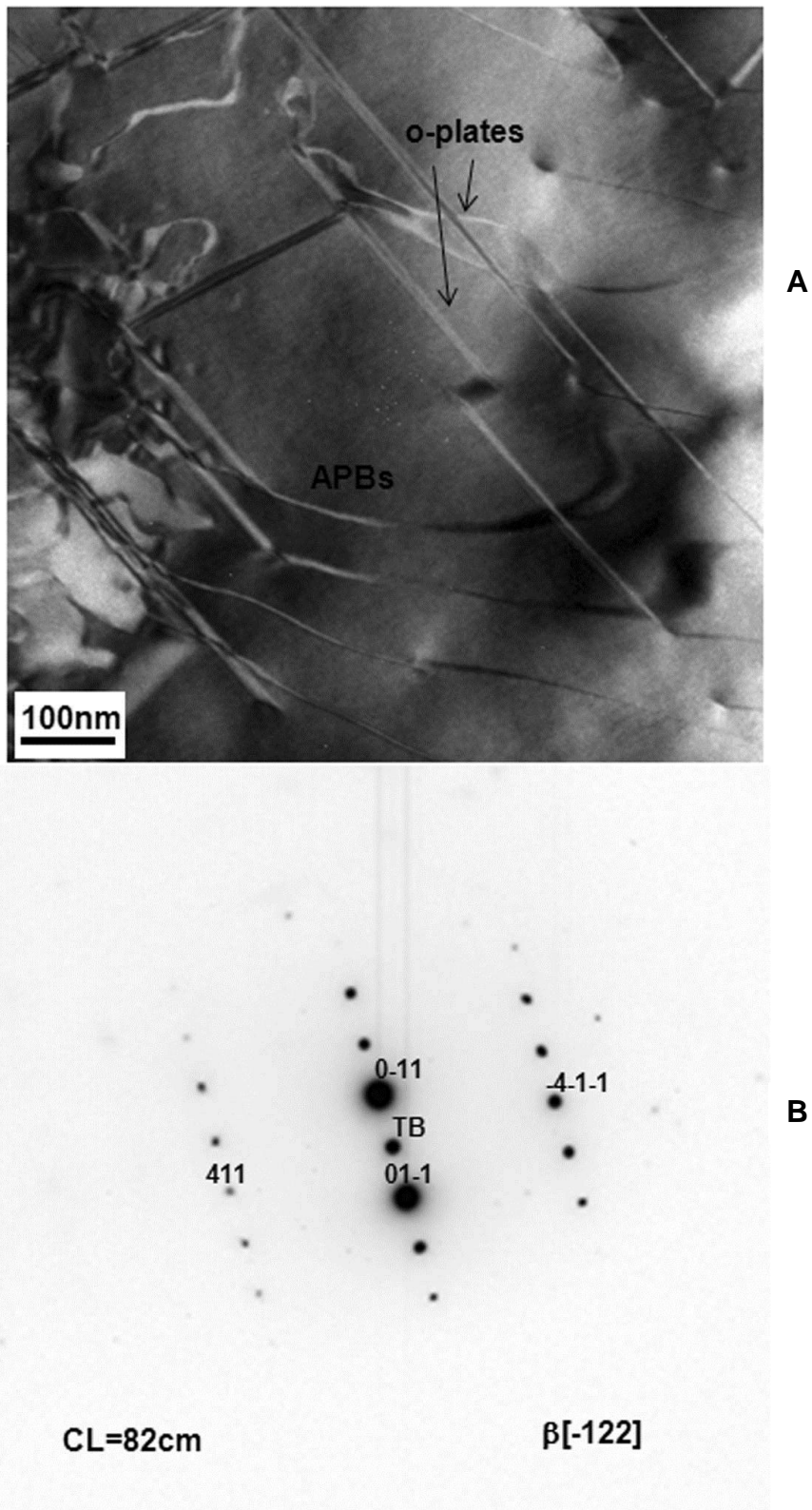


Figure 3-15. Alloy 11, solutionized-WQ. A) TEM BF image  $\alpha$ -phase and APBs in the  $\beta$ -phase matrix. B) Corresponding diffraction pattern of the  $\beta$ -phase matrix along the  $\beta[-122]$  zone axis

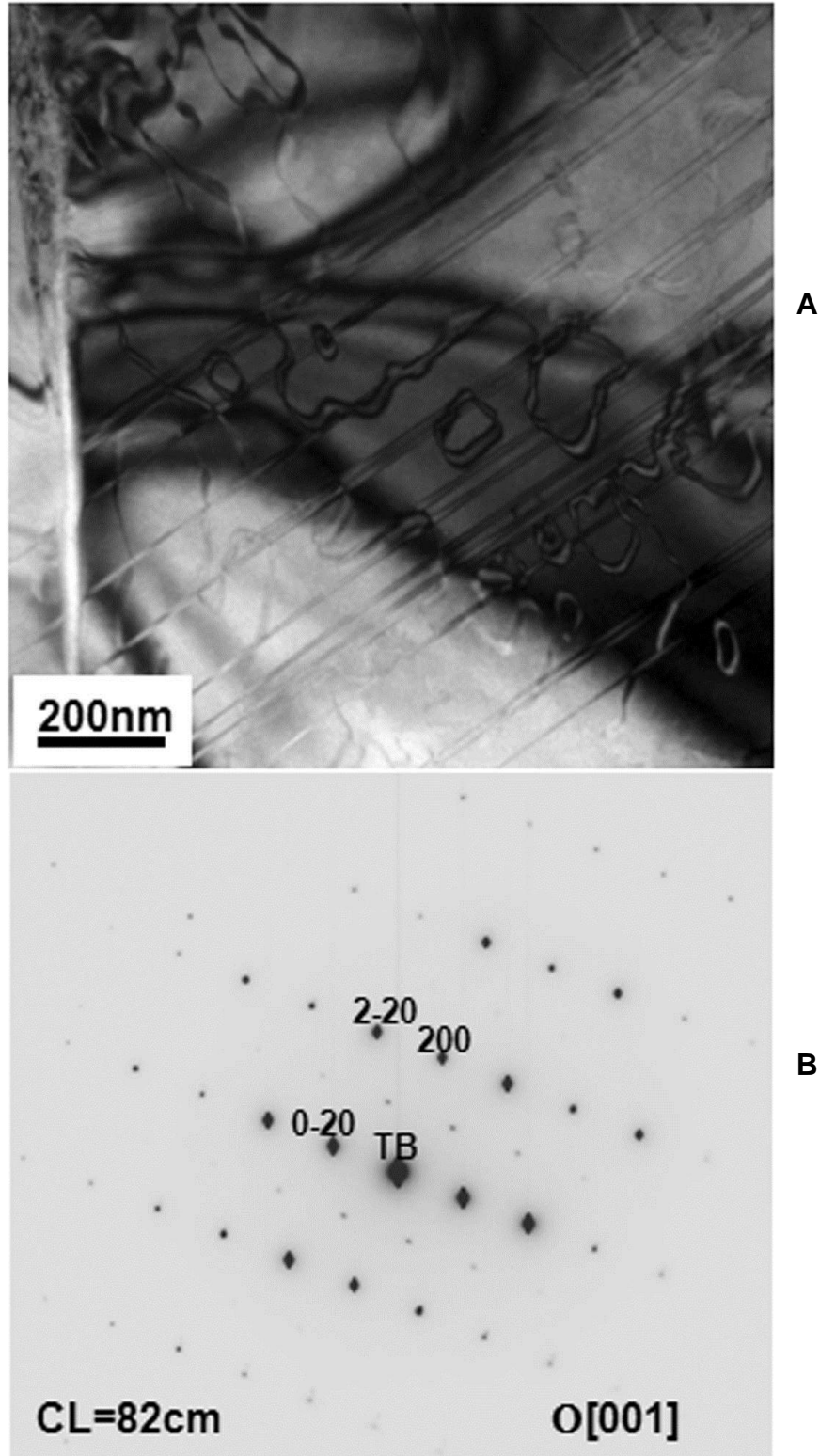


Figure 3-16. Alloy 11, solutionized-WQ. A) TEM BF image showing APBs passing through the  $\sigma$ -phase plates. B) Corresponding diffraction pattern of the  $\sigma$ -phase along the  $\sigma$ [111] zone axis in the solutionized-WQ alloy 11

Table 3-3. Actual compositions of alloy 21 and 31 as measured by the EPMA (at%)

	Al	Ti	Nb
Alloy 21	37.6( $\pm 0.1$ )	37.6( $\pm 0.2$ )	24.8( $\pm 0.3$ )
Alloy 31	41.9( $\pm 0.1$ )	37.8( $\pm 0.1$ )	20.3( $\pm 0.2$ )

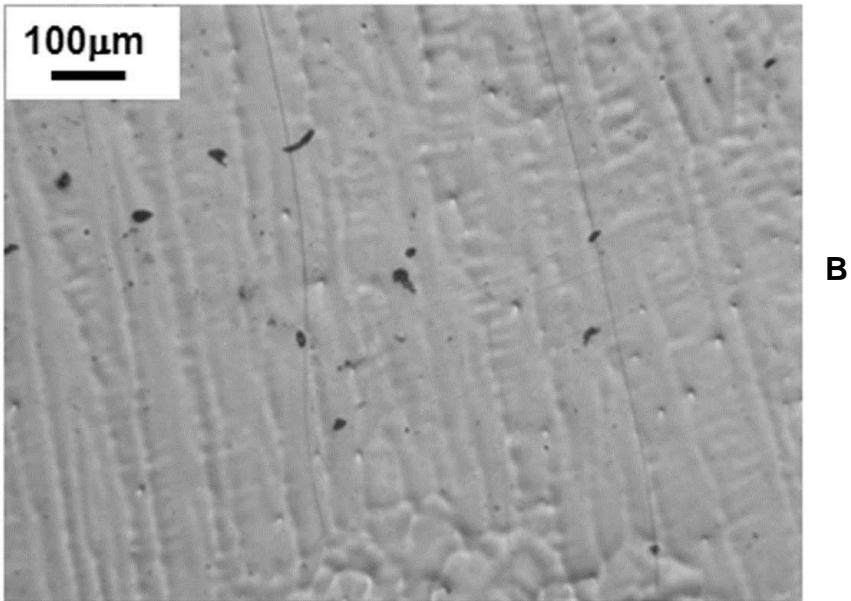
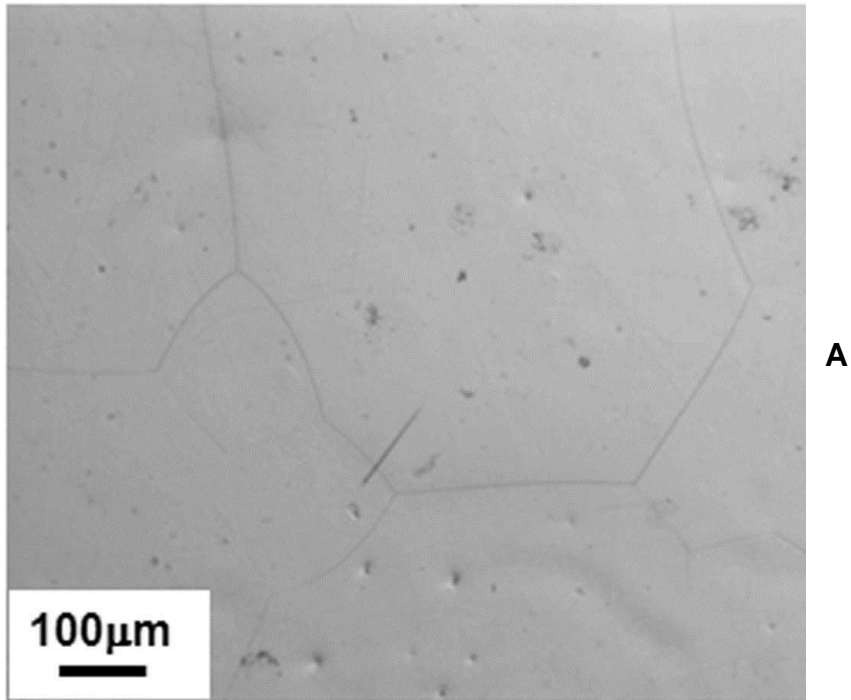


Figure 3-17. Optical micrographs of as-cast microstructure of alloy 21. A) Top region showing equiaxed  $\beta$ -phase grains. B) Bottom region showing columnar  $\beta$ -phase grains and dendrites

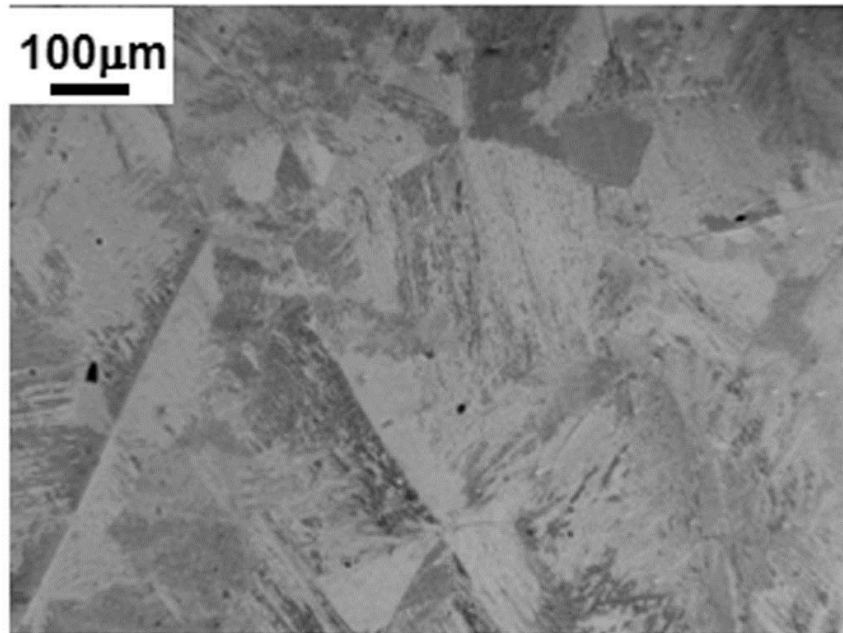


Figure 3-18. Optical micrograph from the top region of the as-cast button of alloy 31 showing equiaxed  $\beta$ -phase grains and fine  $\gamma$ -phase laths

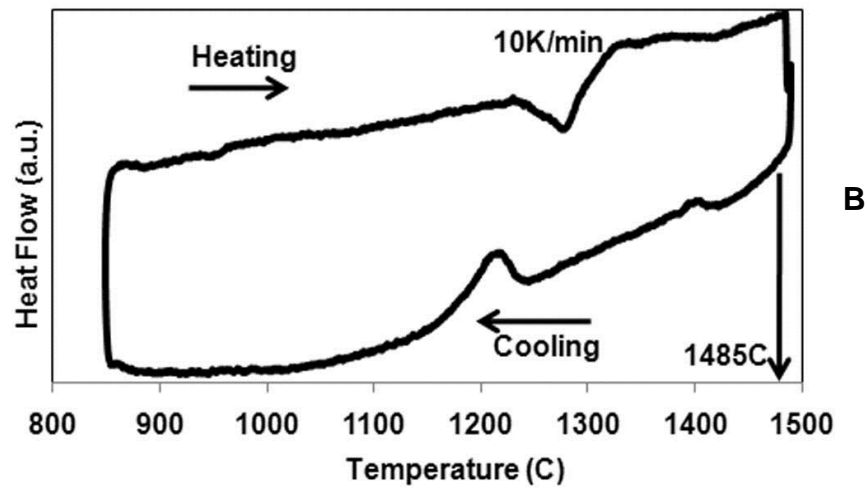
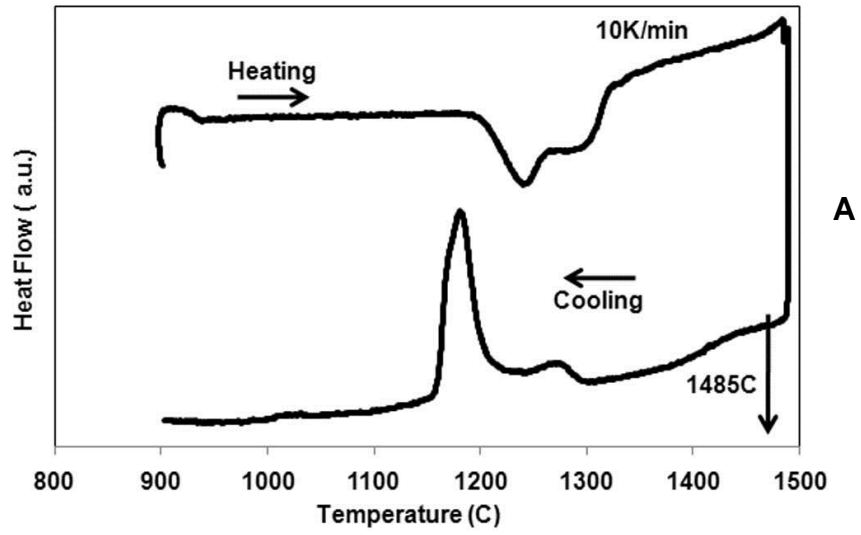


Figure 3-19. DSC profiles showing temperatures chosen for solutionizing. A) Alloy 21.  
 B) Alloy 31

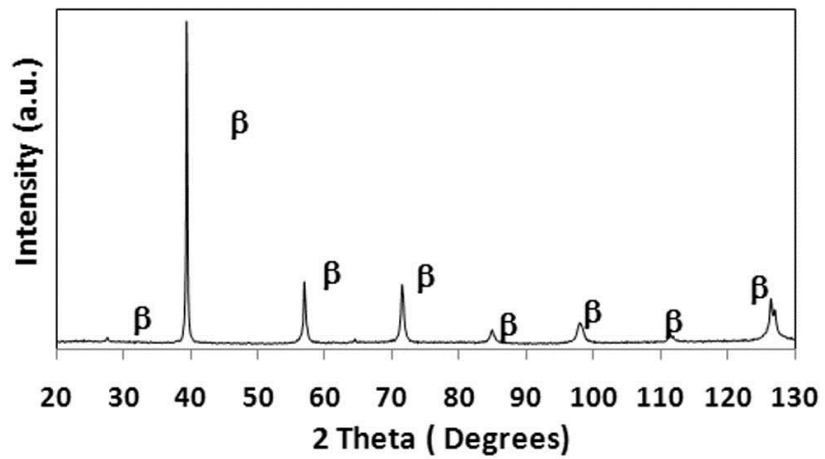
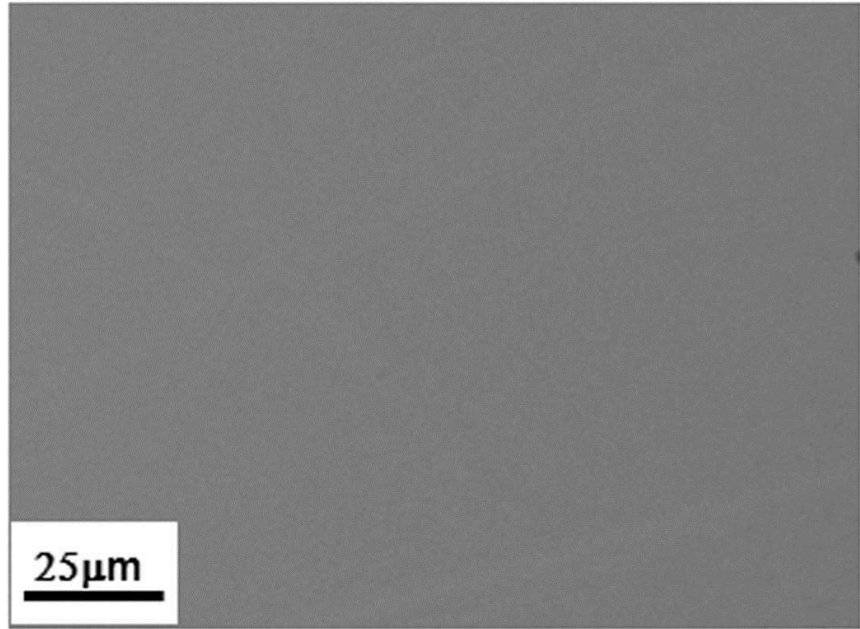


Figure 3-20. Alloy 21, solutionized-WQ. A) BSE micrograph showing a single  $\beta$ -phase. B) XRD profile taken on a powdered sample indicating the presence of a single  $\beta$ -phase

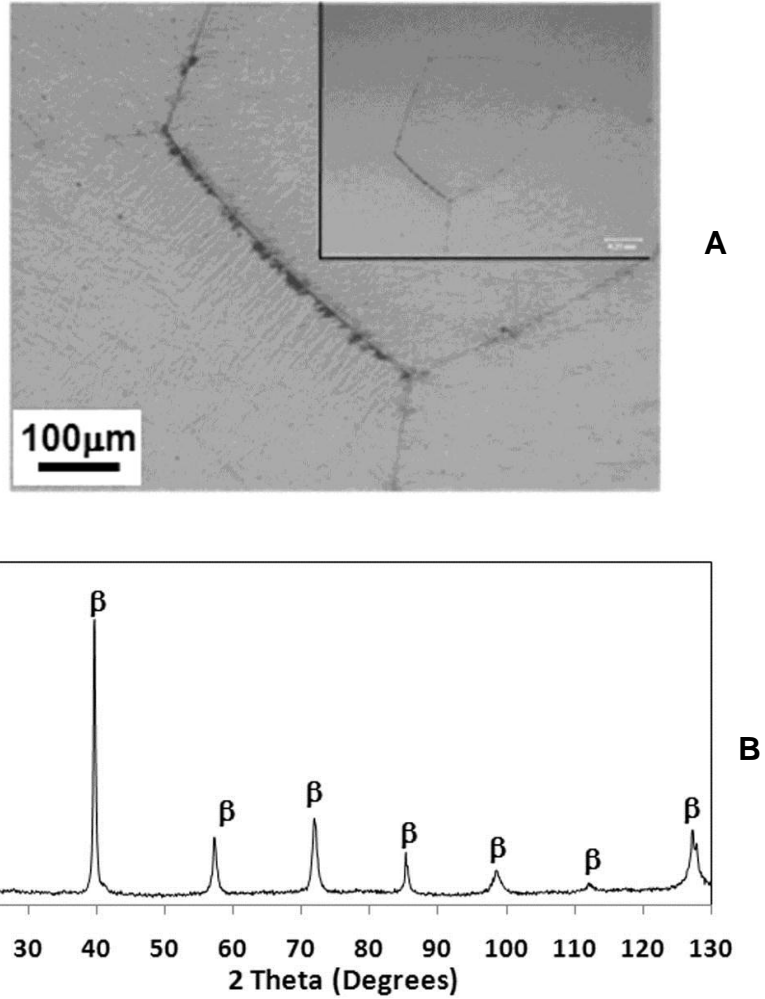


Figure 3-21. Alloy 31, solutionized-WQ. A) Optical micrograph showing fine  $\gamma$ -phase laths at the  $\beta$ -phase grain boundaries; inset-low magnification image showing coarse equiaxed  $\beta$ -grains. B) XRD profile taken on a powdered sample indicating single phase

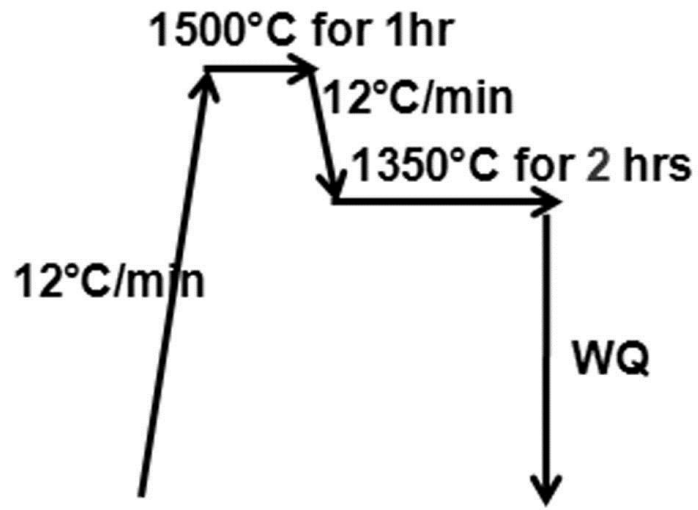


Figure 3-22. A schematic showing the heat treatment schedule performed on alloy 11 sample (DHT1350/2h)

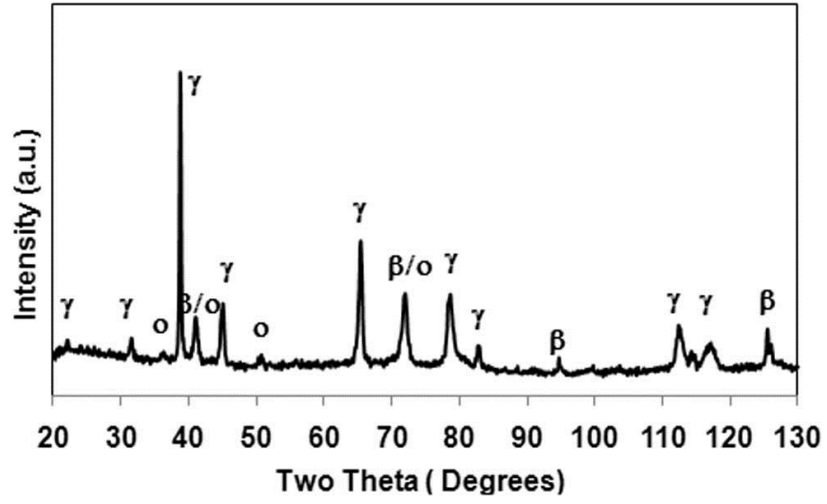


Figure 3-23. XRD profile taken on a powdered sample of DHT1350/2hsample of alloy  
11

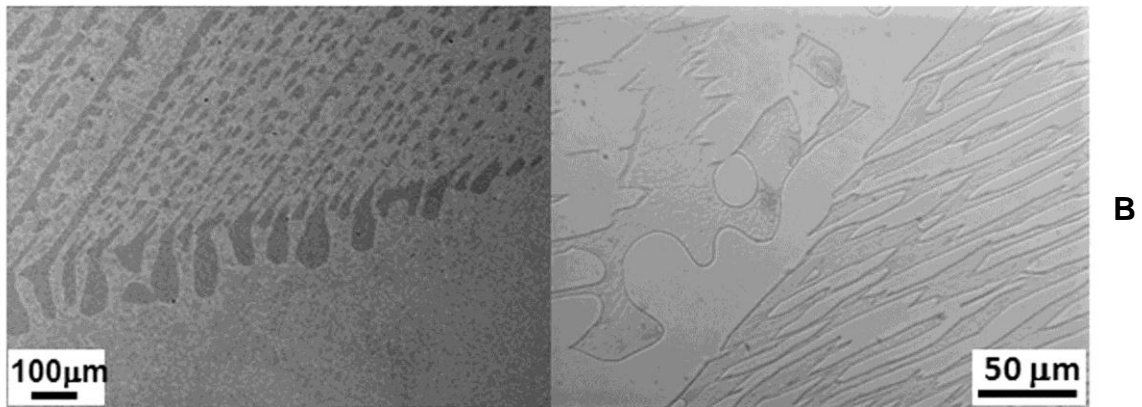
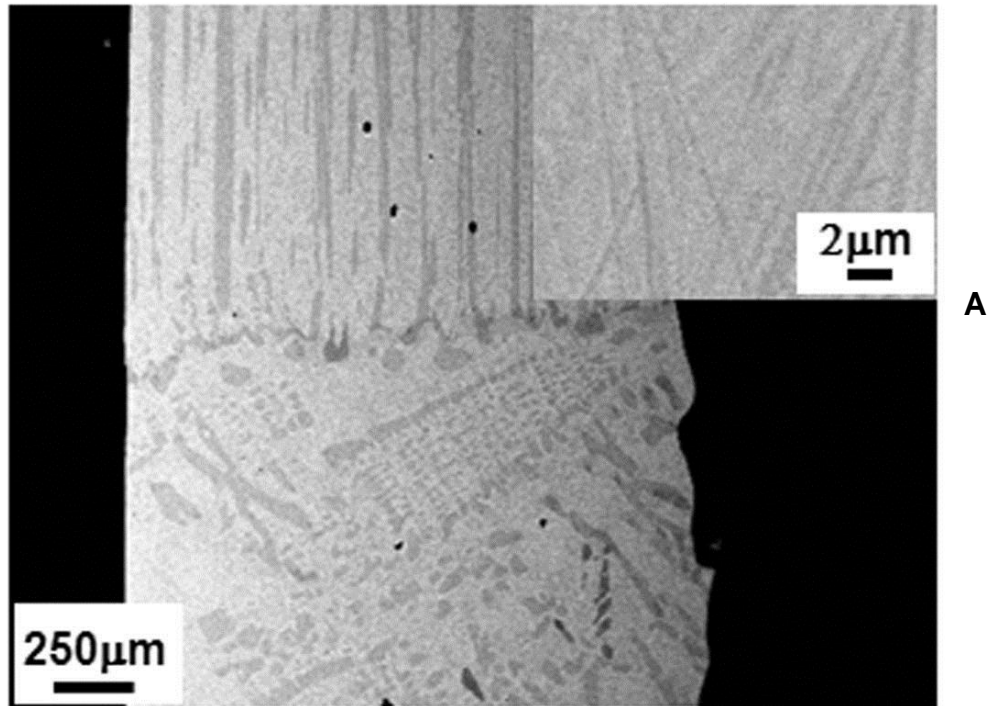


Figure 3-24. Alloy 11 DHT1350/2h. A) BSE image showing coarse Widmanstätten  $\gamma$ -laths; inset- high magnification image of the matrix showing fine  $\alpha$ -phase plates. B) Optical images showing  $\gamma$ -phase allotriomorphs at the  $\beta$ -phase grain boundaries

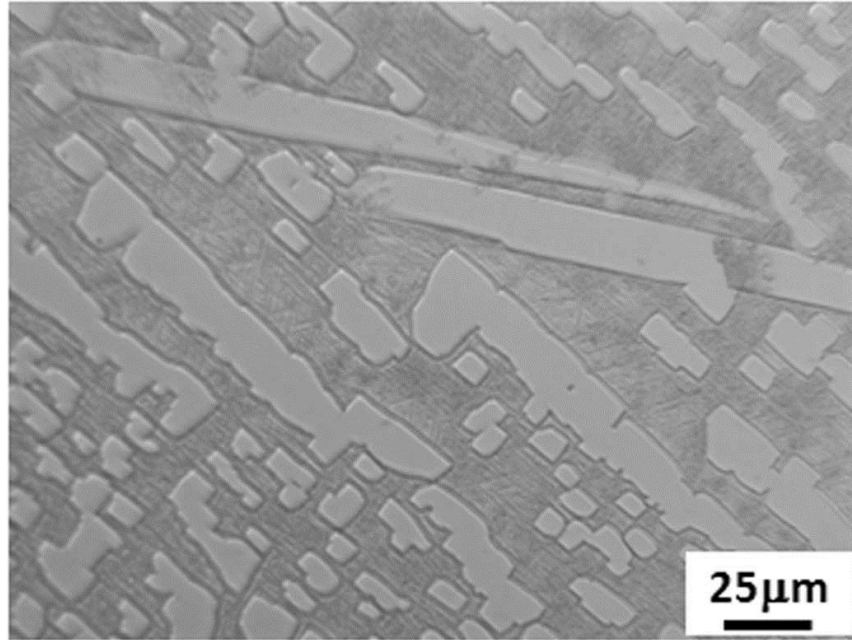


Figure 3-25. Optical image from DHT1350/2h sample of alloy 11 showing square and rectangular cross section of the  $\gamma$ -phase laths

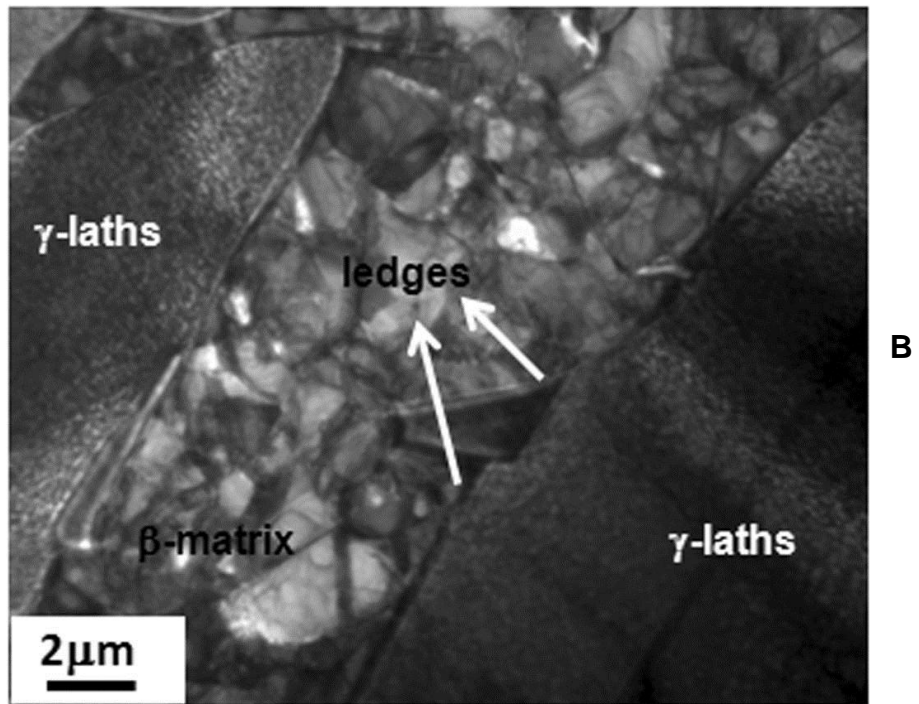
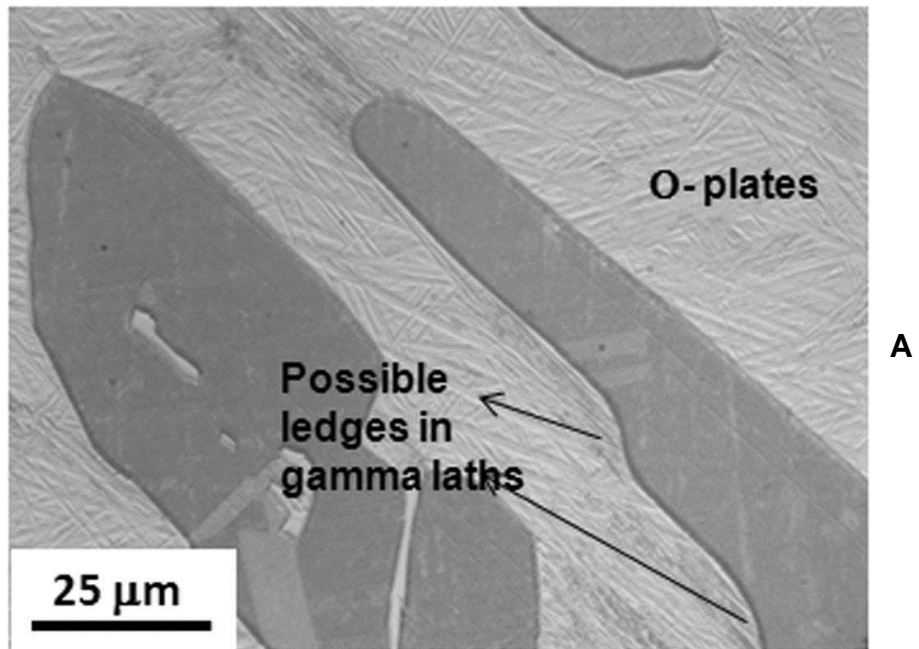


Figure 3-26. Alloy 11 DHT1350/2h. A) Optical image showing ledges in the  $\gamma$ -laths. B) TEM BF image showing ledges in the  $\gamma$ -phase laths

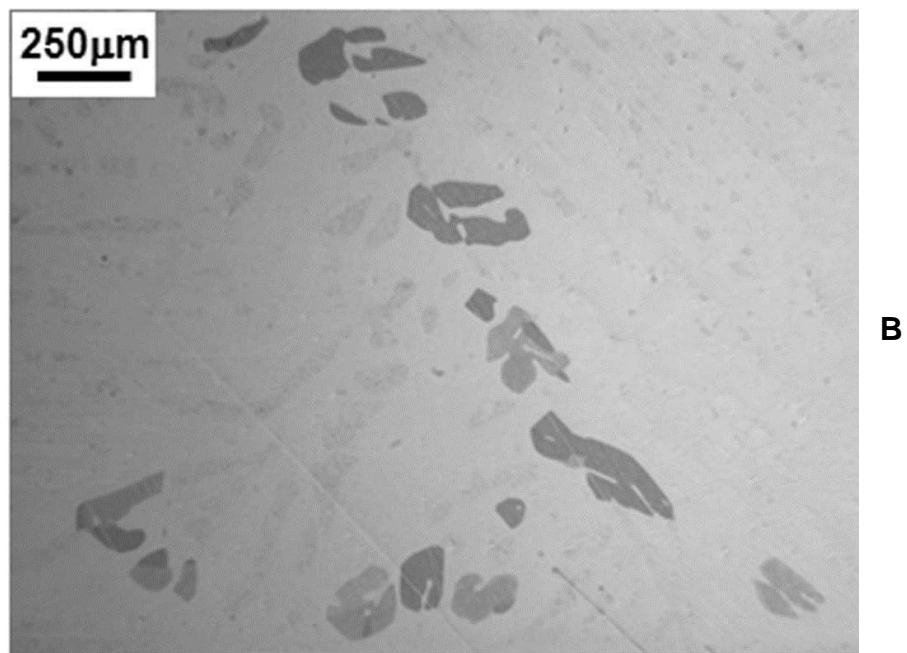
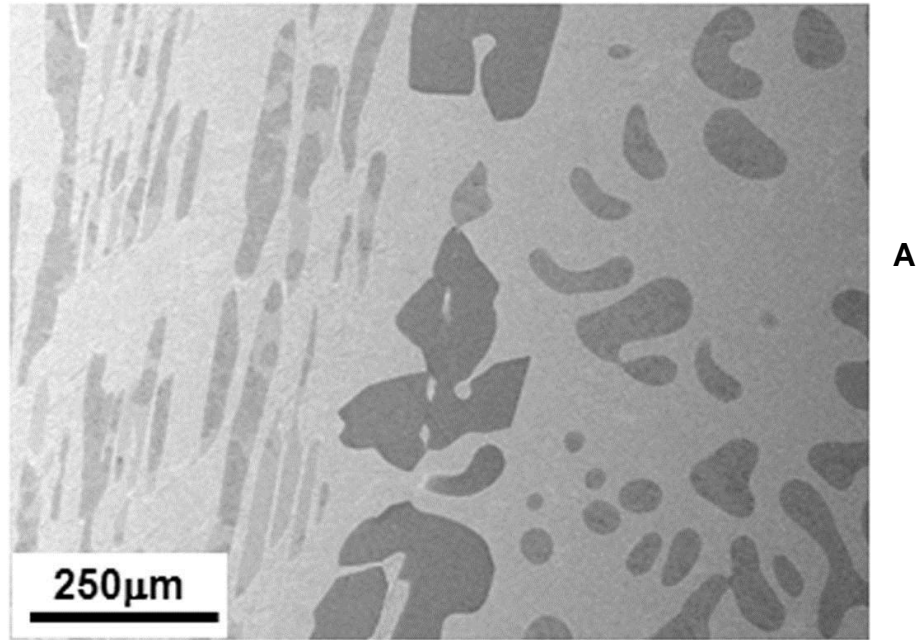


Figure 3-27. Alloy 11 DHT1350/5h. A) BSE image showing  $\gamma$  laths and dark high Al  $\gamma$ -allotriomorphs at the  $\beta$ -grain boundary. B) Optical image from DHT1350/5h sample of alloy 11 showing dark high Al  $\gamma$ -allotriomorphs at the  $\beta$ -grain boundary

Table 3-4. The EPMA compositions of the phases in the DHT samples of alloy 11

		Al	Ti	Nb
DHT1350/2h	$\beta$ -phase	43.2( $\pm$ 0.5)	38.0( $\pm$ 0.4)	18.8( $\pm$ 0.3)
	Light $\gamma$ -laths	44.9( $\pm$ 0.5)	38.1( $\pm$ 0.5)	17.0( $\pm$ 0.1)
	Dark $\gamma$ -allotriomorphs	48.8( $\pm$ 0.3)	35.1( $\pm$ 0.3)	16.1( $\pm$ 0.2)
DHT1350/5h	$\beta$ -phase	43.0( $\pm$ 0.5)	37.9( $\pm$ 0.4)	19.0( $\pm$ 0.2)
	Light $\gamma$ -laths	46.0( $\pm$ 0.2)	37.1( $\pm$ 0.1)	16.8( $\pm$ 0.2)
	Dark $\gamma$ -allotriomorphs	48.9( $\pm$ 0.2)	34.6( $\pm$ 0.1)	16.3( $\pm$ 0.3)

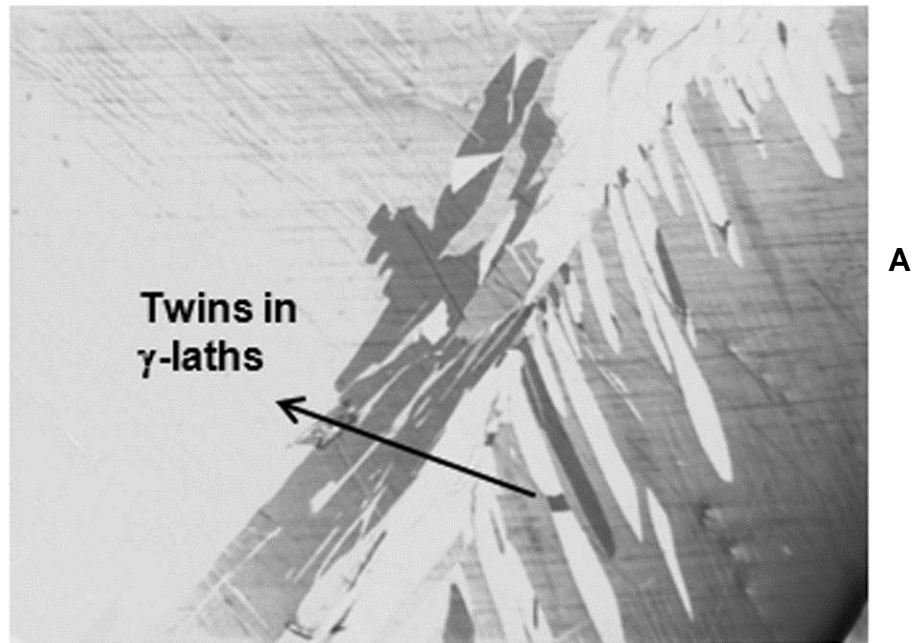


Figure 3-28. Polarized light micrographs of alloy 11 DHT1350/5h. A) at +45degree rotation of the wave-plate. B) at -45degree rotation of the wave-plate

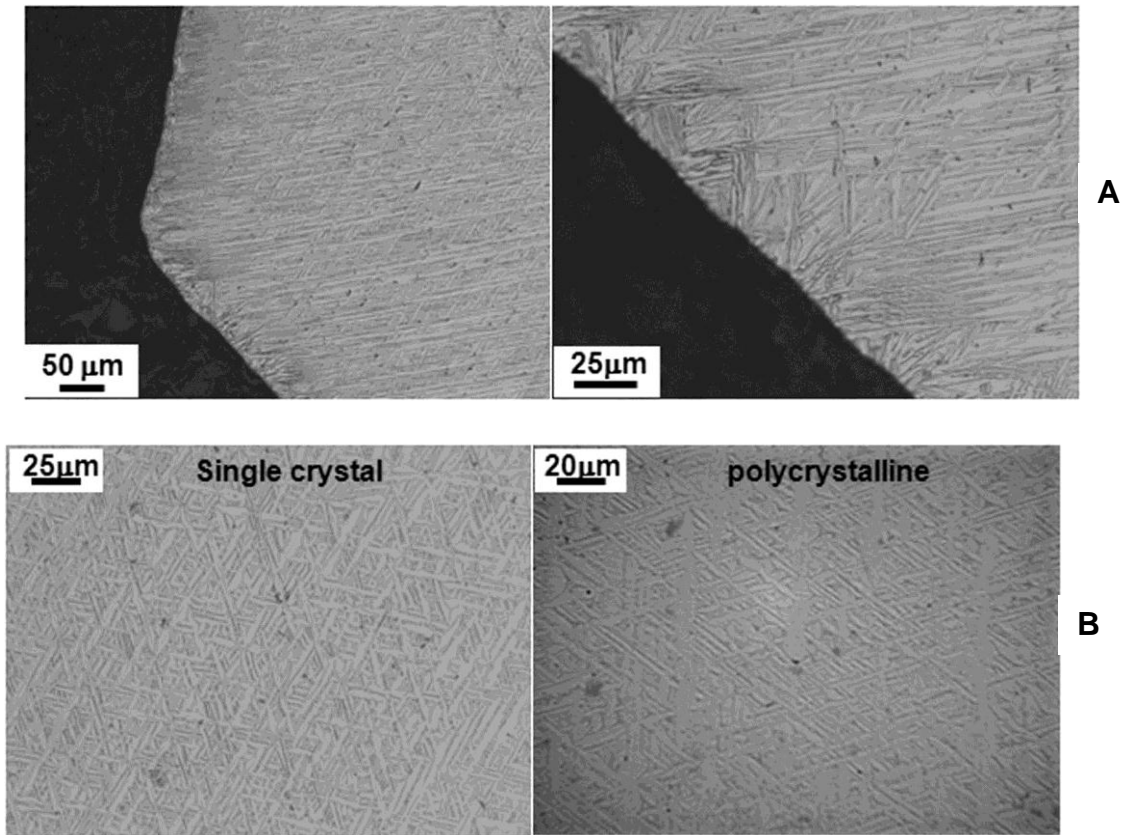


Figure 3-29. Optical micrographs of alloy 11, solutionized-WQ. A) single crystal sample showing  $\gamma$ -lath nucleating at the sample surface. B) images from single and poly crystal sample of alloy 11 showing similarity in the microstructure and scale of the  $\gamma$ -laths

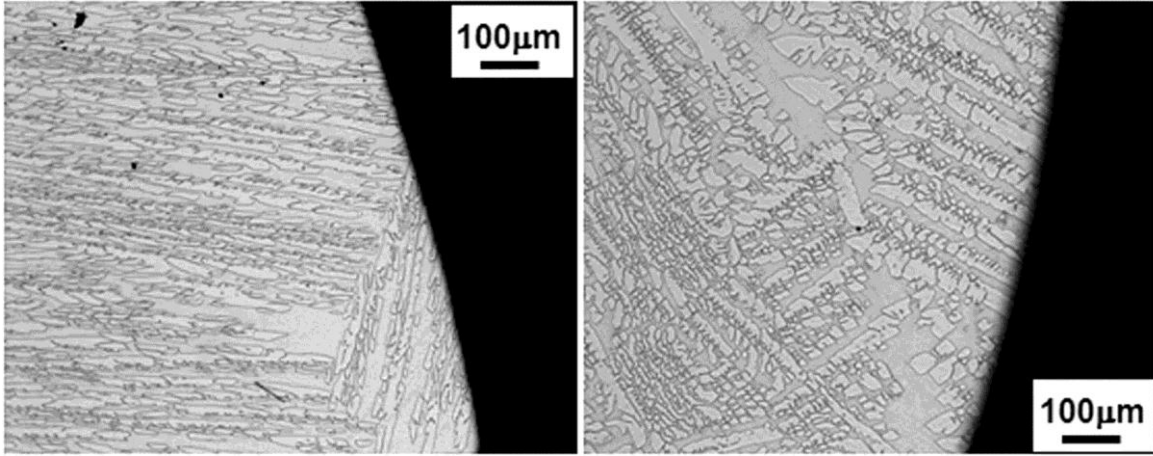


Figure 3-30. Optical images from CC1350 single crystal sample of alloy 11 showing  $\gamma$ -lath nucleating at the sample surface

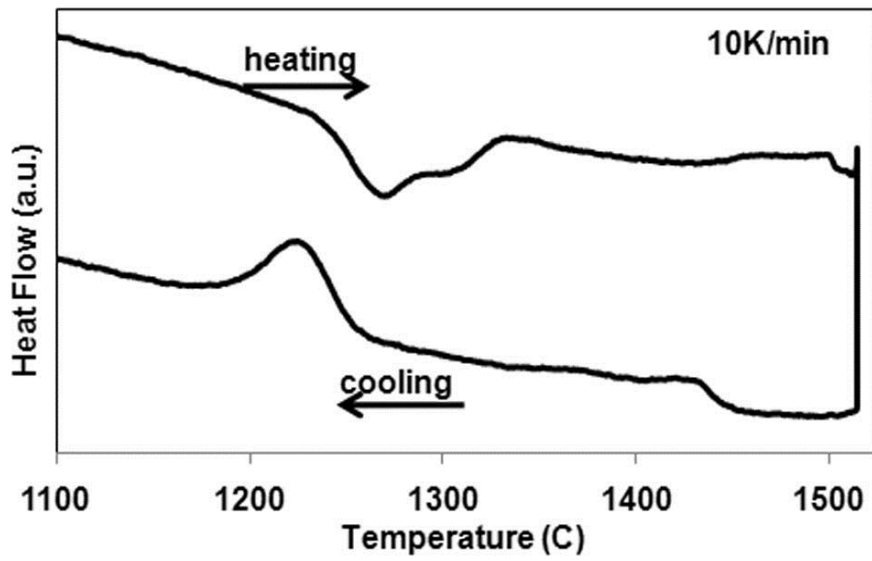


Figure 3-31. DSC plot of the final run of alloy 11 single crystal

## CHAPTER 4 TWO STEP NUCLEATION OF $\gamma$ -PHASE FROM $\beta$ -PHASE

### 4.1 Introduction

Alloy 11, according to previous thermodynamic calculations [2, 19], was expected to solidify as  $\gamma$ -phase. However, it has been shown by more recent phase diagram assessments using a new dataset [22, 24], that this alloy actually solidifies as the single  $\beta$ -phase [26], and quenching heat treatments and high-temperature XRD measurements successfully confirmed the same. According to the new phase diagram (refer to Figure 3-1), upon cooling, the  $\beta$ -to- $\gamma$  phase transformation takes place at 1750 K. Upon further cooling, this alloy enters a three-phase region as  $\sigma$ -phase starts to form at 1485 K. At 1463 K and below, this alloy exists as two-phase  $\gamma+\sigma$ . The  $\gamma+\sigma$  microstructure, once formed, is known to be stable, and any further cooling makes the diffusion rates sluggish with respect to further phase transformations.

Thus, the transformation path of the alloy was expected to be the sequence:

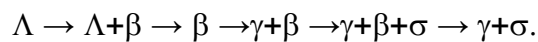


Figure 4-1 shows the DSC plot from alloy 11 run at a ramp rate of 10 K/min. Now combining data from the new phase diagram calculations and from the cooling curve on the DSC plot, the temperatures at which the transformation sequences occur appear to be somewhat close. Thus, the first exothermic peak on the cooling curve of the DSC plot can be attributed to the formation of  $\gamma$ -phase, whereas the second peak can be attributed to the formation of  $\sigma$ -phase. It would then be reasonable to expect that a sample of alloy 11, when solutionized and cooled to room temperature at rates comparable to those during the DSC measurements, a two phase  $\gamma+\sigma$  microstructure would also be obtained.

Figure 4-2 shows a low-magnification BSE micrograph from a sample of alloy 11 that was solutionized and then cooled to room temperature at a rate of 9 K/min. The BSE compositional phase contrast indicates the presence of two phases. An XRD plot of the powdered sample, shown in Figure 4-3, indicates the presence of  $\gamma$  and  $\beta$  phases. Some peaks of the metastable  $\sigma$ -phase are also visible. No peaks of the  $\sigma$ -phase can be discerned. Clearly, the phase with a darker contrast in the BSE micrograph is  $\gamma$ , whereas the lighter phase is  $\beta$ . The absence of  $\sigma$ -phase is neither in accordance with the thermodynamic calculations nor the DSC data, which indeed shows two distinct exothermic peaks on the cooling curve, indicative of two separate phase transformation events.

Further analysis of the slow cooled sample using optical microscopy revealed two distinct morphologies of the  $\gamma$ -phase as presented in Figure 4-4. The morphology (A), seen in Figure 4-4a, consisted of coarser elongated laths of the  $\gamma$ -phase originating from the  $\beta$ -phase grain boundaries. The second morphology (B), shown in Figure 4-4b, comprised a much finer lamellar structure in the matrix region between two coarse elongated  $\gamma$ -laths (morphology (A)). Although the coarse Widmanstätten  $\gamma$ -laths have been observed previously in the DHT1350, CC1350 and CC1305 samples, the lamellar-like morphology was not observed previously, and appears to have formed at temperatures lower than 1305 C. The total volume fraction of the  $\gamma$ -phase was calculated to be approximately 79% in the slow cooled sample.

The absence of the  $\sigma$ -phases raises questions concerning the accuracy of the calculated phase diagram, as well as the interpretation of the two distinct exothermic peaks of the DSC plot of alloy 11. Subsequent sections in the chapter present

elaborated results from the various experiments performed to explain the presence of the two distinct peaks on the DSC cooling curve, the presence of second lamellar-like morphology of the  $\gamma$ -phase, and a discussion of the the absence of the  $\sigma$ -phase in the slow cooled microstructure of alloy 11.

#### **4.2 Transformation Under the First DSC Peak on the Cooling Curve**

In order to investigate the transformations occurring under the two DSC peaks systematically, continuous cooling experiments were designed. Samples were cooled through the first and second peaks after solutionizing, and quenched from different temperatures. This procedure helped to understand the microstructural changes occurring under the two peaks, which assisted in identifying the transformations occurring upon cooling the sample.

##### **4.2.1 Continuous Cooling (CC) Heat Treatments**

The presence of two distinct peaks on the cooling curve of the DSC, the absence of the  $\sigma$ -phase, and the presence of a two phase  $\beta+\gamma$  microstructure in the slow cooled sample of alloy 11 all suggest that both DTA peaks upon cooling are somehow associated with the formation of the  $\gamma$ -phase. To understand how the two DSC peaks were associated with the  $\gamma$ -phase formation, three different samples were solutionized at 1500 C for 1hr, and then continuously cooled (CC) to different temperatures and WQ without delay. The cooling rate employed was 9 K/min, which is the same as that used for the slow cooled sample. Two of the samples were cooled to temperatures between the first and second exothermic peaks, whereas the third was cooled to just at the end of second exothermic peak before WQ.

#### 4.2.1.1 Solutionized-CC1350C-WQ

The first sample was cooled through the first DTA peak at 9C/min. to 1350 C followed by WQ. The BSE micrograph from the sample in Figure 4-5a shows a two-phase  $\beta+\gamma$  microstructure; where the brighter matrix is the  $\beta$ -phase while the dark laths along the  $\beta$  grain boundaries belong to the  $\gamma$ -phase. Figures 4-5 b&c show optical micrographs from the same sample. The prior  $\beta$  grain boundaries were found to be completely covered with coarser  $\gamma$ -phase laths (primary  $\gamma$ -phase laths). Also, a much finer (and lighter contrast)  $\gamma$ -phase was observed to be homogeneously distributed throughout the matrix and away from the grain boundaries. A zone denuded of this finer  $\gamma$  (marked with arrows on Figure 4-5a&c) was detected around all the dark-contrast  $\gamma$  laths, where no finer lighter-contrast  $\gamma$  was found. EPMA analysis of the phases in the sample is given in Table 4-1. The dark-contrast coarser  $\gamma$ -phase clearly has a high Al content, as was observed in the  $\gamma$  allotriomorphs in DHT1350/2h and DHT1350/5h samples discussed in chapter 3. This composition is close to the equilibrium composition of the  $\gamma$ -phase expected at temperatures above 1350 C. It can be concluded now that these  $\gamma$ -laths formed at high temperatures, while cooling through the first DSC peak. Unlike the DHT1350 samples, the samples were not held at 1350 C, and thus not enough time was provided for a change in composition and attainment of the equilibrium composition at 1350 C. Further, it can be implied that the finer lighter-contrast  $\gamma$ -phase formed upon quenching, whereas only the darker-contrast, coarser, high-Al  $\gamma$ -phase existed in the microstructure at the high temperatures before quenching. Presence of the denuded zone around the dark-contrast coarse primary  $\gamma$ -phase laths suggests that the

composition around the dark  $\gamma$ -laths might be different than the bulk matrix due to a concentration gradient arising from diffusion of elements between these laths and the matrix. The phase fractions of the dark- and light-contrast  $\gamma$  phases were calculated to be approximately 30% and 40%, respectively. Thus, at 1350 C, the microstructure consisted of 30%  $\gamma$ -phase.

#### **4.2.1.2 Solutionized-CC1305C-WQ**

A similar heat treatment as described above was performed by cooling the sample from the solutionizing temperature at 9 K/min. to the beginning of the second peak (1305 C), allowing investigation of the phase fraction of the  $\gamma$ -phase prior to the second peak.

Figure 4-6 shows the BSE micrograph from the sample, similar to Figure 4-5a, where two  $\gamma$ -phases with different BSE contrasts are seen. Consistently, the darker- and coarser-contrast  $\gamma$ -phase (primary  $\gamma$ -phase laths) was observed nucleating at the prior  $\beta$  grain boundaries, and the lighter-contrast and finer  $\gamma$ -phase that forms upon quenching was found to be homogeneously distributed throughout the matrix. Further, on closer examination, the dark-contrast  $\gamma$ -phase appears to be transforming to a lighter contrast phase, as shown in the inset of Figure 4-6. In the CC1350 sample all the grain boundary coarse  $\gamma$  was dark-contrast and high in Al, as the change in its composition seems to have taken place upon cooling to 1305 C from 1350 C. This indicates that the dark-contrast high Al  $\gamma$ -phase that nucleates and grows at high temperatures, upon cooling changes its composition to a lower Al content phase that is expected to be more stable at lower temperatures according to the thermodynamic calculations. Quantitative microstructural evaluation revealed that a change in the CC heat treatment temperature from 1350 C to 1305 C did not significantly affect the amount of the phases present.

### 4.3 Transformation Under the Second DSC Peak

Heat treatments were then performed to study the transformations taking place under the second peak, having established that the first peak in the DTA cooling curve corresponded to the formation of about 30%  $\gamma$ -phase. Further cooling to the beginning of the second peak did not significantly increase the  $\gamma$ -phase fraction, but instead caused a compositional change,.

#### 4.3.1. Continuous Cooling (CC) Heat Treatment

Solutionized-CC1240C-WQ. A sample was solutionized at 1500 C and cooled to 1240 C at 12 K/min followed by WQ. Again a two-phase  $\beta+\gamma$  microstructure was obtained as indicated by the XRD profile of the powdered CC1240 sample shown in Figure 4-7. Distinct  $\beta$  and  $\gamma$ - phase peaks as well as some  $\alpha$ -phase peaks are observed. Note, that no  $\sigma$ -phase peaks are present in this sample. Figure 4-8 presents a BSE micrograph of the sample that confirms the presence of only two phases. The microstructure consists of  $\gamma$ -phase, which appears as the dark-contrast phase in the BSE micrograph. The remaining microstructure consists of the  $\beta$ -phase that appears as the lighter contrast phase in Figure 4-8. No third phase contrast is observed in the micrograph, suggesting the absence of  $\sigma$ -phase in the microstructure. Since the sample cooled through the second peak, it is expected to have formed  $\sigma$ -phase, which, as in the slow cooled sample is not present. Upon quenching,  $\alpha$ -phase forms in this  $\beta$ -phase, the peaks for which are observed in the XRD. The scale of the microstructure suggests that the  $\gamma$ -phase formed and existed at high temperatures before the sample was quenched. The amount of the  $\gamma$ -phase in the microstructure was calculated to be 68%, which means that at the quenching temperature of 1240 C, 68%  $\gamma$ -phase existed. In

comparison to the other CC samples, no two  $\gamma$ -phase contrasts were found in the microstructure. However, similar to the slow cooled sample, the  $\gamma$ -phase exhibited two different morphologies as demonstrated in Figure 4-9. The morphology A, consisting of large primary  $\gamma$ -laths is shown in Figure 4-9a. The volume fraction of the  $\gamma$ -phase with morphology A was comparable to the amount of the dark primary  $\gamma$ -phase found in CC1350C and CC1305C samples discussed in section 4.2, suggesting that this  $\gamma$ -phase formed under the first peak. The morphology B, which is characterized by fine lamellar structure, comprised approximately 38% of the microstructure and is shown in Figure 4-9b. This morphology is believed to have formed while cooling through the second DTA peak. Figure 4-9c shows the cross section of the coarse Widmanstätten laths, and the fine lamellar-like  $\gamma$ -phase appears to be nucleating at the  $\beta/\gamma$  interface of the Widmanstätten laths with the  $\beta$  matrix.

#### **4.3.2 Double Heat Treatment (DHT)**

**Solutionized-DHT1240/2h-WQ.** To understand the effect of holding times on the compositions and phase fractions of the phases, two DHT heat treatments were performed-- one between the first and second DSC peak and the other after the second DSC peak. Two samples were solutionized and then cooled at 12 K/min to 1350 C (DHT1350C) and 1240 C (DHT1240C), respectively, held for 2 hours at the respective temperatures, followed by WQ. The DHT1350/2h sample has already been discussed in section 3.7 of chapter 3, and will be further discussed in the following sections.

Figure 4-10 presents the XRD profile from the sample held isothermally under the second peak at 1240 C for two hours (DHT1240). Again, the  $\beta$ - and the  $\gamma$ -phase peaks can be identified. A BSE micrograph shown in Figure 4-11 reveals a two-phase

microstructure, where coarse primary Widmanstätten  $\gamma$ -phase laths can be seen to be nucleated at the  $\beta$  grain boundaries and grown into the  $\beta$  grains. A closer look at the microstructure under the optical microscope reveals the second morphology as shown in Figure 4-12 a & b. These optical images from the sample reveal the presence of the fine lamellar-like morphology forming in an array in the matrix in between the existing coarse  $\gamma$ -laths. The micrographs in the figure show the coarse and long Widmanstätten  $\gamma$ -phase laths as well as their cross sections and lamellar-like structure can be seen to be nucleating at these laths much like those seen in the CC1240 sample. Furthermore, consistent with the CC1240 sample, much higher  $\gamma$ -phase fraction was found in this sample in comparison to the CC1350 or DHT1350C samples (~70% versus ~30%). The compositions of phases obtained by EPMA are given in Table 4-2. Note that there are not two different compositions of the  $\gamma$ -phase like those in CC1350 and DHT1350 samples. The  $\gamma$ -phase appears to have attained its equilibrium low Al compositions upon cooling to lower temperatures. Note that as the heat treatment temperature goes down, and the amount of the  $\gamma$ -phase increases, the composition of the  $\beta$ -phase changes. Comparing the CC1350 and DHT1240 samples, the amount of Al has decreased while those of Ti and Nb have increased in the  $\beta$ -phase as the temperature of heat treatment was lowered. As the  $\gamma$ -phase forms and increases in amount, it does so by rejecting Nb and Ti into the matrix and consuming Al, which causes the corresponding change in the composition of the  $\beta$ -phase.

#### **4.3.3 TEM Analysis of the Secondary $\gamma$ -Phase Morphology (B)**

In order to understand the formation of the secondary lamellar-like morphology of the  $\gamma$ -phase, TEM analysis was performed on the CC1240 sample. Figure 4-13 shows a

diffraction pattern taken from a lamella in the lamellar-like structure. The diffraction pattern was indexed to be of the  $\gamma$ -phase along the  $[112]_{\gamma}$  zone axis. DF imaging of the  $[1-10]_{\gamma}$  plane, lights up alternating  $\gamma$ -lamellae in the DF image shown. Thus, the lamellar structure can be said to consist of more than one phase, one of which is the  $\gamma$ -phase. As can be seen, the  $\gamma$  lamellae are the coarser lamellae in the structure alternating with finer lamellae of another phase. Figure 4-14 shows the diffraction pattern taken from the  $\beta$ -matrix adjacent to the lamellar-like structure. The diffraction pattern is of the  $\beta$ -phase along the  $[023]_{\beta}$  zone axis. When the  $[-200]_{\beta}$  plane on the diffraction pattern was imaged in DF, it lighted up the  $\beta$ -matrix along with the finer lamellae in the lamellar-like structure. Clearly, these finer lamellae belong to the  $\beta$ -phase. Thus, the lamellar-like structure appears to be made of alternating lamellae of the  $\gamma$  and the  $\beta$ -phase. Further, APBs were observed in the matrix  $\beta$ -phase, which can be said to be ordered. When the APBs in the  $\beta$ -lamellae were observed carefully, they were seen to end abruptly at the  $\beta/\gamma$  interface of the lamellae. This clearly indicates that the  $\beta$ -phase ordered after the formation of the lamellar-like structure, i.e., after passing the second DSC peak upon cooling. Figure 4-17 provides a closer look at the structure of the morphology B. In that figure an array of alternating  $\beta/\gamma$  lamellae can be seen between two Widmanstätten  $\gamma$ -laths. It is clear that the morphology B grows in the  $\beta$ -phase between the coarse  $\gamma$  laths and consists of alternating  $\beta$ - and  $\gamma$ -phase lamellae. Further, the interfaces between the two morphologies can be seen as a fringe, which further suggests that these lamellae did not grow from the Widmanstätten laths in the image, but nucleated elsewhere.

#### 4.4 Aging Heat Treatment

No  $\sigma$ -phase was observed in samples cooled to room temperature after solutionizing. Clearly, the driving force required for  $\sigma$ -formation was insufficient upon cooling. An aging heat treatment was designed in order to provide a higher driving force for  $\sigma$ -formation. A sample of the alloy was solutionized at 1500 C for 1 hr. and WQ. This resulted in a  $\gamma+\beta$  microstructure, which was then heated at 12 K/min up to 1200 C and held for 2 hrs followed by WQ. The SEM/BSE micrograph and XRD of the aged sample are shown in Fig 18. The SEM/BSE picture shown in Figure 18a depicts a duplex microstructure. The XRD profile presented in Figure 18b clearly indicates the presence of the  $\gamma$  and  $\sigma$  phases. Based on the BSE contrast in the micrograph it can be said that the finer brighter-contrast phase in the microstructure is the  $\sigma$ -phase, the remaining being the  $\gamma$ -phase. The volume fraction of the  $\sigma$ -phase is calculated to be approximately 14%, which is consistent with the latest thermodynamic calculations by Cupid [22, 24].

#### 4.5 Discussion

From the above results it is clear that the two DSC peaks on the cooling curve, which were thought to be due the  $\gamma$  and  $\sigma$  formation, are indeed both related to the formation of the  $\gamma$ -phase. Also, the results indicate that the nucleation of the  $\gamma$ -phase occurs neither as a single step nor as a continuous process in the alloy, but takes place in two discrete stages that give rise to the two DSC peak. It is an interesting observation that the  $\gamma$ -phase nucleates in two distinct stages and with two different morphologies.

The reason for the two-step nucleation phenomenon can be speculated to be caused by the lack of nucleation sites and low driving force at high temperatures. When the alloy is solutionized, the  $\beta$  grains grow to a few millimeter in diameter, as was noticed in Figure

3-8. This limits the amount of grain boundary area in the sample, which provides the primary nucleation site for the  $\gamma$ -phase. As the alloy cools after solutionizing, there is enough driving force for the formation of the  $\gamma$ -phase at the high energy  $\beta$ -grain boundaries, giving rise to the first DTA peak. This primary  $\gamma$ -phase (dark-contrast high-Al  $\gamma$  that covers  $\beta$ -phase grain boundaries in CC1350C and CC1305C samples) grows even at such high temperatures with long and coarse Widmanstätten lath morphology. Due to limited grain boundary area, these nucleation sites are exhausted before the equilibrium amount of the  $\gamma$ -phase is formed. For any further nucleation of the  $\gamma$ -phase, the next available nucleation sites are the coherent/semicoherent  $\beta/\gamma$  interfaces that form between the now-existing Widmanstätten  $\gamma$ -laths and the  $\beta$  matrix, which have lower energy. Nucleation of the  $\gamma$ -phase at these interfaces requires a higher driving force, and thus, further nucleation is halted at high temperatures. At this point the end of the first DTA peak can be marked. Therefore, the first DTA peak can be correlated with the formation of the primary  $\gamma$ -phase from the  $\beta$  grain boundary.

As this alloy is cooled further to 1350 C past the end of the first peak, the  $\gamma$ -phase retains the high Al composition, due to lack of enough time for diffusion, and is unable to attain its equilibrium composition corresponding to this temperature. The diffusion-assisted growth of this primary  $\gamma$ -phase modifies the surrounding  $\beta$ -phase, as can be noticed in the denuded zone marked in Figure 4-5 a & c. The remaining  $\beta$ -phase thus, exists in a metastable state. At this point when the alloy is quenched without holding, the metastable  $\beta$ -phase becomes unstable at lower temperatures and transforms to more  $\gamma$ , which is observed as the light-contrast  $\gamma$ -phase in the CC microstructures except in the denuded zones. See Figure 5. However, when a sample is held at 1350 C

for 2 hrs, the contrast of the  $\gamma$ -phase changed from dark (high Al) to a lighter one (low Al), consistent with the compositional analysis shown in Table 3-4. Upon quenching this sample, the formation of the quenched  $\gamma$ -phase is inhibited, and, instead, other metastable phases such as the O-phase form. This finding indicates that the Al content of the  $\gamma$ -phase decreases with reducing temperature in the regime investigated, which fits well with the calculations of Cupid et.al [22, 24].

As the solutionized alloy is cooled down past the first peak, the driving force for  $\gamma$ -phase nucleation keeps increasing until it reaches a point where it is sufficient for nucleation to occur at other sites including the low energy  $\beta/\gamma$  interfaces. This second  $\gamma$  nucleation event gives rise to the second DTA peak leading to a drastic increase in the  $\gamma$ -phase volume fraction in the DHT 1240, CC1240C, and slow cooled samples. Unlike the coarse Widmanstätten laths of the primary  $\gamma$ -phase (morphology A) that formed under the first peak,  $\gamma$ -phase forms with a lamellar-like morphology (B) under the second peak. Based on the various optical and TEM images of morphology B, it can be said that these are actually plates of the  $\gamma$ -phase nucleating on the  $\beta/\gamma$  interface. Figure 4-19 is a schematic depicting the morphology of  $\gamma$  plates nucleating on the Widmanstätten primary laths. When a sample cools further below the first DTA peak and attains enough driving force for nucleation at the  $\beta/\gamma$  interfaces, nuclei of the  $\gamma$ -phase form (possibly at ledges on the Widmanstätten  $\gamma$ -phase laths). These nuclei then grow as plates into the adjacent  $\beta$ -matrix up to some maximum length possible in the available  $\beta$ -phase volume. As these nuclei form intermittently along the  $\beta/\gamma$  interface, the growing  $\gamma$ -plates

trap the  $\beta$ -matrix phase between them, thereby giving rise to the alternating  $\beta/\gamma$  lamellae shown in the optical and TEM micrographs.

The reason this morphology is formed under the second DTA peak is suggested to be the high driving force at low transformation temperatures, and the limited available volume of the  $\beta$ -phase between the Widmanstätten  $\gamma$ -laths. Once the sample has cooled to lower temperatures below the first DSC peak, and attains enough driving force, the second nucleation event takes place at the existing  $\beta/\gamma$  interfaces. Now considering that the Widmanstätten laths already exist in the sample, they limit the volume of  $\beta$ -phase available for the growth of new  $\gamma$ -nuclei. Once these nuclei form, they cannot extend into the matrix forming long laths, due to limited available  $\beta$ -phase volume. They eventually encounter one of the existing  $\gamma$ -laths, thus limiting the length of these plates. So in order to achieve the equilibrium amount of the  $\gamma$ -phase, many nuclei are formed. It is possible that these nuclei specifically form at ledges on the Widmanstätten  $\gamma$ -laths, which sets the spacing between two  $\gamma$  plates. Since there are many such nuclei, the equilibrium volume fraction of the  $\gamma$ -phase is achieved even when the plates do not grow extensively, as nucleation rates are more prominent than diffusion and growth at lower temperatures. Given that the  $\beta$  and  $\gamma$  phases share an orientation relationship, and possibly share a low energy interface, formation of these plates is not difficult[93, 94].

When a sample was held for 2 hours at 1240 C (DHT1240C) the relative amount of the two morphologies did not change significantly. The fact that this morphology B was also observed in the slow cooled sample, it can be concluded that it did not form upon quenching, but rather upon cooling through the second DSC peak.

Studies performed on TiAl-based alloys show the  $\gamma$ -phase exhibiting more than one morphology upon cooling from the single phase  $\alpha$  region [32, 33, 39, 45]. The morphology developed depends on cooling rate. At intermediate cooling rates more than one  $\gamma$ -phase morphologies can coexist in the microstructure [31, 33, 34]. The nucleation, growth and coexistence of more than one  $\gamma$ -phase morphologies in a given microstructure was explained by the occurrence of so-called 'sympathetic nucleation' [31], where upon cooling, one crystal of the  $\gamma$ -phase nucleates on a moving interphase boundary of the preexisting crystal of the  $\gamma$ -phase. It has been suggested that the crystals that nucleate, may or may not be exhibiting the same morphology. However, step-by-step nucleation and growth of one morphology over the other has not been investigated in these alloys.

The absence of the  $\sigma$ -phase in the slow-cooled sample suggests that the nucleation of this phase is difficult. The  $\sigma$ -phase, which has a complex crystal structure [89], requires a high driving force in order to nucleate [95]. Since the  $\sigma$ -phase requires extensive diffusion of elements in addition to a high driving force for nucleation, some thermal energy (high temperature) is also required for its nucleation and growth. The aging heat treatment was performed to confirm this fact in the alloy studied. In the solutionized-WQ sample, the  $\gamma+\beta$  microstructure is further away from stability due to the fast cooling rate. Thus, when this highly metastable structure is heated up to be aged, there is enough driving force available for the sample to attain an equilibrium microstructure consisting of the  $\sigma$  and the  $\gamma$  phases.

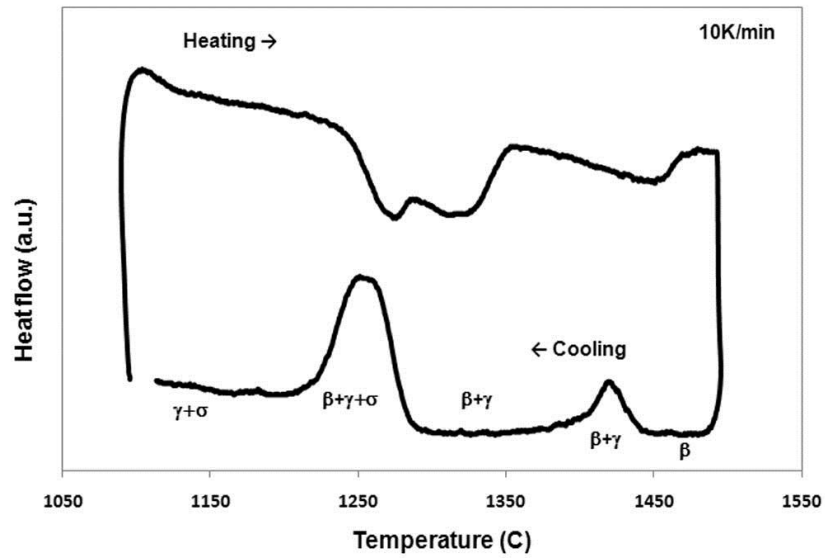


Figure 4-1. DSC curve of alloy 11 showing the expected transformation path of the alloy upon cooling

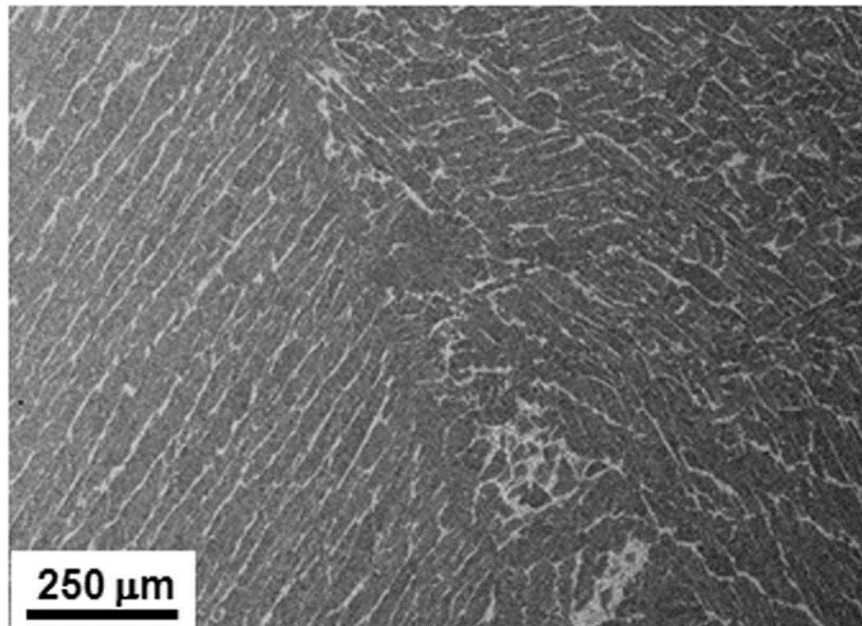


Figure 4-2. BSE micrographs of a solutionized and slow cooled (at 9K/min) sample of alloy 11 showing a two phase microstructure

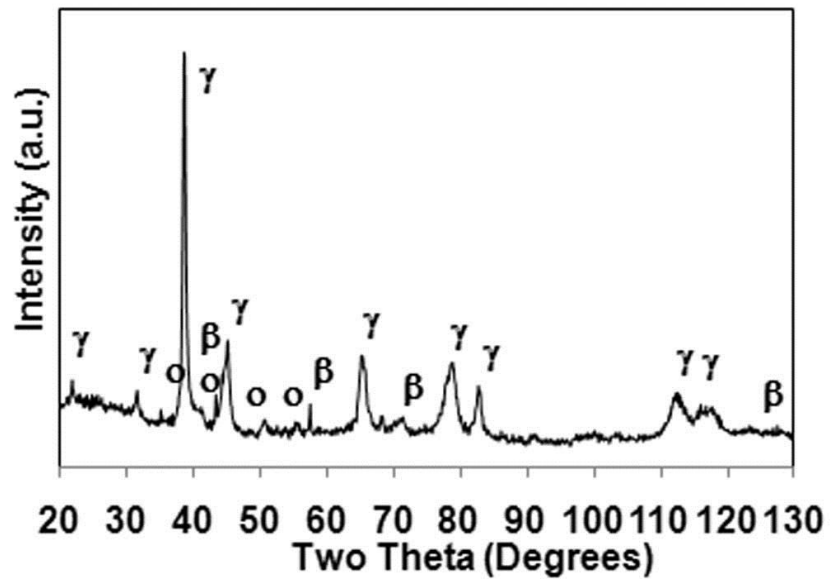


Figure 4-3. XRD plot of a powdered sample of solutionized- slow cooled alloy 11

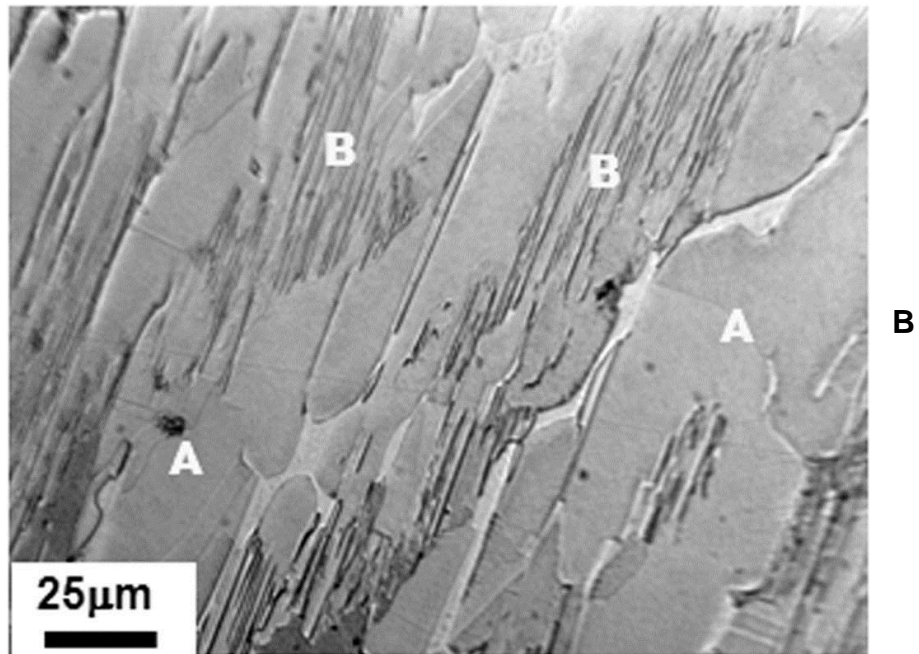
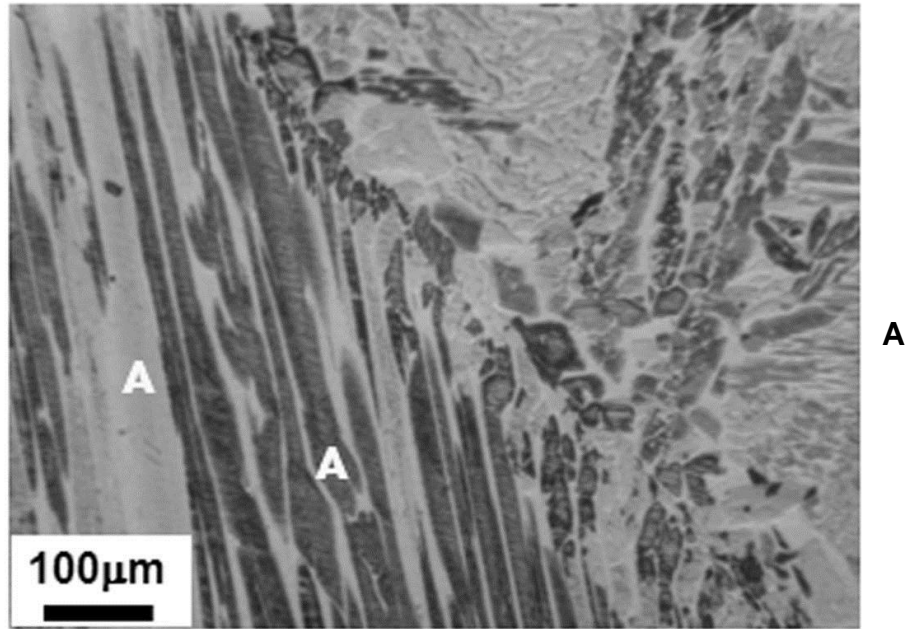


Figure 4-4. Optical micrographs of alloy 11, solutionized-slow cooled. A) Primary Widmanstätten morphology of the  $\gamma$ -phase (morphology A). B) The secondary lamellar-like morphology of the  $\gamma$ -phase (morphology B)

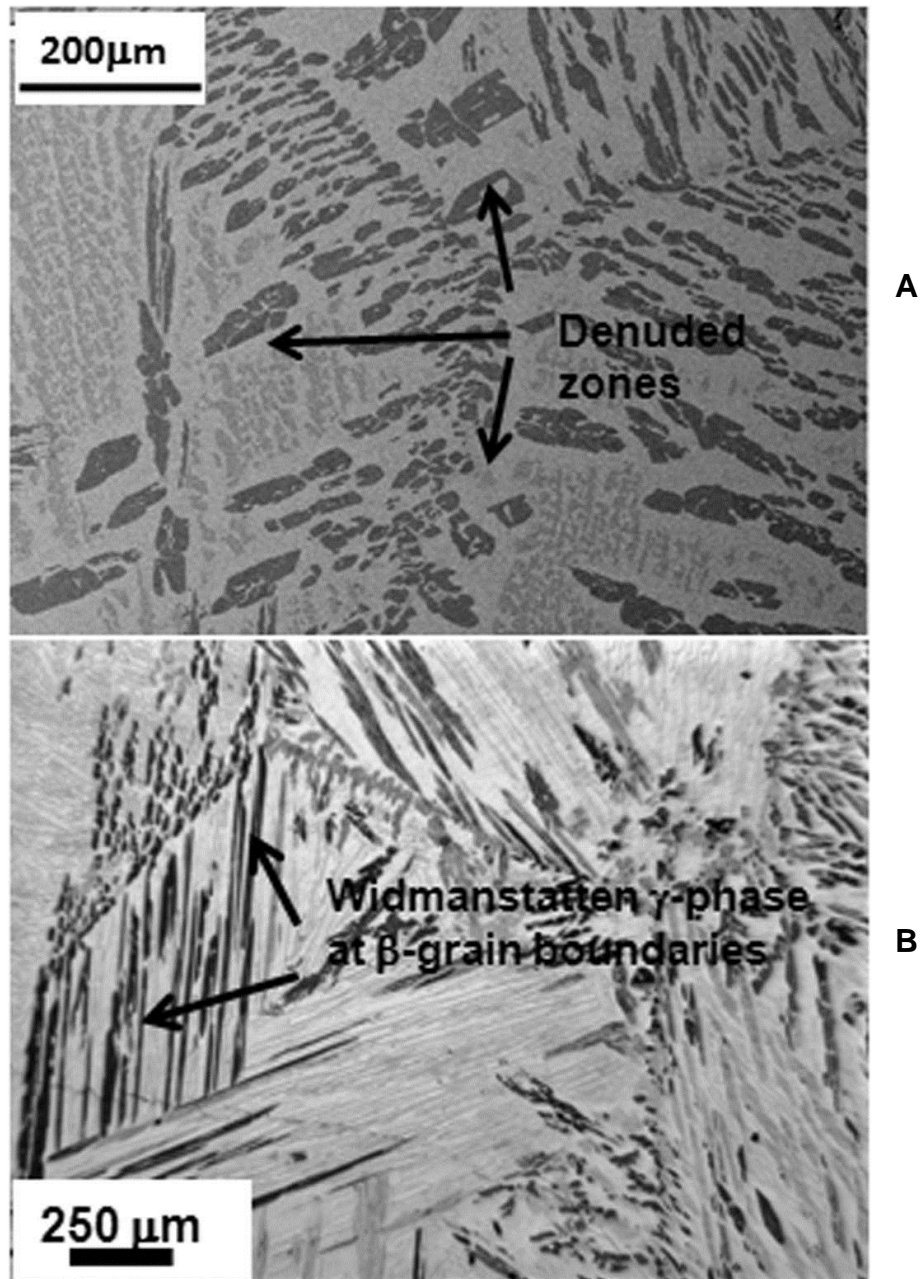


Figure 4-5. Alloy 11 CC1350. A) BSE micrograph showing denuded zones around the Widmanstätten  $\gamma$ -phase laths (dark) and the quenched  $\gamma$ -phase. B) Optical micrographs showing Widmanstätten  $\gamma$ -phase laths (dark) at the  $\beta$  grain boundaries.

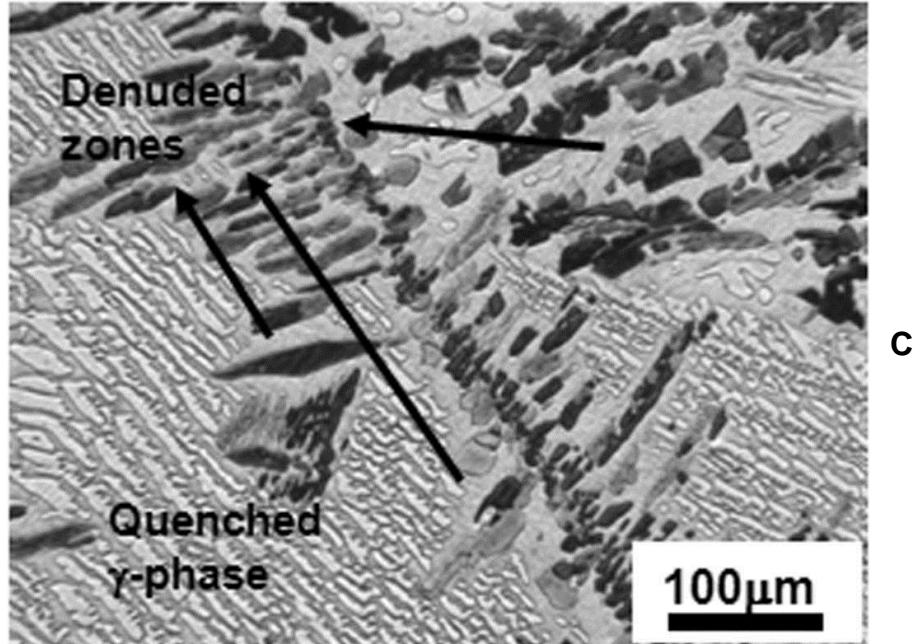


Figure 4-5.Continued. C) Optical micrograph showing denuded zones around the Widmanstatten  $\gamma$ -phase laths (dark) and the quenched  $\gamma$ -phase

Table 4-1. Compositions of phases in CC1350 sample of alloy 11

		Al	Ti	Nb
CC1350	$\beta$ -phase	42.5( $\pm$ 0.2)	38.5( $\pm$ 0.3)	18.9( $\pm$ 0.1)
	Dark primary $\gamma$ -laths	48.7( $\pm$ 0.2)	35.1( $\pm$ 0.1)	16.2( $\pm$ 0.2)
	Quenched $\gamma$ -phase	45.7( $\pm$ 0.2)	37.2( $\pm$ 0.2)	17.1( $\pm$ 0.3)

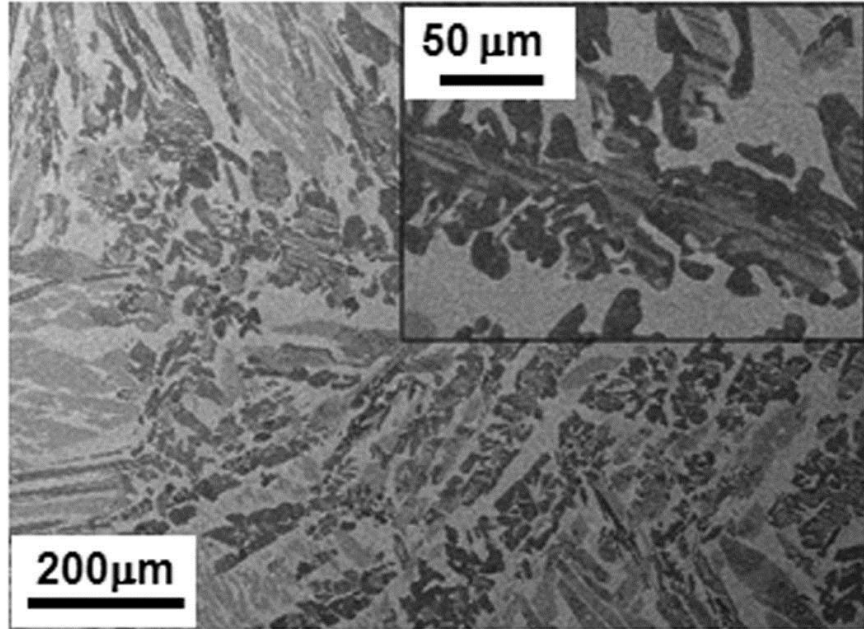


Figure 4-6. BSE micrograph from the CC1305 sample of alloy 11 Widmanstätten  $\gamma$ -phase laths (dark) and the quenched  $\gamma$ -phase; inset: compositional changes in the  $\beta$ -grain boundary Widmantätten  $\gamma$ -phase laths

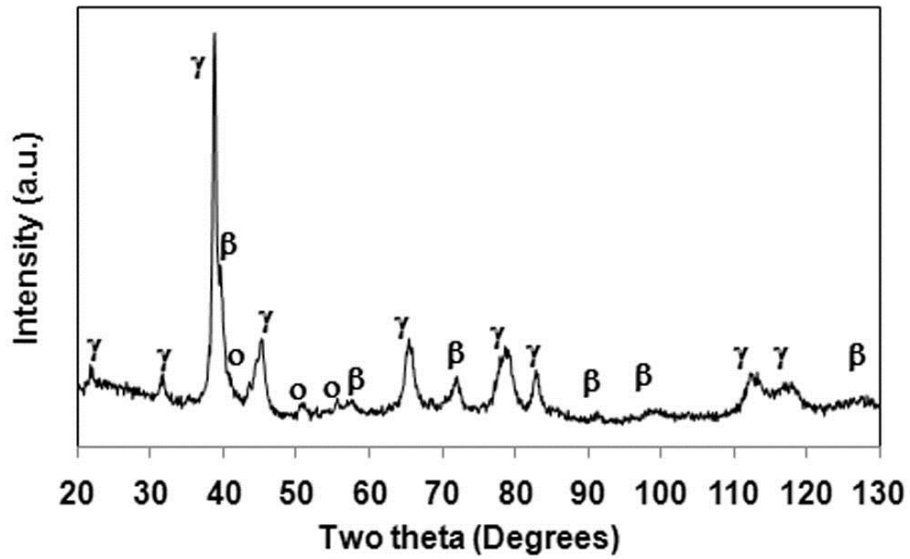


Figure 4-7. XRD plot of a powdered sample of CC1240 sample of alloy 11

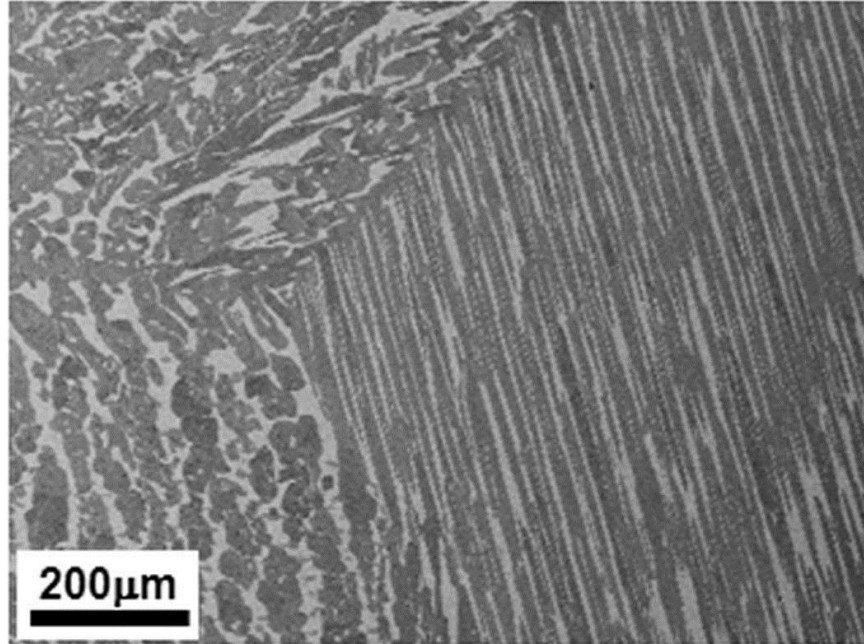


Figure 4-8. BSE micrograph from the CC1240 sample of alloy 11 showing a two phase microstructure with Widmanstätten  $\gamma$ -phase laths (dark) and the quenched  $\beta$ -phase (bright)

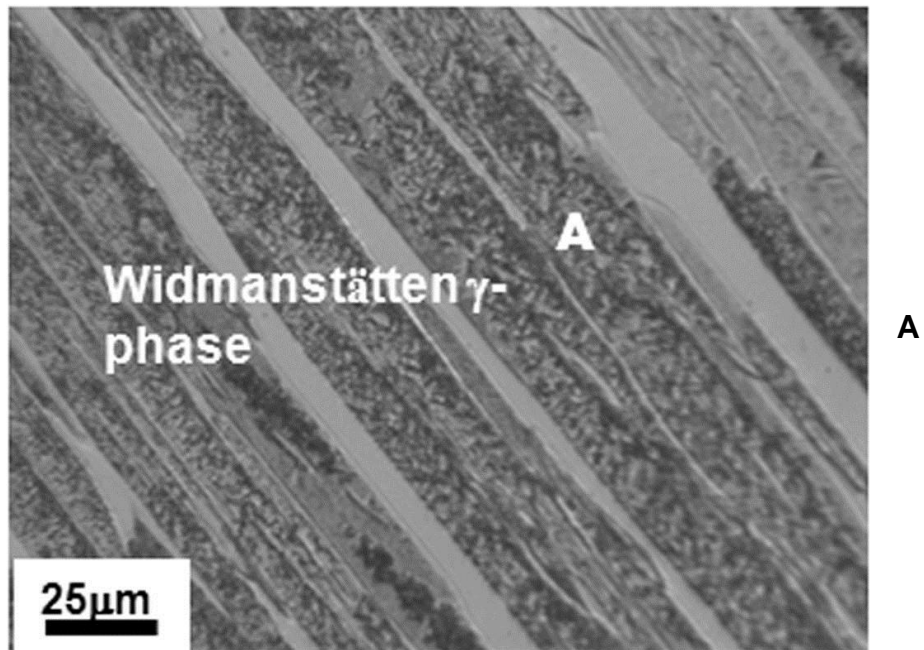


Figure 4-9. Optical micrographs of alloy 11CC1240. A) Coarse primary Widmanstätten  $\gamma$ -phase laths (morphology A)

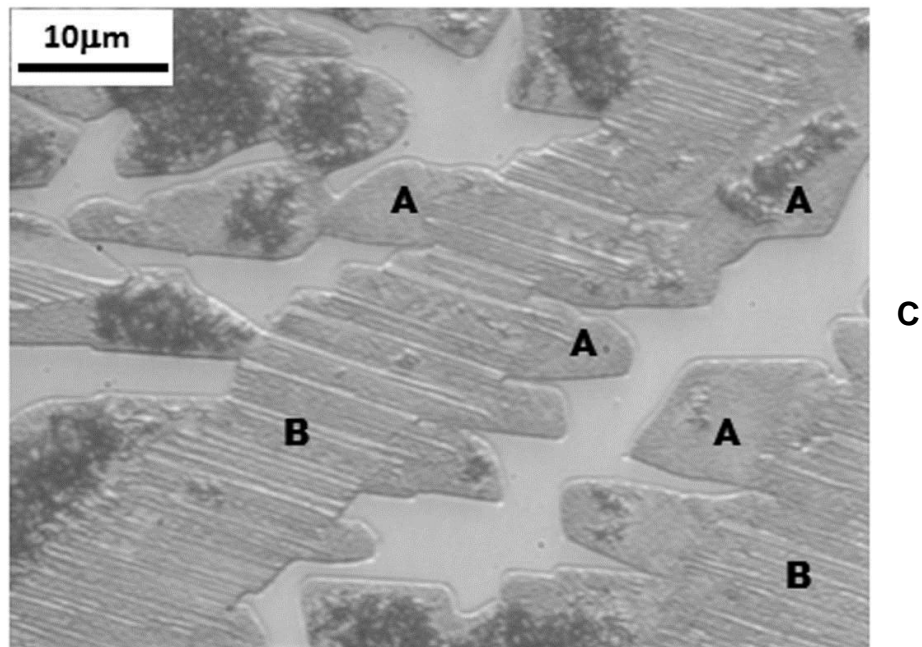
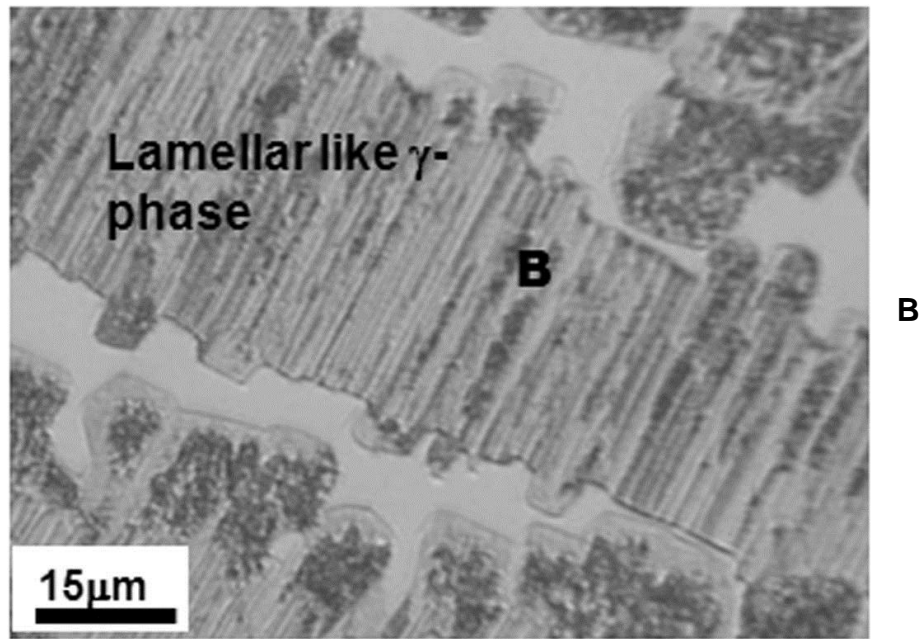


Figure 4-9. Continued. B) Lamellar morphology of the  $\gamma$ -phase (morphology B). C) Lamellar morphology of the  $\gamma$ -phase (B), nucleating at the interface of the coarse primary  $\gamma$ -phase (A) and the  $\beta$  matrix

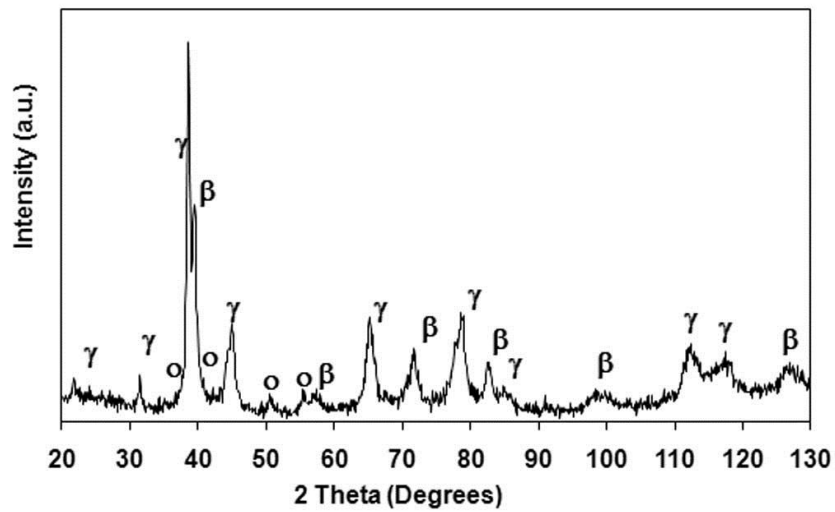


Figure 4-10. XRD plot of a powdered sample of DHT1240 sample of alloy 11

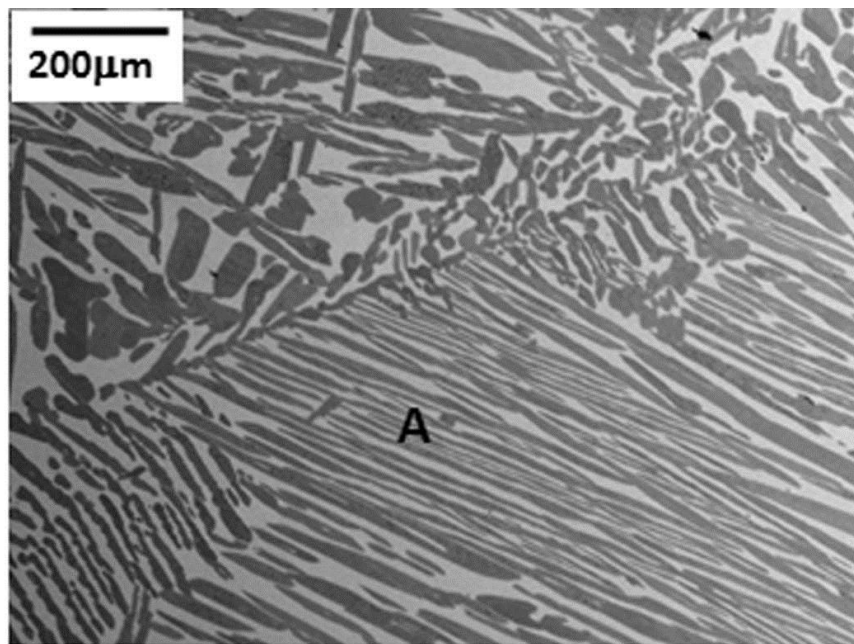


Figure 4-11. BSE micrograph from the DHT11240 sample of alloy 11 showing the coarse primary Widmanstätten  $\gamma$ -phase laths (morphology A) nucleating at the  $\beta$  grain boundaries

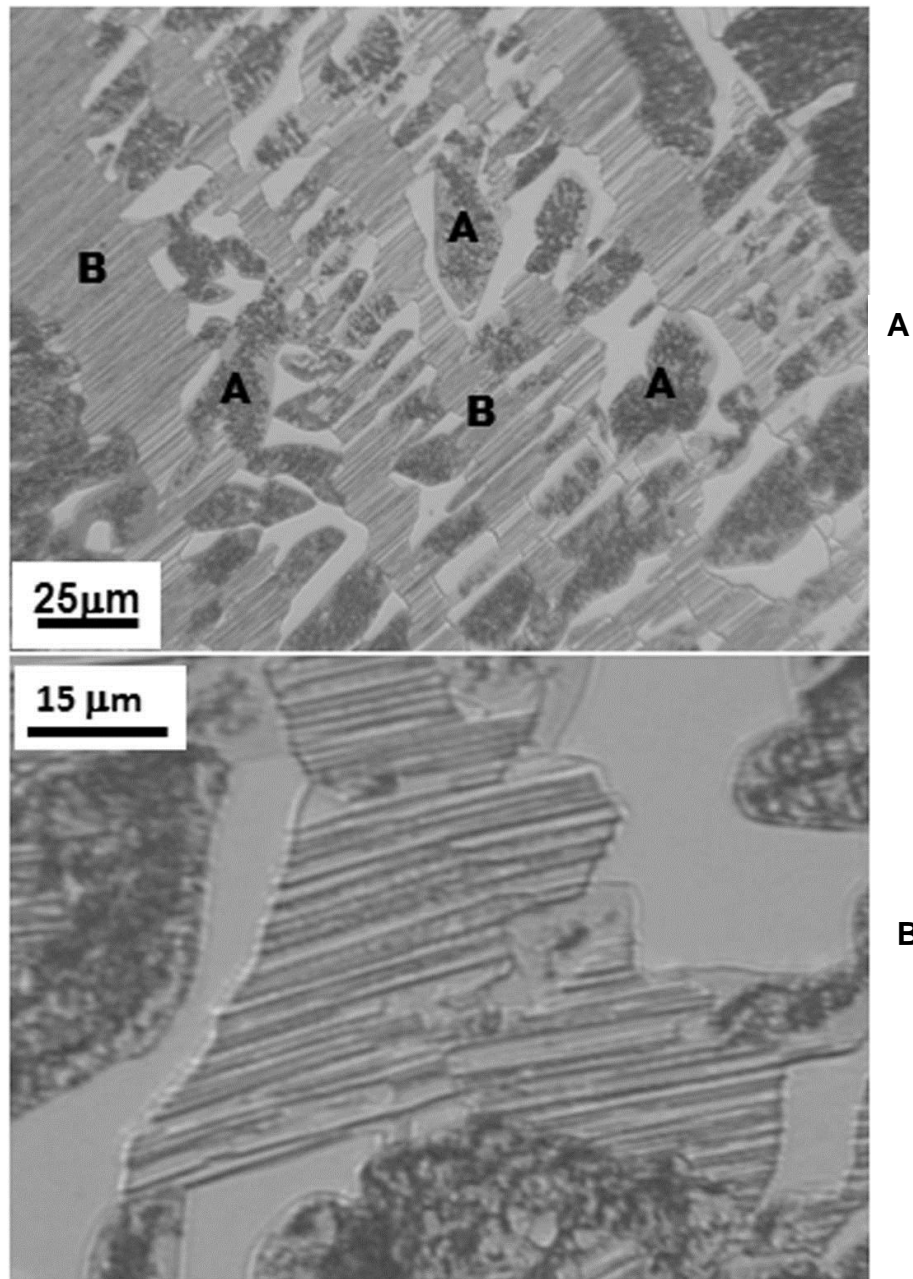


Figure 4-12. Optical micrographs of alloy 11DHT1240/2h. A) Lamellar morphology of the  $\gamma$ -phase (B), and cross sections of the coarse primary  $\gamma$ -phase (A). B) Higher magnification image giving a closer look at the lamellar morphology of the  $\gamma$ -phase (B).

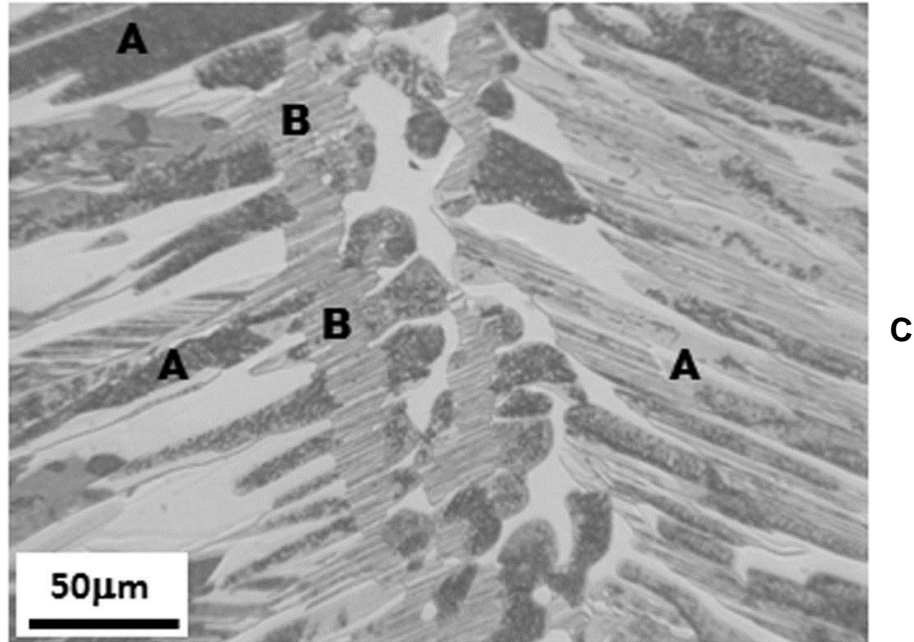


Figure 4-12.Continued. C) Lamellar morphology of the  $\gamma$ -phase (B), growing over the coarse primary  $\gamma$ -phase Widmanstätten laths (A)

Table 4-2. Compositions of phases in DHT1240 sample of alloy 11

		Al	Ti	Nb
DHT1240/2h	$\beta$ -phase	38.0( $\pm$ 0.2)	41.3( $\pm$ 0.1)	20.7( $\pm$ 0.3)
	$\gamma$ -phase	45.6( $\pm$ 0.3)	37.7( $\pm$ 0.2)	16.7( $\pm$ 0.3)

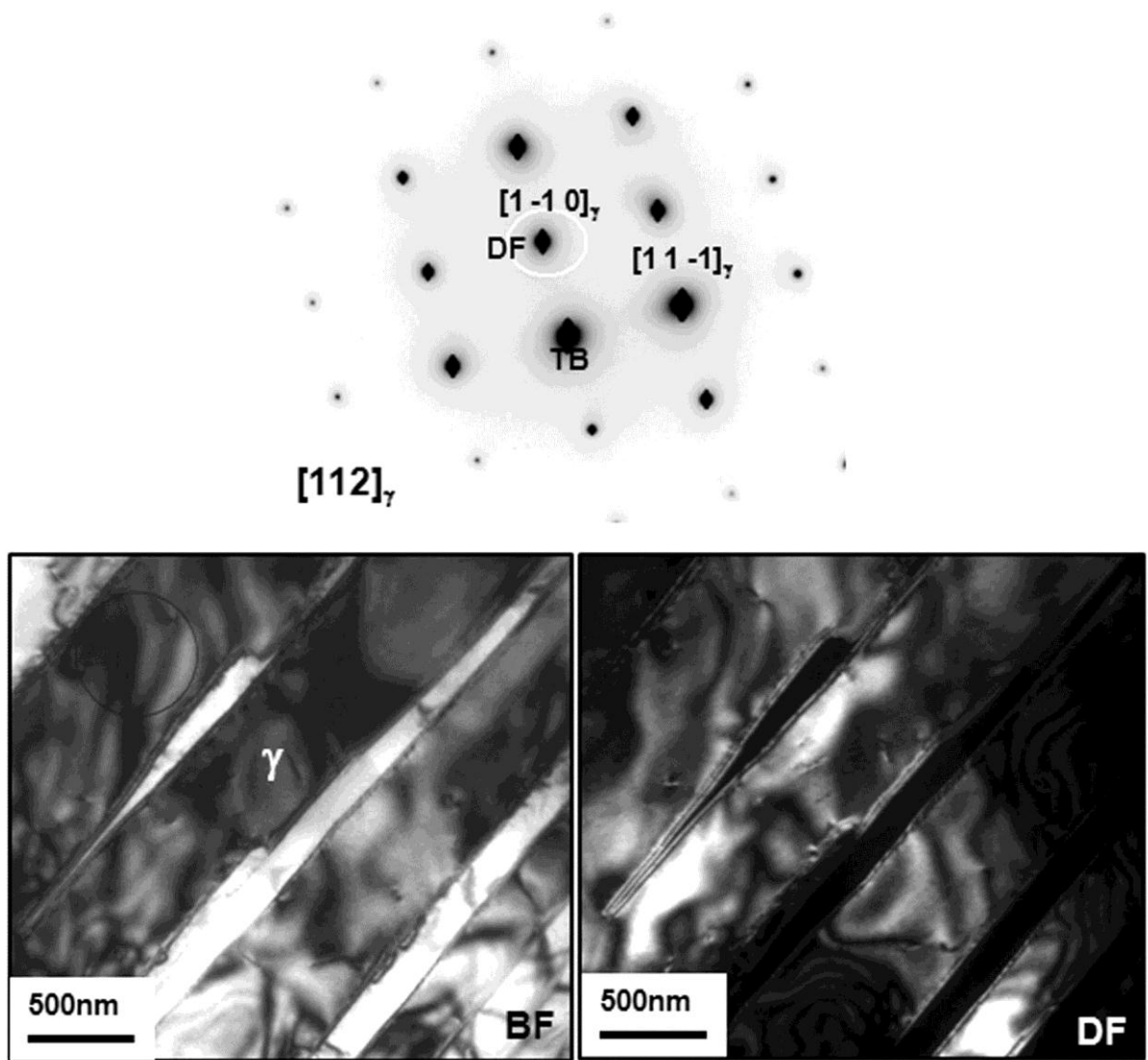


Figure 4-13. TEM micrographs from the CC1240 sample of alloy 11 showing (a) diffraction pattern from the  $\gamma$ -lath along the  $[112]_{\gamma}$  zone axis; (b) & (c) BF and DF imaging of the  $(1-10)_{\gamma}$  plane

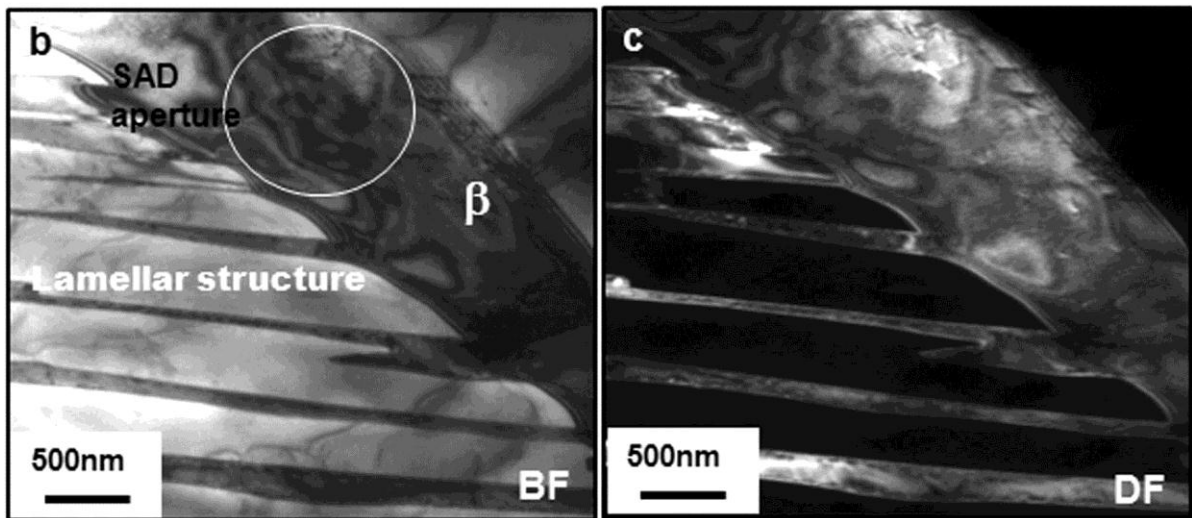
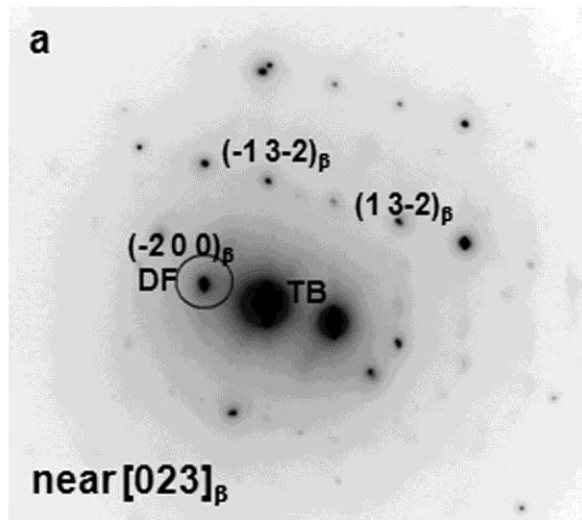


Figure 4-14. TEM micrographs from the CC1240 sample of alloy 11. A) diffraction pattern from the  $\beta$ -matrix along the  $[032]_\beta$  zone axis. B)& C)BF and DF imaging of the  $(-200)_\beta$  plane

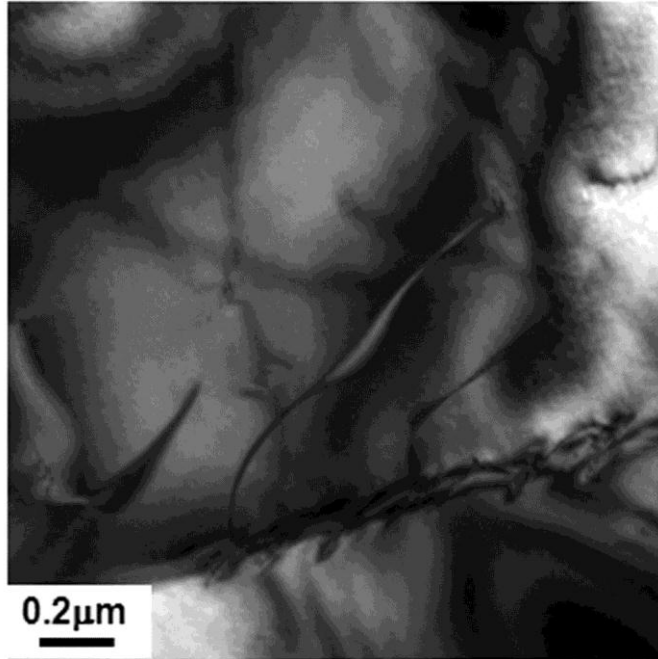


Figure 4-15. TEM micrographs of the CC1240 sample showing APBs in the  $\beta$  matrix

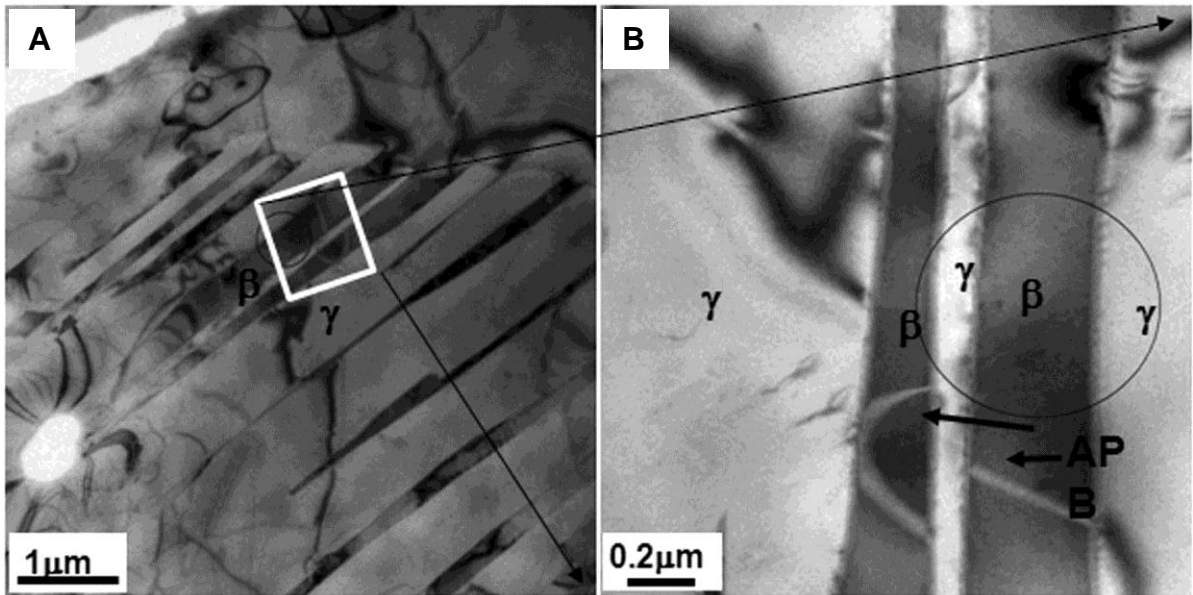


Figure 4-16. TEM micrographs from the CC1240 sample of alloy 11 showing APBs in the  $\beta$  matrix. A) Lower magnification. B) Higher magnification

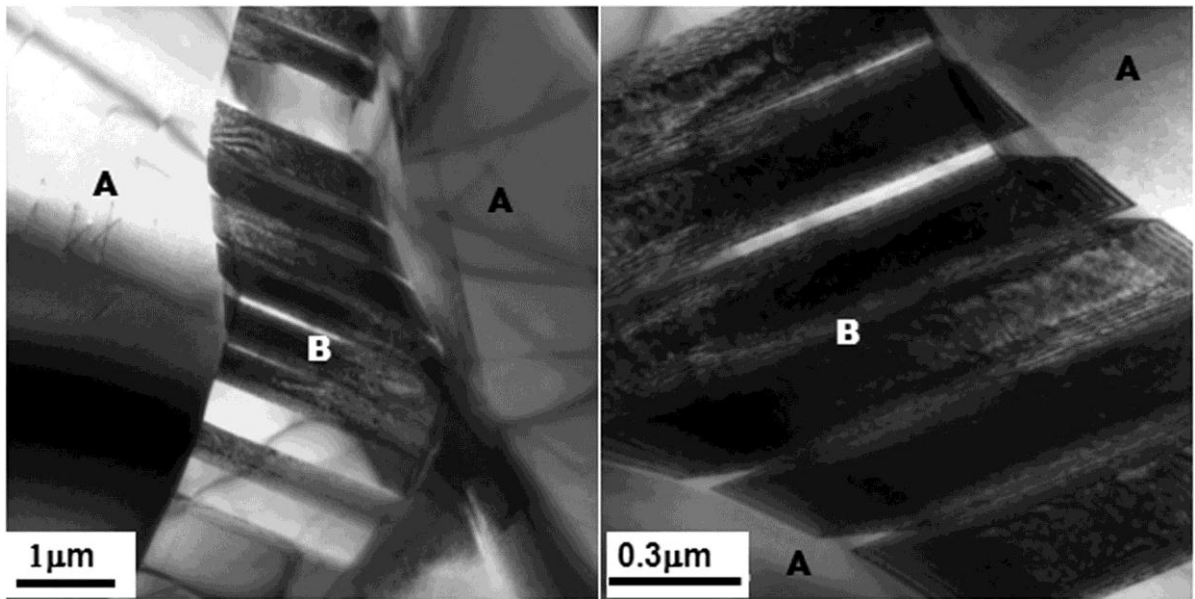


Figure 4-17. TEM micrographs from the CC1240 sample of alloy 11 showing lamellar-like morphology (B) growing between the coarse  $\gamma$ -laths (A)

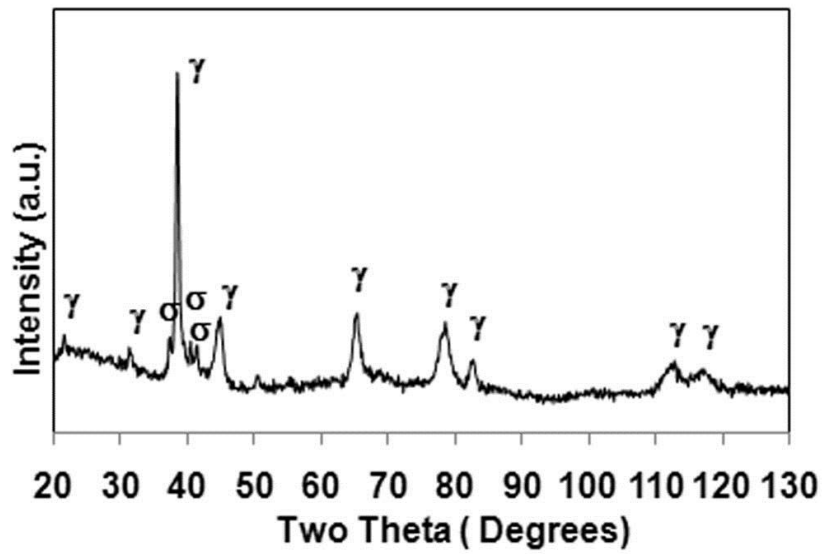
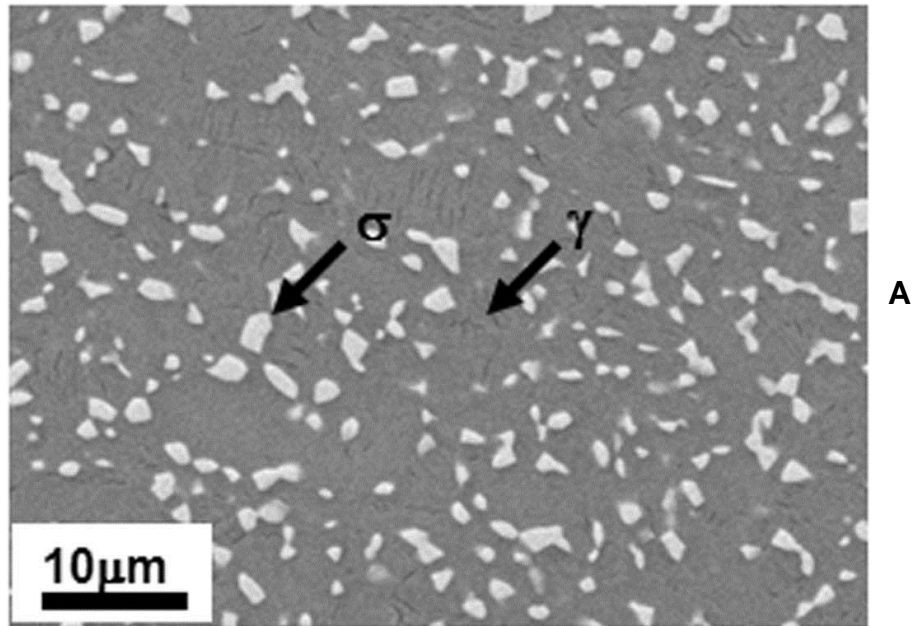


Figure 4-18. Alloy 11 aged at 1200C/2h. A) BSE micrograph showing a two phase  $\gamma+\sigma$  microstructure. B) XRD plot from a powdered sample showing a two phase microstructure

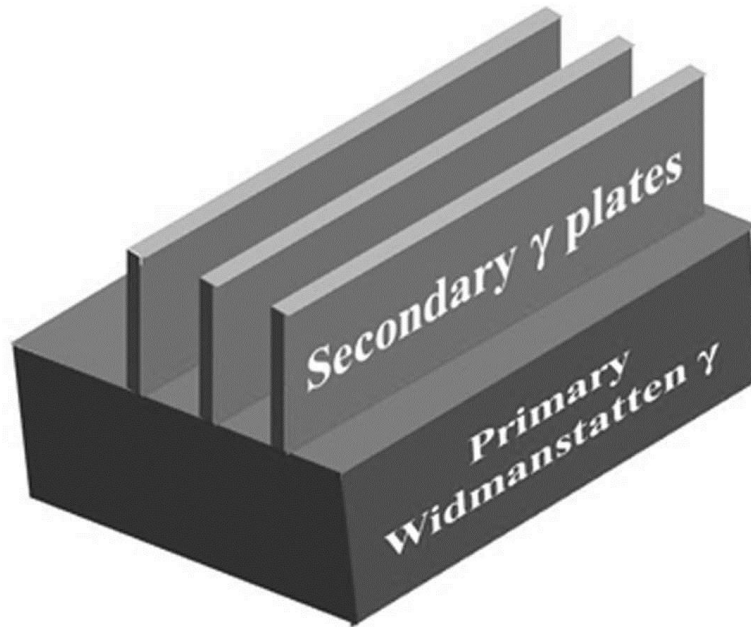


Figure 4-19. Schematic showing the plate-like morphology of the secondary  $\gamma$ -phase (B) growing over the existing primary Widmanstätten  $\gamma$ -phase laths (A)

## CHAPTER 5 EFFECT OF CHROMIUM ADDITION ON THE $\beta$ -TO- $\gamma$ PHASE TRANSFORMATION

### 5.1 Introduction

As discussed previously in Chapter 1, the ideal proposed  $\gamma+\sigma$  alloy would exist as a single  $\beta$ -phase at high temperatures, and upon quenching that microstructure would be retained to room temperature. Upon aging this metastable quenched  $\beta$ -phase, a fine  $\gamma+\sigma$  microstructure is expected to form, as explained in Chapter 1. Further, it has been shown that volume fraction, morphology, and scale of the phases all play an important role in determining the mechanical properties of these alloys. A service temperature microstructure consisting of ultrafine grain  $\gamma$ -phase with a volume fraction of <20% of the nanosized  $\sigma$ -phase is expected to be optimal for these alloys. The volume fraction of the phases is controlled by selecting alloys from a specific calculated region of the TiAlNb ternary phase diagram, as proposed by Cupid et al. The preliminary alloys were chosen based on the above mentioned requirements and calculations ( alloy 11,12), and it was found that although these alloys exist as single  $\beta$ -phase at high temperature, and are expected to have a two phase  $\gamma+\sigma$  microstructure at service temperature, it was not found to be possible to retain the  $\beta$ -phase to room temperature upon quenching. These alloys formed extensive amount of  $\gamma$ -phase upon water-quenching the  $\beta$ -phase from the solutionizing temperature. This  $\gamma$ -phase nucleated at the  $\beta$  grain boundaries and grew with Widmanstätten morphology. The  $\gamma$ -laths thus formed are coarser than desired for the proposed ideal microstructure. When such a quenched  $\beta+\gamma$  microstructure (alloy 11) was aged at 1200 C for 2 hrs, a  $\gamma + \sigma$  microstructure is obtained. This heat treatment and its results were discussed in Figure 4-18, Chapter 4,. The microstructure consisted

of coarse  $\gamma$ -laths that formed upon quenching the solutionized sample, and finer  $\sigma$ -phase that formed in the retained  $\beta$ -phase upon aging. Mechanical testing of such a microstructure revealed that it possessed low fracture toughness due to the presence of coarse phases and Widmanstätten morphology of the  $\gamma$ -phase.

## 5.2 Selection of the $\beta$ -Stabilizer

In order to obtain finer microstructure upon aging it is imperative that the formation of the  $\gamma$ -phase be avoided during quenching.  $\beta$ -phase ought to be retained to room temperature, so that a fine  $\gamma+\sigma$  microstructure develops upon aging. One of the ways to accomplish this is to stabilize the  $\beta$ -phase by the addition of  $\beta$ -stabilizers to the alloy, so as to prevent the  $\beta$ -to- $\gamma$  phase transformation upon quenching,. Various  $\beta$ -stabilizers have been identified in various studies [45, 56, 57, 60, 61, 63]. For the proposed alloys, a minimum of 45 at.% Al is required in order to achieve good oxidation resistance at service temperatures. Thus, the addition of the  $\beta$ -stabilizer could replace either Ti or Nb. Nb is also known to be a  $\beta$ -stabilizer and is denser than Ti. Since lower density is preferred in these alloys, due to their targeted use in aerospace turbine engines, replacing Nb with a stronger  $\beta$ -stabilizer with lower atomic weight would be preferred. Based on the data available on  $\beta$  stabilizers, Cr was chosen for this study. Cr is considered to be a stronger  $\beta$ -stabilizer and has a lower atomic mass than Nb. Adding a certain atomic fraction of Cr to replace Nb would result in a net decrease in the density of the alloy. The effect of Cr addition was studied on 2 alloys: alloy 11 (45Al-37Ti-18Nb) and alloy 12 (45Al-28Ti-27Nb). Four different alloys were arc melted with different amounts of Cr additions: Alloy 11-5Cr ( 45Al-37Ti-13Nb-5Cr), Alloy 12-1.5Cr ( 45Al-28Ti-25.5Nb-1.5Cr), alloy 12-3.5Cr ( 45Al-28Ti-23.5Nb-3.5Cr) and alloy 12-5Cr (45Al-

28Ti-22Nb-5Cr). Results on alloy 11 were already discussed in previous chapters. The present chapter discusses the results on alloy 12 and the alloys with Cr additions, along with the effect of Cr on  $\beta$ -to- $\gamma$  phase transformation upon cooling.

### 5.3 Alloy 11-5Cr

Alloy 11 was observed to exist as a two-phase  $\beta$ + $\gamma$  microstructure in the as-cast and solutionized-WQ samples. Although it was proven that the alloy consists of single phase  $\beta$  at the solutionizing temperatures, cooling of this  $\beta$ -phase even at fast cooling rates such as WQ would not inhibit the  $\gamma$ -phase formation. Thus, alloy 11-5Cr was arc melted with a composition of 45Al-37Ti-13Nb-5Cr.

#### 5.3.1 As-Cast

Figure 5-1a shows a BSE micrograph taken from an as-cast sample of alloy 11-5Cr. The BSE phase contrast indicates the presence of at least 2 phases. The XRD profile of a powdered sample of the as-cast alloy, in Figure 5-1b, confirms the presence of the  $\beta$  and the  $\gamma$  phases, along with that of the metastable  $\sigma$ -phase. Thus, the brighter phase in the BSE micrograph is ascribed as  $\beta$ -phase, and the darker phase as  $\gamma$ -phase. Study of the as-cast sample under the optical microscope revealed the presence of the columnar grains growing from the bottom of the as-cast button, as shown in Figure 5-2a. Fine  $\gamma$ -laths can be seen to grow from these  $\beta$  columnar grain boundaries, similar to those in the as-cast microstructure of alloy 11. The top of the sample contains equiaxed  $\beta$  grains shown in Figure 5-2b. Widmanstätten  $\gamma$ -phase laths can be seen to grow from these grain boundaries. Clearly, the  $\beta$ -phase existed as a single phase at high temperature and the  $\gamma$ -phase formed upon cooling via a solid-state transformation, similar to that occurring in alloy 11. No distinctly noticeable changes in the scale or

phase morphology were observed when compared to the as-cast microstructure of alloy 11. Thus, Cr did not seem to affect the as-cast microstructure in alloy 11-5Cr significantly.

### **5.3.2 Thermal Analysis**

DSC studies were then performed on the alloy under conditions similar to those of alloy 11. A sample of the as-cast alloy 11-5Cr was run in the DSC at a rate of 10 K/min in the temperature range of 850 C and 1425 C until consistent DSC profiles were obtained in consecutive DSC cycles. The final curve thus obtained is shown in Figure 5-3. As can be seen, there are two sharp peaks on the cooling curve, and two small and rather diffuse peaks on the heating curve of this DSC plot. The alloy exists as a single  $\beta$ -phase above 1377 C where the first peak on the cooling curve begins. Some significant differences in the two profiles were observed when comparing the DSC profiles of alloys 11 and 11-5Cr. On the cooling curves of the two DSC plots, the relative ratios of the two peaks remain the same; however, the temperatures of their occurrence have changed. While in alloy 11 the first peak begins at 1474 C, and the second peak begins at 1297 C, in alloy 11-5Cr the first peak on the cooling curve begins at a much lower temperature of about 1377 C. Thus, the first phase transformation event in alloy 11-5Cr occurs at a temperature about 100 C lower than that in alloy 11. This indicates that the single  $\beta$ -phase can exist down to lower temperatures in alloy 11-5Cr as compared to alloy 11. The first peak ends just as the second peak begins on the cooling curve of alloy 11-5Cr. Note, that the second peak on the cooling curve begins at approximately the same temperature as in alloy 11. This means that the second phase transformation event remained unaffected by the addition of Cr. Two distinct peaks can

be seen on the heating curve of alloy 11-5Cr,. The convoluted peaks as seen in the alloy 11 heating curve are no longer present. The two peaks on the heating curve of alloy 11-5Cr have shifted to lower temperatures, and the alloy transforms to single  $\beta$ -phase at lower temperatures as compared to alloy 11.

### 5.3.3 Solutionized-WQ

A sample of alloy 11-5Cr was solutionized-WQ in order to compare the effect of Cr on the  $\beta$ -to- $\gamma$  phase transformation at fast cooling rates. The sample was solutionized at 1400 C for 1hr followed by WQ. The solutionizing temperature is lower than that for alloy 11 due to the addition of Cr. This causes the melting point of the alloy to decrease, and also causes the alloy to exist as single  $\beta$ -phase at lower temperatures, as compared to alloy 11 (ref O.Rios). Figure 5-4a shows an optical micrograph of the solutionized-WQ sample. Large millimeter-sized grains of the prior  $\beta$ -phase can be observed. The grain boundaries are decorated with fine laths of a second phase. However, this phase is only limited to the  $\beta$ -grain boundaries, and cannot be seen in the bulk matrix. Figure 5-4b shows a BSE micrograph of the bulk matrix, the matrix of which clearly contains a high density of fine  $\alpha$ -phase plates. Figure 5-5 presents higher magnification TEM micrographs of the matrix containing fine  $\alpha$ -phase plates. These  $\alpha$ -phase plates formed from the  $\beta$ -phase upon quenching via a martensitic transformation. The XRD plot obtained from a powdered sample of the solutionized-WQ alloy is shown in Figure 5-6. It shows the presence of  $\beta$ ,  $\gamma$  and  $\alpha$  phases. Clearly, the fine laths at the  $\beta$ -grain boundaries observed in Figure 5-4a are  $\gamma$ -phase. Comparing the XRD profiles of the solutionized-WQ alloys 11 (Figure 3-10) and 11-5Cr, and the various peak ratios, it is evident that alloy 11 contains a much higher phase fraction of the  $\gamma$ -phase, whereas

alloy 11-5Cr contain high amounts of  $\beta$  and  $\alpha$  phases. These  $\gamma$ -phase laths form upon quenching the solutionized sample in both alloy 11 and 11-5Cr.  $\gamma$ -phase laths, however, could not grow extensively into the matrix in alloy 11-5Cr as occurred in the case of alloy 11. Clearly, the growth of these  $\gamma$ -phase laths was inhibited due to the fast cooling rates in alloy 11-5Cr. Thus, a higher amount of the  $\beta$ -phase was able to be retained upon quenching from the solutionizing temperature. It can be seen that the addition of Cr caused the retention of a higher amount of the  $\beta$ -phase and limited the growth of the  $\gamma$ -phase upon quenching.

### **5.3.4 Transformations Under the DSC Peaks**

The peaks on the DSC cooling curves of alloy 11 and 11-5Cr appear similar. We speculate that the transformations under the two peaks in both alloys would also be similar. Thus, the two peaks on the DSC cooling curve of alloy 11-5Cr would also be due to the two step formation of  $\gamma$ -phase. In order to confirm this, one DHT heat treatment was performed between the first and the second peak, and another sample was slow cooled from the solutionizing temperature. The first sample was solutionized at 1400 C for 1 hr, cooled to 1320 C (between the first and the second DSC peaks) at a rate of 12 K/min and held for 2 hrs before WQ. Figure 5-7 shows an optical micrograph of the sample, depicting a two phase microstructure. Coarse laths of the  $\gamma$ -phase can be seen nucleated at the prior  $\beta$  grain boundaries. The microstructure is similar to the DHT1350 sample of alloy 11. The phase fraction of the  $\gamma$ -phase observed was ~40%. Thus, the first DSC peak on the cooling curve signifies the nucleation of these Widmanstätten  $\gamma$ -phase laths at the  $\beta$ -phase grain boundaries and accounts for the formation of 40% phase fraction of the  $\gamma$ -phase.

Figure 5-8a shows an optical micrograph from the solutionized slow-cooled sample of alloy 11-5Cr. The sample was solutionized at 1400 C for 1 hr followed by slow cooling to room temperature at a rate of 9 K/min. Coarse  $\gamma$ -phase laths can be seen in the micrograph. A high phase fraction of the  $\gamma$ -phase (~85%) exists in the microstructure. A higher magnification image of the microstructure, in Figure 5-8b, shows fine metastable phases in the  $\beta$  matrix. No  $\sigma$ -phase could be seen in the microstructure. The larger fraction of metastable phases in the  $\beta$ -matrix, as compared to alloy 11 slow cooled sample is probably because the  $\beta$ -phase in alloy 11-5Cr is supersaturated solid solution in case of alloy 11-5Cr. As it cools down,  $\gamma$ -phase nucleates and grows.  $\sigma$ -phase, however, does not form, and the unstable  $\beta$  transforms into metastable phases. Due to the presence of more alloying elements in alloy 11-5Cr, the  $\beta$ -phase, upon cooling, is more unstable as compared to alloy 11, indicating that a higher fraction of the metastable phases is present. The second DTA peak clearly signifies a second  $\gamma$  formation event, since the phase fraction of the  $\gamma$ -phase drastically increases by more than 40% as the alloy cools through the second DTA peak.

Thus, based on the above results it can be said that in both alloy 11 and 11-5Cr the two peaks on the DSC cooling curve represent  $\beta$ -to- $\gamma$  phase transformation. The  $\sigma$ -phase fails to form in both the alloys upon cooling room temperature at the cooling rates employed.

### **5.3.5 Aged**

A sample of the solutionized-WQ alloy was encapsulated and aged in a box furnace at 1200 C for 2 hrs. The resulting microstructure is shown in Figure 5-9, and consists of a two-phase  $\beta$ + $\gamma$  microstructure. The dark phase is the  $\gamma$ -phase, whereas the

brighter contrast comes from the  $\beta$ -matrix. Note that the  $\gamma$ -phase does not exhibit a Widmanstätten lath morphology. It precipitated homogeneously throughout the sample as equiaxed particles. It was seen in the aged sample of alloy 11, that once the  $\gamma$ -phase formed (Widmanstätten) upon the quenching of the  $\beta$ -phase, further aging of the sample did not change its morphology. The solutionized-WQ alloy 11-5Cr consisted of fine  $\gamma$ -laths only at the  $\beta$ -grain boundaries, whereas the bulk  $\beta$ -matrix consisted of a high density of the  $\sigma$ -plates. A homogeneous distribution of equiaxed  $\gamma$ -phase is observed upon aging at 1200 C. This suggests that upon aging, extensive nucleation of the  $\gamma$ -phase occurred 'homogeneously' throughout the sample. The solutionized-WQ sample contained the  $\sigma$ -plates, apart from the  $\beta$ -grain boundaries. During aging,  $\beta$ -grain boundaries might have served as nucleation sites for the  $\gamma$ -phase, leading to their homogeneous distribution in the sample. However, this remains speculation at this point and needs further work in order to be proved.

#### 5.4 Alloy 12

Alloy 12, with a composition of 45Al-28Ti-27Nb solidifies as a single  $\beta$ -phase. The alloy has the same aluminum content as alloy 11, but contains much higher Nb that is known to be a  $\beta$ -stabilizer and a  $\sigma$ -former [40, 54, 86]. The Nb content is the same as in alloy 2 studied previously by D. Hoelzer [8, 73] in his work on TiAlNb alloys. Alloy 2 was discussed in Chapter 1. It existed as a single  $\beta$ -phase at high temperature. Upon cooling, first the  $\sigma$ -phase nucleated in the  $\beta$ -phase, and upon further cooling the  $\gamma$ -phase formed at lower temperatures. The alloy existed as a two-phase  $\gamma+\sigma$  at lower temperatures. Alloy 12 also exists as two-phase  $\gamma+\sigma$  at temperatures at and below  $\sim 1050$  C [22, 24]. However, upon cooling from the solutionizing temperature (1500 C),  $\gamma$

is the first phase to form in the  $\beta$ -phase, whereas  $\sigma$  forms at lower temperatures. The BSE micrographs of the as-cast and solutionized-WQ samples of alloy 12 are shown in Figure 5-10 a & b, respectively. The as-cast alloy exists as  $\gamma+\sigma$  two-phase microstructure, with laths of the  $\gamma$ -phase growing from the  $\beta$ -phase grain boundaries, along with the remaining  $\sigma$ -phase that transformed from the  $\beta$ -phase at lower temperatures during cooling. The solutionized-WQ (1500 C for 1 hr) sample consists of  $\beta$  and  $\gamma$  phases in the microstructure. The XRD profiles of the powdered samples are presented in Figure 5-11. The reason for the existence of a  $\gamma+\sigma$  microstructure in the as-cast and  $\beta+\gamma$  microstructure in the solutionized-WQ sample is the kinetics of  $\sigma$ -formation. As the solutionized sample is quenched from the single-phase  $\beta$  regime,  $\gamma$ -phase forms due to its fast kinetics. As discussed in Chapter 3,  $\gamma$  can form at a fast rate with limited diffusion from the  $\beta$ -phase on quenching. However, the  $\sigma$ -phase has a complex crystal structure that makes its nucleation difficult. High Nb is required for  $\sigma$ -formation, and at such short times as those available in WQ, the diffusion of Nb is not possible, thus inhibiting the  $\sigma$ -phase formation in the solutionized-WQ samples. The as-cast sample, on the other hand, experiences much slower cooling rates. As the arc melted button cools, it solidifies as a single-phase  $\beta$ , which upon cooling goes through a  $\beta+\gamma$  two-phase region. However, higher amount of diffusion occurs due to slower cooling rates, leading to attainment of phase compositions closer to equilibrium. As the alloy cools, Nb partitions into the  $\beta$ -phase, and the phases continue to change composition. At lower temperatures the Nb-rich  $\beta$ -phase transforms to  $\sigma$ -phase.

The two peaks in the DSC cooling curve of the alloy (Figure 5-20) are attributed to the formation of  $\gamma$ - (first peak) and  $\sigma$ - phases (second peak). A sample was solutionized and cooled to 1340 C (past both DSC peaks) at 12 K/min and held for 6 hrs followed by WQ. The BSE micrograph and a corresponding XRD of a powdered sample are presented in Figures 5-12 a & b. The sample consists of a three-phase  $\beta+\gamma+\sigma$  microstructure. The  $\sigma$ -phase plates can also be noticed that formed upon WQ in the  $\beta$ -phase. The  $\sigma$ -phase can be seen to be growing at the interface of the  $\gamma$ - and the  $\beta$ -phases, suggesting that it formed after the formation of the  $\gamma$ -phase. Based on the calculated phase diagram and microstructural evidence, it can be said that two DSC peaks are due to the  $\gamma$ - and- $\sigma$  phase formation and not due to two-stage nucleation of the  $\gamma$ -phase as occurred in alloy 11.

## 5.5 Alloys 12-xCr

Three alloys were arc melted with different Cr contents, namely, alloy12-1.5Cr, 12-3.5Cr and 12-5Cr. The alloys were studied in their as-cast and solutionized-WQ state to study the effect of Cr. The results are presented in the following sections.

### 5.5.1 As-Cast

Figures 5-13 a & b present an optical micrograph and an XRD from a powdered sample of alloy 12-1.5Cr in the as-cast condition. The micrograph clearly shows fine  $\gamma$ -phase laths at the prior  $\beta$  columnar grain boundaries. The XRD shows the presence of  $\gamma$ ,  $\sigma$ , and  $\beta$ -phases in the microstructure. The  $\gamma$ -phase clearly has the largest phase fraction in the microstructure and  $\sigma$  the smallest, based on the XRD relative peak intensities. An optical micrograph and XRD profile of a powdered sample of as-cast 12-3.5Cr alloy is shown in Figures 5-14 a & b, respectively. Again, the columnar grains and

the  $\gamma$  laths can be seen in the micrograph. The microstructure looks similar to the one in Figure 5-13a. However, the XRD profile shows the presence of only  $\gamma$ - and  $\beta$ -phases. No  $\sigma$ -phase is present in the microstructure, unlike in the 12-1.5Cr sample. Again, Figures 5-15 a & b show an optical micrograph and an XRD profile from the as cast sample of alloy 12-5Cr. The microstructure of the as-cast sample looks similar to other 12-xCr as-cast samples. The XRD indicates that the microstructure is composed of  $\beta$ - and  $\gamma$ -phases.

Analysis of the results on the as-cast microstructures of alloy 12-xCr alloys indicate that the microstructure varies gradually upon the addition and increase of the Cr content of the alloy from a two-phase  $\gamma+\sigma$  to a two-phase  $\beta+\gamma$  microstructure. Alloy 12 exists as a two-phase  $\gamma+\sigma$  microstructure in the as-cast sample, where during cooling the  $\gamma$ -laths form first in the  $\beta$ -phase and then, at lower temperatures, the  $\beta$ -phase transforms to the  $\sigma$ -phase. In alloy 12-1.5Cr,  $\beta$ -,  $\gamma$ - and  $\sigma$ -phases are observed, which suggests that  $\beta$ -phase did not completely transform to  $\sigma$  during cooling. Alloys 12-3.5Cr and 12-5Cr exhibit a two-phase  $\gamma+\beta$  microstructure in the as-cast sample indicating that the  $\beta$ -phase did not transform to  $\sigma$  and remained as a metastable phase to room temperature.

### **5.5.2 Solutionized-WQ**

Samples of all three 12-xCr alloys were solutionized for 1 hr at their respective solutionizing temperatures and then WQ. Alloys 12-1.5Cr and 12-3.5Cr were solutionized at 1420 C and alloy 12-5Cr was solutionized at 1400 C. Figure 5-16 presents optical micrographs from the solutionized sample of alloy 12-1.5Cr. The microstructure consists of large, prior  $\beta$ -phase grains with the grain boundaries

decorated with a fine second phase. The matrix consists of fine plates of the  $\alpha$ -phase distributed homogeneously throughout the matrix. A closer look at the  $\beta$  grain boundaries in Figure 5-16b reveals the presence of fine laths of a second phase, possibly  $\gamma$ -phase. Clearly,  $\gamma$ -phase formed upon quenching, but did not grow extensively into the matrix as in the alloy 11 and 12 solutionized-WQ samples. Optical micrographs from the solutionized-WQ sample of alloy 12-3.5Cr are shown in Figure 5-17. The microstructure looks similar to that of alloy 12-1.5Cr with large prior  $\beta$  grains, fine second phase decorating the  $\beta$  grain boundaries, and  $\alpha$ -plates in the matrix. However, a closer examination of the grain boundaries under the optical microscope reveals that the  $\gamma$  laths are distributed unevenly along the grain boundaries. Further, these laths seem to have grown to a lesser extent into the  $\beta$ -matrix. The grain boundary at many places appears to be devoid of any  $\gamma$ -phase. It is possible, however, that a fine layer of  $\gamma$ -phase allotriomorphs is present and has not grown into laths. Figure 5-18 presents the optical micrographs from the solutionized-WQ sample of alloy 12-5Cr. Again, the microstructure is similar to those of alloys 12-1.5Cr and 12-3.5Cr in their solutionized-WQ state, and a further decrease is observed in the continuity of the  $\gamma$ -phase laths at the  $\beta$  grain boundaries. At most places, the  $\beta$  grain boundaries appear to be pristine, and no  $\gamma$  laths can be seen. The XRD profile of a powdered sample of the solutionized-WQ alloy is shown in Figure 5-19. The peaks suggest the presence of a single  $\beta$ -phase with some  $\alpha$ -phase peaks.

### **5.5.3 Double Heat Treatment (DHT)**

A sample of alloy 12-5Cr was solutionized at 1400 C for 1hr, cooled to 1200 C at 12 K/min and held for 2 hrs before WQ (DHT1200). The resulting microstructure

consisted of  $\beta$ - and  $\gamma$ -phase. Figures 5-20 a & b present the BSE micrograph and the XRD of a powdered sample. Coarse  $\gamma$ -phase shows up as the dark phase in the BSE contrast, and the matrix  $\beta$ -phase appears bright. An EPMA compositional analysis was performed on the phases in the sample, the results of which are presented in Table 5-1. The  $\gamma$ -phase is richer in Al, whereas in comparison the  $\beta$ -phase is richer in Ti and Nb. Note that Cr selectively partitioned into the  $\beta$ -phase where its content is three times as much as in the  $\gamma$ -phase. Clearly, Cr has a strong tendency to partition into the  $\beta$ -phase.

## 5.6 Discussion

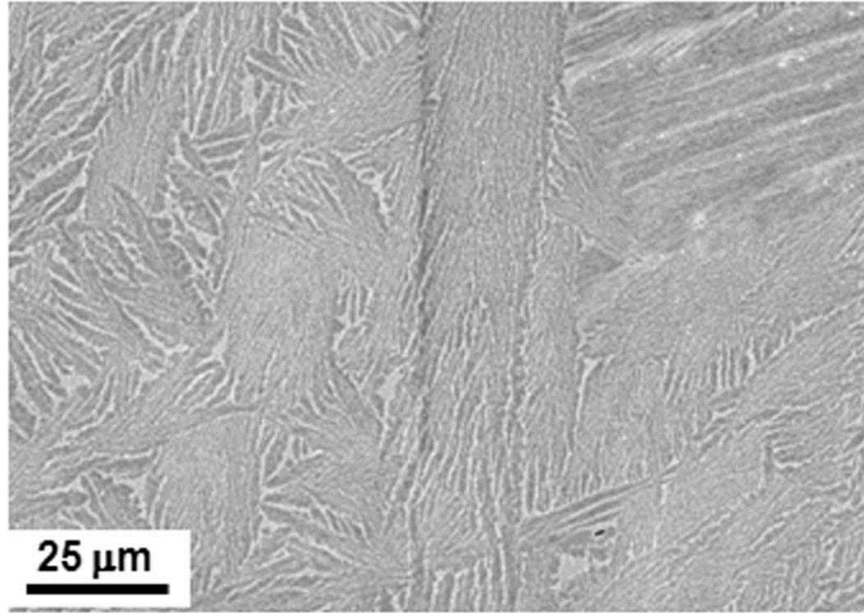
Alloys 11 and 12 both consisted of large amounts of the  $\gamma$ -phase, which formed upon quenching, in the solutionized-WQ samples. Even such fast cooling rates could not prevent its formation. However, the amount of the  $\gamma$ -phase formed upon quenching decreased significantly upon the addition of just 1.5 at%Cr to alloy 12. As the amount of Cr was increased, a decrease occurred in the amount of  $\gamma$ -phase observed. Extensive growth of the laths, as seen in alloys 11 and 12 upon solutionizing and WQ, was not observed in the alloys containing Cr. The  $\gamma$ -phase was limited to the  $\beta$  grain boundaries. Clearly, Cr has affected the growth of these  $\gamma$  laths during quenching and decreases the growth rate, so that in the limited time available during WQ the  $\gamma$ -laths are not able to grow extensively. However, nothing more can be said about the effect of Cr on the nucleation of the  $\gamma$ -phase at the  $\beta$  grain boundaries. In all the alloys containing Cr, the  $\gamma$ -phase was always observed at the grain boundaries, even though the extent of its growth might be limited. Thus, it can be said that  $\gamma$ -phase nucleated during quenching but did not grow.

The compositional analysis performed on the DHT1200 sample of alloy presented in Table 5-1 clearly indicates that Cr strongly partitions into the  $\beta$ -phase. At 1200 C the equilibrium content of Cr in the  $\gamma$ -phase is close to 2.5 at%. Thus, if the Cr content in the  $\beta$  matrix is high, Cr will need to diffuse into the  $\beta$ -phase for the  $\gamma$ -phase to grow. This requires time, which is limited during WQ. The alloys containing Cr show fine  $\gamma$ -phase laths initiating only at the grain boundary, with limited subsequent growth. As the Cr content of the alloy increases, more Cr needs to partition out into the  $\beta$ -phase, and thus there is a corresponding decrease in the growth of the  $\gamma$  laths. Note that effect of Cr on the nucleation of the  $\gamma$ -phase, if any, needs to be studied in future.

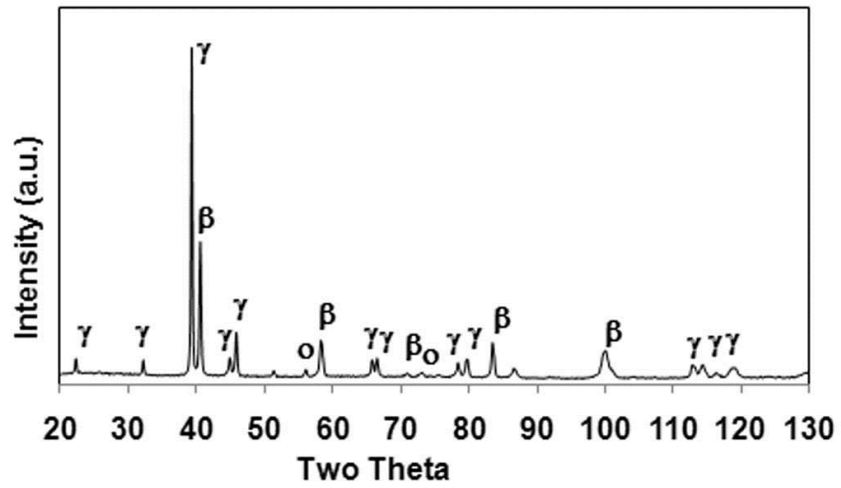
The as-cast microstructures with the addition of Cr show a gradual change from a two-phase  $\gamma+\sigma$  (alloy 12) to a two phase  $\beta+\gamma$  (alloy 12-3.5Cr and 12-5Cr) microstructure. This result suggests that the  $\beta$ -phase becomes more stable at lower temperatures as the Cr content of the alloys increases. This is expected since Cr is a  $\beta$ -stabilizer. Figure 5-21 presents the DSC curves of alloy 12 and 12-5Cr run at 10 K/min. The cooling curve on alloy 12 shows two distinct peaks located adjacent to each other. The first peak represents the formation of the  $\gamma$ -phase, whereas the second peak is that of the  $\sigma$ -phase. In alloy 12-5Cr, however, the second peak has moved to much lower temperatures (lower by >150 K) whereas the first peak remains relatively unaffected (lower by <20 K). The addition of Cr has not affected the transformation temperature of the  $\gamma$ -phase from the single phase  $\beta$  upon cooling. However, the formation of the  $\sigma$ -phase is delayed upon the addition of Cr, which causes the  $\beta$ -phase to be retained to lower temperatures. This would substantiate the microstructures obtained in the as-cast samples of alloys 12 and 12-xCr. Once the  $\gamma$ -phase forms, and the Cr partitions into the

matrix, it makes the  $\beta$ -phase more stable and forces the  $\sigma$  formation temperatures down to lower temperatures.

Figure 5-22 presents the DSC curves of alloys 11 and 11-5Cr. Both alloys exhibit two distinct peaks on the cooling curves, both of which have been shown to be related to the  $\gamma$ -phase (Chapter 4). Comparison between the two DSC cooling curves indicates that the first peak for alloy 12-5Cr has shifted to lower temperatures (lower by  $\sim 100$  K) such that it lies just before and adjacent to the second peak, which remains unaffected by Cr addition. Knowing that the first peak is associated with the formation of the primary Widmanstätten  $\gamma$  laths, it implies that upon addition of Cr to alloy 11, the formation of the primary  $\gamma$  laths is shifted to lower temperatures. Thus, addition of 5 at%Cr to alloy 11 appears to have made the single  $\beta$ -phase regime stable to lower temperatures, such that the first nucleation event of the  $\gamma$ -phase occurs at a lower temperature as compared to alloy 11. The second nucleation event, however, remains unaffected, possibly due to the fact that once the primary  $\gamma$ -laths form, they give rise to the  $\beta/\gamma$  interfaces that serve as the nucleation sites for the secondary  $\gamma$ -phase.

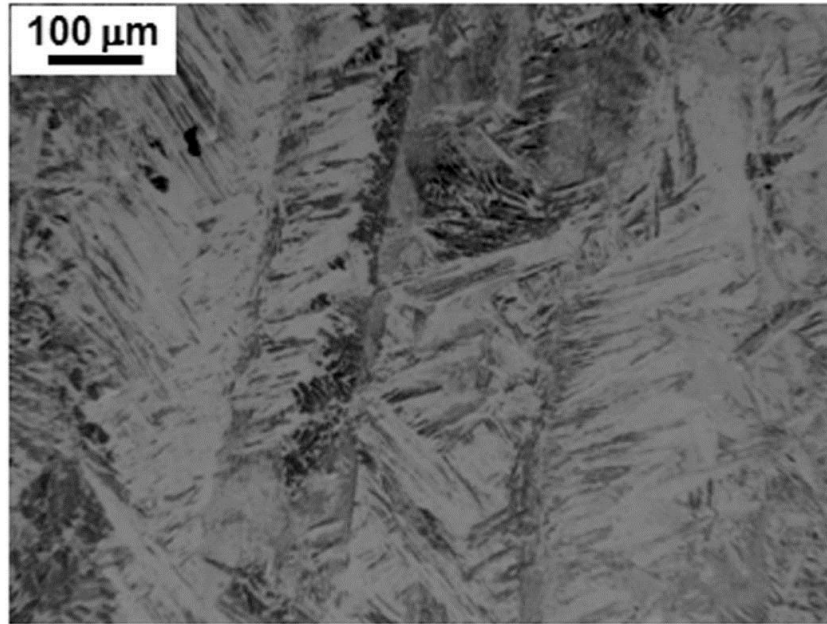


A

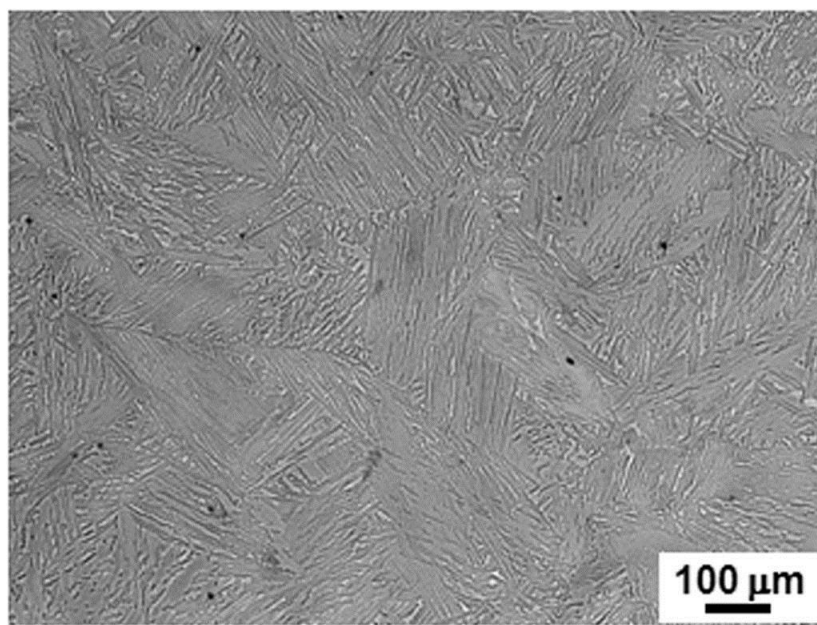


B

Figure 5-1. Alloy 11-5Cr as-cast. A) BSE micrograph. B) XRD profile of a powdered sample



A



B

Figure 5-2. Optical micrograph of alloy 11-5Cr as-cast. A) Bottom of the sample. B) Top of the sample

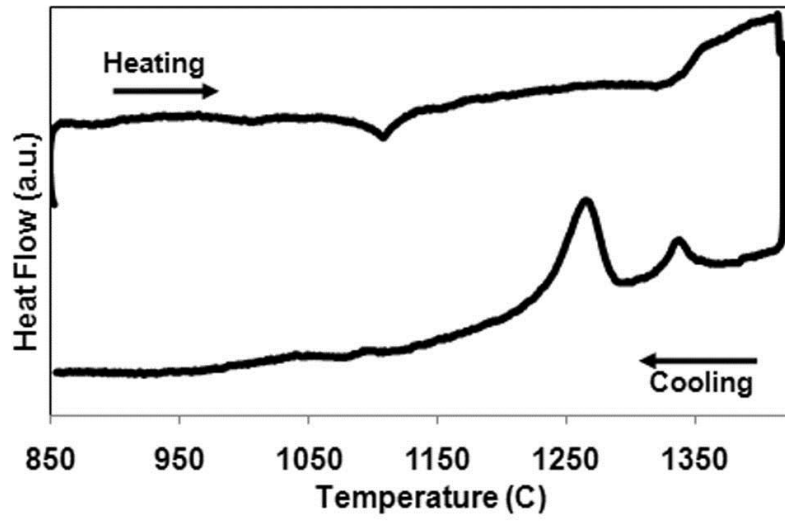
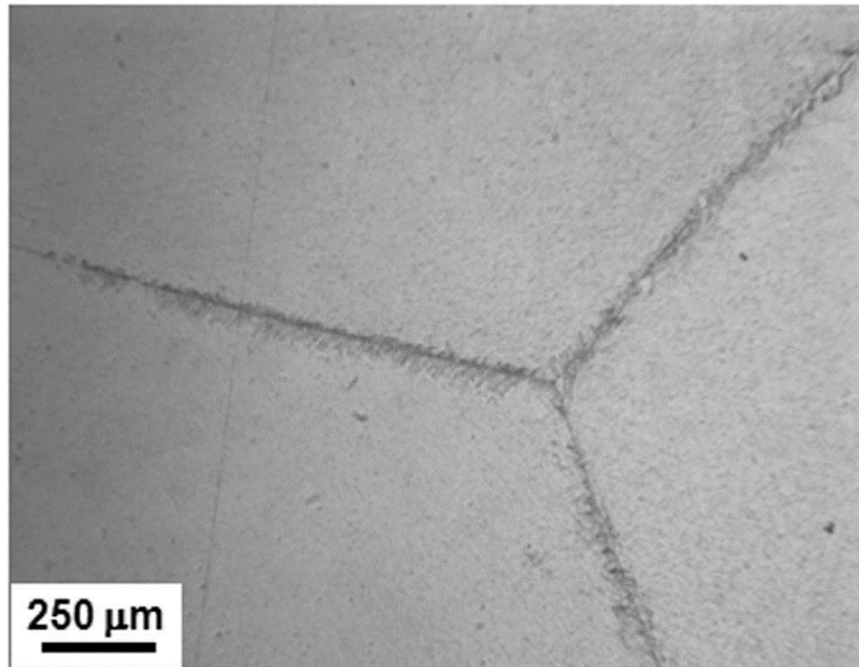
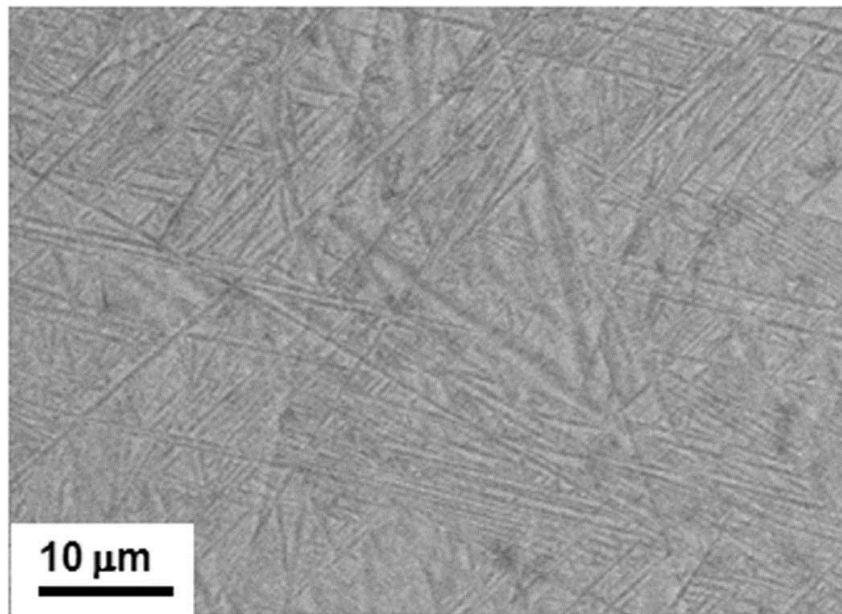


Figure 5-3. DSC profile of the final run of alloy 11-5Cr



**A**



**B**

Figure 5-4. Alloy 11-5Cr solutionized-WQ. A) Optical micrograph. B) BSE micrograph of the matrix

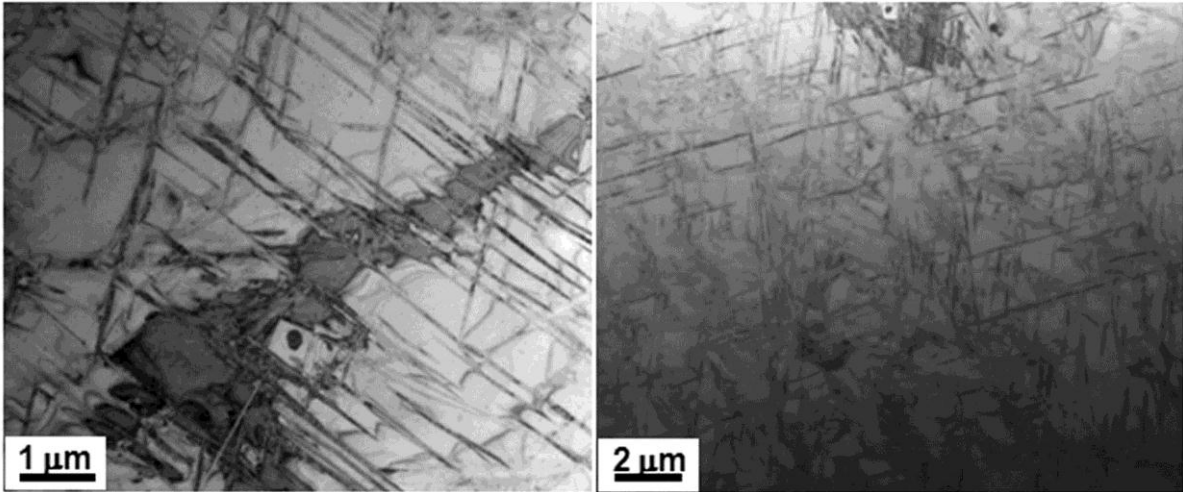


Figure 5-5. TEM BF micrographs of the matrix of solutionized-WQ alloy 11-5Cr showing orthorhombic plates in the  $\beta$ -matrix

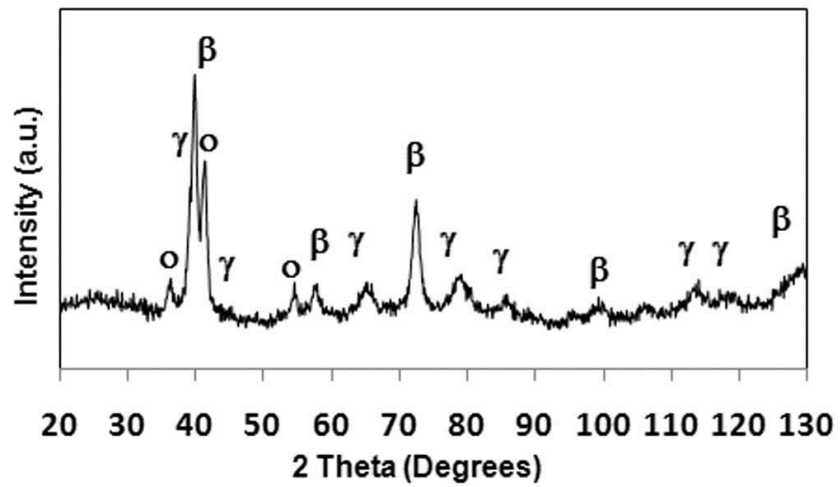


Figure 5-6. XRD profile of the powdered sample of solutionized-WQ alloy 11-5Cr

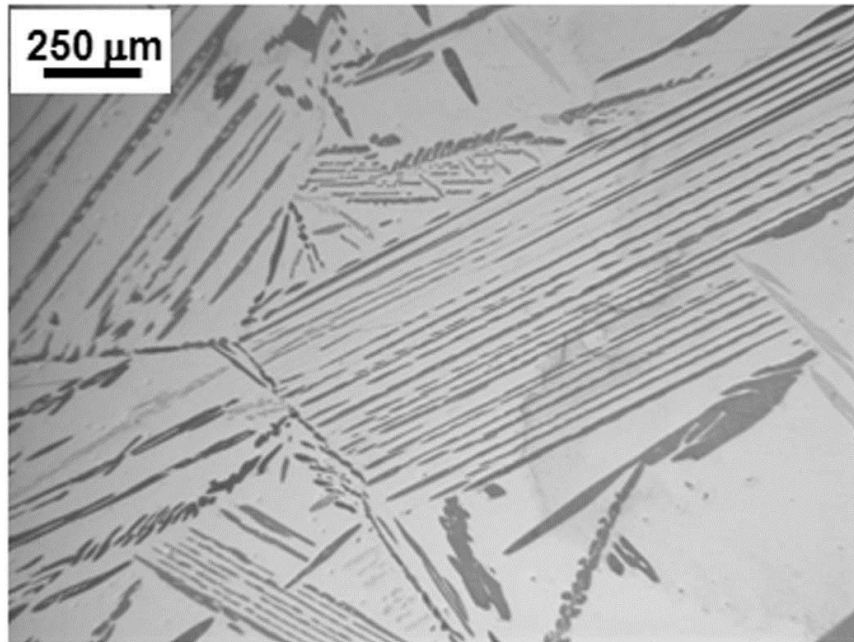
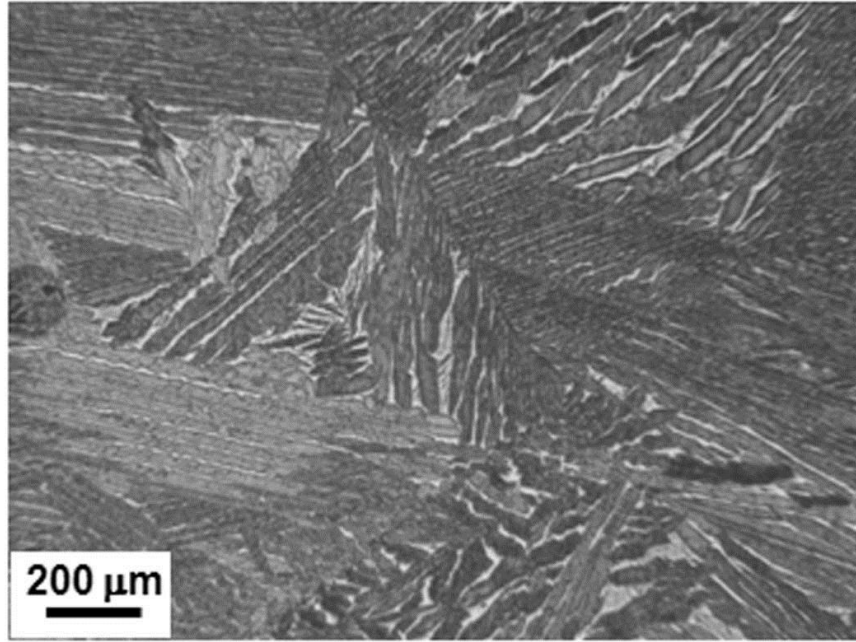


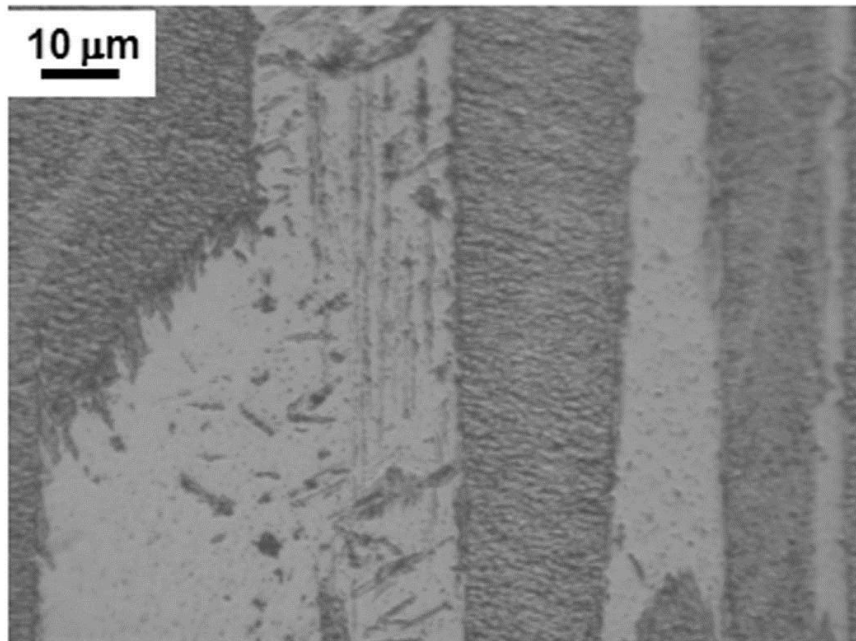
Figure 5-7. Optical micrograph from the DHT1320 sample alloy 11-5Cr

Table 5-1. EPMA compositional analysis of alloy 11-5Cr DHT1320/2h sample

		Al	Ti	Nb	Cr
DHT1200/2h	β-phase	42.8(±0.1)	37.9(±0.2)	13.5(±0.3)	5.8(±0.3)
	γ-phase	49.7(±0.2)	35.5(±0.2)	12.5(±0.2)	2.2(±0.2)



**A**



**B**

Figure 5-8. Optical micrographs of alloy 11-5Cr solutionized-slow cooled. A) Low magnification. B) Higher magnification

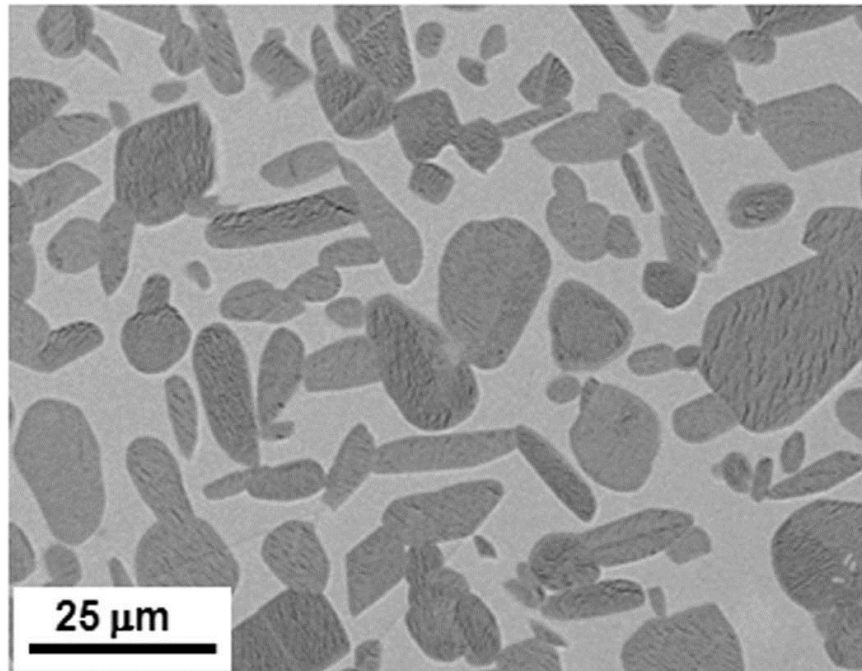


Figure 5-9. BSE micrograph of aged sample of alloy 11-5Cr

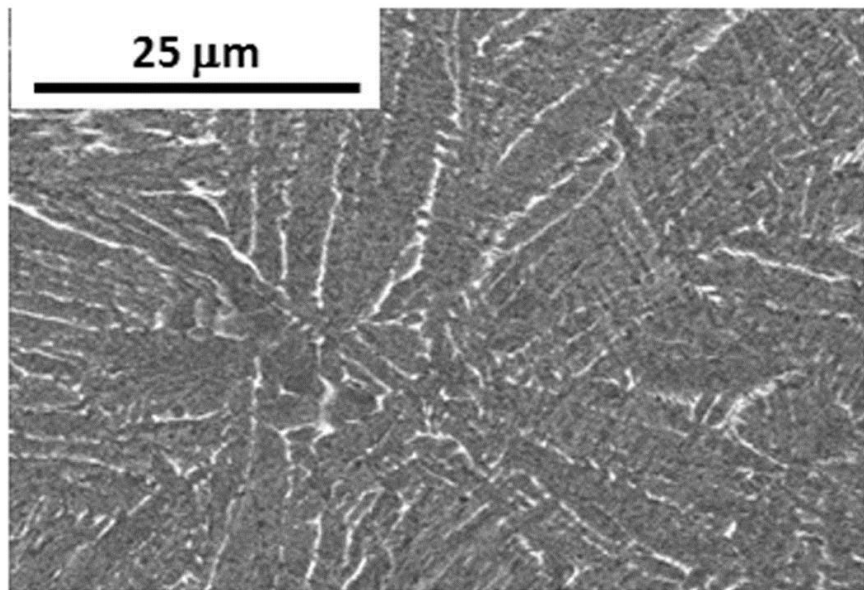
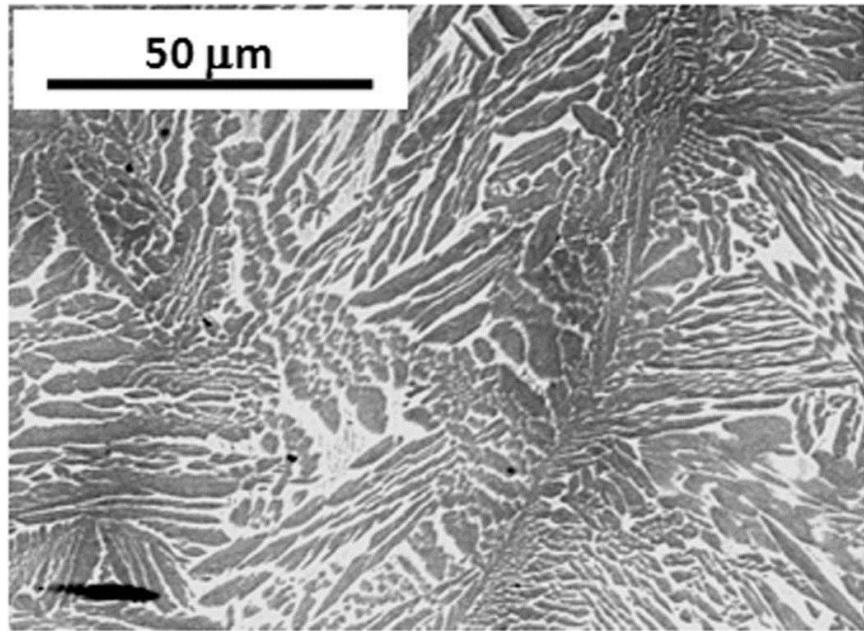
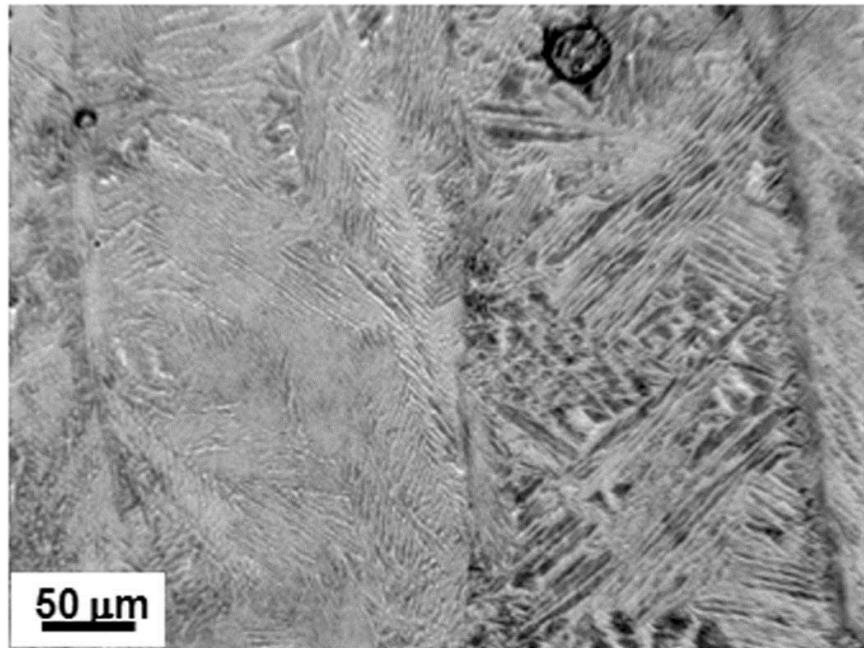


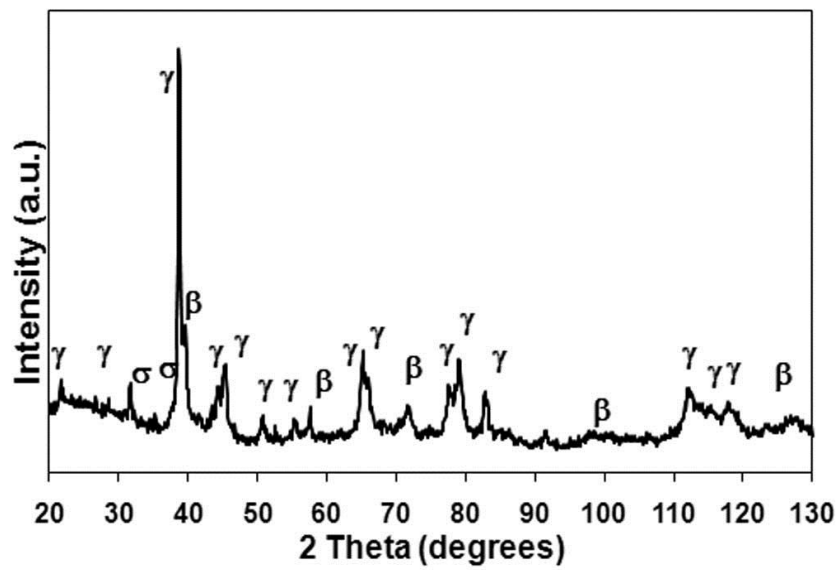
Figure 5-10. BSE micrographs of alloy 12. A) As-cast. B) BSE. Figures courtesy: Michael Kesler, University of Florida





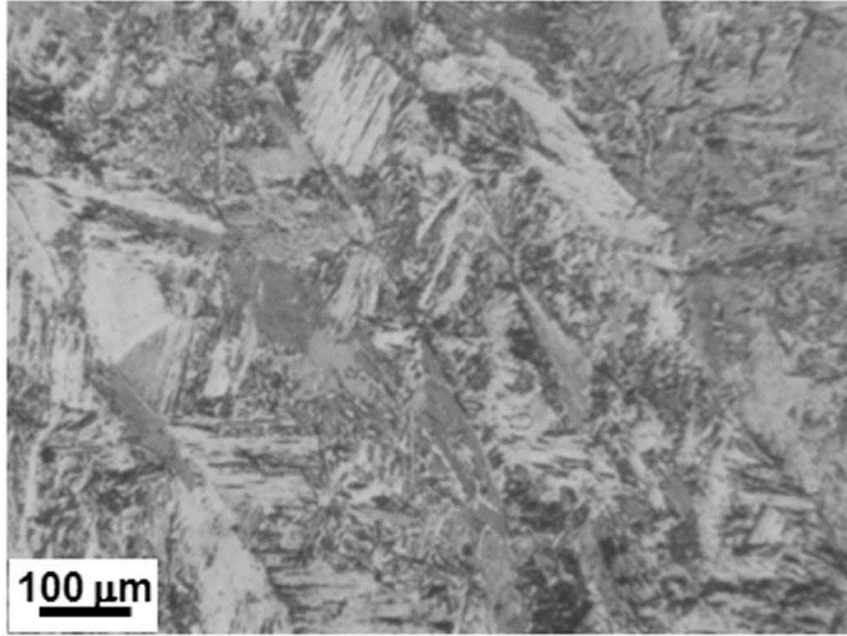


A

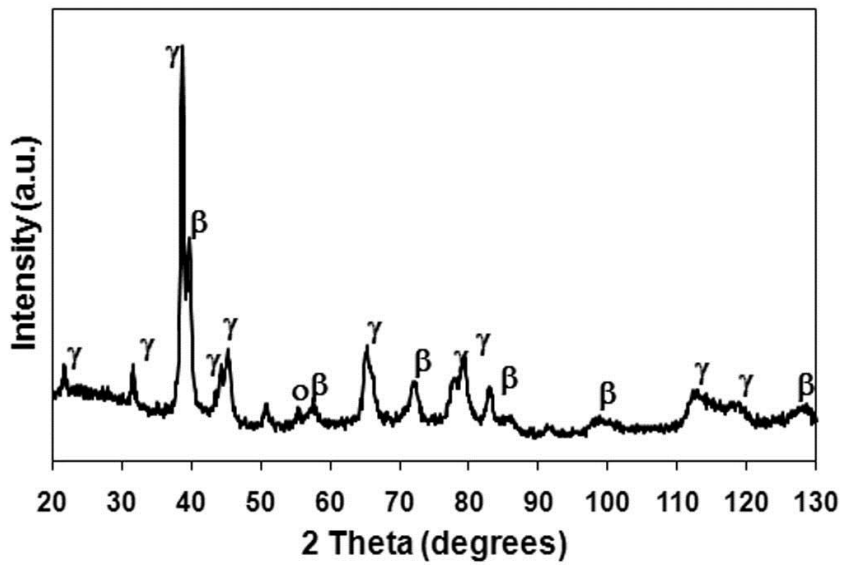


B

Figure 5-13. Alloy 12-1.5Cr as-cast. A) Optical micrograph. B) Corresponding XRD plot of a powdered sample

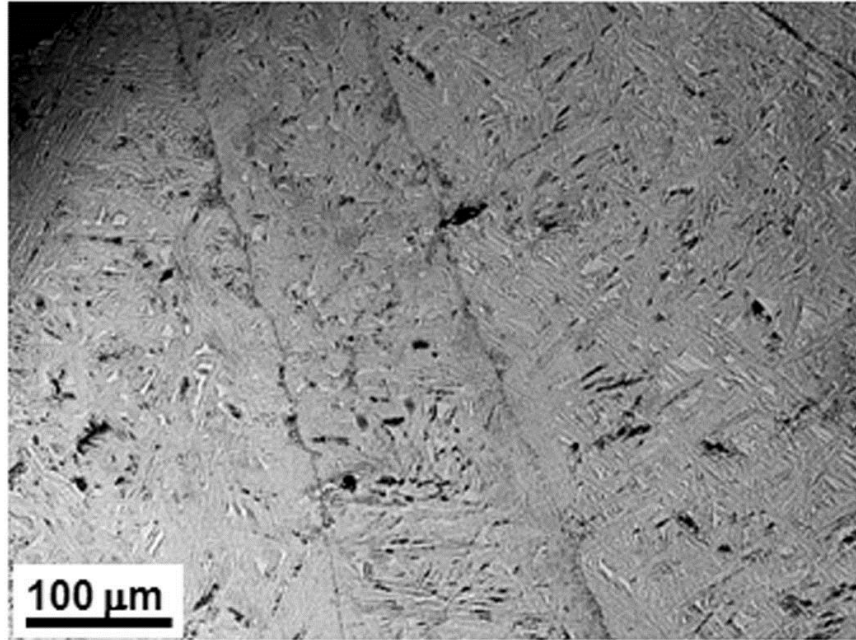


A

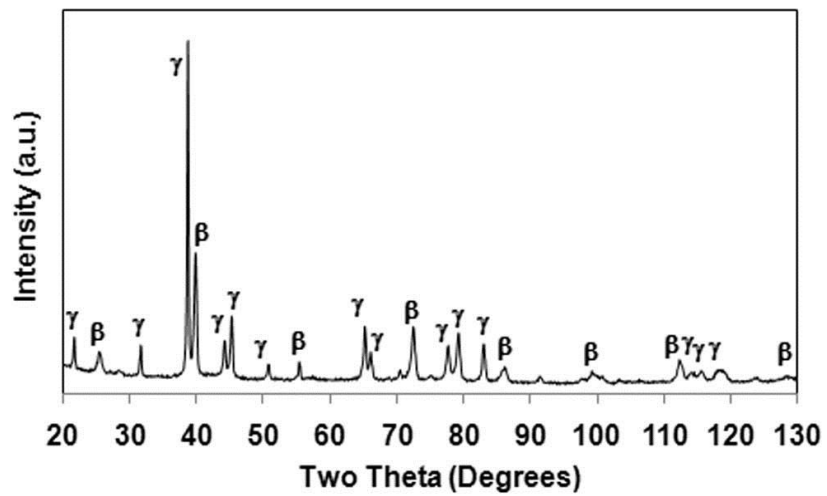


B

Figure 5-14. Alloy 12-3.5Cr as-cast. A) Optical micrograph. B) Corresponding XRD plot of a powdered sample



A



B

Figure 5-15. Alloy 12-5Cr as-cast. A) Optical micrograph. B) Corresponding XRD plot of a powdered sample. Figures courtesy: Michael Kesler, University of Florida

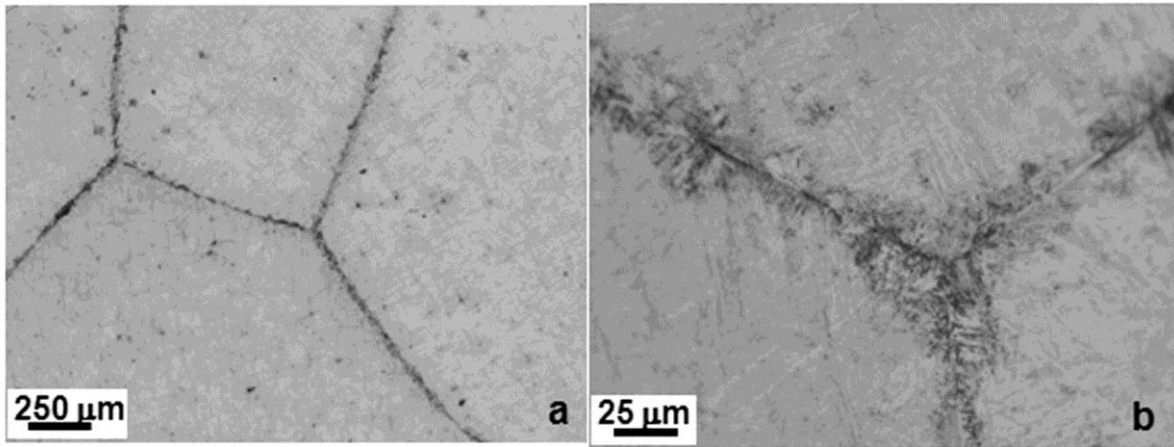


Figure 5-16. Optical micrographs of solutionized-WQ alloy 12-1.5Cr

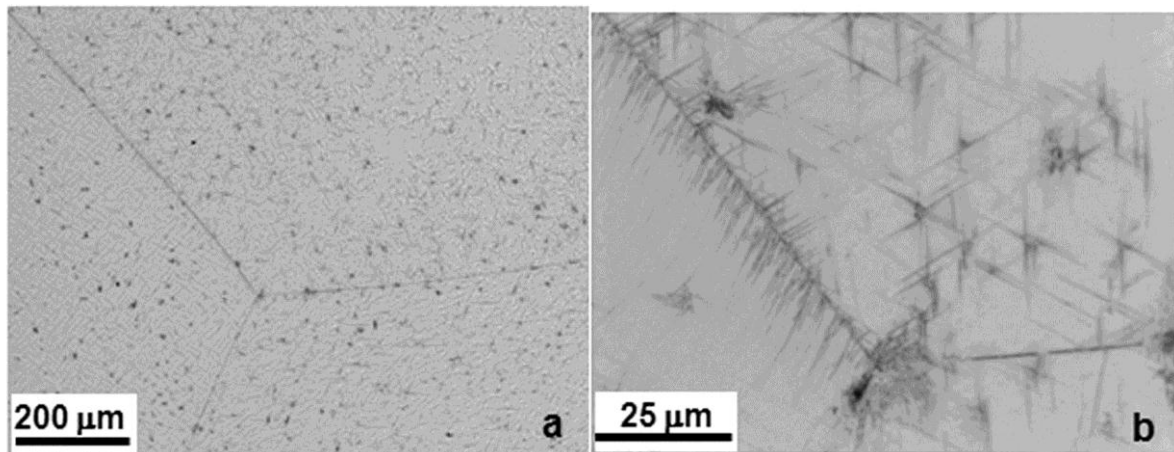


Figure 5-17. Optical micrographs of solutionized-WQ alloy 12-3.5Cr

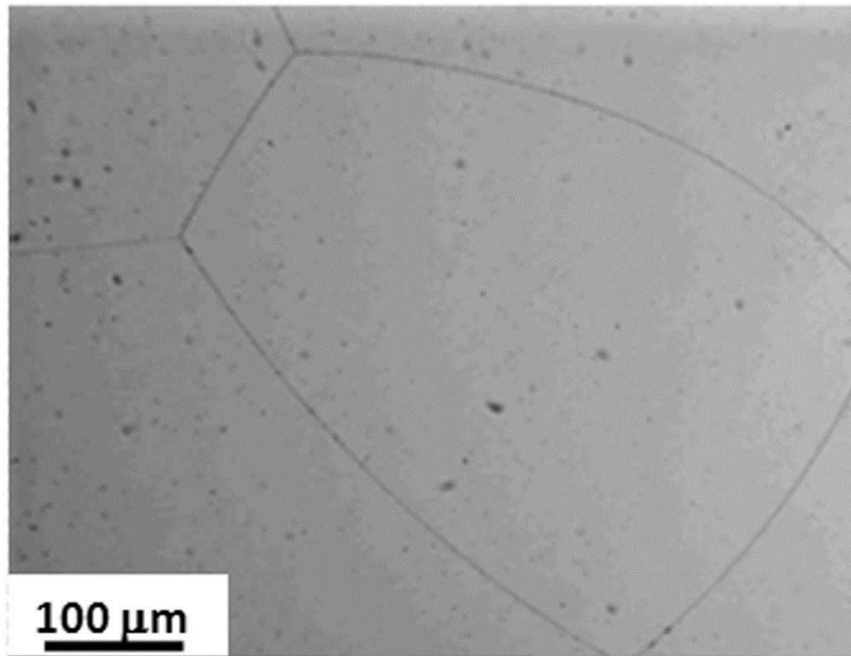


Figure 5-18. Optical micrograph of solutionized-WQ alloy 12-5Cr

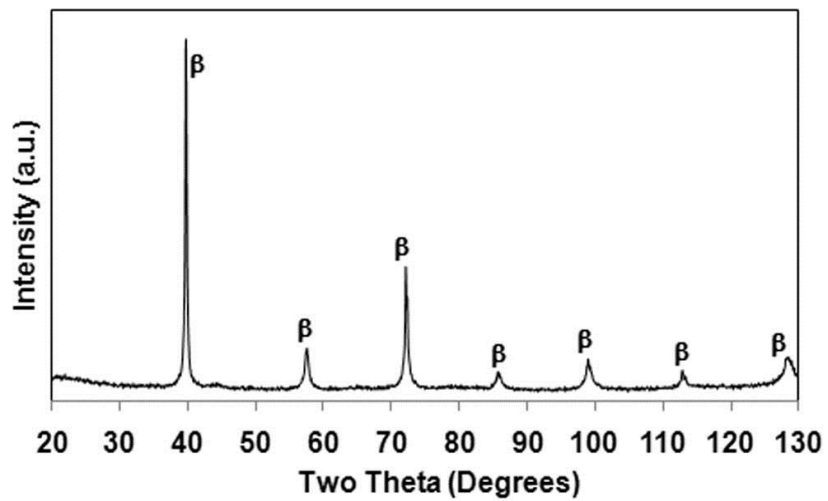
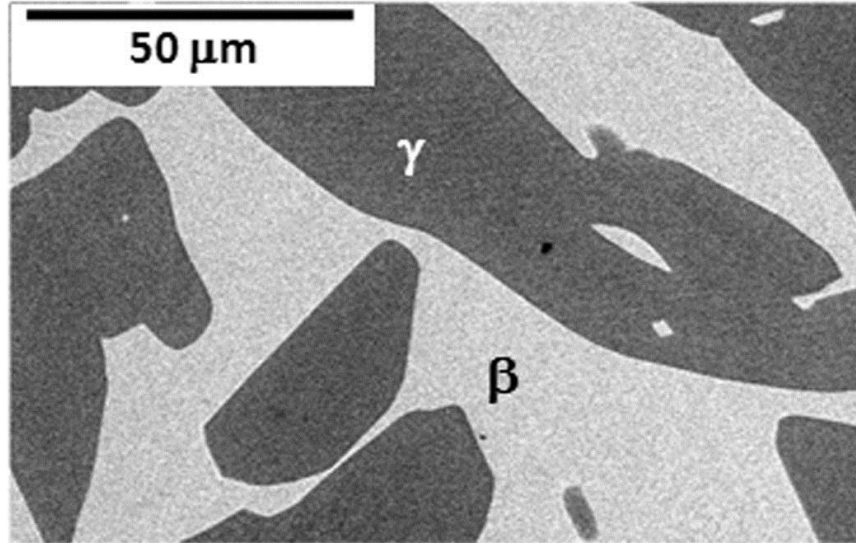
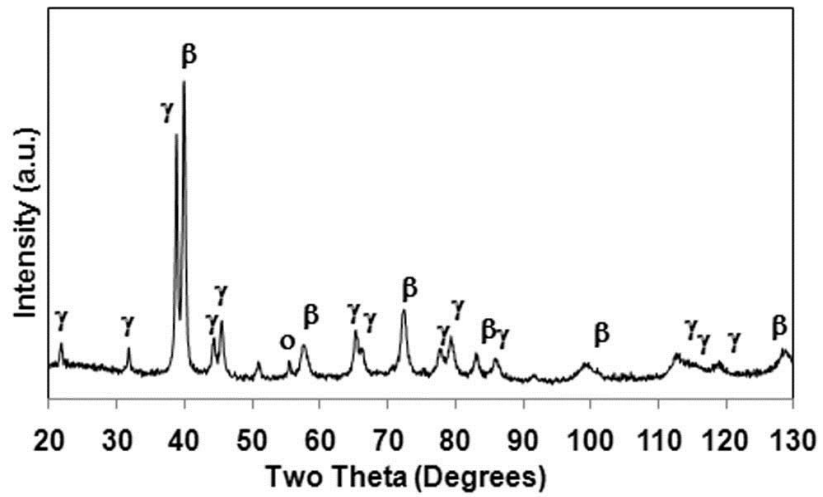


Figure 5-19. XRD plot of a powdered sample of alloy 12-5Cr in the solutionized-WQ condition



A



B

Figure 5-20. Alloy 12-5Cr DHT1200/2h. A) BSE micrograph. B) Corresponding XRD plot of a powdered sample. Figures courtesy: Michael Kesler, University of Florida

Table 5-2. EPMA compositional analysis of alloy 12-5Cr DHT1200/2h sample

		Al	Ti	Nb	Cr
DHT1200/2h	Bulk	43.5(±0.4)	28.9(±0.2)	22.6(±0.4)	5.0(±0.1)
	β-phase	40.3(±0.3)	28.6(±0.4)	23.7(±0.2)	7.4(±0.3)
	γ-phase	49.7(±0.2)	27.7(±0.5)	20.2(±0.3)	2.5(±0.4)

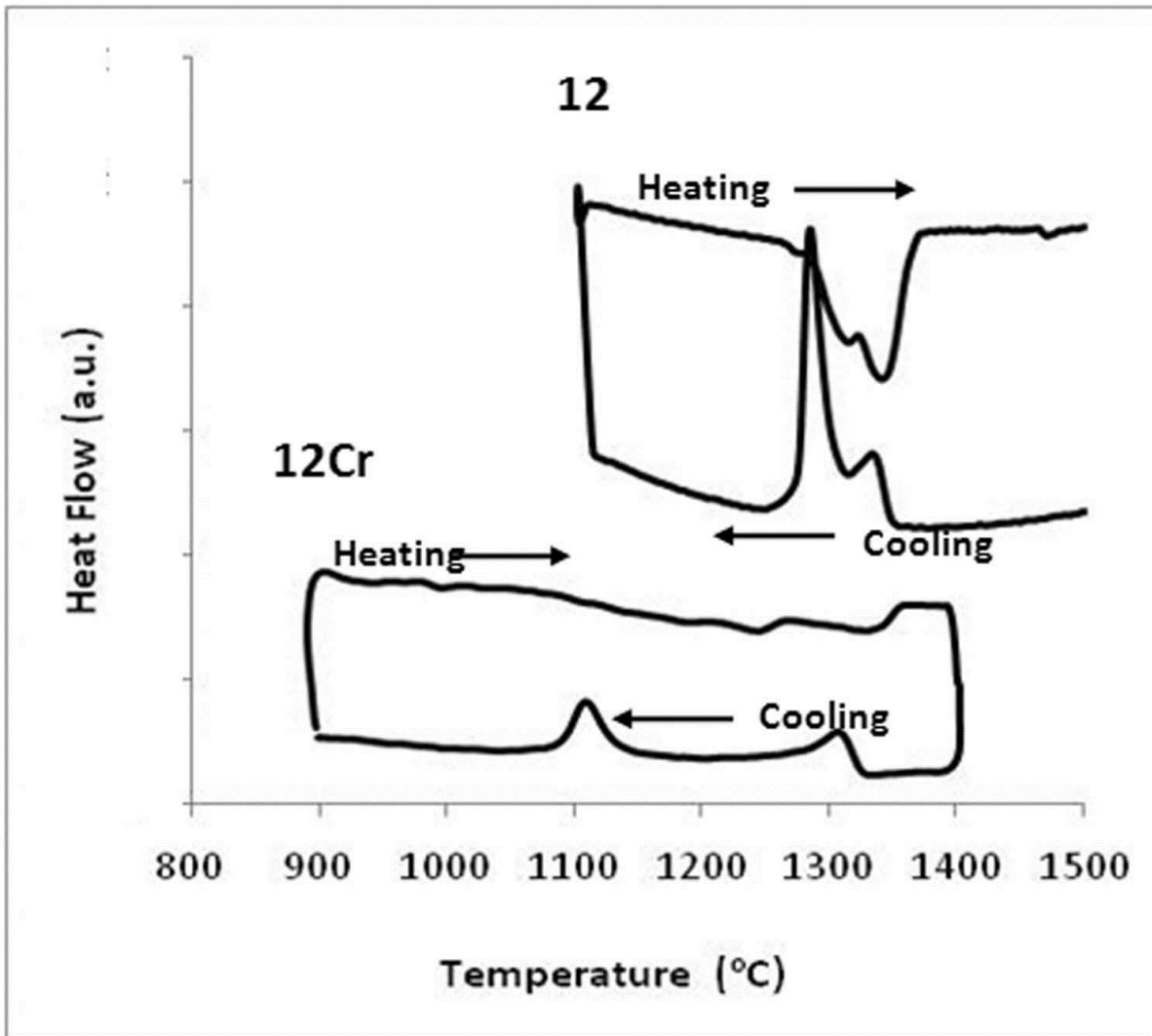


Figure 5-21. DSC profiles of alloys 12 and 12-5Cr [92]

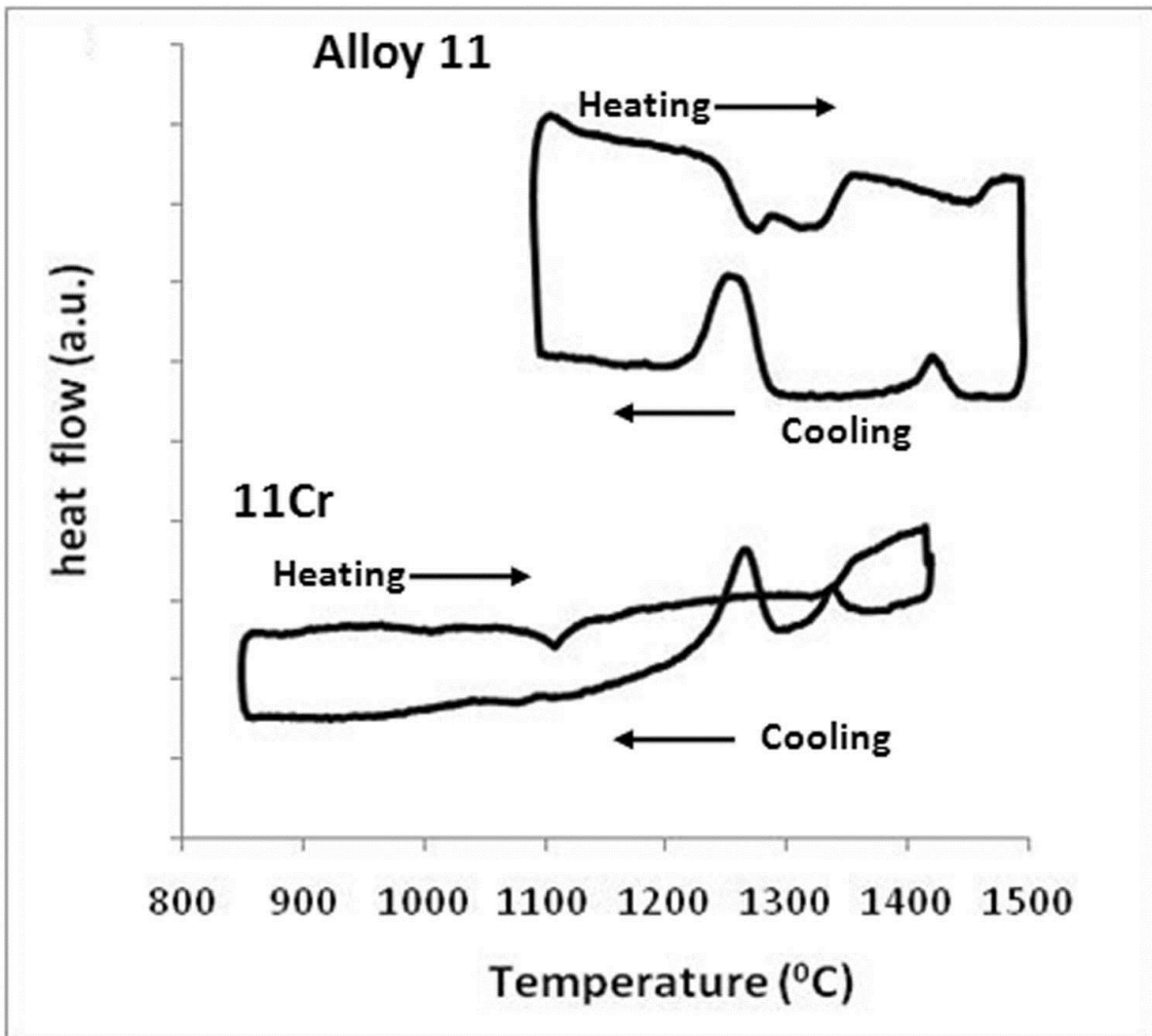


Figure 5-22. DSC profiles of alloys 11 and 11-5Cr

## CHAPTER 6 EFFECT OF BORON ON THE $\beta$ -TO- $\gamma$ PHASE TRANSFORMATION

### 6.1 Introduction

Studies of the  $\beta$ -to- $\gamma$  phase transformation showed that the  $\gamma$ -phase nucleates at the  $\beta$ -phase grain boundaries [96]. In some alloys a second nucleation stage of the  $\gamma$ -phase was also noticed during slow cooling, where it was observed to nucleate at the existing  $\beta/\gamma$  interfaces [96, 97]. But the first nucleation sites for the primary  $\gamma$ -phase were always the  $\beta$ -phase grain boundaries in both solutionized-WQ and slow cooled samples. Also, there is a strong tendency of the  $\gamma$ -phase to exhibit Widmanstätten morphology, not only in fast-cooled microstructures, but also upon holding at, or slow cooling through, high temperatures [25, 96, 97]. The rate of  $\beta$ -to- $\gamma$ -phase transformation is high, so that quenching a solutionized sample from the single  $\beta$ -phase region also leads to the formation of fine Widmanstätten  $\gamma$ -phase nucleating at the  $\beta$ -phase grain boundaries [25].

It can be speculated, based on these studies, that any change in the nucleation of  $\gamma$ -phase could be directly related to a change in the nature of the  $\beta$ -phase grain boundary energy and/or structure. Segregation of solute atoms at boundaries and interfaces has been known to affect phase transformations in various alloy systems. In steels, for example, boron was shown to affect formation of ferrite and increase hardenability [98, 99], whereas phosphorous was shown to increase hardenability [100, 101] and also promote cementite nucleation [101]. Both these effects in steel were attributed to segregation of solute elements at the prior austenite grain boundaries. Although the nucleation of ferrite was inhibited by B and P segregation, the nucleation

of cementite was accelerated by P segregation, with both elements segregating at the austenite grain boundaries. Note, that at the concentrations of B and P used in these studies, both elements were in solution and did not form precipitates.

Boron is known to be a potent surface-active element such that additions of a few ppm of B to steels could completely inhibit ferrite formation and drastically improve hardenability [98]. It was, therefore, thought to be interesting to study the effect of B on the  $\beta$ -to- $\gamma$ -phase transformation in the current study, where an understanding of the effect of B in solution on the  $\beta$ -to- $\gamma$  phase transformation was sought. Thus, small amounts of B were added to these alloys. Thermal and microstructural analysis were performed to obtain the preliminary results of this study.

For the second stage of this study, a new alloy was chosen with a nominal composition of 43Al-40Ti-17Nb (at%) ( alloy 41). The same three different amounts of B were added to it and then the as-cast and solutionized-WQ structures were examined for the analysis of the B effect on the  $\beta$ -to- $\gamma$  phase transformation. The alloys processed were: 41+0.002wt%B, 41+0.005wt%B and 41+0.01wt%B.

## **6.2 Alloys 11-5Cr+xwt%B**

The preliminary studies were performed on alloy 11-5Cr to which three different amounts of B were added. Since alloy 11-5Cr solutionized-WQ microstructure consisted of the fine  $\gamma$ -phase laths only at the  $\beta$ -grain boundaries, the effect of B on  $\gamma$ -nucleation was expected to be noticeable, as compared to other alloys studied that had large amounts of the  $\gamma$ -phase. Thus alloys 11-5Cr+0.002wt%B, 11-5Cr+0.005wt%B and 11-5Cr+0.01wt%B were arc melted and studied in the as-cast and solutionized-WQ state.

### 6.2.1 As-Cast

Optical micrographs from the as-cast samples of all four 11-5Cr+x wt%B alloys are presented in Figure 6-1. Columnar  $\beta$ -phase grains and fine  $\gamma$ -phase laths within the  $\beta$ -grains are visible. Microstructures from all four samples were similar, and no significant changes in the scale or morphology of the phases was observed. Alloy 11-5Cr was shown to have  $\beta$  and  $\gamma$  phases in the microstructure,  $\gamma$ -phase having a much higher phase fraction. The alloys with B do not seem to show any changes in the microstructure when compared to alloy 11-5Cr in the as-cast state.

### 6.2.2 Solutionized-WQ

To study the effect of B on the formation of the  $\gamma$ -phase at fast cooling rates, slices of the 11-5Cr+x wt%B alloys were solutionized at 1400 C for 1hr followed by WQ. Optical micrographs from all samples including alloy 11-5Cr are shown in Figure 6-2. Large millimeter size equiaxed  $\beta$ -phase grains were observed in all alloys. In alloy 11-5Cr+0.01wt%B the grain boundaries were observed to have sharp curvatures in the grain boundaries, suggesting possible pinning. It is possible that at these B contents, borides formed and pinned the grain boundaries during grain growth at the solutionizing temperatures. Note that as the B content of the alloy is increased, the amount of the  $\gamma$ -phase at the  $\beta$  grain boundaries increases. Further, in alloys with B, the  $\gamma$ -phase is observed in the matrix, which was not seen in alloy 11-5Cr. With the increase in B content, the amount of  $\gamma$ -phase in the matrix increases. XRD profiles of powdered samples of the solutionized-WQ alloys are shown in Figure 6-3. It can be said, based on the peak ratios, that the amount of the  $\gamma$ -phase is seen to increase as the B content of

the alloy increases. Alloy 11-5Cr exhibits much more  $\beta$  and  $\alpha$ -phases than  $\gamma$ -phase, however, clearly, the amount of the  $\gamma$ -phase increases in alloy 11-5Cr+0.005wt%B.

### **6.3 Alloys 41 and 41+xwt%B**

The addition of B resulted in an increase in the amount of the  $\gamma$ -phase in alloy 11-5Cr+xwt%B alloys. To investigate the effect of B on  $\gamma$ -phase formation further, an alloy was chosen that upon solutionizing and WQ did not form any  $\gamma$ -phase and the  $\beta$ -phase was fully retained. Then different amounts of B were added to the alloy, and the corresponding effect on the as-cast and solutionized-WQ microstructures was observed. Alloy 41, with a nominal composition of 43Al-40Ti-17Nb, was chosen for this study, and three different amounts of B were added to it resulting in alloys 41+0.002wt%B (41-002B), 41+0.005wt%B(41-002B) and 41+0.01wt%B(41-01B).

#### **6.3.1 As-Cast**

Optical micrographs of the as-cast samples of alloys 41+xwt%B are shown in Figure 6-4. Microstructures look similar, and no significant variation can be observed as the composition of the alloys changes. The  $\gamma$ -phase is present in majority in the microstructure and clearly formed upon cooling from the single  $\beta$ -phase region as the melt cooled down. The phase fraction of the  $\gamma$ -phase in alloy 41 in the as-cast condition is calculated to be >90%, thus any increase in the amount of the  $\gamma$ -phase upon the addition of B would not be noticeable.

#### **6.3.2 Solutionized-WQ**

Slices of the 4 alloys namely 41, 41-002B, 41-005B and 41-01B were solutionized in the single high temperature  $\beta$ -phase region at 1470C for 1 hr followed by WQ. The optical micrographs from the samples thus obtained are shown in Figure 6-5. As can be

seen, the alloy 41 sample exhibits no visible  $\gamma$ -phase at the grain boundaries, which are the preferred nucleation sites for  $\gamma$ -phase formation upon quenching from the high temperature  $\beta$ -phase. In micrographs from the 41-002B and 41-005B samples,  $\gamma$ -phase can be visibly identified at the  $\beta$ -phase grain boundaries. The grain boundaries in 41-005B samples appear to be homogeneously covered with the  $\gamma$ -phase, whereas those in 41-002B have region where there appears to be less  $\gamma$ -phase present or none at all. The sample from alloy 41-01B also shows  $\gamma$ -phase at the  $\beta$ -phase grain boundaries, and possibly within the matrix. The samples exhibit large 3-5 mm size  $\beta$ -phase grains. These samples show 120 degree triple junctions with smoothly curved boundaries, indicating local grain boundary equilibrium, except the 41-01B sample that shows sinuous grain boundaries indicating pinning by borides that could have formed as the boron concentration increased in the alloy.

Samples were studied in the SEM to investigate the presence of any borides in the boron-addition alloys. BSE micrographs from sample 41-01B are shown in Figure 6-6. It was found that there were fine borides present at and near the  $\beta$ -phase grain boundaries. Some borides were also found in the matrix, but in a much lower concentration. The dendritic morphology of the borides indicates that they formed from the liquid during cooling of the arc melted buttons. During solutionizing, as the  $\beta$ -grains grew and the boundaries moved, they became pinned around these boride particles giving rise to the reverse curvatures observed. The 41-002B and 41-005B alloys were also investigated under the SEM, but no borides could be observed. It can then be concluded that at lower concentrations of boron (0.005 wt% B and lower), boron

remains in solution, and at higher concentrations (0.01 wt% B) borides start to form and pin the boundaries.

Figure 6-7 shows the XRD profiles of alloys 41 and 41-01B samples in the solutionized-WQ state. Alloy 41 depicts single  $\beta$ -phase with some possible peaks from the  $\alpha$ -phase that is, again, formed upon quenching of the  $\beta$ -phase. Alloy 41-01B clearly indicates the presence of  $\gamma$ -phase along with the  $\beta$ - and  $\alpha$ -phases.

For further tests on the study of effect of boron on the  $\beta$ -to- $\gamma$ -phase transformation, alloy 41-01B was excluded, due to the presence of borides in its microstructure.

### **6.3.3 DTA Studies**

DTA tests were performed on alloy 41 and 41-005B samples in the as cast condition and cycled several times until consistent profiles were obtained. Figure 8 shows the DTA curves of the fourth and final run on the two samples run at a rate of 10K/min. Comparing the cooling curves on the two DTAs, one major peak can be seen in both the DTAs between 1150 C and 1250 C. However, in alloy 41-005B, a small peak is also observed between temperatures of 1450 C and 1500 C. This peak is much smaller and more diffused in the DTA of alloy 41.

### **6.3.4 Continuous Cooling Heat Treatments**

Heat treatments were then performed to account for the peaks obtained on the DTA cooling curves of the alloys. The first test was performed by solutionizing the samples at 1470 C for 1hr, cooling to 1280 C at 9 K/min followed by immediate WQ. The temperature of 1280 C was chosen as it lies beyond the end of the first peak and before the second DTA peak on the cooling curve of the two DTAs. This test was aimed at understanding the difference in phase transformation in alloys 41 and 41-005B upon

cooling through the first DTA peak. Figure 6-9 a & b show the optical micrographs of the CC1280 heat treated samples of the two alloys. As can be noticed, alloy 41 sample exhibits no coarse second-phase particles at the grain boundaries or in the matrix. On the other hand, alloy 41-005B alloy sample contains coarse particles of a second phase distributed in the matrix and at the grain boundaries. Their coarseness indicates that they formed at high temperature while cooling to 1280 C. Again, the fine needle-like phase is the  $\alpha$ -phase formed upon quenching of the  $\beta$ -phase. Phase fractions of the  $\alpha$ -phase in alloy 4, if any, could not be calculated, and in 41-005B the phase fraction was calculated to be approximately 45%.

To investigate the formation of  $\gamma$ -phase further in the two alloys upon cooling, samples of both alloys were solutionized at 1470 C for 1 hr and cooled to 1050 C at 9 K/min. and then immediately WQ. This temperature lies below the second cooling peak on DTA cooling curve for both alloys. Figure 6-10 shows the optical micrographs of the CC1050 samples of both alloys. Comparing their respective microstructure showed an increase in the  $\gamma$ -phase fraction in both alloys. Coarseness of the  $\gamma$ -phase confirms that it formed at high temperature while cooling to 1050 C from the solutionizing temperature. The phase fraction of the  $\gamma$ -phase in alloy 41 increased to about 78%, whereas in alloy 41-005B it increased approximately from 45% to 74% as the alloys cooled through the second peak. Thus at 1050 C, both alloys contains approximately the same amount of the  $\gamma$ -phase. Apart from the increase in the  $\gamma$ -phase fraction, it can also be noticed that there are two distinct  $\gamma$ -phase morphologies visible in both the CC1050 samples [97]. One of the morphologies is a coarse  $\gamma$ -phase lath (primary  $\gamma$ -phase) that forms at higher temperatures by nucleating at the  $\beta$ -phase grain boundaries.

The other morphology is a finer, lamellar-like structure (secondary  $\gamma$ -phase) that forms at lower temperatures and at the  $\beta/\gamma$  interface of the now existing  $\gamma$ -phase laths (refer Chapter 4).

#### 6.4 Discussion

There are various theories to explain why segregation of solute atoms at grain boundaries could affect phase transformation kinetics such as nucleation,.

It has been shown by this work that boron has a small solid solubility in alloy 41, such that at concentrations of 0.01 wt% B, boride formation was observed. Solute with low solubility have been shown to have a high interfacial activity [98-100]. Lattice accommodation and misfit strain in the matrix, and availability of more open structure at the grain boundaries are known to be the primary reasons for such behavior of solute atoms. Thus, it can be speculated that in the alloys studied, B will tend to have a high affinity for segregation at interfaces.

The solutionized-WQ microstructures clearly indicate that addition and increase in the amount of B facilitates  $\gamma$ -phase formation at the  $\beta$ -phase grain boundaries upon WQ from the single high temperature  $\beta$ -phase region. It is known that the  $\gamma$ -phase nucleates at the  $\beta$ -phase grain boundaries and its nucleation can be affected by altering the grain boundary structure, which in this case is caused by B-segregation at the  $\beta$ -phase grain boundaries. Thus, it can be said that the segregation of B must be taking place at the solutionizing temperatures such that upon quenching, formation of the  $\gamma$ -phase is enhanced. Further increases in the bulk concentration of boron appeared to increase the amount of  $\gamma$ -phase formed upon quenching. It has been reported that segregation of solute elements increases with the bulk concentration of the solute [99, 102].

Consequently the effect of segregation, the enhancement of the  $\gamma$ -phase formation at the  $\beta$ -phase grain boundaries, would also increase. Beyond a certain bulk concentration of B, formation of borides is facilitated, as seen in the 41-01B alloy. Borides eventually pin the  $\beta$ -phase grain boundaries during grain growth at the solutionizing temperatures.

Comparison of the DTAs of alloy 41 and 41-005B indicate a difference in the transformation peaks upon cooling. This was confirmed by the CC1280 heat treatment. As seen in the microstructures of the CC1280 sample of alloy 41-005B, the  $\gamma$ -phase forms at the  $\beta$ -phase grain boundaries and exhibits a Widmanstätten morphology. Segregation of B to  $\beta$ -grain boundaries and increases in the amount of the  $\gamma$ -phase at the grain boundaries is indicative that boron somehow facilitates the formation (nucleation) of  $\gamma$ -phase.

Different studies performed to evaluate the effect of segregation of solute elements on phase transformations have led to various theories explaining the phenomena [98-100, 102, 103]. Ultimately, all such theories suggest that misfit of the solute atoms within the matrix is the primary driving force for segregation, and that such solute segregation at the boundaries takes place due to ability of the solute atom to be able to form different and more favorable chemical bond geometries that are not available within the matrix [99]. This is attributed to the more 'open structure' of the boundaries that facilitate absorption and accommodation of surface-active solute atoms. In steels, this concept of segregation was further extended to explain the inhibition of ferrite formation by B-segregation, and was suggested that boron segregated at the austenite grain boundaries as it lowered the misfit strain and thereby the grain boundary energy. This process would then lead to a lowering of the thermodynamic barrier to

ferrite nucleation and inhibit nucleation [98-100]. Clearly, this cannot be applied in the present case as segregation of boron enhances the  $\gamma$ -phase nucleation. Thus, grain boundary energy considerations alone cannot lead to a complete explanation of the phenomena, and taking into account the effect of segregation on the grain boundary structure therefore becomes important [100, 103].

Multiple studies have been performed on segregation and its effect on grain boundary structures. Different type of boundaries were studied and was shown that more segregation occurred at higher energy boundaries, perhaps due to their more open and disordered structure and higher misorientation. It was also shown that available free volume at grain boundaries is a crucial factor in deciding the amount of segregation in addition to the grain boundary energy, as no segregation of P was observed at coherent boundaries as opposed to incoherent ones that exhibited segregation in Ni-Cr steel [100, 101]. Further it was shown, that the amount of segregation can vary not only with the type of grain boundary in question, but also at different points along the same boundary depending on its local defect structure (facets, dislocations etc.) and the surrounding bulk solute concentration. This phenomenon can be observed if one compares the solutionized-WQ microstructures of alloys 41-002 and 41-005B. Although in the latter alloy continuous formation of the grain boundary  $\gamma$ -phase can be seen, it seems to be broken and discontinuous at certain regions of the  $\beta$ -phase grain boundary in the former alloy. This observation can be explained as the alloy 41-005B has more bulk boron concentration, and there is higher segregation to grain boundaries, given the same time at temperature as compared to 41-002B. Thus, for the

same amount of segregation to occur at all points, 41-002 may require higher temperature and/or time at temperature.

Comparing all available theories, the one proposed by McMahon for ferrite nucleation seems to be appropriate in explaining the present results [99, 100]. It suggests that certain regions of the grain boundary can provide more effective nuclei than others in initiating phase formation. The arrangement of atoms in such regions would be more favorable to the formation of nuclei of the new phase, such that a slight disturbance or change in atom position (climb/glide) would produce an atomic arrangement characteristic of the new phase. This fresh nucleus would then grow in the usual manner if it possessed a supercritical nucleus size. In case of B-segregation and its effect on hardenability in steel it was suggested that if the segregant atoms occupy positions within these grain boundary regions and stabilize the grain boundary structure (such as forming Cottrell atmospheres). Alternatively, they could reduce the effectiveness of these regions in providing potential nuclei, thereby inhibiting ferrite formation. A study done on the effect of segregation on boundary dislocation structure revealed that segregation has a strong influence on the dislocation structure formed [ref]. Thus, depending on which dislocation structure is favored, the ease with which a potential nucleus region turns into a supercritical nucleus of the new phase will be affected.

The CC1050 heat treatments revealed that at 1050 C, both alloys 41 and 41-005B have approximately the same  $\gamma$ -phase fraction. Thus B does not affect the tie line at this temperature. However, it is clear that it affects the kinetics by enhancing nucleation. Both these samples exhibit two different  $\gamma$ -phase morphologies that have been reported

before. It appears that segregation of B significantly affects only the high angle, high energy  $\beta$ -phase grain boundaries, thereby affecting the nucleation of the primary  $\gamma$ -phase laths [100, 103] that nucleate at the  $\beta$ -phase boundaries. Once the primary  $\gamma$ -phase forms, the secondary  $\gamma$ -phase nucleates on the existing  $\beta/\gamma$  interfaces.

The above study on the effect of B is preliminary in nature. Detailed microanalysis to detect the presence and position of B in the grain boundary is required. More significantly, the exact nature of the effect of B segregation, whether it be changed in free volume per unit atom, changed in grain boundary energy, or changed in dislocation structure, all need to be studied in detail to achieve a better understanding of this phenomena in the current range of alloys.

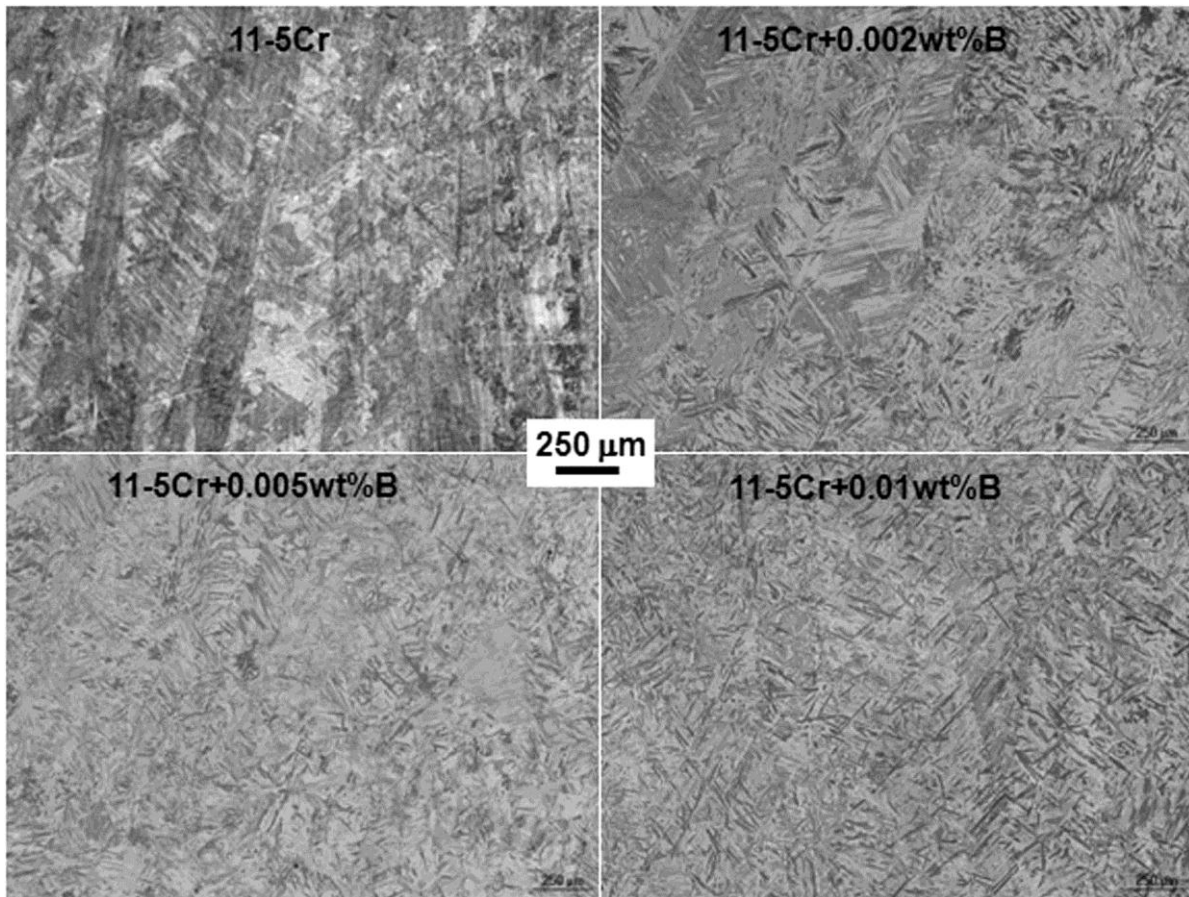


Figure 6-1. Optical micrographs of alloys 11-5Cr and 11-5Cr+xwt%B in the as-cast condition

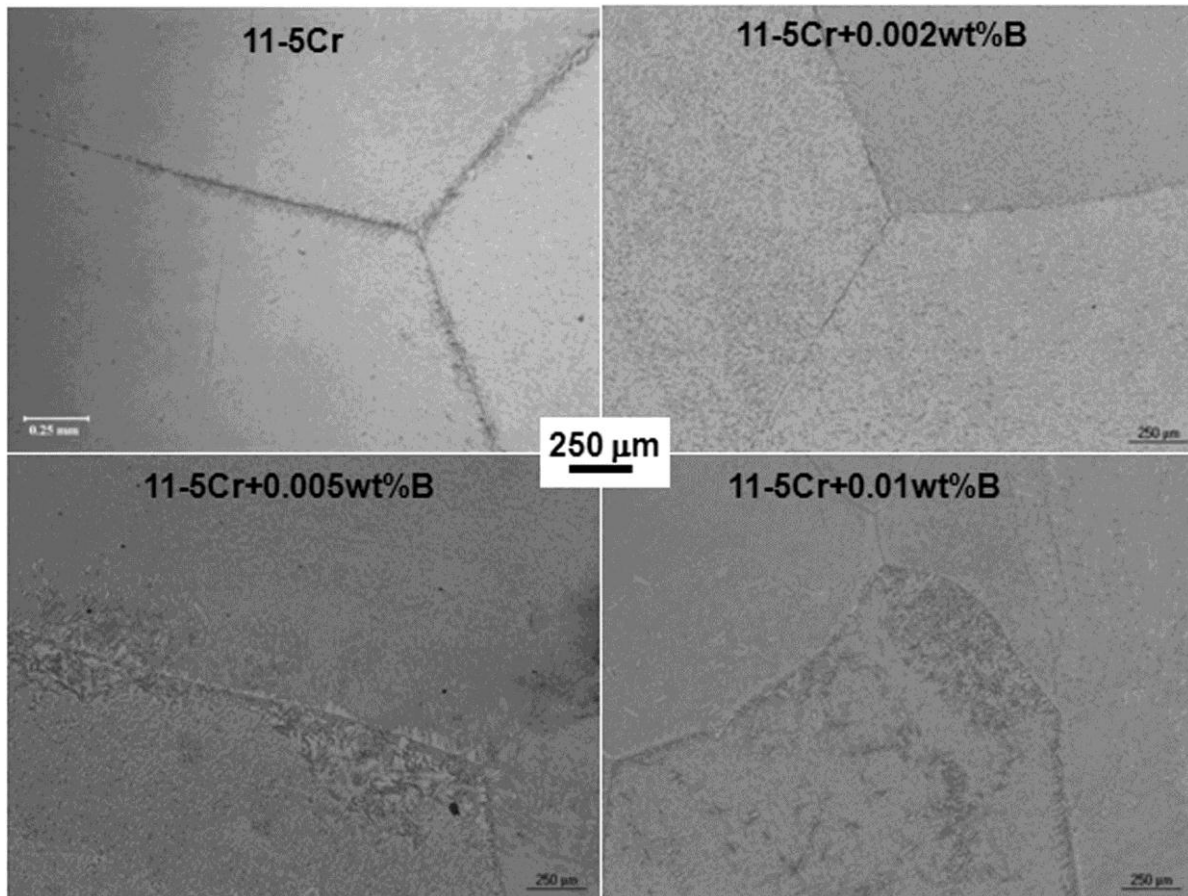


Figure 6-2. Optical micrographs of alloys 11-5Cr and 11-5Cr+xwt%B in the solutionized-WQ state

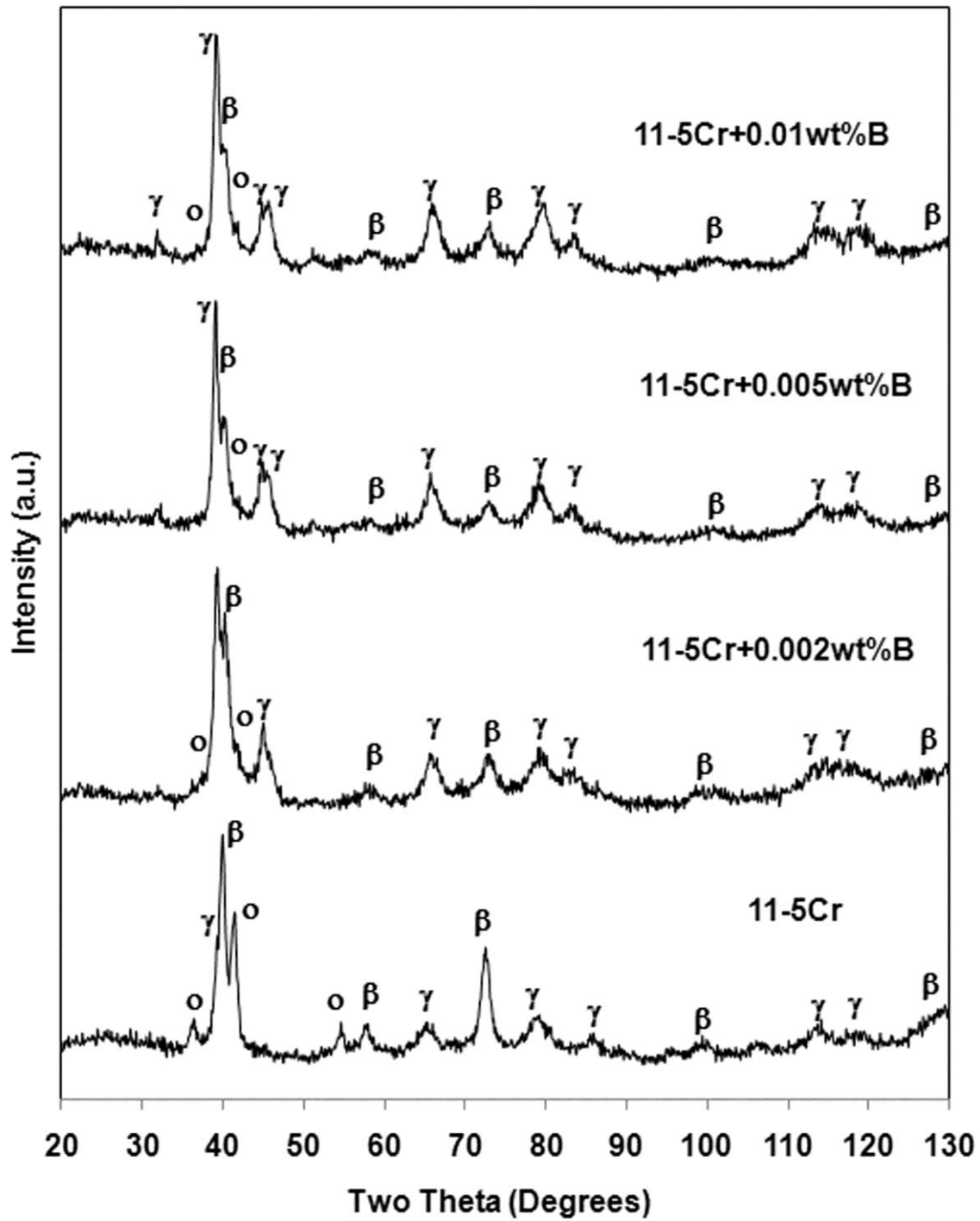


Figure 6-3. XRD profiles of alloys 11-5Cr and 11-5Cr+xwt%B in the solutionized-WQ condition

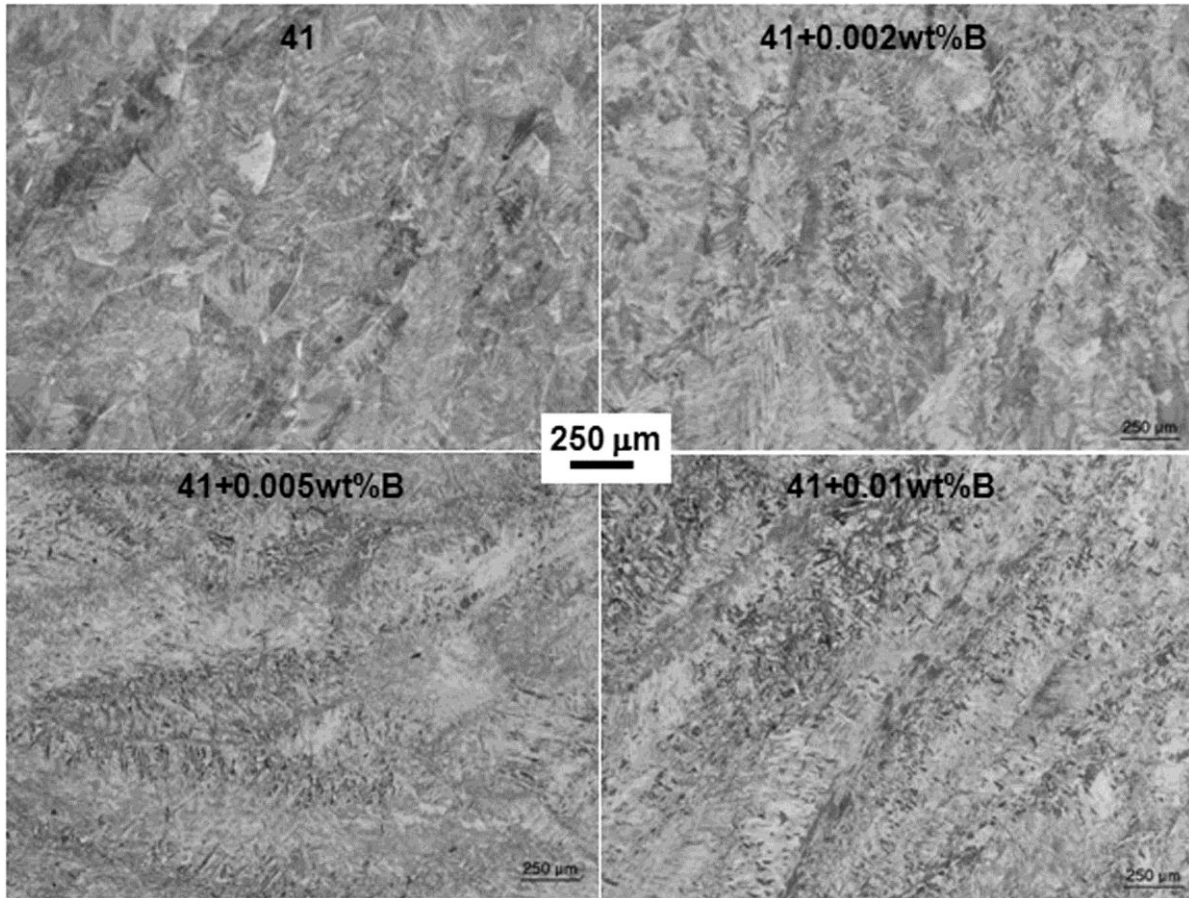


Figure 6-4. Optical micrographs of alloys 41 and 41+xwt%B in the as-cast condition

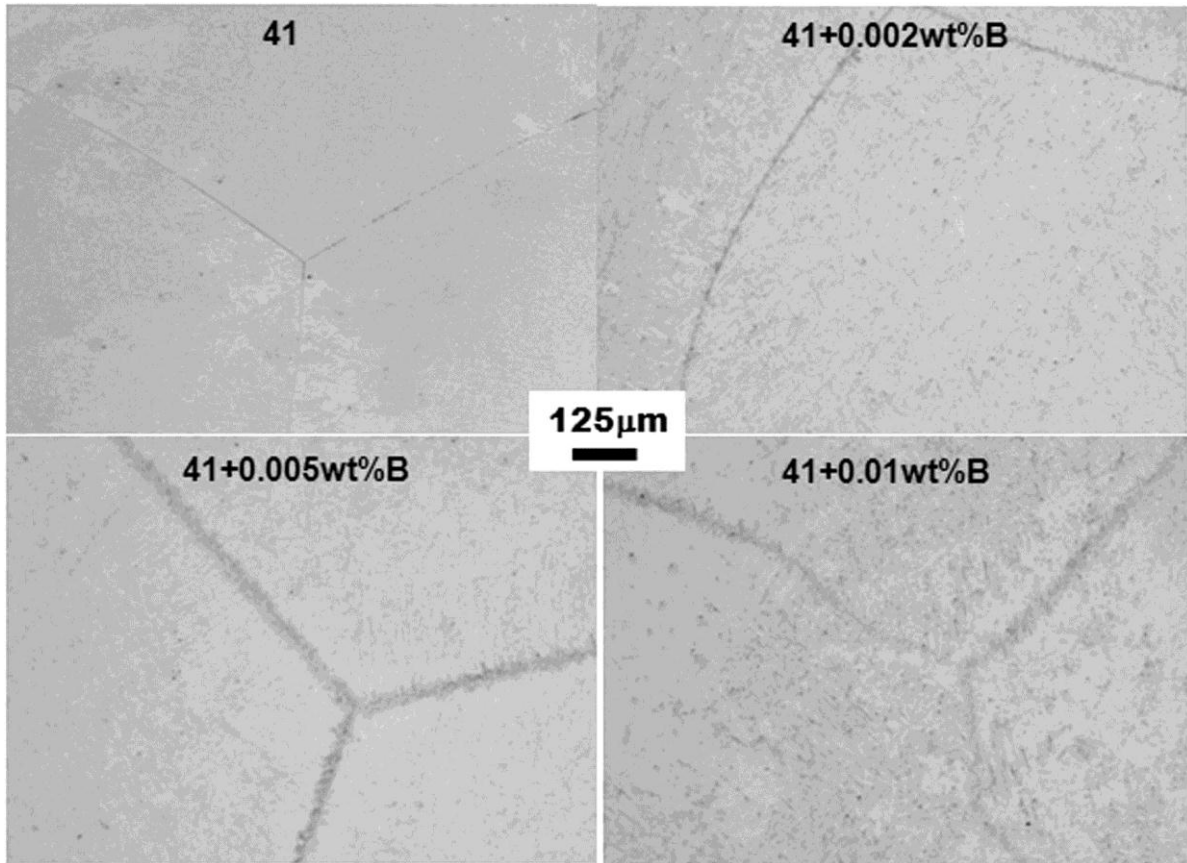


Figure 6-5. Optical micrographs of alloys 41 and 41+xwt%B in the solutionized-WQ state

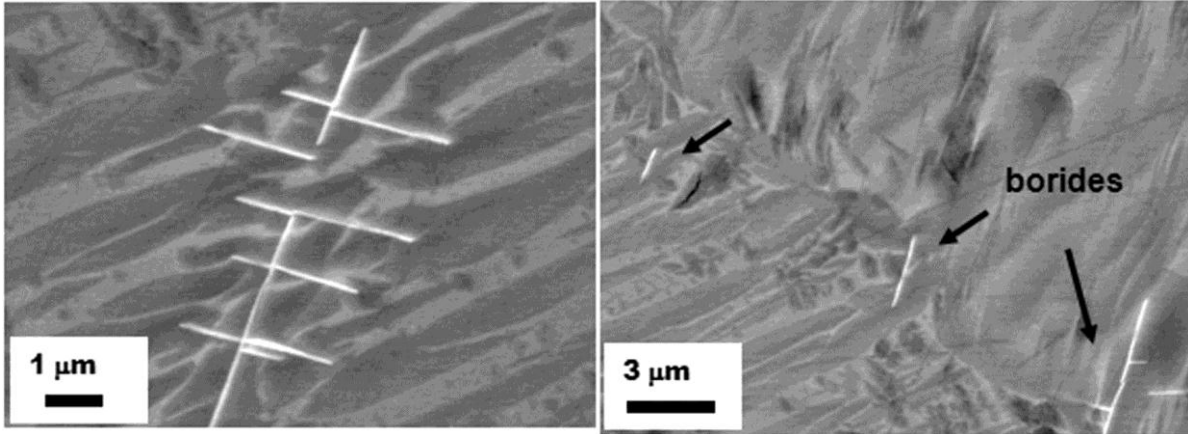


Figure 6-6. BSE micrographs from alloy 41+0.01 wt%B in the solutionized-WQ state, showing presence of fine borides

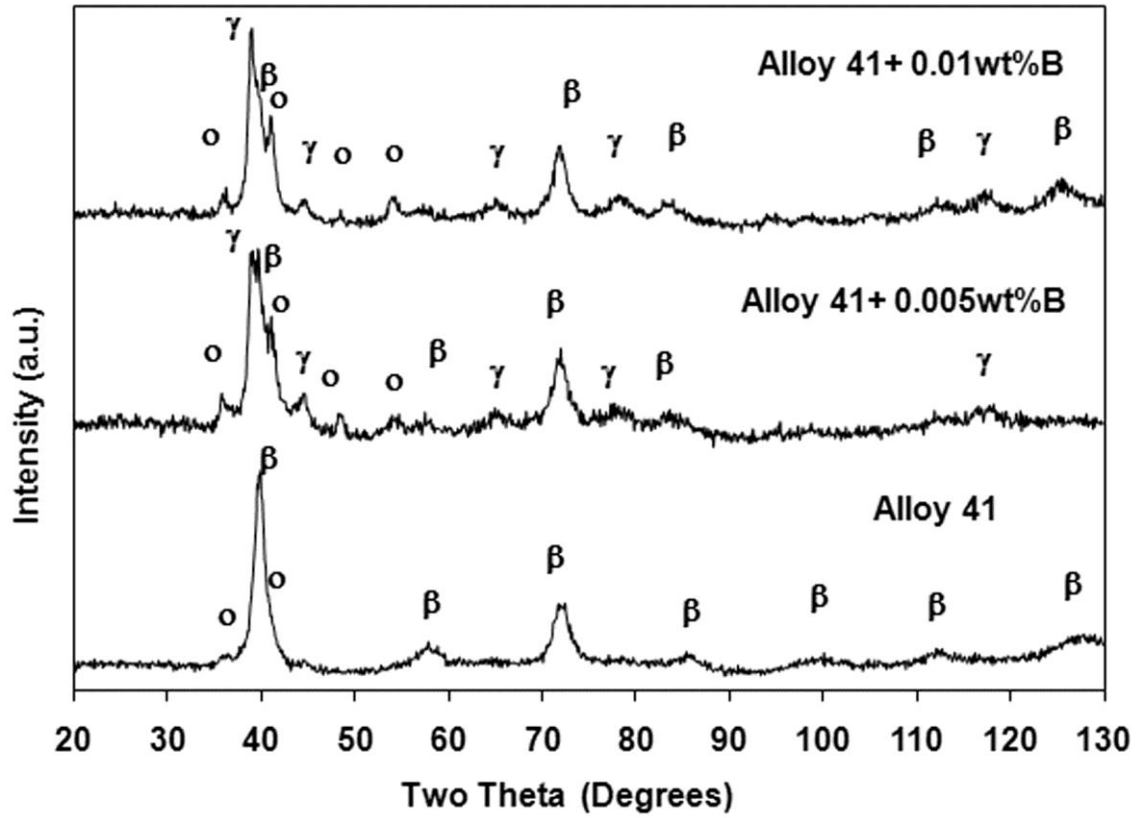


Figure 6-7. XRD profiles of alloys 41 and 41+xwt%B in the solutionized-WQ condition

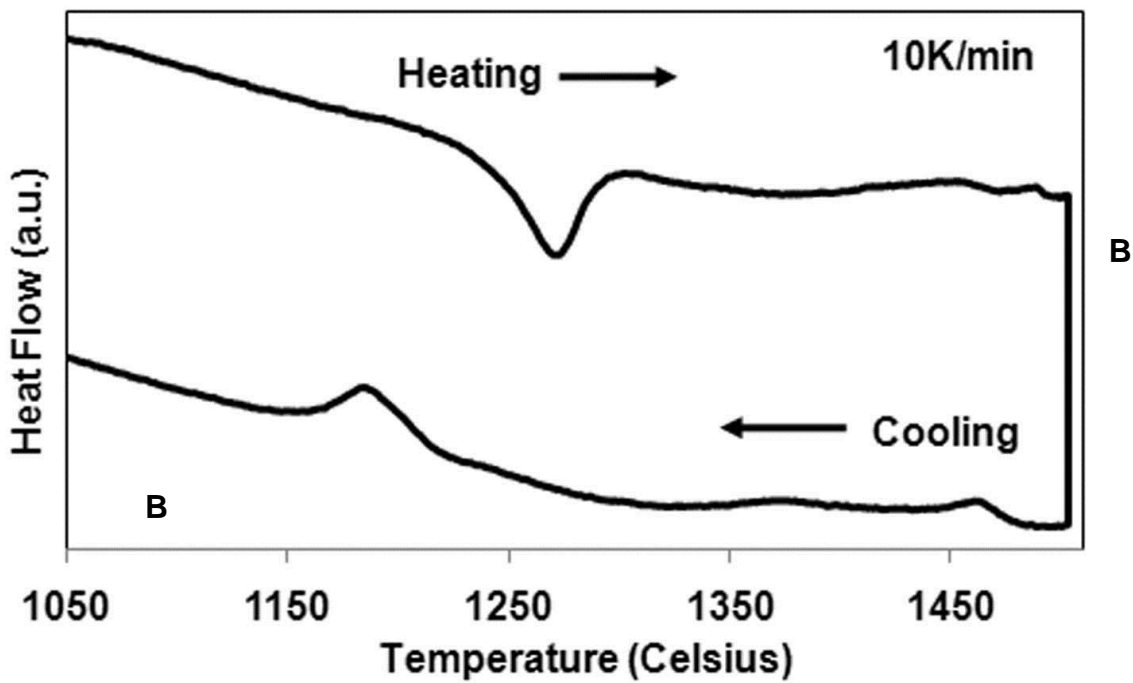
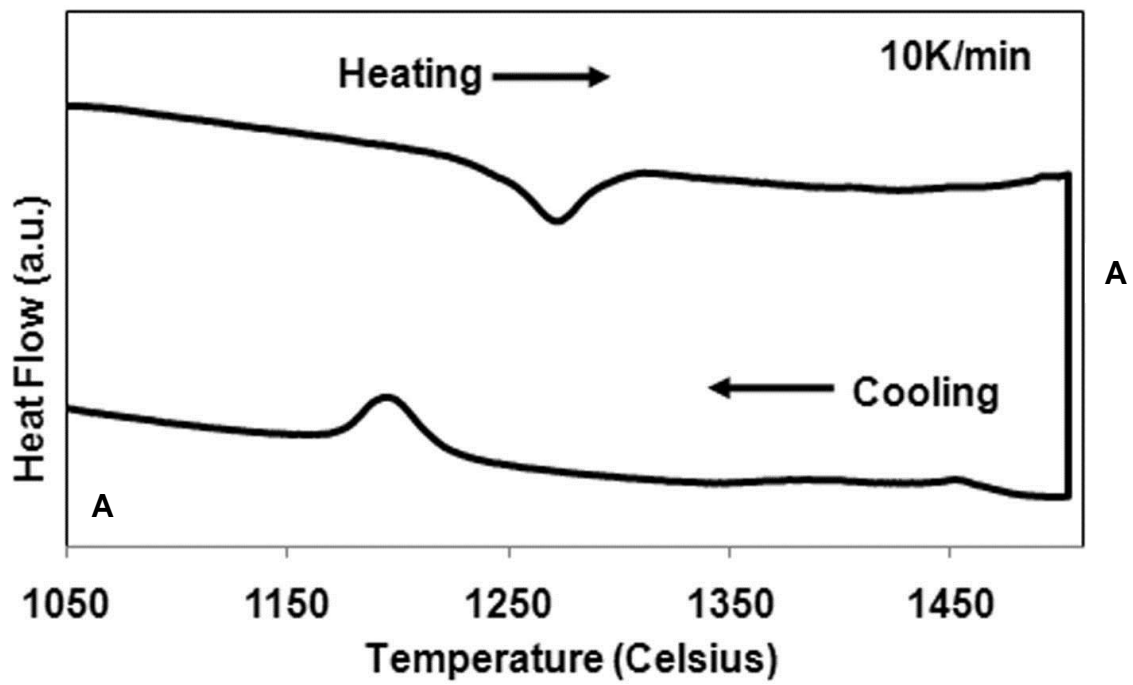


Figure 6-8. DSC plots. A) Alloy 41. B) Alloy 41+0.005wt%B

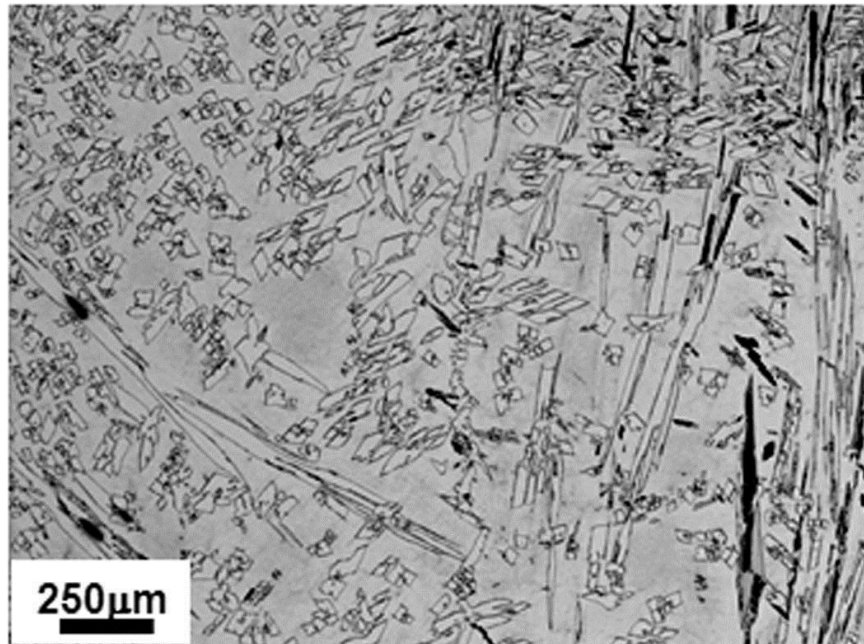
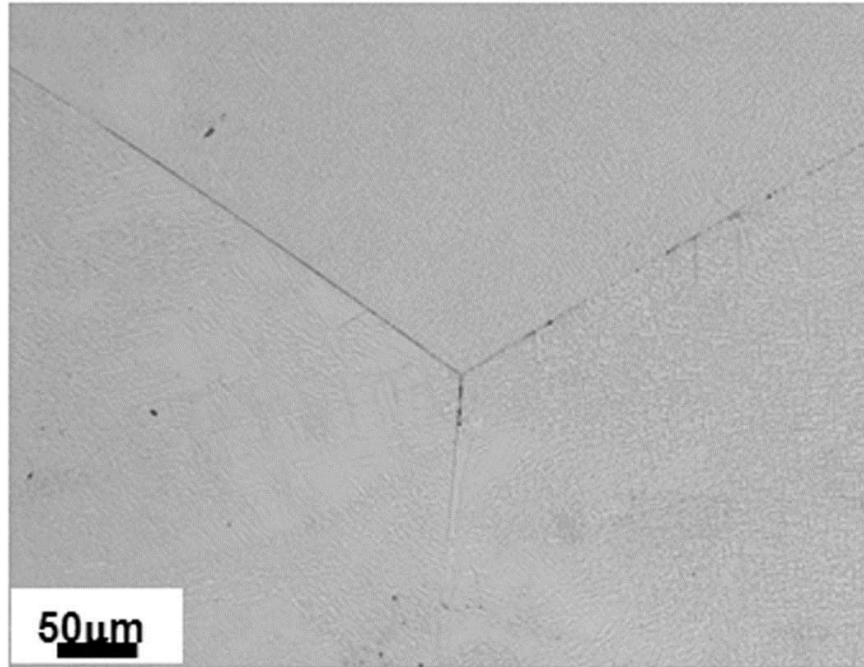


Figure 6-9. Optical micrographs from CC1280 samples. A) Alloy 41. B) Alloy 41+0.005wt%B

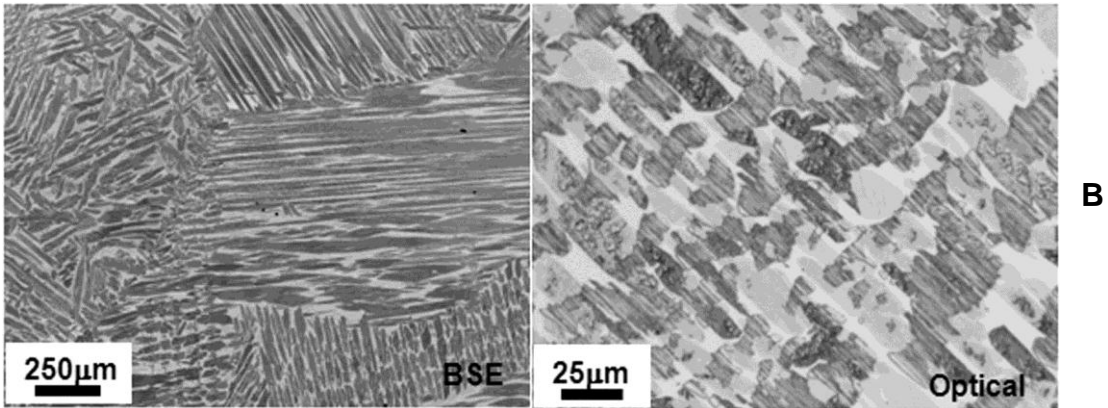
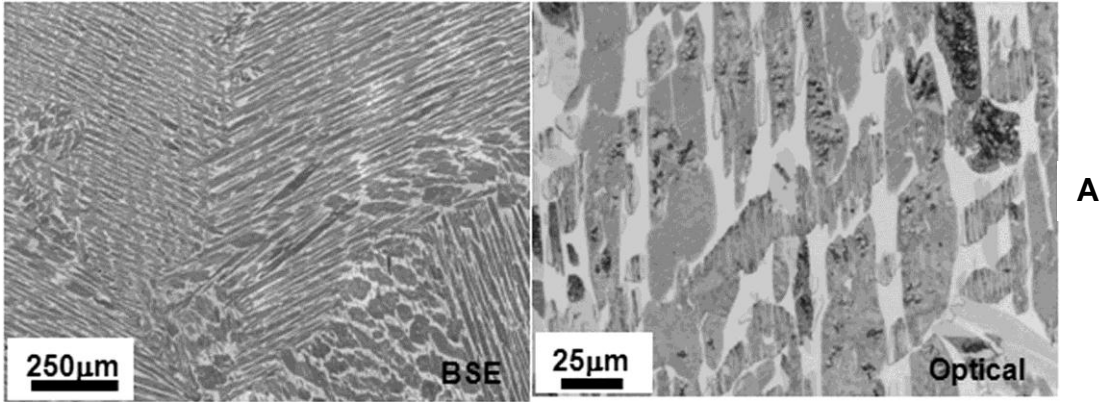


Figure 6-10. Micrographs from CC1050 samples. A) Alloy 41. B) Alloy 41+0.005 wt%B

## CHAPTER 7 SUMMARY

The  $\beta$  to  $\gamma$  phase transformation was studied in high-Nb TiAlNb alloys through the examination of microstructures, compositions, phase morphologies and transformation temperatures. This study was motivated by the results presented in the past regarding the potential of high-Nb  $\gamma+\sigma$  alloys for application in the aerospace turbine engines and their inability to quench the  $\beta$ -phase to room temperature for further aging due to the inevitable formation of the  $\gamma$ -phase. Only a specific region of the ternary was chosen for alloy selection. Chosen alloys were required to have (1) single  $\beta$ -phase region at high temperatures, (2) have  $\gamma$  as the first phase forming from the  $\beta$ -phase upon cooling, (3) have high Al content for oxidation resistance, (4) have  $\gamma+\sigma$  microstructure at lower temperatures. In this study the  $\beta$ -to  $\gamma$ -phase transformation was studied upon cooling and the effect of cooling rates, grain boundaries, free surfaces and composition were studied. Further, effect of addition of Cr-a  $\beta$ -stabilizer and B-a segregant were studied in an attempt to prevent the formation of the  $\gamma$ -phase upon quenching  $\beta$ .

The results showed that the formation of the  $\gamma$ -phase could not be prevented upon cooling the  $\beta$ -phase even at high cooling rates such as water-quenching. It was found that  $\beta$ -phase grain boundaries were the primary nucleation sites for the formation of the  $\gamma$ -phase. The  $\gamma$ -phase was observed to form with Widmanstätten morphology. Tests performed on single crystal samples showed that in the absence of grain boundaries, free surfaces served as primary nucleation sites. It has been suggested that the orientation relationship between  $\beta$  and  $\gamma$ , the ability of the  $\gamma$ -phase to form at compositions close to that of the  $\beta$ -phase at high cooling rates and the instability of the

$\beta$ -phase at lower temperatures due to super-saturation are main reasons for the fast kinetics of the  $\beta$ -to  $\gamma$ -phase transformation. Further, sequence of transformations occurring upon quenching the  $\beta$ -phase was evaluated under the TEM. It was found that as the  $\beta$ -phase cooled during quenching, the  $\gamma$ -phase nucleated first and at lower temperatures the metastable  $\sigma$ -phase formed. Ordering of the  $\beta$ -phase was found to occur before the formation of the  $\sigma$ -phase. Alloys where  $\sigma$  was the first phase to form from the  $\beta$ -phase upon cooling, complete quenching of the  $\beta$ -phase was observed. It was attributed to the high amount of Nb diffusion required for  $\sigma$  formation and its complex crystal structure. These factors make the formation of the  $\sigma$ -phase a much slower process such that at high cooling rates such as WQ its formation can be completely inhibited.

Alloy 11, according to the latest thermodynamic calculations, is expected to exhibit a two phase  $\gamma+\sigma$  microstructure and the DSC profile of the alloy indicated two distinct transformations upon cooling. However, elaborate heat treatment tests and extensive microstructural analysis using optical, SEM and TEM confirmed that both transformations upon cooling were related to the formation of  $\gamma$ -phase. The  $\gamma$ -phase was observed to nucleate at two distinct stages, (1) at  $\beta$ -phase grain boundaries with a coarse Widmanstätten morphology and (2) fine plate-like morphology nucleating at the interface of the Widmanstätten  $\gamma$ -laths and the  $\beta$ -matrix. The Widmanstätten laths were shown to be single crystal laths and not composed of several finer laths as is the case in  $\alpha_2+\gamma$  alloys. A detailed analysis of the plate-like morphology was performed under TEM and was shown that it consisted of alternate  $\gamma$  and  $\beta$  phase lamellae. Upon cooling,

the  $\beta/\gamma$  interfaces serve as the nucleation sites for fine  $\gamma$ -phase plates. These plates shoot into the  $\beta$ -matrix thereby trapping the  $\beta$ -phase in between and giving rise to the lamellar-like morphology. No  $\sigma$ -phase was observed in samples slow cooled to room temperatures. However, aging of a quenched metastable  $\beta$ -phase led to the formation of the  $\gamma+\sigma$  microstructure as expected by the phase diagram calculations. Thus low driving force for the  $\sigma$ -phase nucleation upon cooling the  $\beta$ -phase was suggested to be the reason for the absence of  $\sigma$ -phase in slow cooled samples.

Addition of Cr, a  $\beta$ -stabilizer was found to reduce the kinetics of the  $\gamma$ -phase upon quenching. Addition of just 1.5at% Cr was found to considerably reduce the phase fraction of the  $\gamma$ -phase that formed upon quenching in alloys 11 and 12. Even though fine laths of the  $\gamma$ -phase were found to be present in the solutionized-WQ samples, their presence was limited to the  $\beta$ -phase grain boundaries with very limited growth into the bulk matrix. Compositional analysis of heat treated samples showed that Cr had a strong tendency to partition into the  $\beta$ -phase. The partitioning of Cr into  $\beta$ -phase reduced the kinetics of  $\gamma$ -phase growth such that the fine laths that nucleated at the  $\beta$ -grain boundaries were unable to grow into the matrix thereby reducing the observed phase fraction of the  $\gamma$ -phase. DSC analysis of the alloys indicated that Cr also stabilized  $\beta$ -phase in alloy 11 to lower temperatures.

Effect of B segregation at  $\beta$ -grain boundaries was studied on selected alloys. Small amounts of B were added such that B remained in solution. It was found that addition of more than 0.005wt%B caused the formation of borides that pinned the  $\beta$ -grain boundaries during solutionizing. Further, microstructural and XRD analysis

showed that in both alloys 11+5Cr and 41, addition of B increased the amount of the  $\gamma$ -phase formed upon quenching. Based on DSC profiles and microstructural analysis of heat treated samples it was suggested that B increased the nucleation rate of the  $\gamma$ -phase at the  $\beta$ -grain boundaries during WQ.

The results of this study are useful in understanding the nature and kinetics  $\beta$  to  $\gamma$ -phase transformation in TiAlNb alloys. Few results from the studies on alloys 11 and 12 were employed in the optimization of the TiAlNb ternary by Cupid et.al. Only few studies have been performed on TiAlNb alloys in the past and a limited understanding of the microstructural evolution in these alloys is available. The  $\beta$ -to  $\gamma$ -phase transformation is different in many ways from the  $\alpha$ -to  $\gamma$ -phase transformation that has been studied extensively in the recent past. The results of this study will be useful in controlling the microstructure in the high-Nb  $\gamma+\sigma$  alloys in future.

## CHAPTER 8 FUTURE WORK

The current study provided an overview of the nature of the  $\beta$ -to  $\gamma$ -phase transformation in high-Nb TiAlNb alloys and effect of alloying additions on it. The focus of this research was to obtain an understanding of the transformation in order to be able to suppress it during quenching of the  $\beta$ -phase. However, a detailed analysis of many aspects could not be performed due to lack of time and/or resources. TiAlNb is a complex system with many equilibrium and metastable phases. An understanding of all these phases and phase transformations is a lengthy and time consuming process. It is important to select an area of interest and focus time and resources on it to obtain maximum output. During the course of this research, many questions were encountered some of which still remain unanswered and would prove to be interesting areas of research for future work. The following are some of such aspects are:

1. Determine the effect of increase in  $\beta$ -grain boundary area on the two-phase nucleation of the  $\gamma$ -phase.  $\gamma$ -phase nucleates in two stages because of the exhaustion of the primary nucleation sites ( $\beta$ -grain boundaries). It would be interesting to study the effect of increase in  $\beta$ -grain boundary area by reducing the grain size, on the  $\gamma$ -nucleation process.
2. Determine the  $\beta/\gamma$  interface. It is known that  $\beta$  and  $\gamma$ -phases share an orientation relationship. However, the  $\beta/\gamma$  interface has not been identified. Knowledge of the interface plane would help in further understanding the energy and nature of the interface and the phase morphologies.
3. Obtain microstructural evidence of the nucleation of the  $\gamma$ -phase at  $\alpha$ -phase. Based on some heat treatments and microstructural analysis in this study, it has been suggested that upon aging a quenched  $\beta$ -phase,  $\gamma$ -phase nucleates at the  $\alpha$ -phase plates. However, no microstructural evidence was noticed. The determination of this phenomenon would help in refining the aged microstructures.
4. Determine the presence and segregation of B at  $\beta$ -grain boundaries. It has been shown in this study that addition of B enhances the nucleation rate of the  $\gamma$ -phase upon quenching. However, detailed atomistic analysis of B segregation is required

to fully understand the effect of B and its effect on grain boundary energy and/or structure.

## LIST OF REFERENCES

- [1] J.C.L. T.J. Jewett, N.R. Bonda, L.E. Setzman, K.C. Hsieh, Y.A. Chang, J.H. Perepezko, Experimental determination of the Ti-Nb-Al phase diagram at 1200C.
- [2] A. Hellwig, M. Palm, G. Inden, Phase equilibria in the Al-Nb-Ti system at high temperatures, *Intermetallics*, 6 (1998) 79-94.
- [3] G.L. Chen, X.T. Wang, K.Q. Ni, S.M. Hao, J.X. Cao, X. Zhang, Investigation on the 1000, 1150 and 1400 degrees C isothermal section of the Ti-Al-Nb system, *Intermetallics*, 4 (1996) 13-22.
- [4] J.J. Ding, S.M. Hao, Reply to the "Comment on 'Investigation on the 1000, 1150 and 1400 degrees C isothermal section of the Ti-Al-Nb system'" - Part II. Modification of 1000 and 1150 degrees C isothermal sections of the Ti-Al-Nb system, *Intermetallics*, 6 (1998) 329-334.
- [5] T.J. Jewett, Investigation on the 1000, 1150 and 1400 degrees C isothermal section of the Ti-Al-Nb system - Comment, *Intermetallics*, 5 (1997) 157-159.
- [6] K.J. Leonard, J.C. Mishurda, V.K. Vasudevan, Phase equilibria at 1100 degrees C in the Nb-Ti-Al system, *Mat Sci Eng a-Struct*, 329 (2002) 282-288.
- [7] K.J. Leonard, V.K. Vasudevan, Phase equilibria and solid state transformations in Nb-rich Nb-Ti-Al intermetallic alloys, *Intermetallics*, 8 (2000) 1257-1268.
- [8] F.E. D.T. Hoelzer, An investigation of phase stability in the ternary Niobium-Titanium-Aluminum system, *High temperature Niobium alloys*, The Minerals, Metals and Materials Society, (1991).
- [9] A.R. L.A. Bendersky, W.J. Boettinger, Phase transformations in the (Ti,Nb)<sub>3</sub>Al section of the Ti-Al-Nb system system I: Microstructural predictions based on a subgroup relations between phases, *Acta Metallurgica and Materialia*, 42 (1994).
- [10] W.J.B. L.A. Bendersky, Phase transformations in the (Ti,Nb)<sub>3</sub>Al section of the Ti-Al-Nb system II: Experimental TEM study of microstructures, *Acta Metallurgica and Materialia*, 42 (1994).
- [11] W.J.B. L.A. Bendersky, A. Roytburd, Coherent precipitates in the BCC/Orthorhombic two-phase field of the Ti-Al-Nb system, *Acta Metallurgica and Materialia*, 39 (1990) 32.
- [12] H. Nakamura, M. Takeyama, Y. Yamabe, M. Kikuchi, Phase-Equilibria in TiAl Alloys Containing 10 Percent and 20 at Percent Nb at 1473-K, *Scripta Metallurgica Et Materialia*, 28 (1993) 997-1002.

- [13] X.T.W. G.L. Chen, K.Q. Ni, S.M. Hao, J.X. Cao, J.J. Ding, X. Zhang, Investigation on the 1000, 1150 and 1400C isothermal section of the Ti-Al-Nb system, *Intermetallics*, (1994) 13-22.
- [14] I. Ohnuma, Y. Fujita, H. Mitsui, K. Ishikawa, R. Kainuma, K. Ishida, Phase equilibria in the Ti-Al binary system, *Acta Mater*, 48 (2000) 3113-3123.
- [15] V. Raghavan, Al-Nb-Ti (Aluminum-Niobium-Titanium), *Journal of phase equilibria and diffusion*, (2005).
- [16] S.G. K. Kaltenbach, .G. Pinatti, K. Schulze, E.T. Henig, A contribution to the ternary system Al-Nb-Ti, *Zeitschrift Fur Metallkunde*, 80 (1989).
- [17] U.R. Kattner, W.J. Boettinger, Thermodynamic Calculation of the Ternary Ti-Al-Nb System, *Mat Sci Eng a-Struct*, 152 (1992) 9-17.
- [18] A. Zdziobek, M. Durandcharre, J. Driole, F. Durand, Experimental Investigation of High-Temperature Phase-Equilibria in the Nb-Al-Ti System, *Zeitschrift Fur Metallkunde*, 86 (1995) 334-340.
- [19] C. Servant, I. Ansara, Thermodynamic assessment of the Al-Nb-Ti system, *Ber Bunsen Phys Chem*, 102 (1998) 1189-1205.
- [20] C. Servant, I. Ansara, Thermodynamic assessment of the Al-Nb system, *J Chim Phys Pcb*, 94 (1997) 869-888.
- [21] C. Servant, I. Ansara, Thermodynamic modelling of the order-disorder transformation of the orthorhombic phase of the Al-Nb-Ti system, *Calphad*, 25 (2001) 509-525.
- [22] D.M. Cupid, O. Fabrichnaya, O. Rios, F. Ebrahimi, H.J. Seifert, Thermodynamic re-assessment of the Ti-Al-Nb system, *Int J Mater Res*, 100 (2009) 218-233.
- [23] D.M. Cupid, O. Fabrichnaya, F. Ebrahimi, H.J. Seifert, Thermodynamic assessment of the Al-Mo system and of the Ti-Al-Mo System from 0 to 20 at.% Ti, *Intermetallics*, 18 (2010) 1185-1196.
- [24] D.M. Cupid, Thermodynamic assessment of the Ti-Al-Nb, Ti-Al-Cr and Ti-Al-Mo systems, PhD Dissertation, University of Florida, Gainesville, (2009).
- [25] O. Rios, S. Goyel, M.S. Kesler, D.M. Cupid, H.J. Seifert, F. Ebrahimi, An evaluation of high-temperature phase stability in the Ti-Al-Nb system, *Scripta Mater*, 60 (2009) 156-159.
- [26] F. Ebrahimi, O. Rios, S. Goyel, M.S. Kesler, D.M. Cupid, H.J. Seifert, An evaluation of high-temperature phase stability in the Ti-Al-Nb system, *Scripta Mater*, 60 (2009) 156-159.

- [27] F. Ebrahimi, O. Rios, D.M. Cupid, H.J. Seifert, Characterization of the invariant reaction involving the L, eta, gamma and sigma phases in the Ti-Al-Nb system, *Acta Mater*, 57 (2009) 6243-6250.
- [28] X.H. Wu, Review of alloy and process development of TiAl alloys, *Intermetallics*, 14 (2006) 1114-1122.
- [29] A. Dlouhy, K. Kucharova, Creep and microstructure of near-gamma TiAl alloys, *Intermetallics*, 12 (2004) 705-711.
- [30] S. Bystrzanowski, A. Bartels, H. Clemens, R. Gerling, F.P. Schimansky, G. Dehm, H. Kestler, Creep behaviour and related high temperature microstructural stability of Ti-46Al-9Nb sheet material, *Intermetallics*, 13 (2005) 515-524.
- [31] S.R. Dey, A. Hazotte, E. Bouzy, Crystallography and phase transformation mechanisms in TiAl-based alloys - A synthesis, *Intermetallics*, 17 (2009) 1052-1064.
- [32] S.R. Dey, A. Hazotte, E. Bouzy, S. Naka, Development of Widmanstatten laths in a near-gamma TiAl alloy, *Acta Mater*, 53 (2005) 3783-3794.
- [33] D. Srivastava, D. Hu, I.T.H. Chang, M.H. Loretto, The influence of thermal processing route on the microstructure of some TiAl-based alloys, *Intermetallics*, 7 (1999) 1107-1112.
- [34] S. Zghal, M. Thomas, S. Naka, A. Finel, A. Couret, Phase transformations in TiAl based alloys, *Acta Mater*, 53 (2005) 2653-2664.
- [35] H. Clemens, A. Bartels, S. Bystrzanowski, H. Chladil, H. Leitner, G. Dehm, R. Gerling, F.P. Schimansky, Grain refinement in gamma-TiAl-based alloys by solid state phase transformations, *Intermetallics*, 14 (2006) 1380-1385.
- [36] C.T. Yang, C.H. Koo, Improving the microstructure and high temperature properties of the Ti-40Al-16Nb alloy by the addition of a minor Sc or La-rich Misch metal, *Intermetallics*, 12 (2004) 235-251.
- [37] P.R. Munroe, I. Baker, Solute partitioning in TiAl/Ti3Al alloys, *Scripta Mater*, 41 (1999) 1295-1299.
- [38] M.A. Munoz-Morris, I. Gil, D.G. Morris, Microstructural stability of gamma-based TiAl intermetallics containing beta phase, *Intermetallics*, 13 (2005) 929-936.
- [39] A.J. Huang, D. Hu, M.H. Loretto, X.H. Wu, The formation of grain boundary gamma during cooling of Ti46Al8Nb, *Intermetallics*, 17 (2009) 285-290.
- [40] T.T. Cheng, M.R. Willis, I.P. Jones, Effects of major alloying additions on the microstructure and mechanical properties of gamma-TiAl, *Intermetallics*, 7 (1999) 89-99.

- [41] D. Hu, A.J. Huang, X. Wu, TEM characterisation of Widmanstatten microstructures in TiAl-based alloys, *Intermetallics*, 13 (2005) 211-216.
- [42] W.J. Zhang, L. Francesconi, E. Evangelista, G.L. Chen, Characterization of Widmanstatten laths and interlocking boundaries in fully-lamellar TiAl-base alloy, *Scripta Mater*, 37 (1997) 627-633.
- [43] F.J. Gil, M.P. Ginebra, J.M. Manero, J.A. Planell, Formation of alpha-Widmanstatten structure: effects of grain size and cooling rate on the Widmanstatten morphologies and on the mechanical properties in Ti6Al4V alloy, *J Alloy Compd*, 329 (2001) 142-152.
- [44] H.I. Aaronson, D. Eylon, C.M. Cooke, M. Enomoto, F.H. Froes, The Widmanstatten-Start (Ws) Temperature, as Affected by Matrix Grain Size, in Ti 6-Percent Al 4-Percent-V and in Fe-C Alloys, *Scripta Metall Mater*, 23 (1989) 435-440.
- [45] D. Hu, A.J. Huang, X. Wu, On the massive phase transformation regime in TiAl alloys: The alloying effect on massive/lamellar competition, *Intermetallics*, 15 (2007) 327-332.
- [46] Y.W. Kim, *Journal of Metals*, 40 (1994).
- [47] Y.W. Kim, *Journal of organometallic chemistry*, 46 (1994).
- [48] Y.W. Kim, *Acta Metallurgica and Materialia*, 40 (1992).
- [49] T.T. Cheng, The mechanism of grain refinement in TiAl alloys by boron addition-an alternative hypothesis, *Intermetallics*, 8 (1999) 29-37.
- [50] A.J.H. D. Hu, D. Novovic, X. Wu, The effect of boron and alpha grain size on the massive transformation in Ti-46Al-8Nb-xB alloys, *Intermetallics*, 14 (2006) 818-825.
- [51] Q.F. Xia, J.N. Wang, J. Yang, Y. Wang, On the massive transformation in TiAl-based alloys, *Intermetallics*, 9 (2001) 361-367.
- [52] C.Q.C. C.E. Wen, *Scripta Metallurgica and Materialia*, 33 (1995).
- [53] X.H. Wu, D. Hu, M.H. Loretto, Alloy and process development of TiAl, *J Mater Sci*, 39 (2004) 3935-3940.
- [54] B. Liu, Y. Liu, L. Huang, J.S. Huang, Y.H. Zhang, B.Y. Huang, Effect of trace tungsten on the microstructure of TiAl alloys containing Nb and B, *Rare Metals*, 26 (2007) 323-329.

- [55] U. Prasad, Q. Xu, M.C. Chaturvedi, Effect of cooling rate and manganese concentration on phase transformation in Ti-45 at.% Al based alloys, *Mat Sci Eng a-Struct*, 329 (2002) 906-913.
- [56] R.V.R. P.J. Maziasz, C.T. Liu, J.L. Wright, Effects of B and W alloying additions on the formation and stability of lamellar structures in two-phase gamma-TiAl, *Intermetallics*, 5 (1996) 83-95.
- [57] Y. Mizuhara, K. Hashimoto, N. Masahashi, Microstructure and phase stability of TiAl-W ternary alloy, *Intermetallics*, 11 (2003) 807-816.
- [58] Y. Yamamoto, M. Takeyama, Physical metallurgy of single crystal gamma titanium aluminide alloys: orientation control and thermal stability of lamellar microstructure, *Intermetallics*, 13 (2005) 965-970.
- [59] L.G. Zhou, L. Dong, L.L. He, C.B. Zhang, Ab initio pseudopotential calculations on the effect of Mn doped on lattice parameters of L1(0) TiAl, *Intermetallics*, 8 (2000) 637-641.
- [60] S. Kim, D.J. Larson, G.D.W. Smith, Alloying elements partitioning in TiAl-Ru intermetallic alloys, *Intermetallics*, 7 (1999) 1283-1290.
- [61] G.W. Qin, G.D.W. Smith, B.J. Inkson, R. Dunin-Borkowski, Distribution behaviour of alloying elements in alpha(2)(alpha)/gamma lamellae of TiAl-based alloy, *Intermetallics*, 8 (2000) 945-951.
- [62] A.K. Singh, S. Azad, R.K. Mandal, Effect of Mo addition on transformation behavior of (alpha(2)+gamma) based Ti-Al alloys, *Mat Sci Eng a-Struct*, 429 (2006) 219-224.
- [63] W. Wolf, R. Podlucky, P. Rogl, H. Erschbaumer, Atomic modelling of Nb, V, Cr and Mn substitutions in gamma-TiAl .2. Electronic structure and site preference, *Intermetallics*, 4 (1996) 201-209.
- [64] R. Yu, L.L. He, Z.Y. Cheng, J. Zhu, H.Q. Ye, B2 precipitates and distribution of W in a Ti-47Al-2W-0.5Si alloy, *Intermetallics*, 10 (2002) 661-665.
- [65] H.R. Jiang, M. Hirohase, Y. Lu, H. Imanari, Effect of Nb on the high temperature oxidation Ti-(0-50 at.%)Al, *Scripta Mater*, 46 (2002) 639-643.
- [66] M. Yoshihara, K. Miura, Effects of Nb Addition on Oxidation Behavior of Tial, *Intermetallics*, 3 (1995) 357-363.
- [67] D.G. Konitzer, I.P. Jones, H.L. Fraser, Site Occupancy in Solid-Solutions of Nb in the Intermetallic Compounds Tial and Ti3al, *Scripta Metall Mater*, 20 (1986) 265-268.
- [68] J.D.B. S.L. Kampe, L.Christoudoulou, *Metallurgical transactions*, 22 (1991).

- [69] A.B. C. Koeppe, J. Seeger, H. Mecking, metallurgical transactions, 24 (1993).
- [70] A.K.G. D. Banerjee, T.K. Nandy, K. Muraleedharan, R.S. Mishra, Structural intermetallics, The minerals, metals and materials society, (1993) 19-33.
- [71] H. Shankar, N.E. Prasad, A.K. Singh, T.K. Nandy, Low temperature flow behavior of B2 intermetallic phase in Ti-Al-Nb system, Mat Sci Eng a-Struct, 424 (2006) 71-76.
- [72] F. Ebrahimi, J.G.L. RuizAparicio, Diffusivity in the Nb-Ti-Al ternary solid solution, J Alloy Compd, 245 (1996) 1-9.
- [73] D.T. Hoelzer, Phase transformations in the central portion of the Nb-Ti-Al ternary system, PhD Dissertation, University of Florida, Gainesville, (1996).
- [74] M.P. Brady, B. Gleeson, I.G. Wright, Alloy design strategies for promoting protective oxide scale formation, Jom-J Min Met Mat S, 52 (2000) 16-21.
- [75] A.K. Singh, S. Banumathy, R.K. Mandal, Structure of orthorhombic martensitic phase in binary Ti-Nb alloys, J Appl Phys, 106 (2009).
- [76] D. Banerjee, The intermetallic Ti<sub>2</sub>AlNb, Prog Mater Sci, 42 (1997) 135-158.
- [77] V.K. Vasudevan, K.J. Leonard, R. Tewari, A. Arya, J.C. Mishurda, G.K. Dey, Decomposition of the PO phase to the P6(3)/mcm, hP18 structure in Nb-(24-36)Ti-40Al alloys, Acta Mater, 57 (2009) 4440-4453.
- [78] W.J.B. L.A. Bendersky, Transformation of BCC and B2 high temperature phases to HCP and orthorhombic structures in the Ti-Al-Nb system. Part II: Experimental TEM study of microstructures, Journal of research of the national institute of standards and technology, 98 (1993).
- [79] W.J.B. L.A. Bendersky, F.S. Biancanello, Intermetallic Ti-Al-Nb alloys based on strengthening of the orthorhombic phase by omega-type phases, Materials Science and Engineering A, A152 (1992) 41-47.
- [80] L.A. Bendersky, W.J. Boettinger, B.P. Burton, F.S. Biancanello, C.B. Shoemaker, The Formation of Ordered Omega-Related Phases in Alloys of Composition Ti<sub>4</sub>Al<sub>3</sub>Nb, Acta Metallurgica Et Materialia, 38 (1990) 931-943.
- [81] Y. Murakami, T. Yano, D. Shindo, Y. Hayasaka, S. Kuramoto, Transmission electron microscopy studies on nanometer-sized omega phase produced in Gum Metal, Scripta Mater, 63 (2010) 536-539.
- [82] F. Ebrahimi, D.T. Hoelzer, J.R. Castillogomez, Fracture-Toughness of Sigma+X Microstructures in the Nb-Ti-Al System, Mat Sci Eng a-Struct, 171 (1993) 35-45.

- [83] F. Ebrahimi, B.J.G. Dearagao, J.R. Castillogomez, Evaluation of Fracture-Toughness of Duplex Microstructures by an Indentation Technique, *Mat Sci Eng a-Struct*, 177 (1994) L7-L10.
- [84] F. Ebrahimi, J.R. Castillogomez, The Effect of Plastic-Deformation on Fracture Morphology of the Sigma-Phase in the Nb-Ti-Al System, *Acta Metallurgica Et Materialia*, 40 (1992) 1409-1416.
- [85] B.J.G. deAragao, F. Ebrahimi, High temperature deformation of Nb-Ti-Al alloys with sigma+gamma microstructure, *Mat Sci Eng a-Struct*, 208 (1996) 37-46.
- [86] D. Banerjee, T.K. Nandy, A.K. Gogia, Site Occupation in the Ordered Beta Phase of Ternary Ti-Al-Nb Alloys, *Scripta Metall Mater*, 21 (1987) 597-600.
- [87] K. Das, S. Das, Order-disorder transformation of the body centered cubic phase in the Ti-Al-X (X = Ta, Nb, or Mo) system, *J Mater Sci*, 38 (2003) 3995-4002.
- [88] J.L.T. P. Duwez, Crystal structure of TiAl, *Journal of Metals*, 4 (1952).
- [89] S.L.A. E.O Hall, Sigma Phase, *Journal of the institute of metals*, 94 (1966).
- [90] W.J.B. L.A. Bendersky, Transformation of BCC and B2 high temperature phases to HCP and orthorhmbc structures in the Ti-Al-Nb system. Part I, *Journal of research of the national institute of standards and technology*, 98 (1993).
- [91] J.C. Mishurda, V.K. Vasudevan, An estimate of the kinetics of the beta(0) to orthorhombic phase transformation in the Nb-Ti-Al system, *Scripta Mater*, 45 (2001) 677-684.
- [92] O.Rios, Examination of the high temperature equilibrium in the Ti-Al-Nb ternary alloy system, PhD Dissertation, University of Florida, Gainesville, (2009).
- [93] T.F. H.I. Aaronson, W.T. Reynolds Jr., On the mechanism of formation of diffusional plate-shaped transformation products, *Acta Mater*, 54 (2005) 1227-1232.
- [94] B.C.M. H.I. Aaronson, J.F. Nie, On recent developments in the debate about the formation mechanism of precipitate plates, *Scripta Mater*, 41 (1999) 203-208.
- [95] M.B. S. Tournier, D.M. Herlach, B. Vinet,, *Acta Mater*, 4 (1997) 191.
- [96] S.G. Michael S. Kesler, Orlando Rios, Damian M. Cupid, Hand J. Seifer, Fereshteh Ebrahimi, A study of phase transformation in a TiAlNb alloy and effect of Cr addition, *Materials Science and Engineering A*, 527 (2010) 2857-2863.
- [97] F. Ebrahimi, S. Goyel, O. Rios, M.S. Kesler, Two-step nucleation of the gamma-phase in a Ti-45Al-18Nb alloy, *Intermetallics*, 18 (2010) 1491-1497.

- [98] D.A. Mortimer, Segregation of Boron to grain boundaries in iron and a stainless steel, *Journal De Physique*, C4 (1975) 137.
- [99] C.J. McMahon, The role of solute segregation in promoting the hardenability of steel, *Metallurgical transactions*, 11A (1980) 531.
- [100] C.J.M. T. Ogura, Jr H.C. Feng, V.Vitek, Structure dependent intergranular segregation of phosphorus in austenite in a Ni-Cr steel, (1978) 1317.
- [101] G.K. Teiichi Ando, The effect of phosphorus content on grain boundary cementite formation in AISI 52100 steel, *Metallurgical transactions*, 12A (1981) 1283.
- [102] L.S. K. Sickafus, Observation of a grain boundary phase transformation induced by solute segregation, *Journal of Vac. Science and Technology*, 3 (1985) 1525.
- [103] T.M. T. Watanabe, S. Karashima, Misorientation dependence of grain boundary segregation, *Scripta Mater*, 12 (1978) 361-365.

## BIOGRAPHICAL SKETCH

Sonalika Goyel was the first child of Jawahar Goyel and Asha Goyel and was born in New Delhi, India. She attended the prestigious Sardar Patel Vidyalaya in New Delhi from kindergarten through class XII. She maintained an excellent academic record throughout her school and was an all rounder. She won many accolades in dramatics, poetry writing/recitation, dancing, choreography, singing, writing and public speaking. She was the school topper and state rank holder in the All India board exams conducted by the CBSE in 2000. After finishing schooling in 2002 she was selected as the state nominee, due to her exceptional academic and extra-curricular record, to attend undergraduate college education in the department of Metallurgical and Materials Engineering at the prestigious Bengal Engineering College, West Bengal. During her four years of undergraduate study in materials, she maintained an excellent academic record was one of the 25 students who graduated with Honors out of a batch of more than 400 students in the summer of 2006. During the undergraduate years, she discovered her interest in the field of metals, alloys and modern materials and thus decided to pursue further studies in the field. She came to the U.S. to pursue her MS in the fall 2006 with the aim of pursuing her PhD subsequently. She was offered the Alumni Fellowship by Dr. Fereshteh Ebrahimi and thus entered the direct PhD program offered by the department. She worked on her courses and research work from the fall of 2006 to 2010 and defended her dissertation in the spring of 2011.